Quantum dissipation and decoherence of collective excitations in metallic nanoparticles

Guillaume Weick

Quantum dissipation and decoherence of collective excitations in metallic nanoparticles

— Guillaume Weick —

A dissertation submitted to
Université Louis Pasteur, Strasbourg I
&
Universität Augsburg
for the degrees of
Docteur de l'Université Louis Pasteur, Strasbourg I
(Spécialité : Physique de la matière condensée)
&
Doktor der Naturwissenschaften
der Mathematisch-Naturwissenschaftlichen Fakultät der Universität Augsburg

Thesis defence in Strasbourg, 22 September 2006 in front of the jury comprising

Supervisor ULP:	Prof. Rodolfo A. Jalabert (IPCMS, Strasbourg)
Supervisor Augsburg:	Prof. Gert-Ludwig Ingold (Institut für Physik, Augsburg)
Referees:	Dr. Jean-Yves Bigot (IPCMS, Strasbourg)
	Prof. Ulrich Eckern (Institut für Physik, Augsburg)
	Prof. Éric Suraud (IRSAMC, Toulouse)
Examiner:	Prof. Hermann Grabert (Physikalisches Institut, Freiburg)
Invited member:	Dr. Dietmar Weinmann (IPCMS, Strasbourg)

À Caroline

Contents

Remerciements (acknowledgments in French)

Je souhaite tout d'abord, et comme il se doit, remercier les membres du jury qui ont accepté de lire et juger cette thèse, à savoir Jean-Yves Bigot, Ulrich Eckern, Éric Suraud, Hermann Grabert, et Dietmar Weinmann.

J'aimerais exprimer toute ma gratitude à mes deux directeurs de thèse, Rodolfo Jalabert et Gert Ingold. Durant ces trois années, ils m'ont constamment supporté et guidé dans mes recherches. Cela a été un grand plaisir de discuter avec eux de physique, mais également de bien d'autres choses. Merci à Rodolfo entre autres de m'avoir initié à la « religion » de la physique semiclassique, de m'avoir appris comment aborder un problème de physique si complexe qu'il semble de prime abord insurmontable, et d'avoir guidé mon intuition lorsqu'il s'agissait de calculer une affreuse intégrale (« Prenez la limite semiclassique ! »). Merci à Gert notamment pour sa grande rigueur scientifique et pour m'avoir appris l'art de rédiger un article de façon lisible (promis Gert, plus de parenthèses : ça coûte trop cher !)

Un grand merci à Dietmar Weinmann pour son soutien tout au long de cette thèse, ainsi que pour son écoute et ses conseils constants. Merci également pour les sessions d'escalade qui permettent de penser à autre chose qu'à la physique !

Merci à Rafael Molina pour notre collaboration fructueuse, pour son aide avec le code numérique TDLDA, et pour notre quête sans relâche du désormais fameux « facteur de trois. » Merci également à Axel Freyn pour son aide durant l'élaboration du code numérique de diagonalisation exacte.

Je tiens à remercier Valérie Halté et Jean-Yves Bigot pour nos discussions sur les expériences de type pompe-sonde, ainsi que Paul-Antoine Hervieux pour nos entretiens fructueux sur bien des aspects des nanoparticules métalliques. Merci également à François Gautier pour ses conseils et réflexions toujours très avisés, ainsi qu'à Sigmund Kohler pour son expertise sur les équations maîtresses.

Mention spéciale à mes collègues de l'IPCMS et de l'Institut für Physik d'Augsburg, notamment à Peter Falloon, Michael Schindler, Gerhard Schmid, Michael Straß, Ralf Utermann, et Gabriel Vasseur.

Un grand merci à André Bieber et Jean-Pierre Münch pour leurs conseils et soutien tout au long de mes études à Strasbourg.

Je remercie le soutien financier du Deutscher Akademischer Austausch Dienst (DAAD) et d'Égide (programme Procope), du Centre de Coopération Universitaire Franco-Bavarois / Bayerisch-Französisches Hochschulzentrum (CCUFB/BFHZ), et de l'Université

Franco-Allemande / Deutsch-Französische Hochschule (UFA/DFA).

Je remercie tout particulièrement ma famille pour son soutien durant toutes ces années, spécialement ma mère et mes grands-parents, ainsi que tous mes amis que je ne vais pas énumérer ici (la liste est trop longue, mais ils se reconnaîtront d'eux-mêmes.)

Enfin, tout mon amour à Caroline, sans qui cette thèse aurait été bien plus difficile à achever.

Summary

Metallic nanoparticles are an ideal laboratory for the study of electronic correlations in the transition regime between microscopic and macroscopic systems. Consequently, their optical properties which depend on those correlations are currently intensively studied. Furthermore, the proposed applications of metallic nanoparticles (electro-optical devices, biological markers, nonvolatile memories, etc.) render crucial the comprehension of the optical properties of those objects. Pump-probe experiments permit to address directly the electronic degrees of freedom and to study the dynamics of the relaxation after a strong excitation in those mesoscopic systems.

The excitation of a nanoparticle by a laser pulse creates a collective mode of the electrons, the so-called *surface plasmon*. It decays because of surface effects and electron-electron interactions, creating particle-hole excitations (Landau damping). The thermal equilibrium of the electronic system is reached after about hundred femtoseconds, and only on a much larger time scale, the electron-phonon interactions permit the relaxation of the electronic energy to the ionic lattice.

The treatment of the surface plasmon as a quantum particle provides a model system for the study of decoherence and quantum dissipation in confined nanoscopic systems, where the role of the electronic correlations is preponderant.

Throughout this work we treat the metallic nanoparticle in the jellium approximation where the ionic structure is replaced by a continuous and homogeneous positive charge. Such an approximation allows to decompose the electronic Hamiltonian into a part associated with the electronic center of mass, a part describing the relative coordinates (treated here in the mean-field approximation), and finally a coupling between the two subsystems. The external laser field puts the center of mass into a coherent superposition of its ground and first excited state and thus creates a surface plasmon. The coupling between the center of mass and the relative coordinates causes decoherence and dissipation of this collective excitation.

We have developed a theoretical formalism well adapted to the study of this dissipation, which is the reduced-density-matrix formalism. Indeed, writing the general evolution of the density matrix of the total system, one can, by eliminating the environmental degrees of freedom (the relative coordinates in our case), deduce the equations of the temporal evolution of the center-of-mass system. Within the Markovian approximation (where the memory effects are neglected), one is then able to solve analytically or numerically these equations. There are mainly two parameters which govern the surface

plasmon dynamics: the decay rate of the plasmon (its inverse giving the lifetime of the collective excitation), and the resonance frequency.

An experimentally accessible quantity is the photoabsorption cross section of the metallic cluster, where the surface plasmon excitation appears as a broad resonance spectrum. The width of the plasmon resonance peak (the decay rate) is a quantity that one can determine in different manners. A numerical approach consists of the resolution of the time-dependent Kohn-Sham equations in the local density approximation (TDLDA).[1] This yields the absorption spectrum for a given nanoparticle size, and one can then deduce the lifetime of the surface plasmon excitation. For nanoparticle sizes larger than approximately 1 nm, the width γ of the peak follows Kawabata and Kubo's law which predicts that γ is proportional to the inverse size of the nanoparticle. For sizes smaller than 1 nm, γ presents oscillations as a function of the size, consistently with existing experimental data. By means of a semiclassical formalism using Gutzwiller's trace formula for the density of states, we have shown that those oscillations are due to the correlations of the density of states of the particles and holes in the nanoparticle. The semiclassical theory reproduces quantitatively the numerical calculations.

If one considers a noble-metal nanoparticle (where one has to take into account the screening of the s-electrons by the d-electrons) in an inert matrix (for example a glass matrix), we have shown that a naive application of the Kubo formula for the surface plasmon linewidth fails to reproduce the TDLDA numerical results, which are however consistent with experimental results. We have modified the Kubo theory in order to solve this discrepancy. Indeed, it is necessary to take into account the details of the mean-field potential (that one can obtain from the LDA calculations), especially its slope at the nanoparticle-matrix interface.

If the intensity of the exciting laser field is sufficiently strong, one can ask the question if it is possible to have an excitation of the second quantum level of the center of mass, that we call *double plasmon*. This is possible if this second excited state is well defined, i.e., its width is sufficiently small compared to the other energy scales of the system. Up to now it has not been possible to answer this question from the experimental point of view, although indirect observations could render imaginable the existence of such a collective state. We have shown, by extending our semiclassical theory to the nonlinear case, that the double plasmon is indeed well defined. In certain cases, the electronic ionization can result from the excitation of the double plasmon, and this is observed in experiments. We have calculated the lifetime of the double plasmon associated to this second-order effect, and the obtained values are in qualitative agreement with the existing experiments.

In addition to the width, we have also addressed the value of the resonance frequency. The classical electromagnetic Mie theory gives for the resonance frequency of the surface plasmon the plasma frequency of the considered metal, divided by a geometrical factor $\sqrt{3}$. However, the experimentally observed frequency is redshifted relative to the classical frequency. One usually attributes this shift to the spill-out effect that we have calculated semiclassically. The electronic density of the ground state extends outside

[1] TDLDA: Time-Dependent Local Density Approximation.

of the nanoparticle, resulting in the decrease of the electronic density inside the cluster compared to its bulk value. This has the consequence to redshift the resonance frequency. We have shown by means of perturbative calculations that the coupling to the electronic environment produces an additional redshift of the surface plasmon resonance. This phenomenon is analogous to the Lamb shift in atomic systems. Both effects, spill-out and Lamb shift, have to be taken into account in the description of the numerical and experimental results.

Furthermore, we have extended our semiclassical calculations of the linewidth of the surface plasmon peak, of the spill-out, and of the environment-induced shift to the case of finite temperatures. We have shown that when the temperature increases, there is a broadening of the lineshape of the surface plasmon, as well as an additional redshift of the resonance frequency compared to the zero-temperature case. Even though the effect of the temperature is weak, it is essential for the comprehension of the electronic thermalization in pump-probe experiments. The study of the effect of the temperature has allowed us to qualitatively explain the differential transmission curves measured in time-resolved experiments.

Related publications

- G. Weick, R. A. Molina, D. Weinmann, and R. A. Jalabert, *Lifetime of the first and second collective excitations in metallic nanoparticles*, Phys. Rev. B **72**, 115410 (2005).
- G. Weick, G.-L. Ingold, R. A. Jalabert, and D. Weinmann, *Surface plasmon in metallic nanoparticles: renormalization effects due to electron-hole excitations*, arXiv:cond-mat/0605389, Phys. Rev. B, in press (2006).
- G. Weick, D. Weinmann, G.-L. Ingold, and R. A. Jalabert, *Anomaly of the relaxation dynamics close to the surface plasmon resonance*, in preparation.
- G. Weick, G.-L. Ingold, R. A. Jalabert, and D. Weinmann, *Resonance fluorescence of the surface plasmon in metallic nanoparticles*, in preparation.

Résumé

Les nanoparticules métalliques sont un laboratoire idéal pour l'étude des corrélations électroniques dans la transition entre les systèmes microscopiques et macroscopiques. En conséquence, leurs propriétés optiques, qui relèvent de ces corrélations, sont étudiées intensivement à l'heure actuelle. De plus, les applications proposées des nanoparticules métalliques (dispositifs électro-optiques, marqueurs biologiques, mémoires non-volatiles, etc.) rendent la compréhension des propriétés optiques de ces objets cruciale. Les expériences de type pompe-sonde permettent d'adresser directement les degrés de liberté électroniques et d'étudier la dynamique de relaxation après une forte excitation dans ces systèmes mésoscopiques.

L'excitation d'une nanoparticule par une impulsion laser résulte en un mode collectif des électrons, le *plasmon de surface*. Celui-ci décroît à cause des effets de surface et des interactions électron-électron, donnant lieu à des excitations du type particule-trou (amortissement de Landau). L'équilibre thermique du système électronique est atteint après environ une centaine de femtosecondes, et seulement sur des échelles de temps beaucoup plus longues, les interactions électron-phonon permettent la relaxation de l'énergie électronique vers le réseau ionique.

Le traitement du plasmon de surface comme une particule quantique fournit un système modèle pour l'étude de la décohérence et de la dissipation quantique dans les systèmes nanoscopiques confinés, où le rôle des corrélations électroniques est prépondérant.

Tout au long de ce travail, nous traitons la nanoparticule métallique dans l'approximation du jellium où la structure ionique est remplacée par une charge positive continue et homogène. Une telle approximation permet de décomposer le hamiltonien électronique en une partie associée au centre de masse électronique, une partie décrivant les coordonnées relatives (traitées ici dans l'approximation du champ moyen), et enfin une partie de couplage entre les deux sous-systèmes. Le champ laser extérieur place le centre de masse dans une superposition cohérente de son état de base et de son premier état excité, et créé de la sorte un plasmon de surface. Le couplage entre le centre de masse et les coordonnées relatives cause la décohérence et la dissipation de cette excitation collective.

Nous avons développé un formalisme théorique bien adapté à l'étude de cette dissipation, qui est le formalisme de la matrice densité réduite. En effet, écrivant l'évolution générale de la matrice densité du système total, on peut, en éliminant les degrés de liberté de l'environnement (les coordonnées relatives dans notre cas), en déduire les équations

d'évolution temporelle du système centre de masse. Dans le cadre de l'approximation markovienne (où les effets de mémoires sont négligés), on est alors capable de résoudre analytiquement ou numériquement ces équations. Il y a principalement deux paramètres qui régissent la dynamique du plasmon de surface : le taux d'amortissement du plasmon (son inverse donnant le temps de vie de l'excitation collective), et la fréquence de la résonance.

Une quantité accessible expérimentalement est la section efficace de photo-absorption de la nanoparticule métallique, où le plasmon de surface apparaît comme un large spectre de résonance. La largeur du pic de résonance plasmon (le taux d'amortissement) est une quantité que l'on peut extraire microscopiquement de différentes manières. Une approche numérique consiste à résoudre les équations de Kohn-Sham dépendantes du temps dans l'approximation locale (TDLDA).[2] Ceci donne alors le spectre d'absorption pour une taille de nanoparticule donnée, et l'on peut alors en déduire le temps de vie associé au plasmon de surface. Pour des tailles de nanoparticules supérieures à environ 1 nm, la largeur γ du pic suit la loi de Kawabata et Kubo, qui prédit que γ est proportionnel à l'inverse de la taille de la particule. Pour des tailles plus petites que 1 nm, γ présente des oscillations en fonction de la taille, en accord avec les données expérimentales existantes. Grâce à un formalisme semiclassique utilisant la formule de trace de Gutzwiller pour la densité d'états, nous avons montré que ces oscillations sont dues aux corrélations de densité d'états entre les particules et les trous dans la nanoparticule. La théorie semiclassique reproduit quantitativement les calculs numériques.

Si l'on considère une nanoparticule de métal noble (où l'on doit prendre en compte l'écrantage des électrons s par les électrons d) dans une matrice inerte (par exemple en verre), nous avons montré qu'une application naïve de la formule de Kubo pour la largeur de raie du plasmon de surface ne permet pas de reproduire les résultats numériques TDLDA, qui sont eux-mêmes en accord avec les résultats expérimentaux. Nous avons modifié la théorie de Kubo afin de résoudre ce désaccord. En effet, il faut prendre en compte les détails du potentiel de champ moyen (que l'on peut obtenir numériquement grâce aux calculs de type Kohn-Sham), notamment la pente de celui-ci à l'interface nanoparticule-matrice environnante.

Si l'intensité du laser excitateur est suffisament forte, on est en droit de se demander s'il est possible d'avoir une excitation du deuxième niveau quantique du centre de masse électronique, que l'on appelle *double plasmon*. Ceci est possible si ce deuxième niveau excité est bien défini, c'est-à-dire s'il a une largeur suffisamment faible par rapport aux autres échelles d'énergie du système. Jusqu'à présent, il n'a pas été possible de répondre à cette question d'un point de vue expérimental, bien que des observations indirectes pourraient rendre envisageable l'existence d'un tel état. Nous avons montré, en étendant notre théorie semiclassique au cas non linéaire, que le double plasmon est en effet bien défini. Dans certains cas, la ionisation électronique peut résulter de l'excitation du double plasmon, et ceci est observé expérimentalement. Nous avons calculé le temps de vie du double plasmon associé à cet effet du second ordre, et obtenu des valeurs en accord qualitatif avec les expériences existantes.

[2]TDLDA : Time-Dependent Local Density Approximation.

En plus de la largeur, nous avons également analysé la valeur de la fréquence de résonance. La théorie électromagnétique classique de Mie donne pour la fréquence de résonance du plasmon de surface la fréquence plasma du métal considéré, que divise un facteur géométrique $\sqrt{3}$. Or, la fréquence observée expérimentalement est décalée vers le rouge par rapport à la fréquence classique. On attribue généralement ce décalage à l'effet de « spill-out » que nous avons calculé semiclassiquement. La densité électronique de l'état de base s'étend à l'extérieur de la nanoparticule, ce qui a pour conséquence de diminuer la densité électronique à l'intérieur de la particule par rapport à sa valeur du massif. La fréquence de résonance est alors décalée vers le rouge par l'effet de spill-out. Nous avons montré grâce à des calculs pertubatifs que l'environnement électronique produit un décalage vers le rouge supplémentaire de la résonance du plasmon de surface. Ce phénomène est analogue au décalage de Lamb dans les systèmes atomiques. Les deux effets, spill-out et décalage de Lamb, doivent être pris en compte pour la description des résultats numériques et expérimentaux.

De plus, nous avons étendu nos calculs semiclassiques de la largeur de raie du pic plasmon, du spill-out et du décalage de Lamb, au cas de températures finies. Nous avons montré que lorsque la température augmente, le pic du plasmon de surface s'élargit et la fréquence du plasmon est encore plus décalée vers le rouge par rapport au cas à température nulle. Bien que l'effet de la température soit faible, celui-ci est indispensable à la compréhension de la thermalisation électronique dans les expériences de type pompe-sonde. L'étude de l'effet de la température nous a de la sorte permis d'expliquer qualitativement les courbes de transmission différentielle observées dans les expériences résolues en temps de type pompe-sonde.

Chapter 1

Introduction

La liberté est pour la Science ce que l'air est à l'animal.

(Henri Poincaré, 1854-1912, in Dernières Pensées)

The understanding of electronic and optical properties of artificial structures at the nanometer scale is one of the great challenges of contemporary physics. In this age of miniaturization of electronic devices, a need for the comprehension of their properties has emerged, both on the fundamental and practical levels. Metallic nanoparticles are aggregates composed of a relatively small number of atoms, starting with clusters consisting of a few atoms to large nanoparticles with more than 10^5 atoms (see Fig. 1.1). Thus, these objects are intermediate in size between the domain of atoms and small molecules, which require a full quantum mechanical treatment, and the bulk, where the standard tools of solid-state and statistical physics can be applied. Metallic nanoparticles could therefore answer the old question: "How many atoms does it take to make a solid?"

At the mesoscopic scale between the microscopic and macroscopic worlds, matter exhibits a wide number of new and interesting phenomena. This is due to two main elements. Firstly, the spectrum of the electronic states at this scale is discrete, although the interaction of the system with the environment may broaden the energy levels. Secondly, the motion of the electrons is coherent: An electron can propagate through the whole system without experiencing inelastic or phase-breaking scattering. Thus, the phase of its wave function remains well-defined, opening the possibility to observe interferences and coherent behavior.[1]

In metallic nanoparticles, the most striking evidence of the quantization of the electronic states in the confinement created by the ions and the remaining electrons is the so-called *electronic shell structure* which was observed by Knight *et al.* in 1984 [5]. In Fig. 1.2, we reproduce the experimental results of Ref. 5. The top panel shows a continuous mass spectrum of sodium clusters with number of atoms $N = 4$–75, and a separate

[1]For a review of mesoscopic phenomena, see, e.g., Refs. 1–4.

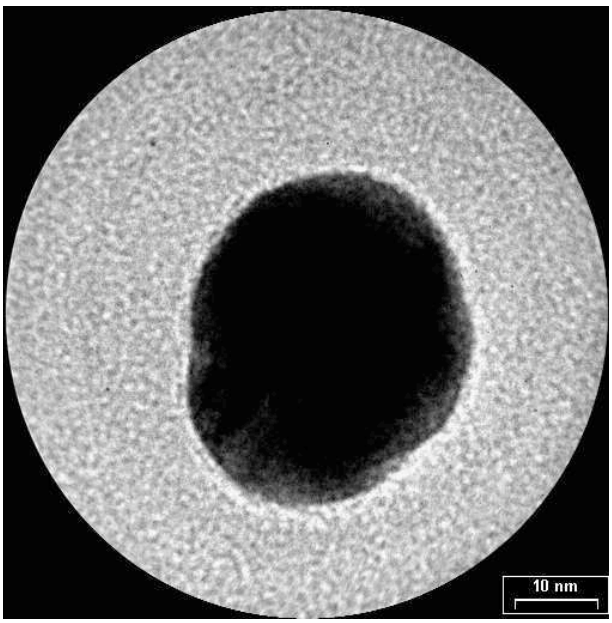

Figure 1.1: Image of a single gold nanoparticle (dark central spot) of size $\sim$ 30 nm obtained by transmission electron microscopy (courtesy of J.-Y. Bigot and collaborators).

mass scan for $N = 75$–100. Each peak represents the number of clusters of fixed size N detected during a fixed time interval in a molecular beam of sodium seeded in argon. Large steps or peaks appear for certain masses, corresponding to $N = 8$, 20, 40, 58, and 92. The authors explained the stability of these special clusters by means of a model similar to the well-known nuclear shell model [6, 7]. They assumed that the valence electrons are confined in a spherically symmetric effective (or mean-field) one-electron potential of the Woods-Saxon form [8]

$$V(r) = -\frac{V_0}{\exp\left[(r-a)/\alpha\right]+1}, \tag{1.1}$$

where $V_0 = \varepsilon_\mathrm{F} + W$ is the sum of the Fermi energy ε_F and the work function W. We denote by $a = r_\mathrm{s}N^{1/3}$ the effective radius of the cluster sphere, where $r_\mathrm{s} = (3/4\pi n_\mathrm{e})^{1/3}$ is the mean distance between electrons [9],[2] and n_e being the bulk electronic density. The parameter α accounts for the variation of the potential at the edge of the sphere. Solving numerically the Schrödinger equation for this potential, they obtained the electronic energy $E(N)$ for each cluster with N atoms by summing the eigenenergies of the occupied states. Defining $\Delta(N) = E(N) - E(N-1)$ as the difference in electronic energy between adjacent states, they obtained the result depicted in Fig. 1.2b. They concluded that the peaks or steps at some special numbers of atoms N are related to the electronic properties of the clusters: The most stable clusters have filled angular-momentum shells. One calls

[2]The parameter r_s is sometimes also called the Wigner-Seitz radius.

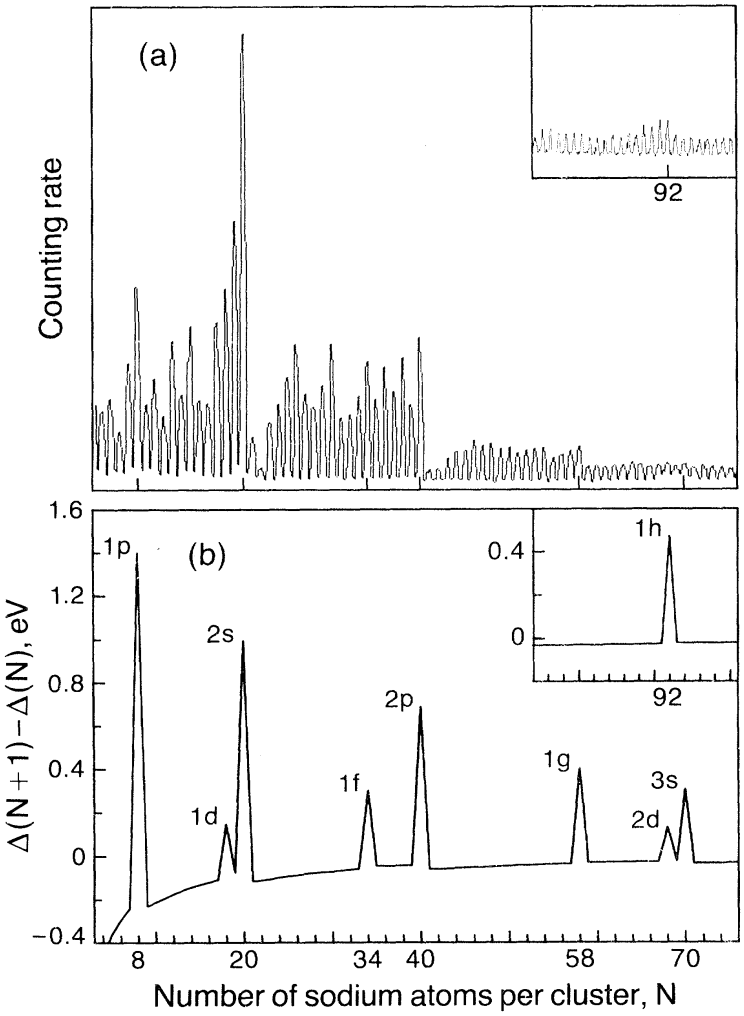

Figure 1.2: (a) Mass spectrum of sodium clusters with number of atoms N between 4 and 75 (inset: $N = 75$–100). (b) Calculated change in the energy difference $\Delta(N+1) - \Delta(N)$ as a function of N (see text). The labels of the peaks correspond to the closed angular-momentum shells (in spectroscopic notation, where s, p, d, ... correspond to $l = 0, 1, 2, \ldots$). (Reproduced from Ref. 5.)

those special numbers "magic numbers" because of the analogy with atomic physics. It turns out that a sphere is a reasonable approximation for electronically closed-shell nanoparticles [10,11]. However, for open-shell structures, the spherical shape is unstable since distortions occur due to the Jahn-Teller effect [10,12]. In this thesis, we will restrict ourselves to the study of spherical nanoparticles.

A powerful technique, both experimentally and theoretically, to analyze some of the electronic properties of a metallic nanoparticle, is to study the response of the system to an external perturbation. Electromagnetic fields provide one of the most impor-

tant methods for probing such many-particle systems. In this context, we will restrict ourselves in this thesis to the optical properties of metallic clusters.

1.1 Surface plasmon excitation

One of the most prominent features of a metallic nanoparticle subject to an external driving field is a collective electronic excitation, the so-called *surface plasmon* [10,11,13–16]. From a fundamental point of view, surface plasmons appear as interesting resonances to study given the various languages that we can use for their description, which are associated with different physical images. In Fig. 1.3, we schematize such a collective effect. An external electrical field, whose wavelength is much larger than the size of the nanoparticle, exerts a force on the valence electrons and on the ions which constitute the metallic cluster. Since the mass of the ions is three orders of magnitude larger than the one of the electrons, the ions remain fixed while the electrons are displaced from their equilibrium positions. This creates uncompensated charges at the surface of the nanoparticle as depicted in Fig. 1.3, and due to the restoring force felt by the electrons, the electronic cloud oscillates around its equilibrium position. The origin of the term *surface plasmon* stems from the fact that, although all the electrons are oscillating with respect to the positive ionic background, the main effect producing the restoring force is the polarization of the surface. As we will see, the collective surface plasmon excitation has a finite lifetime, as well as a well-defined resonance frequency.

A very similar collective effect exists in nuclei. There, the external electromagnetic field produces a force acting on the positively charged protons, thus separating them from the neutrons. The nuclear restoring force results in an oscillation of the protons with respect to the neutrons. This is the so-called *giant dipole resonance* of nuclei [6,7,16,17]. This resonance is quite sharp in nuclei like the one of oxygen [7], even if its energy appears in the continuum of unbound single-particle states [16].

An experimentally accessible quantity is the photoabsorption cross section. It is the probability that the system absorbs a photon multiplied by the area illuminated by the photon beam. From the electronic shell structure of metallic nanoparticles depicted above, one could expect, in analogy with atoms, that the optical spectral features relate to transitions between the single-particle states of the shell model. However, it turns out that the absorption spectra are dominated by the collective surface plasmon resonance. The experimental photoabsorption cross section of singly-charged lithium clusters of various sizes [18] is shown in Fig. 1.4. In this typical experiment on alkaline metals, the clusters are formed in beams and probed with photons while still in the beam. This condition is needed since alkaline clusters are quite fragile and chemically reactive, and thus would disappear on contact with a surface or with another particle. The photoabsorption cross section appears as a broad spectrum centered around a resonance frequency of several eV corresponding to the visible range. The same kind of feature appears in experiments on noble-metal clusters made for instance of gold or silver. In those experiments, the clusters are embedded in an inert matrix (e.g., a glass matrix) [13]. This is possible since noble metals are much more stable than alkaline metals. Unlike

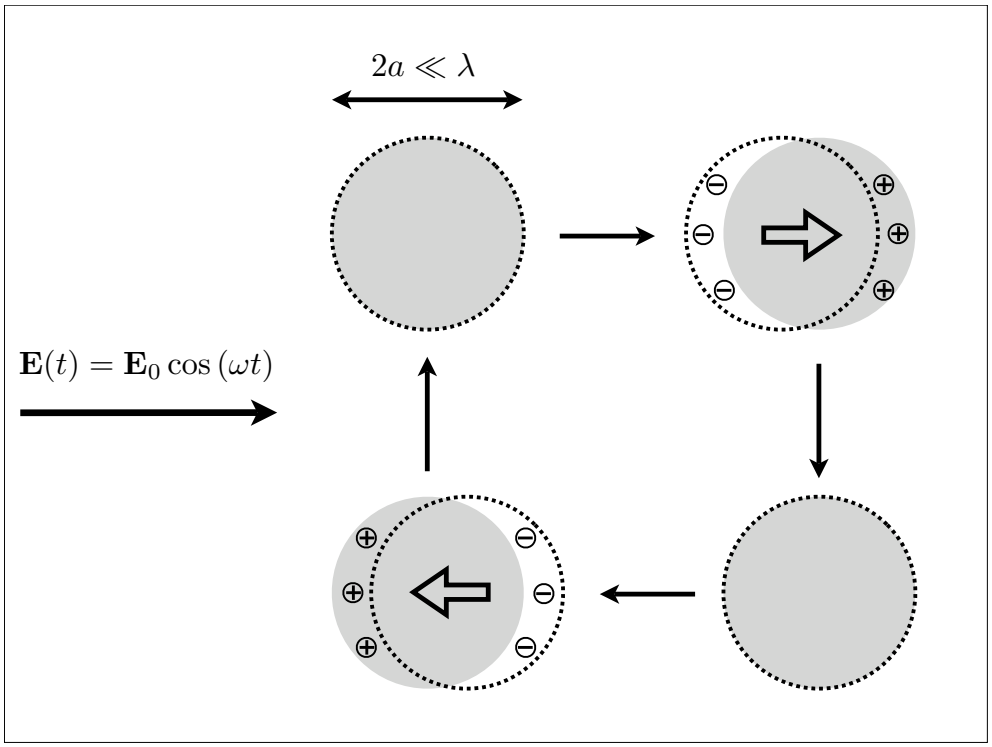

Figure 1.3: Schematic representation of the surface plasmon resonance in small metallic nanoparticles. The wavelength λ of the exciting electrical field $\mathbf{E}(t)$ is much larger than the diameter $2a$ of the cluster. Thus, the electrical field penetrating the nanoparticle is nearly uniform. The gray regions symbolize the ionic background, while the dashed circles represent the electronic cloud. The "−" and "+" signs account for the negative and positive charges which are not compensated. The electrical field exerts a force on the positively charged ions and an equal force on the electrons in the opposite direction. Since the mass of the ions is three orders of magnitude larger than the one of the electrons, the ions are almost at rest while the electronic cloud oscillates around the equilibrium position, due to the restoring force exerted by the uncompensated charges.

the case of giant dipole resonances of nuclei, surface plasmons in metallic nanoparticles are generally in the energy range corresponding to bound single-particle states [16].

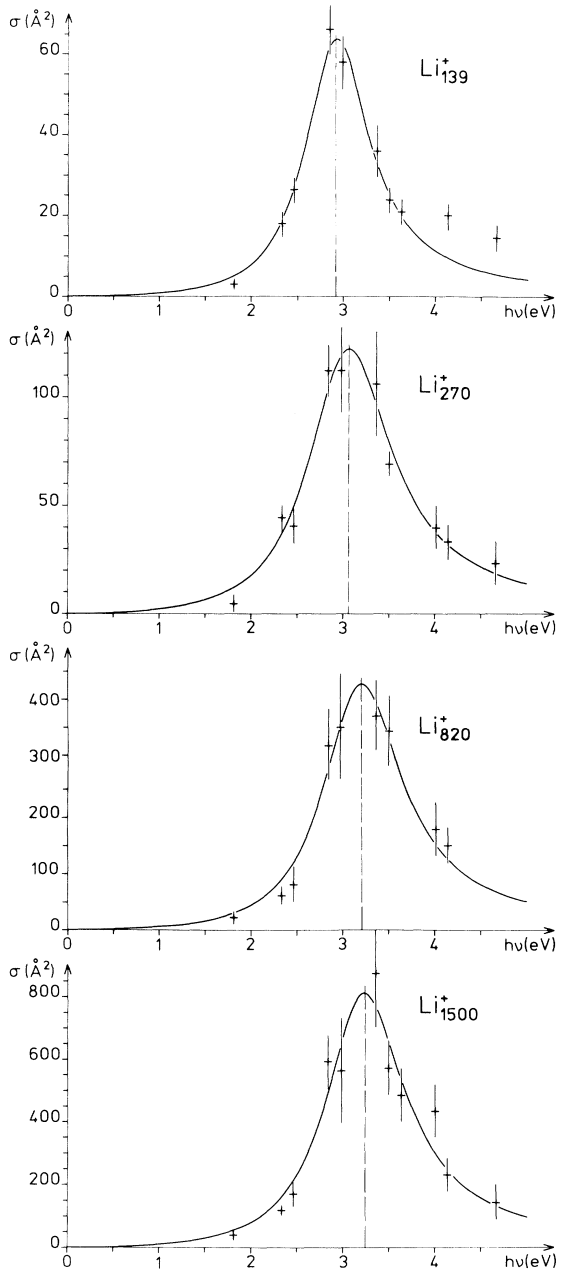

Figure 1.4: Experimental photoabsorption cross section σ for singly-charged lithium clusters Li_N^+ as a function of the photon energy. The solid line shows a fit to the experimental data. (Reproduced from Ref. 18.)

1.1.1 Mie theory

At a classical level, the photoabsorption spectrum can be understood by means of the Mie theory [13, 19, 20]. Already in 1908, Mie applied Maxwell's equations to the case

of a dielectric metal sphere with appropriate boundary conditions. His result can be applied to an ensemble of nanoparticles in a dielectric matrix provided that the clusters are well separated so that one can neglect interparticle electromagnetic interactions and multiple scattering. In the case where the sphere of radius a is very small compared to the wavelength of the external electrical field, the photoabsorption cross section is given within this theory by [13]

$$\sigma(\omega) = \frac{9\omega\epsilon_{\mathrm{m}}^{3/2}\mathcal{V}}{c}\frac{\epsilon_2(\omega)}{\left[\epsilon_1(\omega)+2\epsilon_{\mathrm{m}}\right]^2+\epsilon_2(\omega)^2}, \tag{1.2}$$

where ω is the frequency of the external field, c the speed of light, and $\mathcal{V} = 4\pi a^3/3$ the volume of the nanoparticle.[3] ϵ_{m} is the dielectric function of the embedding medium (assumed to be independent of ω in the optical range), while $\epsilon(\omega) = \epsilon_1(\omega) + \mathrm{i}\epsilon_2(\omega)$ is the complex dielectric function of the metal. Note that the expression (1.2) yields normally the extinction cross section $\sigma_{\mathrm{ext}} = \sigma + \sigma_{\mathrm{sca}}$, where σ_{sca} is the scattering cross section. However, σ_{sca} is proportional to $\mathcal{V}^2$, such that for small metallic particles, the extinction is dominated by the absorption, and $\sigma_{\mathrm{ext}} \simeq \sigma$ [13].

We see on the denominator of (1.2) that a resonance appears in the photoabsorption cross section when $[\epsilon_1(\omega) + 2\epsilon_{\mathrm{m}}]^2 + \epsilon_2(\omega)^2$ takes its minimum value. An estimate of the resonance frequency can be obtained by considering a simple free-electron Drude model [9] for the dielectric constant describing the metal. Within this approximation,

$$\epsilon(\omega) = \epsilon_{\mathrm{d}} - \frac{\omega_{\mathrm{p}}^2}{\omega(\omega+\mathrm{i}\gamma_{\mathrm{i}})}, \tag{1.3}$$

where $\omega_{\mathrm{p}} = \sqrt{4\pi n_{\mathrm{e}} e^2/m_{\mathrm{e}}}$ is the plasma frequency, γ_{i}^{-1} the relaxation or collision time, while e, m_{e} and n_{e} stand for the electron charge, mass and bulk density, respectively. ϵ_{d} is the dielectric constant of the metal without the free-carrier contribution. It accounts for example in the case of noble-metal clusters for the screening of the s-electrons by the d-electrons. In a Drude approach, the relaxation constant γ_{i} can be related to the mean free path ℓ via the Fermi velocity v_{F} by $\gamma_{\mathrm{i}} = v_{\mathrm{F}}/\ell$. For example in sodium, we have $\ell \simeq 34\,\mathrm{nm}$,[4] and thus $\hbar\gamma_{\mathrm{i}} \simeq 20\,\mathrm{meV}$. Therefore, for frequencies $\omega \gg \gamma_{\mathrm{i}}$, the real and imaginary parts of the dielectric function read

$$\epsilon_1(\omega) = \epsilon_{\mathrm{d}} - \frac{\omega_{\mathrm{p}}^2}{\omega^2}, \tag{1.4a}$$

$$\epsilon_2(\omega) = \frac{\gamma_{\mathrm{i}}\omega_{\mathrm{p}}^2}{\omega^3}. \tag{1.4b}$$

Then, the resonance condition is simplified to $\epsilon_1(\omega) \simeq -2\epsilon_{\mathrm{m}}$ since $\epsilon_2(\omega)$ is small, and one obtains with (1.4a) the Mie frequency

$$\omega_{\mathrm{M}} = \frac{\omega_{\mathrm{p}}}{\sqrt{\epsilon_{\mathrm{d}}+2\epsilon_{\mathrm{m}}}} \tag{1.5}$$

[3] In the remaining of this thesis, we will use c.g.s. units.

[4] This value is extracted from the electrical resistivity of sodium at 273 K [9].

at which the resonance occurs. In the case of an alkaline-metal nanoparticle in vacuum, $\epsilon_\mathrm{d} = \epsilon_\mathrm{m} = 1$, and the Mie frequency reduces to $\omega_\mathrm{M} = \omega_\mathrm{p}/\sqrt{3}$. For example, in the case of free sodium nanoparticles, the Mie frequency is $\hbar\omega_\mathrm{M} = 3.48\,\mathrm{eV}$. The Mie frequency then provides the classical value at which the electronic cloud oscillates with respect to the ionic background (see Fig. 1.3).

Inserting (1.4) into (1.2), one obtains for the photoabsorption cross section near the resonance

$$\sigma(\omega) = \frac{9\omega_\mathrm{p}^2\mathcal{V}}{2c}\frac{\epsilon_\mathrm{m}^{3/2}}{(\epsilon_\mathrm{d}+2\epsilon_\mathrm{m})^2}\frac{\gamma_\mathrm{i}/2}{(\omega-\omega_\mathrm{M})^2+(\gamma_\mathrm{i}/2)^2}. \tag{1.6}$$

The Mie theory, together with the Drude model for free electrons, therefore predicts that the photoabsorption cross section is a Lorentzian peaked at the frequency ω_M and with a full width at half maximum γ_i. The inverse of the linewidth γ_i yields normally the lifetime of the collective surface plasmon excitation depicted in Fig. 1.3. The prediction of (1.6) qualitatively reproduces the experimental results (see Fig. 1.4). However, the measured resonance frequency appears to be smaller than the Mie value (1.5), while the measured linewidth γ_t is much larger than γ_i. As we will see in the sequel, this is due to the classical treatment that we have briefly presented here. To obtain further insight into the relaxation process of the surface plasmon excitation, one has to appeal to quantum mechanical effects, which turn out to be preponderant in metallic clusters.

Since the first spectroscopic measurement of the surface plasmon resonance in the absorption cross section of free sodium clusters [21], much progress has been made in the characterization of this collective resonance, both experimentally [10, 18, 22–25] and theoretically [11, 16, 26–31]. The proposed application of metallic nanoparticles [32, 33] or nanocrystals [34] as markers in biological systems such as cells or neurons renders crucial the understanding of their optical properties.

The first experiments have been made on ensembles of nanoparticles, where the inhomogeneous broadening of the resonance resulting from the size dependence of the resonance frequency (see below) masks the homogeneous linewidth [35–37]. In order to gain detailed information on the collective resonance, considerable effort has lately been devoted to the measurement of single-cluster optical properties [38–44]. The possibility of overcoming the inhomogeneous broadening resulted in a renewed interest in the theory of the optical response of metallic clusters.

1.1.2 Spill-out effect

As mentioned above, the experimentally obtained surface plasmon frequency is smaller than the frequency predicted by the Mie theory (1.5) (see Fig. 1.5). This redshift with respect to the classical Mie value is usually attributed to the so-called *spill-out effect* [10,11,13]. In the small metallic particles we are considering, the zero-temperature electronic density is determined quantum-mechanically by the ground-state many-body wave function. However, this wave function extends outside of the geometrical boundary of the nanoparticle defined by the radius a. Therefore, there is a non-negligible number N_out of electrons outside the cluster, and the average electronic density inside the

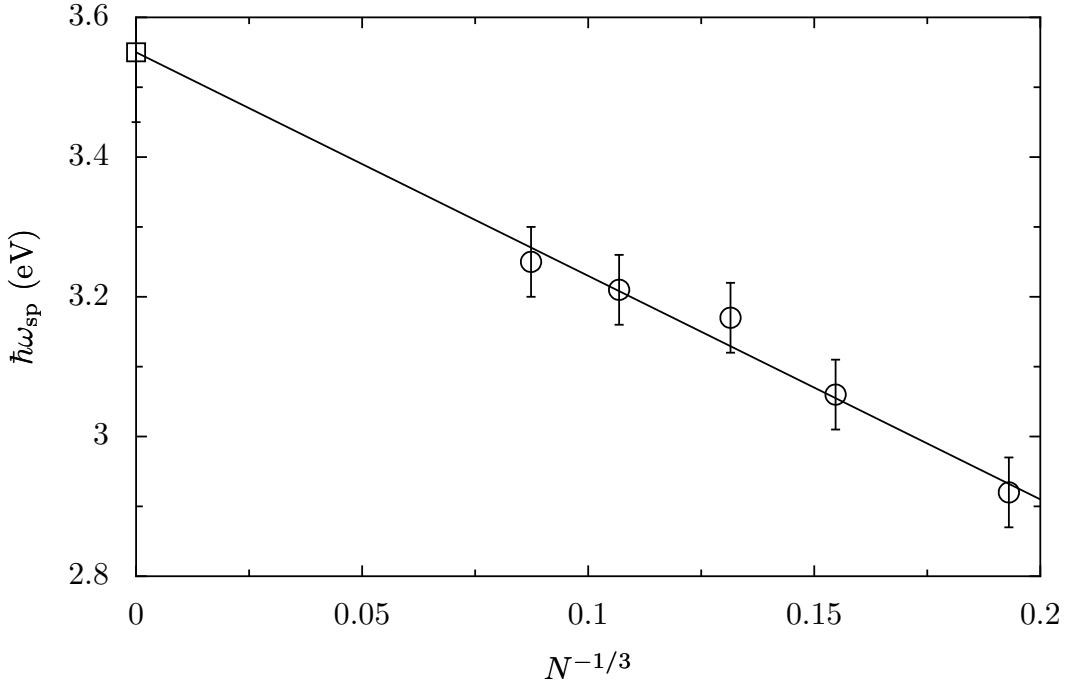

Figure 1.5: Measured resonance energy $\hbar\omega_{\rm sp}$ of the surface plasmon excitation in singly-charged lithium clusters Li_N^+ as a function of $N^{-1/3} = r_{\rm s}/a$ (open circles). It corresponds to the maximum of the photoabsorption curve shown in Fig. 1.4. The square shows the experimental Mie energy $\hbar\omega_{\rm M} = 3.55 \pm 0.1\,\mathrm{eV}$. It is obtained by measuring the dielectric constant of bulk lithium. The data are taken from Ref. 18. The straight line is a linear fit $\hbar\omega_{\rm sp} = \hbar\omega_{\rm M} - CN^{-1/3}$.

nanoparticle is lowered. The surface plasmon frequency can therefore be expected to change according to [11]

$$\tilde{\omega}_{\rm M} = \omega_{\rm M}\sqrt{1 - \frac{N_{\rm out}}{N}}. \tag{1.7}$$

We will see in Chapter 2 how this expression can be obtained rigorously.

As we can see in Fig. 1.5, the measured surface plasmon frequency increases as the size of the cluster increases, and attains the asymptotic value $\omega_{\rm M}$ in the limit $N \to \infty$. This can be understood with the following simple argument: If the fraction $N_{\rm out}/N$ of spill-out electrons is small, we have according to (1.7)

$$\tilde{\omega}_{\rm M} \simeq \omega_{\rm M} - \frac{\omega_{\rm M}}{2}\frac{N_{\rm out}}{N}. \tag{1.8}$$

Now, $N_{\rm out}/N$ is equal to the fraction $\mathcal{V}_{\rm out}/(\mathcal{V} + \mathcal{V}_{\rm out})$ where $\mathcal{V}_{\rm out}$ is the volume of the shell where the spill-out electrons are located. Denoting by $l_{\rm s}$ the depth of this spill-out layer, we obtain $N_{\rm out}/N \simeq 3l_{\rm s}/a$. Assuming that the spill-out length is independent of the size, inserting this result in (1.8) shows that the surface plasmon frequency decreases

linearly with the inverse size of the nanoparticle. This feature is observed in experiments (see Fig. 1.5).

The spill-out will be analyzed by means of a semiclassical expansion in Chapter 5. However, as we show in this thesis, the spill-out is not quantitatively sufficient to explain the redshift of the surface plasmon frequency. This is why we do not identify $\tilde{\omega}_{\mathrm{M}}$, the surface plasmon frequency redshifted by the spill-out effect from (1.7), with ω_{sp}, the measured surface plasmon resonance frequency. There is indeed an additional redshift which comes from the coupling of the surface plasmon excitation to the electronic environment (see Chapters 3 and 5).

1.2 Surface plasmon linewidth and quantum size effects

1.2.1 Free path effect

In the framework of classical electrical conductivity [9], the relaxation time γ_{i}^{-1} entering (1.6) accounts for the various processes which lead to elastic or inelastic scattering in bulk metals, such as interactions with phonons, electrons, impurities, etc. For this reason, we call γ_{i} the *intrinsic* linewidth since it takes into account processes present in a bulk material. From Mathiessen's rule [9], we have $\gamma_{\mathrm{i}} = 1/\tau_{\mathrm{i}} = \sum_{\alpha} 1/\tau_{\alpha}$ where τ_{α} is the relaxation time associated with each processes mentioned above. The elastic mean free path is related to the corresponding relaxation time by $\ell_{\mathrm{el}} = v_{\mathrm{F}}\tau_{\mathrm{el}}$, while in the diffusive regime the inelastic mean free path is given by $\ell_{\mathrm{in}} = \sqrt{D\tau_{\mathrm{in}}}$, where the diffusion constant is given by $D = v_{\mathrm{F}}^2\tau_{\mathrm{el}}/3$. For sodium and silver, one has for the mean free path at room temperature $\ell = 34\,\mathrm{nm}$ and $\ell = 52\,\mathrm{nm}$, respectively [9]. When the size of the nanoparticle is such that $2a \lesssim \ell$, we can think of an effective mean free path of the order of the size of the nanoparticle since we have an additional scattering process for the conduction electrons, namely the collisions with the surface. Extending the above arguments, we can write a size-dependent linewidth $\gamma(a) \sim v_{\mathrm{F}}/a$. According to Mathiessen's rule, the surface plasmon resonance should exhibit a total linewidth

$$\gamma_{\mathrm{t}}(a) = \gamma_{\mathrm{i}} + \gamma(a) \tag{1.9}$$

which is increased by the size-dependent contribution $\gamma(a)$. This is the so-called *free path effect* [13]. Such an estimation of the surface plasmon linewidth is in qualitative agreement with the experiments for nanoparticles of sizes $0.5\,\mathrm{nm} \lesssim a \lesssim 10\,\mathrm{nm}$ (see, e.g., Refs. 10, 13, 45–47 and Fig. 1.6). As an example, if we consider a sodium nanoparticle of radius $a = 2.5\,\mathrm{nm}$, we have $\hbar v_{\mathrm{F}}/a \simeq 280\,\mathrm{meV}$, such that $\hbar\gamma_{\mathrm{i}} \simeq 20\,\mathrm{meV}$ can be neglected. However, as we discuss in the following section, the interpretation of the size-dependent surface plasmon linewidth in terms of the free path effect is not conceptually correct, even if it yields valuable results as compared to the experimental results.

1.2.2 Linear response theory

As pointed out by Kawabata and Kubo in 1966 [48], the interpretation of the surface plasmon linewidth in terms of the free path effect is "too naive, if not entirely incorrect,

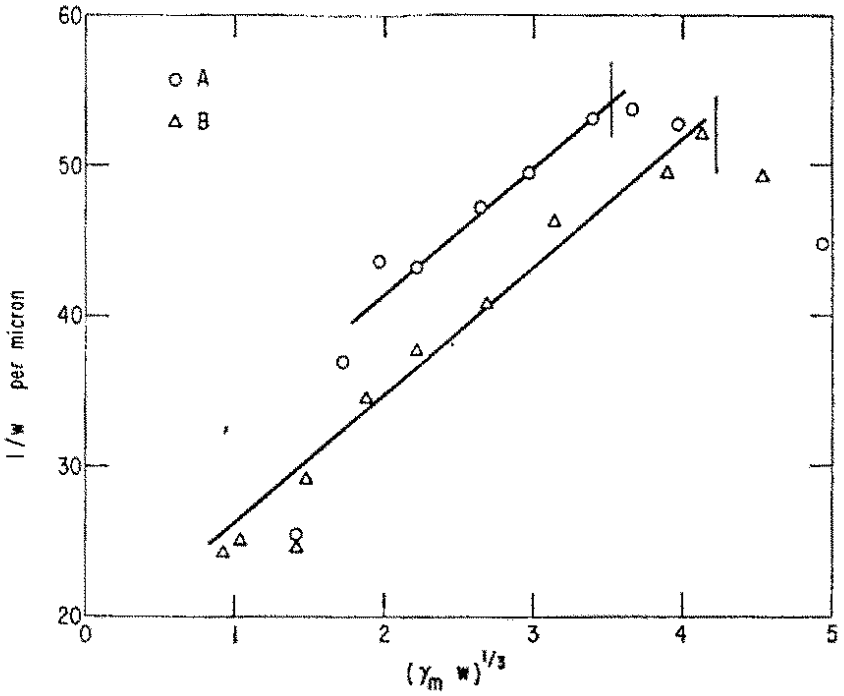

Figure 1.6: Measurement of the inverse surface plasmon linewidth for silver nanoparticles embedded in a glass matrix. The quantity represented on the abscissa is proportional to the radius a of the nanoparticles (between ~ 4 and 10 nm), while the vertical axis shows the inverse of the linewidth, γ_t^{-1}. It clearly demonstrates the relevance of the linear size-scaling of the surface plasmon lifetime. The circles and triangles correspond to two different samples. (Reproduced from Ref. 47.)

because in such a small particle the electron states are quantized into discrete levels which are determined by the boundary conditions at the surface." Indeed, in the small nanoparticles we are considering, the electronic states are quantized, and the classical interpretation of the free path effect is fallacious. The authors of Ref. 48 adopted a mean-field approach to treat the electron-electron interaction, which turns out to be a reasonable approximation for clusters containing more than a hundred of atoms.[5] Using linear response theory [49] and the fluctuation-dissipation theorem [50], they showed that one has to add to the size-independent imaginary part of the dielectric function $\epsilon_2(\omega)$ entering (1.2) and given within the Drude model by (1.4b), the size-dependent

[5]Even for clusters containing only 8 valence electrons, the mean-field approach gives valuable results, as it has been shown by comparing mean-field self-consistent calculations with quantum chemistry calculations [11].

contribution

$$\epsilon_2(\omega, a) = \frac{4\pi^2\hbar}{\omega^3 \mathcal{V}} \sum_{\alpha,\beta} \frac{[1 - f(\varepsilon_\alpha)]\, f(\varepsilon_\beta)}{\varepsilon_\alpha - \varepsilon_\beta} \left| \langle \alpha | \dot{J}_z | \beta \rangle \right|^2 \delta(\hbar\omega - \varepsilon_\alpha + \varepsilon_\beta). \tag{1.10}$$

In the above expression, $|\alpha\rangle$ denotes a single-particle state of energy ε_α in the electronic mean-field, while $f(\varepsilon_\alpha)$ is the related occupation number of the state $|\alpha\rangle$ (Fermi-Dirac distribution). $\dot{J}_z$ is the rate of change of the current operator and is essentially related to the dipole operator z [48]. The damping of the collective surface plasmon excitation then results in particle-hole excitations, similarly to the Landau damping in bulk metals [16,51]. Assuming that the single-particle states are confined within the metallic particle by a spherically-symmetric hard-wall potential which simulates the mean field, Kawabata and Kubo obtained at zero temperature

$$\epsilon_2(\omega, a) = \frac{4}{\pi} \frac{e^2}{\hbar\omega a} \frac{g_{\mathrm{KK}}(\nu)}{\nu^2}, \tag{1.11}$$

where

$$g_{\mathrm{KK}}(\nu) = \frac{1}{\nu} \int_{\nu_0}^{1} \mathrm{d}x \sqrt{x^3(x+\nu)} \tag{1.12}$$

is a decreasing function of the parameter $\nu = \hbar\omega/\varepsilon_{\mathrm{F}}$ with $g_{\mathrm{KK}}(0) = 1$.[6] In (1.12), $\nu_0 = 1 - \nu$ if $\nu < 1$, while $\nu_0 = 0$ if $\nu \geqslant 1$. According to (1.2), the full width at half maximum is given by $\gamma = 2\epsilon_2/|\mathrm{d}\epsilon_1/\mathrm{d}\omega|$ evaluated at the resonance frequency $\omega = \omega_{\mathrm{M}}$, and using (1.4a) and (1.11), one obtains

$$\gamma(a) = \frac{3v_{\mathrm{F}}}{4a} g_{\mathrm{KK}} \left(\frac{\hbar\omega_{\mathrm{M}}}{\varepsilon_{\mathrm{F}}} \right) \tag{1.13}$$

for the size-dependent linewidth entering (1.9). Thus, although the interpretation in terms of the free path effect is not correct, the size dependence of the resulting linewidth remains $1/a$ in the quantum theory of Kawabata and Kubo.

Linear response theory was later applied by Barma and Subrahmanyam [29]. Their evaluation confirmed the $1/a$-law of (1.13). However they obtained a slightly different frequency dependence and showed that the function g_{KK} has to be replaced by the function g_0 that will be given in (4.57). Their result

$$\gamma(a) = \frac{3v_{\mathrm{F}}}{4a} g_0 \left(\frac{\varepsilon_{\mathrm{F}}}{\hbar\omega_{\mathrm{M}}} \right) \tag{1.14}$$

implies an increase of the surface plasmon linewidth as compared to the result of Kawabata and Kubo. The difference between the two results can be understood in the following way. The single-particle eigenenergies are crucial to evaluate (1.10). In a spherical hard-wall potential, these are given by the zeros of a spherical Bessel function. However,

[6] The result presented in the original paper of Kawabata and Kubo [48] has some computational errors. We present here the corrected result which is quoted in Ref. 52.

the location of the zeros are not known analytically, and thus one has to consider appropriate asymptotic limits to find it. The difference between the two results comes from the fact that the authors of Ref. 29 used a more accurate expression for the location of the eigenenergies.

The size-dependent linewidth $\gamma(a)$ results from the decay of the surface plasmon into particle-hole pairs by a Landau damping mechanism, which is the dominant decay channel for nanoparticle sizes $0.5\,\mathrm{nm} \lesssim a \lesssim 10\,\mathrm{nm}$ considered in this work. For larger clusters, the interaction of the surface plasmon with the external electromagnetic field becomes the preponderant source of damping [13]. This is the so-called *radiation damping*. One can show that the damping constant corresponding to the radiation damping scales as $\gamma_{\mathrm{rad}} \sim a^3$ (see, e.g., Ref. 48). This shows that for small metallic clusters, γ_{rad} can be neglected as compared to the Landau damping linewidth (1.14). For nanoparticle sizes smaller than 0.5 nm, there is not enough appropriate particle-hole excitations for the surface plasmon to decay. For such sizes, the coupling of the surface plasmon to the ionic lattice can lead to the damping of the collective excitation.

1.2.3 Random phase approximation

In principle, the Landau damping linewidth γ can be directly extracted from the photoabsorption cross section, which according to Fermi's golden rule reads [53]

$$\sigma(\omega) = \frac{4\pi e^2 \omega}{3c} \sum_f |\langle f|z|0\rangle|^2 \, \delta(\hbar\omega - E_f + E_0). \tag{1.15}$$

In the above expression, $|f\rangle$ and E_f are, respectively, the many-body excited states and eigenenergies of the electronic system. The ground state is noted as $|0\rangle$ and its energy is E_0. From the knowledge of the many-particle eigenstates of the electronic system, one could then construct the cross section (1.15) and extract from it the full width at half maximum of the absorption curve which yields γ. However, to obtain the many-body eigenstates is exceedingly difficult, even for clusters consisting of only few atoms.

An alternative derivation of the Landau damping linewidth γ has been carried out by Yannouleas and Broglia in Ref. 30. In analogy with nuclear many-body studies, the discrete-matrix random phase approximation (RPA) was used to describe the photoabsorption of metallic clusters. In this section, we briefly review the main ingredients of their approach.

Within the RPA, the many-body eigenstates of the system entering (1.15) are approximated with the solutions of the linearized equations of motion inside a particle-hole subspace S of finite dimension [7,54]. The RPA many-body eigenstates in this subspace are given by $|\nu\rangle = Q_\nu^\dagger|0\rangle$, while the RPA creation operator is a linear superposition of particle-hole excitations, i.e.,

$$Q_\nu^\dagger = \sum_{ph} \left[X_{ph}(\omega_\nu) c_p^\dagger c_h - Y_{ph}(\omega_\nu) c_h^\dagger c_p \right]. \tag{1.16}$$

In the above equation, p and h denote particle and hole states, with energies above and below the Fermi energy, respectively. ω_ν are the eigenenergies determining the

many-body states $|\nu\rangle$, while $c^\dagger$ and c are the usual fermionic creation and annihilation operators, respectively. The amplitudes $X_{ph}(\omega_\nu)$ and $Y_{ph}(\omega_\nu)$, and the eigenenergies ω_ν, can be obtained from the RPA equations of motion which are usually solved numerically. From those solutions, one can deduce the strength function [16]

$$S(\omega) = \sum_\nu |\langle\nu|z|\mathrm{RPA}\rangle|^2 \delta(\hbar\omega - \hbar\omega_\nu + E_{\mathrm{RPA}}) \tag{1.17}$$

which characterizes the excitation of the system by the dipole operator z. In the above expression, $|\mathrm{RPA}\rangle$ denotes the approximate RPA ground state of energy E_{RPA}.[7] From the strength function, one can readily obtain an approximation for the photoabsorption cross section (1.15).

However, when among the states $|\nu\rangle$ there exists a prominent collective state $|c\rangle$ carrying most of the oscillator strength in (1.17), it is helpful to divide the full problem into two steps. The authors of Ref. 30 divided the full particle-hole space S in two parts: $\mathrm{S} = \mathrm{S_R} + \mathrm{S_A}$. The "restricted subspace" $\mathrm{S_R}$ at low energy is responsible for building up the collective state $|c\rangle$, while the "additional subspace" $\mathrm{S_A}$ at high energy is responsible for the broadening of the collective resonance peak. Even though $|c\rangle$ is a superposition of low-energy states, its energy lies in the range of the subspace $\mathrm{S_A}$. While the collective state $|c\rangle$ is an eigenstate of $\mathrm{S_R}$ and therefore is a sharp line without any broadening, the additional subspace $\mathrm{S_A}$ forms a quasi-continuum of states degenerate with the collective state. Due to the coupling between the two subspaces, the collective state broadens and acquires a finite width γ. From these considerations, the RPA equations of motion can be simplified, and a closed formula for the linewidth γ has been obtained, namely

$$\gamma \propto \sum_{ph\in \mathrm{S_A}} |\langle p|z|h\rangle|^2 \, \delta(\hbar\omega_c - \varepsilon_p + \varepsilon_h). \tag{1.18}$$

In this expression, ph is a particle-hole excitation belonging to the additional subspace $\mathrm{S_A}$. The particle-hole pair is composed of a particle with energy ε_p and of a hole with energy ε_h, while $\hbar\omega_c$ is the energy of the collective state. Identifying ω_c with the Mie frequency ω_{M}, and following a calculation of the particle and hole eigenstates similar to Ref. 29, the authors of Ref. 30 finally arrived to the result of (1.14).

1.2.4 Time-dependent local density approximation

An alternative to the previous approaches is given by numerical calculations using the time-dependent local density approximation (TDLDA). This method was developed by Zangwill and Soven [55] and by Stott and Zaremba [56] for the calculation of atomic polarizabilities. It was later adapted by Ekardt [26–28] to the case of metallic clusters in the context of the spherical jellium approximation, where the ionic structure of the

[7] The RPA ground state can be obtained requiring that $Q_\nu|\mathrm{RPA}\rangle = 0$, where Q_ν is the hermitic conjugate of the operator defined in (1.16). Unlike the Hartree-Fock ground state, it contains correlations.

nanoparticle is disregarded and replaced by a homogeneous positively charged spherical background.

The local-density approximation for spherical clusters follows the ideas of Lang and Kohn developed for metallic planar surfaces [57]. Within this approximation, the Coulomb and exchange-correlation interactions of the electrons are added to the background potential to obtain an effective potential in which the delocalized electrons move independently from each other. Since the above interactions depend on the electronic density, the eigenfunctions and thus the effective potential have to be found self-consistently by solving iteratively the Kohn-Sham equation [11]. Note that this approximation is justified for the ground state properties. The excited self-consistent states however are used within the TDLDA without any justification.

The photoabsorption cross section (1.15) is related to the frequency-dependent dipole polarizability $\alpha(\omega)$ via

$$\sigma(\omega) = \frac{4\pi\omega}{c}\Im\alpha(\omega). \tag{1.19}$$

The polarizability can be found according to [55, 58]

$$\alpha(\omega) \propto -\int \mathrm{d}^3\mathbf{r}\, z\delta n_\mathrm{e}(\mathbf{r},\omega). \tag{1.20}$$

Within linear-response theory, the change of the electronic density induced by the external field is given by

$$\delta n_\mathrm{e}(\mathbf{r},\omega) = \int \mathrm{d}^3\mathbf{r}'\chi(\mathbf{r},\mathbf{r}';\omega)V_\mathrm{ext}(\mathbf{r}',\omega), \tag{1.21}$$

where $V_\mathrm{ext}(\mathbf{r},\omega)$ is the Fourier transform (with respect to time) of the external potential associated with the electrical field. In the long-wavelength limit, it is proportional to the dipole operator z. In (1.21), $\chi(\mathbf{r},\mathbf{r}';\omega)$ is the density-density correlation function [55]. However, an exact determination of this correlation function is impossible, and within the TDLDA, it is determined by the following integral equation:

$$\chi(\mathbf{r},\mathbf{r}';\omega) = \chi^0(\mathbf{r},\mathbf{r}';\omega) + \int \mathrm{d}^3\mathbf{r}'' \int \mathrm{d}^3\mathbf{r}'''\chi^0(\mathbf{r},\mathbf{r}'';\omega)K(\mathbf{r}'',\mathbf{r}''')\chi(\mathbf{r}''',\mathbf{r}';\omega). \tag{1.22}$$

In the above expression, $\chi^0(\mathbf{r},\mathbf{r}';\omega)$ is the mean-field density-density correlation function. It can be obtained from the single-particle wavefunctions which are determined by solving the Kohn-Sham equation. The so-called residual interaction $K(\mathbf{r},\mathbf{r}')$ is given by [27]

$$K(\mathbf{r},\mathbf{r}') = V_\mathrm{C}(\mathbf{r},\mathbf{r}') + \left.\frac{\mathrm{d}v_\mathrm{xc}}{\mathrm{d}n_\mathrm{e}}\right|_\mathrm{gs}\delta(\mathbf{r}-\mathbf{r}'), \tag{1.23}$$

where $V_\mathrm{C}(\mathbf{r},\mathbf{r}')$ is the Coulomb interaction, and $v_\mathrm{xc}[n_\mathrm{e}]$ is the local exchange-correlation functional. In the above expression, gs means that the derivative is evaluated for the ground-state electronic density. Usually, $v_\mathrm{xc}[n_\mathrm{e}]$ is approximated by the parametrized form of Gunnarsson and Lundqvist [59]. The Dyson-type equation (1.22) is then solved

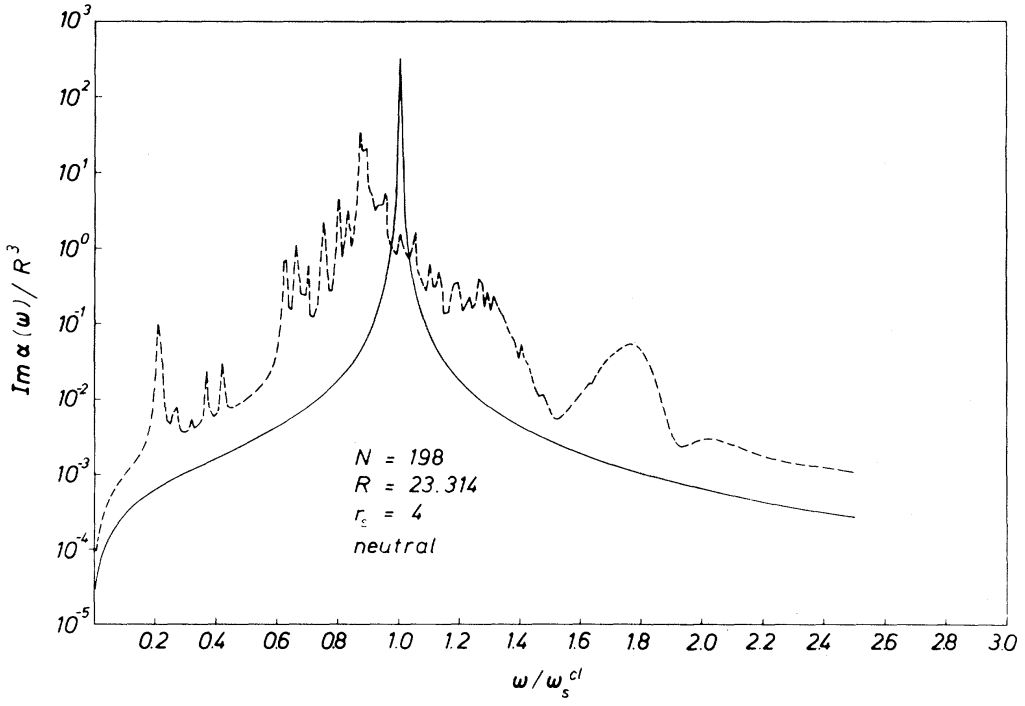

Figure 1.7: Imaginary part of the complex polarizability $\alpha(\omega)$, in units of a^3, as a function of $\omega/\omega_{\rm M}$. Dashed line: TDLDA calculations. Solid line: Result of the classical Mie theory. The results shown are for a spherical nanoparticle with $N = 198$ valence electrons, and for $r_{\rm s} = 4\,a_0$ corresponding (approximately) to sodium, with $a_0 = 0.53\,\text{Å}$ the Bohr radius. (Reproduced from Ref. 26. In Ekardt's notations, R is the radius of the nanoparticle, and $\omega_{\rm s}^{\rm cl}$ is the classical Mie frequency.)

by standard matrix manipulations, and the induced density (1.21) can be found. From it, one deduces the polarizability according to (1.20), and thus one has access to the photoabsorption cross section (see Eq. 1.19). A numerical estimate of the size-dependent linewidth $\gamma(a)$ can then be extracted from the knowledge of the photoabsorption cross section.

As an example for the application of the TDLDA calculations, we reproduce in Fig. 1.7 the results obtained by Ekardt [26] for a neutral spherical nanoparticle consisting of $N = 198$ atoms. The dashed line represents the imaginary part of the complex polarizability (1.20) proportional to the photoabsorption cross section according to (1.19), as a function of the frequency ω scaled by the classical Mie frequency $\omega_{\rm M}$. The solid line represents the same quantity as deduced from the classical Mie theory. The TDLDA result shown in the figure reproduce the main features of the experimentally obtained photoabsorption cross section (see Fig. 1.4). The surface plasmon appears indeed as a well-defined resonance (notice the logarithmic scale in Fig. 1.7). The resonance frequency is slightly below the one predicted by Mie's theory, while the absorption curve is broader than the classical

case which yields the linewidth γ_{i}. Furthermore, the TDLDA result presents much more structures than the classical prediction of Mie's theory. These structures reveal the electron-hole transitions that occur in the nanoparticle when the surface plasmon excitation decays.

1.2.5 Approach of this thesis

In this thesis, we will use the separation in center-of-mass and relative coordinates for the electron system [60] within a mean-field approach which allows to describe the surface plasmon as the oscillation of a collective coordinate, which is damped by the interaction with an environment constituted by a large number of electronic degrees of freedom. Within such a decomposition, the effects of finite size, a dielectric material, or the finite temperature of the electron gas are readily incorporated. Since the excitation by a laser field in the optical range only couples to the electronic center of mass, this approach is particularly useful.

Furthermore, throughout this thesis we will make use of semiclassical expansions. Even if this analytical approach cannot compete with the accuracy of numerical calculations like the TDLDA, we do believe that it yields further physical insight into the relaxation process of the surface plasmon excitation. Moreover, the semiclassical approach allows us to obtain the parametric dependence (in size, temperature, Fermi energy, etc.) of the quantities we address like the surface plasmon lifetime or its resonance frequency. This technique permits to compute the optical properties of arbitrarily large clusters, while extensions of this analytical scheme allows also for the description of smaller nanoparticles. It can as well be extended to nonlinear processes such as the ionization of an electron by an intense laser field, and constitute therefore a powerful method. Whenever it is possible, we will verify our semiclassical calculations by comparing them to the results of TDLDA numerical calculations.

1.3 Time-resolved pump-probe spectroscopy

In femtosecond time-resolved pump-probe experiments on metallic nanoparticles [61–65] the surface plasmon plays a key role. In this type of experiments, a very intense and ultrashort laser pulse of typically a hundred femtoseconds (the pump laser) heats the electron system via an excitation of the surface plasmon collective mode. After a certain time delay, the probe laser whose intensity is much weaker than the pump pulse then tests the absorption spectrum of the hot electron gas in the nanoparticle, and therefore it is important to understand the temperature dependences of the surface plasmon linewidth and of the frequency of the resonance. By tuning the delay time between the pump and probe pulses, one is then able to scan the relaxation process of the electronic system at various timescales.

Often, pump-probe experiments are done with an ensemble of noble-metal nanoparticles embedded in an inert matrix (e.g., made of glass). The concentration of clusters in the matrix is sufficiently low to suppress the possible effects of interactions between

the nanoparticles.

The energy relaxation following the strong excitation by the femtosecond pump pulse involves different timescales. This is schematize in Fig. 1.8. Initially, the energy is transferred to the electrons by absorption of photons and the corresponding electronic distribution is nonthermal (symbolized by the uppermost image in Fig. 1.8). On the timescale of a few femtoseconds, the electronic system is highly correlated and the collective surface plasmon mode is excited. After the excitation of the surface plasmon, its energy is transferred on the femtosecond timescale to the electronic environment, resulting in the heating of the latter.[8] As the electronic distribution becomes thermal, the temperature of the electron system can reach several hundreds of degrees, depending on the intensity of the pump laser field. The collective mode has decayed at that point into quasiparticle excitations, resulting from electron-electron and electron-surface scattering. On a much longer timescale, of the order of a picosecond, the energy transfer from the electron system to the lattice (phonons) results in the decrease of the electronic temperature with time and in the cooling of the electronic distribution. Finally, on the timescale of several picoseconds, the energy is transferred to the matrix where the nanoparticles are embedded.

An experimentally accessible quantity which reflects the relaxation process following the excitation of the system by the pump pulse is the differential transmission $\Delta\mathcal{T}/\mathcal{T}$. It is defined as the normalized difference of transmission of the sample with and without the pump laser field, $\Delta\mathcal{T}/\mathcal{T} = (\mathcal{T}_{\text{on}} - \mathcal{T}_{\text{off}})/\mathcal{T}_{\text{off}}$. This quantity can be measured as a function of the probe frequency and as a function of the delay time between the pump and the probe pulses.

In Fig. 1.9, we show an experimental differential transmission curve [62]. It is plotted as a function of the probe energy for a time delay between the pump and the probe pulses of 3 ps. The experiment of Ref. 62 is on an ensemble of silver nanoparticles with an average diameter of 6.3 nm embedded in a glass matrix. Those nanoparticles present a broad surface plasmon resonance located at 2.85 eV which corresponds to a wavelength of 434.5 nm. In the case of silver, the surface plasmon resonance is situated well below the interband transition thresholds d→p (3.99 eV) and p→s (3.85 eV) from the occupied p states to the unoccupied s states [63]. The surface plasmon resonance is therefore well defined. As we will see in Chapter 6, the shape of the differential transmission curve is directly related to the photoabsorption cross section and to its temperature dependence. This is why it is important to analyze the temperature dependences of the surface plasmon linewidth and frequency.

Fig. 1.10 shows the differential transmission as a function of the time delay between the pump and the probe pulses, for different probe energies in the vicinity of the surface plasmon resonance. Here, the nanoparticles are made of copper and have a mean diameter of 10 nm. They are embedded in a glass matrix. In the case of copper, the surface plasmon resonance is located near the interband transition d→p (2.17 eV) from

[8] On such a timescale, the phonons are effectively "frozen" since the typical frequency of phonons in metals is of the order of 10^{12} Hz [9], while the frequency of the surface plasmon excitation ω_{M} is of the order of 10^{15} Hz. This is the reason why coherent effects not only appear at very low temperatures, as it is the case for usual experiments in mesoscopic physics [1, 2].

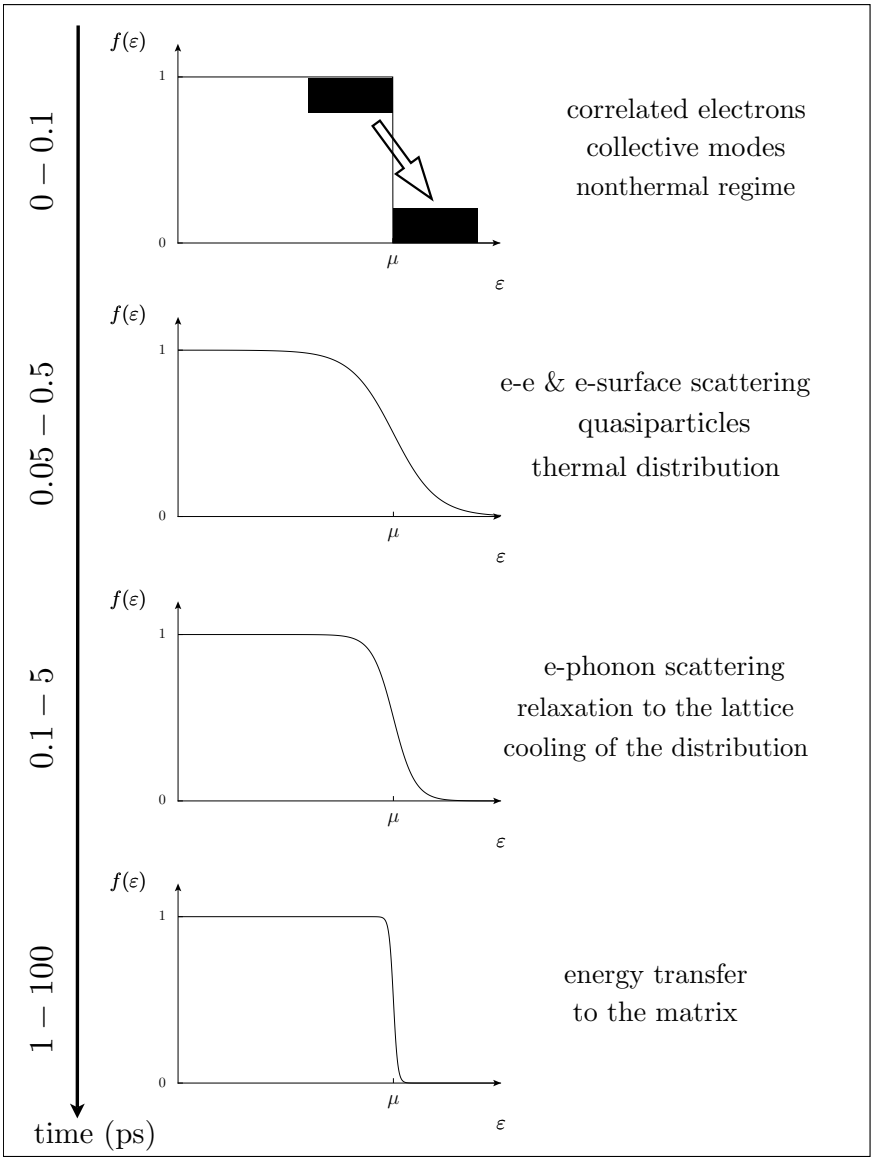

Figure 1.8: Sketch of the relaxation processes in a metallic nanoparticle after an excitation by a strong and ultrashort femtosecond laser pump pulse. $f(\varepsilon)$ is a sketch of the electronic distribution, while μ is the chemical potential. The arrow in the uppermost image symbolizes the effect of the pump laser on the electronic system. (Figure inspired by Ref. 63.)

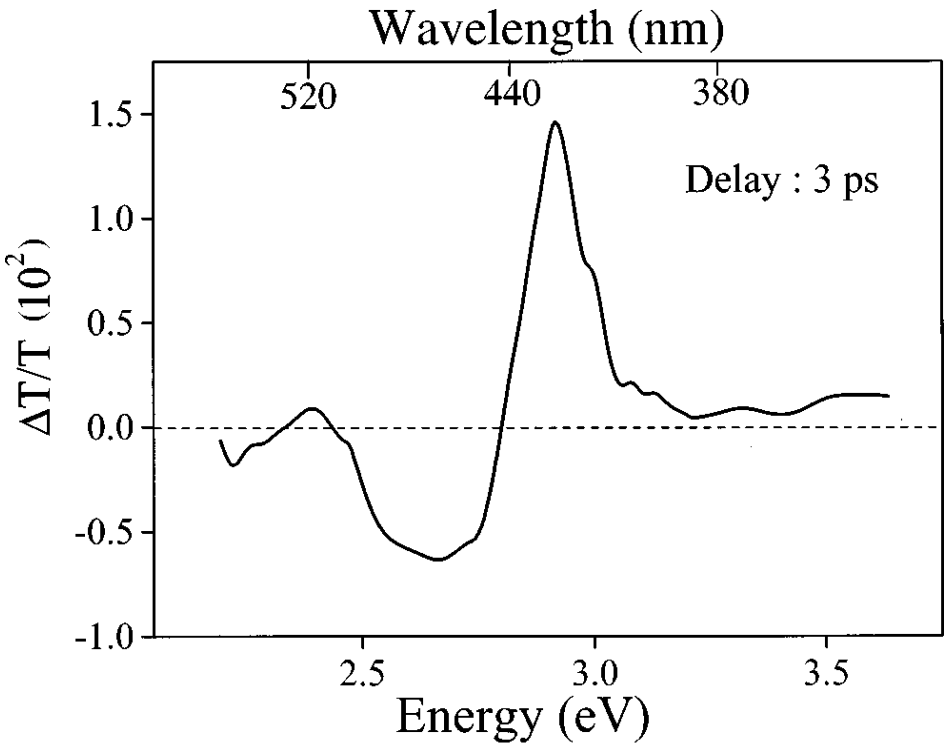

Figure 1.9: Experimentally observed differential transmission $\Delta\mathcal{T}/\mathcal{T}$ as a function of the probe laser energy for a delay time between the pump and probe pulses of 3 ps. The result shown is for an ensemble of silver nanoparticles with an average diameter of 6.3 nm, embedded in a glass matrix. (Reproduced from Ref. 62.)

the d band to the unoccupied states in the p conduction band [63]. Therefore, contrarily to the case of silver, the surface plasmon resonance is degenerate with the interband transitions, making the interpretation of the experiment more involved. As it can be seen on Fig. 1.10, the differential transmission decreases as a function of time, reflecting the relaxation of the electronic energy to the lattice. Note that a slowing of the relaxation process has been observed near the surface plasmon resonance [61–63] (see dots in Fig. 1.10). This is in contrast to time-resolved spectroscopy studies of copper thin films, where the dynamics is identical over the entire energy range around the d→p transition [61–63].

Various theoretical models have been investigated to study the relaxation process in pump-probe experiments. In Refs. 61–63, a two-temperature model has been adopted to account for the cooling of the electron system. In this model, the metal is described by two subsystems that exchange energy, corresponding to the electrons and the phonons, with appropriate specific heats. These two subsystems are coupled and their dynamics as a function of time is described by heat equations. Together with a description of

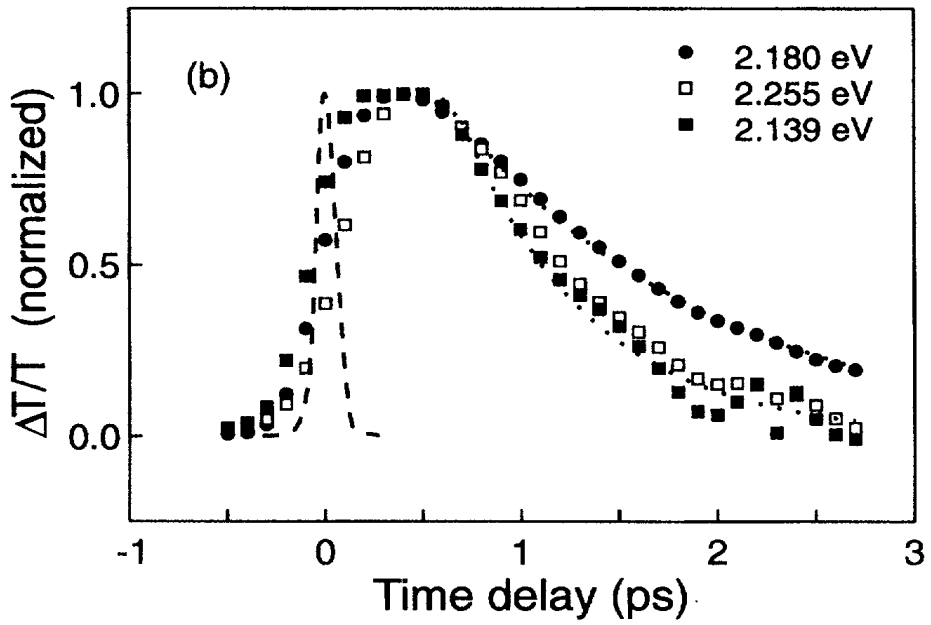

Figure 1.10: Experimental differential transmission $\Delta\mathcal{T}/\mathcal{T}$ as a function of the delay time between the pump and probe pulses, for different probe photon energies. The nanoparticles in this experiment are made of copper and embedded in a glass matrix. They have an average diameter of 10 nm. The plasmon resonance is located close to $\hbar\omega_{\mathrm{sp}} \simeq 2.2\,\mathrm{eV}$. (Reproduced from Ref. 61.)

the dielectric constant of the metal which includes intra- and interband processes by means of an effective medium, this allows to qualitatively reproduce the experimental results. Self-consistent numerical calculations [66, 67] have also been carried out in the linear regime. By means of temperature-dependent TDLDA calculations, together with the two-temperature model, the authors of Refs. 66 and 67 were able to qualitatively reproduce the experimental results. Nonlinear effects on the electronic dynamics in the case of a strong laser excitation have also been investigated using the nonlinearized TDLDA or the semiclassical Vlasov equation [68, 69].

The effects of correlations in the case of strong excitations has been considered by studying the semiclassical electron dynamics beyond mean-field [70]. The inclusion of a collision term was shown to be important in the case of excitations longer than a few femtoseconds, as well as for the description of the resulting heating of the electron gas. Most of these numerical results have been obtained in very small clusters (typically Na_9^+). Since the nanoparticles that we treat are considerably larger, we expect the correlation effects to be less important.

In this thesis, we adopt a theoretical scheme which allows us to obtain an analytical description of the differential transmission curve profile. As we will show, the obtained

low-temperature features of the surface plasmon linewidth and resonance frequency qualitatively reproduce the experimentally observed results.

1.4 Outline of this thesis

In this thesis we consider the problem of the surface plasmon excitation in spherical metallic nanoparticles and of its quantum dissipation and decoherence. We adopt a description of the system using methods from quantum optics, and elaborate an analytical scheme which allows us to give a simplified description of the surface plasmon dynamics. This approach allows us to characterize not only the dissipation of the surface plasmon excitation, but also its decoherence. Semiclassical expansions will be used to determine the main parameters describing the dynamical evolution of the system, namely the surface plasmon linewidth and the resonance frequency of the collective excitation. The manuscript is organized as follows:

In Chapter 2, we present our model and the separation of the electronic degrees of freedom into the center of mass and the relative coordinates (Sec. 2.1). The center-of-mass coordinate provides a natural description of the spatial collective oscillations of the electronic cloud around its equilibrium position resulting from a laser excitation. In Sec. 2.2, we present our mean-field approximation for the electronic correlations which provides a route to the analytical description of the surface plasmon dynamics. The interaction of an external driving field with the system is briefly described in Sec. 2.3.

In Chapter 3, we describe the dynamics of the surface plasmon excitation in presence of an external driving field. To this end, we develop in Sec. 3.1 a density-matrix description of the center-of-mass degree of freedom. Within a two-level system approach, we solve the resulting master equation in Sec. 3.2 and discuss the temporal evolution of the system in different physical situations.

The coupling between the center of mass and the relative coordinates is responsible for the broadening of the surface plasmon resonance that we evaluate in Chapter 4. In Sec. 4.1, we present an approximate determination of the single-particle mean-field states that are determinant for the calculation of the surface plasmon linewidth. We determine in Sec. 4.2 the dominant dependence of the surface plasmon linewidth on the size of the nanoparticle and explore its low-temperature properties. In Sec. 4.3, we demonstrate that, in addition to its smooth size dependence, the surface plasmon linewidth exhibits a nonmonotonic behavior as a function of the size of the nanoparticle.

In Chapter 5, we concentrate on the resonance frequency of the surface plasmon excitation. We evaluate in Sec. 5.1 the spill-out effect, focusing on its dependence on size and temperature of the nanoparticle. We show by means of time-dependent local density approximation calculations that the spill-out effect is not sufficient to quantitatively describe the redshift of the surface plasmon frequency as compared to the classical Mie value. In Sec. 5.2, we propose an estimation of the environment-induced redshift of the surface plasmon resonance which adds to the spill-out effect. Both effects together, spill-out and frequency shift due to the electronic environment, could explain the observed redshift of the resonance frequency.

In Chapter 6, we draw the consequences of our findings for pump-probe experiments. The temperature dependences of the linewidth and frequency of the surface plasmon resonance peak permit to qualitatively explain the time dependence of the measured optical transmission as a function of the delay between the pump and the probe laser field.

Under a weak initial optical excitation, only the first surface plasmon (that we simply refer to as "surface plasmon" when there is no possibility of confusions) is excited. With sufficiently strong initial excitations, we can also reach the second quantum level of the center-of-mass motion, known as the second (or double) plasmon. Such a resonance will be experimentally relevant provided its lifetime is sufficiently large (on the scale of ω_{M}^{-1}). The lifetime is limited by the anharmonicities of the center-of-mass system and by its interaction with other degrees of freedom. Like in the case of the single plasmon, the Landau damping is an important channel for the decay of the second plasmon, but a new channel appears when $2\hbar\omega_{\mathrm{M}}$ is larger than the ionization energy so the cluster loses an electron into the continuum [71]. Such a process was discussed in order to interpret the ionization of charged Na_{93}^{+} clusters observed by Schlipper and collaborators [72,73]. The relevance and the existence of the double plasmon in metallic nanoparticles is therefore debated in Chapter 7. We present a semiclassical description of the two main channels contributing to the decay of the double plasmon: Landau damping (Sec. 7.1) and particle ionization (Sec. 7.2).

In Chapter 8 we study the experimentally relevant case of noble-metal nanoparticles embedded in a dielectric medium and present the need to improve the existing theory for the surface plasmon linewidth in this case. It is shown that one has to consider the details of the mean-field potential near the boundary of the nanoparticle to solve a qualitative discrepancy between the analytical and numerical results. This is done semiclassically in Sec. 8.1, while in Sec. 8.2 we estimate the shape of the mean-field potential from a simple Thomas-Fermi model. This yields a qualitative agreement between the numerical and analytical approaches, as shown in Sec. 8.3.

We finally conclude and discuss the perspectives of this work in Chapter 9.

Chapter 2

Metallic nanoparticles: A model system for the study of quantum dissipation and decoherence

> J'aimais et j'aime encore les mathématiques pour elles-mêmes comme n'admettant pas l'hypocrisie et le vague, mes deux bêtes d'aversion.
>
> *(Stendhal, 1783-1842, in Vie de Henry Brulard)*

In this chapter, we present the model that will serve us to study the dynamics of the surface plasmon excitation in metallic nanoparticles. Within the spherical jellium model, the electronic Hamiltonian will be separated into a part associated with the electronic center of mass, a part which describes the relative coordinates (the electronic environment or "heat bath" in our case), and a coupling between the two subsystems which causes decoherence and dissipation of the collective surface plasmon excitation.

2.1 Electronic Hamiltonian within the jellium model

We consider a neutral metallic nanoparticle containing N valence electrons. Furthermore, we restrict ourselves to spherical nanoparticles of radius a. As mentioned in the introduction of this thesis, spherical nanoparticles have closed angular momentum shells, the first closed-shell sizes being $N = 8, 20, 40, 58, \ldots$ [11]. In analogy with atomic physics, one calls those specific numbers of valence electrons "magic numbers". Neglecting the ionic dynamics (adiabatic Born-Oppenheimer approximation [9]), the electronic Hamiltonian for an alkaline-metal nanoparticle in vacuum is given within the so-called

jellium model by

$$H = \sum_{i=1}^{N} \left[\frac{p_i^2}{2m_\mathrm{e}} + U(r_i) \right] + \frac{e^2}{2} \sum_{\substack{i,j=1 \\ (i \neq j)}}^{N} \frac{1}{|\mathbf{r}_i - \mathbf{r}_j|}, \tag{2.1}$$

where e and m_e are the electronic charge and mass, respectively. In (2.1), $\mathbf{r}_i$ is the position of the i^{th} conduction electron, $r_i = |\mathbf{r}_i|$, and $\mathbf{p}_i$ is the associated momentum. The spherically symmetric single-particle potential $U(r)$ represents the electrostatic interaction between the electrons and the ionic background. Within the spherical jellium model, the ions are treated as a continuous, homogeneous positively charged sphere of total charge $+Ne$, which produces a charge density

$$\rho_\mathrm{i}(r) = \frac{Ne}{\mathcal{V}} \Theta(a - r), \tag{2.2}$$

$\Theta(x)$ being the Heaviside step function and $\mathcal{V} = 4\pi a^3/3$ the volume of the nanoparticle.[1]

For large metallic clusters, it is convenient to use the jellium approximation which neglects the ionic structure of the cluster. This model is simple enough to be applied to spherical nanoparticles containing up to several thousands of atoms, and is still accurate enough to describe the essential physical properties of such objects. Even for the smallest sizes where the ionic structure could presumably play an important role, the spherical jellium model gives valuable results [11].

Note that in the case of a noble-metal nanoparticle embedded in a dielectric medium, the electron-electron interaction is modified in (2.1) by a dielectric constant ϵ_d which takes into account the screening of the conduction electrons by the d-electrons, as well as by the dielectric constant ϵ_m of the matrix. In this case, the expression for the Coulomb potential is much more complicated since it is not any more translationally invariant, due to the dielectric discontinuity at the interface between the cluster and the matrix.

2.1.1 Single-particle confinement

We now detail the determination of the single-particle confinement $U(r)$ appearing in the electronic Hamiltonian H (2.1). Considering the homogeneously charged sphere of radius a and of total charge $+Ne$, Gauss's theorem yields the radial electrical field $\mathbf{E}(\mathbf{r}) = E(r)\mathbf{r}/r$ produced by the charge distribution (2.2), with

$$E(r) = \frac{Ne}{a^2} \left[\frac{r}{a} \Theta(a - r) + \left(\frac{a}{r} \right)^2 \Theta(r - a) \right]. \tag{2.3}$$

The single-particle confinement $U(r)$ is given by the electrostatic potential $\phi(r)$ multiplied by the electronic charge,

$$U(r) = -e \int_0^r \mathrm{d}r'\, E(r') + \text{constant}. \tag{2.4}$$

[1] Note that we consider monovalent metals for which the number of valence electrons equals the number of ions.

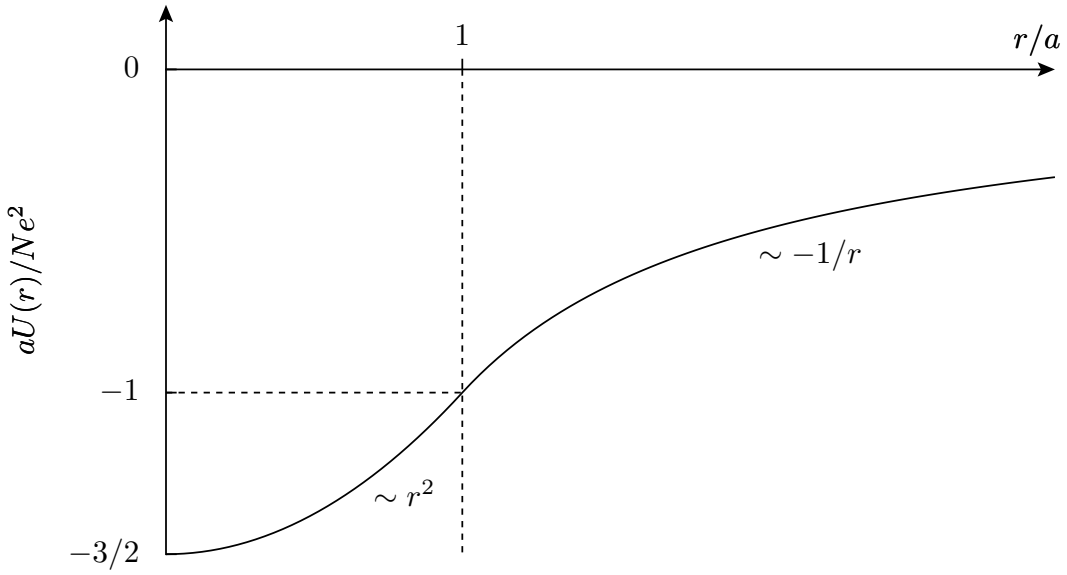

Figure 2.1: Single-particle confinement potential U as a function of the radial coordinate r, scaled by the nanoparticle radius a. It is harmonic for $r < a$, and Coulomb-like for $r > a$, so we refer to it as "Harlomb".

Imposing that $\lim_{r\to\infty} U(r) = 0$ and the continuity of $\phi(r)$ at the interface a, we find the "Harlomb" potential

$$U(r) = \frac{Ne^2}{2a^3}\left(r^2 - 3a^2\right)\Theta(a-r) - \frac{Ne^2}{r}\Theta(r-a) \tag{2.5}$$

which is harmonic with the Mie frequency $\omega_{\mathrm{M}} = \sqrt{Ne^2/m_{\mathrm{e}}a^3}$ inside the nanoparticle and Coulomb-like outside (see Fig. 2.1).

2.1.2 Separation into collective and relative coordinates

In principle, the photoabsorption cross section (1.15) can be determined from the knowledge of the eigenstates of H. The linewidth and the resonance frequency of the surface plasmon excitation could then be obtained from the analysis of the cross section. However, except for clusters containing only few conduction electrons, this procedure is exceedingly difficult even if we are already within the jellium model, and one has to treat this problem using suitable approximation schemes.

A particularly useful decomposition [60] of the Hamiltonian (2.1) can be achieved by introducing the coordinate of the electronic center of mass $\mathbf{R} = \sum_i \mathbf{r}_i/N$ and its conjugated momentum $\mathbf{P} = \sum_i \mathbf{p}_i$. The relative coordinates are denoted by $\mathbf{r}'_i = \mathbf{r}_i - \mathbf{R}$ and $\mathbf{p}'_i = \mathbf{p}_i - \mathbf{P}/N$. Then, using $\sum_i \mathbf{r}'_i = 0$ and $\sum_i \mathbf{p}'_i = 0$, the Hamiltonian (2.1) can be written as

$$H = \frac{\mathbf{P}^2}{2Nm_{\mathrm{e}}} + H_{\mathrm{rel}} + \sum_{i=1}^{N}\left[U(|\mathbf{r}'_i + \mathbf{R}|) - U(r'_i)\right]. \tag{2.6}$$

We have defined

$$H_{\rm rel} = \sum_{i=1}^{N} \left[\frac{p_i'^2}{2m_{\rm e}} + U(r_i') \right] + \frac{e^2}{2} \sum_{\substack{i,j=1 \\ (i \neq j)}}^{N} \frac{1}{|\mathbf{r}_i' - \mathbf{r}_j'|} \tag{2.7}$$

as the Hamiltonian for the relative-coordinate system.

Assuming that the displacement $\mathbf{R}$ of the center of mass is small compared to the size of the nanoparticle, we can expand the last term on the r.h.s. of (2.6). To second order, we obtain

$$U(|\mathbf{r}' + \mathbf{R}|) - U(r') \simeq \mathbf{R} \cdot \boldsymbol{\nabla} U(r') + \frac{1}{2} (\mathbf{R} \cdot \boldsymbol{\nabla})^2 U(r'), \tag{2.8}$$

where the derivatives are taken at $\mathbf{r} = \mathbf{r}'$ ($\mathbf{R} = \mathbf{0}$). With this expansion, the dependence on the relative coordinates in the last term of (2.6) has dropped out, thus justifying our definition (2.7). Choosing the oscillation axis of the center of mass in the z-direction, $\mathbf{R} = Z\mathbf{e}_z$, we obtain with (2.5)

$$\mathbf{R} \cdot \boldsymbol{\nabla} U(r') = Z m_{\rm e} \omega_{\rm M}^2 \left[z' \Theta(a - r') + \frac{z' a^3}{r'^3} \Theta(r' - a) \right] \tag{2.9}$$

which represents a first order coupling in Z between the center-of-mass and the relative-coordinate system, and

$$(\mathbf{R} \cdot \boldsymbol{\nabla})^2 U(r') = Z^2 N e^2 \left[\frac{1}{a^3} \Theta(a - r') + \frac{1 - 3\cos^2\theta'}{r'^3} \Theta(r' - a) \right]. \tag{2.10}$$

In second order, the first term on the r.h.s. of (2.10) is the dominant contribution to the confinement of the center of mass. The second term on the r.h.s. of (2.10) is negligible compared to the first-order coupling of (2.9) and thus we only keep

$$(\mathbf{R} \cdot \boldsymbol{\nabla})^2 U(r') \simeq Z^2 \frac{N e^2}{a^3} \Theta(a - r'). \tag{2.11}$$

Inserting (2.8) and (2.11) into (2.6), we obtain

$$H = \frac{\mathbf{P}^2}{2N m_{\rm e}} + \frac{1}{2} \frac{N e^2}{a^3} \mathbf{R}^2 \sum_{i=1}^{N} \Theta(a - r_i) + H_{\rm rel} + H_{\rm c}, \tag{2.12}$$

where

$$H_{\rm c} = \sum_{i=1}^{N} \mathbf{R} \cdot [\boldsymbol{\nabla} U(r_i')] \Big|_{\mathbf{R}=\mathbf{0}} \tag{2.13}$$

is the coupling between the center-of-mass and the relative coordinates to the first order in the displacement $\mathbf{R}$ of the center of mass according to (2.9). The remaining sum over i in (2.12) defines the number of electrons inside the nanoparticle, i.e., $N - N_{\rm out}$ where $N_{\rm out}$ is the number of spill-out electrons, and finally we rewrite the Hamiltonian as

$$H = H_{\rm cm} + H_{\rm rel} + H_{\rm c}. \tag{2.14}$$

The Hamiltonian of the center-of-mass system is

$$H_{\mathrm{cm}} = \frac{\mathbf{P}^2}{2Nm_{\mathrm{e}}} + \frac{1}{2}Nm_{\mathrm{e}}\tilde{\omega}_{\mathrm{M}}^2\mathbf{R}^2. \tag{2.15}$$

It is the Coulomb tail of the single-particle confinement (2.5) which modifies the frequency to $\tilde{\omega}_{\mathrm{M}}$ defined in (1.7) instead of ω_{M} for the effective harmonic trap that is experienced by the center-of-mass system. The electronic spill-out thus redshifts the frequency of the surface plasmon excitation from the classical Mie value ω_{M}.

Eq. 2.14 with (2.7), (2.13), and (2.15) recovers up to the second order in $\mathbf{R}$ the decomposition derived in Ref. 60. However, in contrast to that work, we do not need to appeal to an effective potential for the center-of-mass system. The authors of Ref. 60 expanded this effective potential up to the fourth order, and obtained a correction to the harmonic confinement of (2.15) which goes as $\alpha\mathbf{R}^4$. However, they showed that the size-dependent constant α is very small, and tends to zero when the size of the nanoparticle is increasing. We will therefore restrict ourselves to the harmonic term in (2.15).

The structure of (2.14) is typical for quantum dissipative systems [74]: The system under study (H_{cm}) is coupled via H_{c} to an environment or "heat bath" described by H_{rel}. The system-environment coupling results in dissipation and decoherence of the collective excitation. In our case the environment is peculiar in the sense that it is not external to the nanoparticle, but it represents a finite number of degrees of freedom of the gas of conduction electrons.

If the single-particle confining potential $U(r)$ of (2.5) were harmonic for all r, Kohn's theorem [75] would imply that the center of mass and the relative coordinates are decoupled, i.e., $H_{\mathrm{c}} = 0$, and thus the surface plasmon has an infinite lifetime. This can be easily seen on (2.9): In the case of a perfectly harmonic confinement, we would have $\mathbf{R}\cdot\boldsymbol{\nabla}U(r') = Zm_{\mathrm{e}}\omega_{\mathrm{M}}^2 z'$. Thus according to (2.13), $H_{\mathrm{c}} = Zm_{\mathrm{e}}\omega_{\mathrm{M}}^2\sum_i z_i'$ which vanishes since $\sum_i z_i' = 0$. The Coulomb part of $U(r)$ in (2.5) leads to the coupling of the center of mass and the relative coordinates, and translates into the decay of the surface plasmon. Furthermore, it redshifts from ω_{M} the frequency of the center-of-mass system according to (1.7).

2.1.3 Alternative derivation of the coupling Hamiltonian

In this section, we present an alternative derivation of the coupling Hamiltonian H_{c} which yields a simple physical picture of such a coupling. Furthermore, it allows us to generalize the derivation of Ref. 16 considering the Coulomb interaction to the case of a dielectric mismatch between the nanoparticle and the surrounding matrix in which it is embedded.

Assuming that at equilibrium the electron density is uniform within a sphere of radius a, $n_{\mathrm{e}}(\mathbf{r}) = n_{\mathrm{e}}\Theta(a-r)$, a rigid displacement with a magnitude Z along the z-direction changes the density at $\mathbf{r}$ from $n_{\mathrm{e}}(\mathbf{r})$ to

$$n_{\mathrm{e}}(\mathbf{r}-\mathbf{R}) = n_{\mathrm{e}}(\mathbf{r}) + \delta n_{\mathrm{e}}(\mathbf{r}). \tag{2.16}$$

To first order in the field $\mathbf{R} = Z\mathbf{e}_z$, we can write

$$\delta n_{\mathrm{e}}(\mathbf{r}) = -\mathbf{R}\cdot\boldsymbol{\nabla} n_{\mathrm{e}}(\mathbf{r}) = Z n_{\mathrm{e}}\cos(\theta)\delta(r-a). \tag{2.17}$$

We have neglected the oscillations of the density in the inner part of the particle due to shell effects, and also the extension of the electronic density outside the particle, i.e., the spill-out effect [10,11]. Denoting $V_{\mathrm{C}}(\mathbf{r},\mathbf{r}')$ the Coulomb electron-electron interaction, the change in the mean-field potential seen by the electrons due to the rigid shift (transition potential) is

$$\delta V(\mathbf{R},\mathbf{r}) = \int \mathrm{d}^3\mathbf{r}'\delta n_{\mathrm{e}}(\mathbf{r}')V_{\mathrm{C}}(\mathbf{r},\mathbf{r}'). \tag{2.18}$$

As we show in the sequel, the transition potential of (2.18) is actually the same as $\mathbf{R}\cdot\boldsymbol{\nabla}U(r)$. Thus, the coupling Hamiltonian of (2.13) can be rewritten as

$$H_{\mathrm{c}} = \sum_{i=1}^{N}\delta V(\mathbf{R},\mathbf{r}_i'). \tag{2.19}$$

Let us now prove the equivalence between $\delta V(\mathbf{R},\mathbf{r})$ and $\mathbf{R}\cdot\boldsymbol{\nabla}U(r)$: From the definitions of the transition potential (2.18) and of the displaced density (2.17), writing explicitly the Coulomb interaction yields

$$\delta V(\mathbf{R},\mathbf{r}) = -e^2\mathbf{R}\cdot\int \mathrm{d}\mathbf{r}'^3\frac{\boldsymbol{\nabla}_{\mathbf{r}'}n_{\mathrm{e}}(\mathbf{r}')}{|\mathbf{r}-\mathbf{r}'|}. \tag{2.20}$$

Now,

$$\mathbf{R}\cdot\boldsymbol{\nabla}U(r) = -e\mathbf{R}\cdot\boldsymbol{\nabla}\phi(r) \tag{2.21}$$

with $\phi(r)$ the electrostatic potential created by the jellium background. Using the definition of $\phi(r)$, we thus have

$$\begin{aligned}\mathbf{R}\cdot\boldsymbol{\nabla}U(r) &= -e^2\mathbf{R}\cdot\boldsymbol{\nabla}_{\mathbf{r}}\int \mathrm{d}\mathbf{r}'^3\frac{n_{\mathrm{e}}(r')}{|\mathbf{r}-\mathbf{r}'|}\\ &= e^2\mathbf{R}\cdot\int \mathrm{d}\mathbf{r}'^3 n_{\mathrm{e}}(r')\boldsymbol{\nabla}_{\mathbf{r}'}\frac{1}{|\mathbf{r}-\mathbf{r}'|}.\end{aligned} \tag{2.22}$$

To obtain the second line of the above expression, we have used

$$\boldsymbol{\nabla}_{\mathbf{r}'}\frac{1}{|\mathbf{r}-\mathbf{r}'|} = -\boldsymbol{\nabla}_{\mathbf{r}}\frac{1}{|\mathbf{r}-\mathbf{r}'|}. \tag{2.23}$$

Integrating (2.22) by parts, we finally obtain the result of (2.20), and thus

$$\delta V(\mathbf{R},\mathbf{r}) = \mathbf{R}\cdot\boldsymbol{\nabla}U(r). \tag{2.24}$$

Transition potential without dielectric mismatch

When we consider an alkaline-metal nanoparticle in vacuum, there is no dielectric mismatch between the metallic cluster and the surrounding environment. In order to proceed with (2.18), the multipolar decomposition of the Coulomb interaction is very useful [76]. It reads

$$V_{\mathrm{C}}(\mathbf{r},\mathbf{r}') = 4\pi e^2 \sum_{l=0}^{\infty} \sum_{m=-l}^{+l} \frac{1}{2l+1} \frac{r_<^l}{r_>^{l+1}} Y_l^{m*}(\theta',\varphi') Y_l^m(\theta,\varphi), \tag{2.25}$$

with $r_< = \min(r,r')$, $r_> = \max(r,r')$, and $Y_l^m(\theta,\varphi)$ are the spherical harmonics. Inserting (2.17) and (2.25) into (2.18), one obtains for the transition potential [16]

$$\delta V(\mathbf{R},\mathbf{r}) = Z\frac{4\pi n_{\mathrm{e}} e^2}{3}\left[z\Theta(a-r) + \frac{za^3}{r^3}\Theta(r-a)\right], \tag{2.26}$$

similarly to (2.9). We notice that a displacement of the electron system leads to a dipolar field inside the nanoparticle, and that its magnitude decays as $1/r^2$ outside the particle.

Transition potential with dielectric mismatch

If we now consider the case of a noble metal nanoparticle (where the d-electrons are taken into account through a dielectric constant ϵ_{d}) embedded in a matrix (of dielectric constant ϵ_{m}), the Coulomb interaction between electrons is given by [77]

$$V_{\mathrm{C}}(\mathbf{r},\mathbf{r}') = 4\pi e^2 \begin{cases} \dfrac{1}{\epsilon_{\mathrm{d}}} \displaystyle\sum_{lm} \frac{1}{2l+1}\left[\frac{r_<^l}{r_>^{l+1}} + \frac{r^l r'^l}{a^{2l+1}} \frac{(l+1)(\epsilon_{\mathrm{d}}-\epsilon_{\mathrm{m}})}{\epsilon_{\mathrm{d}} l + \epsilon_{\mathrm{m}}(l+1)}\right] Y_l^{m*}(\theta',\varphi') Y_l^m(\theta,\varphi) & \\ \qquad\qquad \text{for } r,\ r' \leqslant a, & \\ \displaystyle\sum_{lm} \frac{r_<^l}{r_>^{l+1}} \frac{Y_l^{m*}(\theta',\varphi') Y_l^m(\theta,\varphi)}{\epsilon_{\mathrm{d}} l + \epsilon_{\mathrm{m}}(l+1)} & \text{for } r_< \leqslant a,\ r_> > a, \\ \dfrac{1}{\epsilon_{\mathrm{m}}} \displaystyle\sum_{lm} \frac{1}{2l+1}\left[\frac{r_<^l}{r_>^{l+1}} + \frac{a^{2l+1}}{r^{l+1} r'^{l+1}} \frac{l(\epsilon_{\mathrm{m}}-\epsilon_{\mathrm{d}})}{\epsilon_{\mathrm{d}} l + \epsilon_{\mathrm{m}}(l+1)}\right] Y_l^{m*}(\theta',\varphi') Y_l^m(\theta,\varphi) & \\ \qquad\qquad \text{for } r,\ r' > a. & \end{cases} \tag{2.27}$$

Inserting this expression into (2.18), we obtain the result of (2.26) with the additional multiplying factor $3/(\epsilon_{\mathrm{d}} + 2\epsilon_{\mathrm{m}})$.

In both cases (with and without a dielectric mismatch), the expression (2.26) can be written as

$$\delta V(\mathbf{R},\mathbf{r}) = Z m_{\mathrm{e}} \omega_{\mathrm{M}}^2 \left[z\Theta(a-r) + \frac{za^3}{r^3}\Theta(r-a)\right], \tag{2.28}$$

where the Mie frequency is given in (1.5). The only effect of the dielectric constants on the transition potential, as compared to the free case, is through the redshift of the Mie frequency. We thus recover, once δV is summed over the relative coordinates, the coupling Hamiltonian of (2.13).

2.2 Mean-field approximation and second quantization procedure

Even if the decomposition into center-of-mass and relative coordinates of the electronic Hamiltonian H is useful in the sense that it clearly shows the origin of the coupling between the two subsystems, it is still intractable because of the electronic interactions appearing in the relative-coordinate Hamiltonian (2.7). Thus, we will use a mean-field approximation which represents a substantial simplification for those degrees of freedom. Together with the second quantization procedure [54], this approximation scheme will be our starting point for the description of collective excitations in metallic nanoparticles.

2.2.1 Center-of-mass Hamiltonian

To proceed with the center-of-mass Hamiltonian (2.15), we introduce the standard annihilation and creation operators [78]

$$b = \sqrt{\frac{N m_\mathrm{e} \tilde{\omega}_\mathrm{M}}{2\hbar}} Z + \frac{\mathrm{i}}{\sqrt{2N m_\mathrm{e} \hbar \tilde{\omega}_\mathrm{M}}} P_Z, \tag{2.29a}$$

$$b^\dagger = \sqrt{\frac{N m_\mathrm{e} \tilde{\omega}_\mathrm{M}}{2\hbar}} Z - \frac{\mathrm{i}}{\sqrt{2N m_\mathrm{e} \hbar \tilde{\omega}_\mathrm{M}}} P_Z, \tag{2.29b}$$

with P_Z the conjugated momentum to Z. If $|n\rangle$ is an eigenstate of H_cm, we have the usual relations $b|n\rangle = \sqrt{n}|n-1\rangle$ and $b^\dagger|n\rangle = \sqrt{n+1}|n+1\rangle$. The operators (2.29) satisfy the usual bosonic commutation relations, and H_cm then reads

$$H_\mathrm{cm} = \hbar \tilde{\omega}_\mathrm{M} b^\dagger b \tag{2.30}$$

without taking into account the zero-point energy $\hbar\tilde{\omega}_\mathrm{M}/2$.

2.2.2 Hamiltonian of the relative coordinates

The Hamiltonian (2.7) of the relative-coordinate system contains the electron-electron interactions. In order to overcome this difficulty, we then treat it within the mean-field approximation. Furthermore, the second-quantization procedure is a convenient tool that allows to easily take into account the statistics of the particles (fermionic or bosonic) [54]. Passing to second quantization, H_rel can then be expressed as

$$H_\mathrm{rel} = \sum_\alpha \varepsilon_\alpha c_\alpha^\dagger c_\alpha. \tag{2.31}$$

ε_α are the eigenenergies for the effective mean-field potential V and $c_\alpha^\dagger$ (c_α) creates (annihilates) the one-body eigenstates $|\alpha\rangle$. Those operators are fermionic ones, and satisfy the usual anticommutation relations.[2]

[2] In the remaining of this thesis, we do not use different symbols for the operators acting on the Hilbert space (first-quantized form) and on the Fock space (second-quantized form), even though these operators are conceptually totally different. This is done in order to simplify the notations.

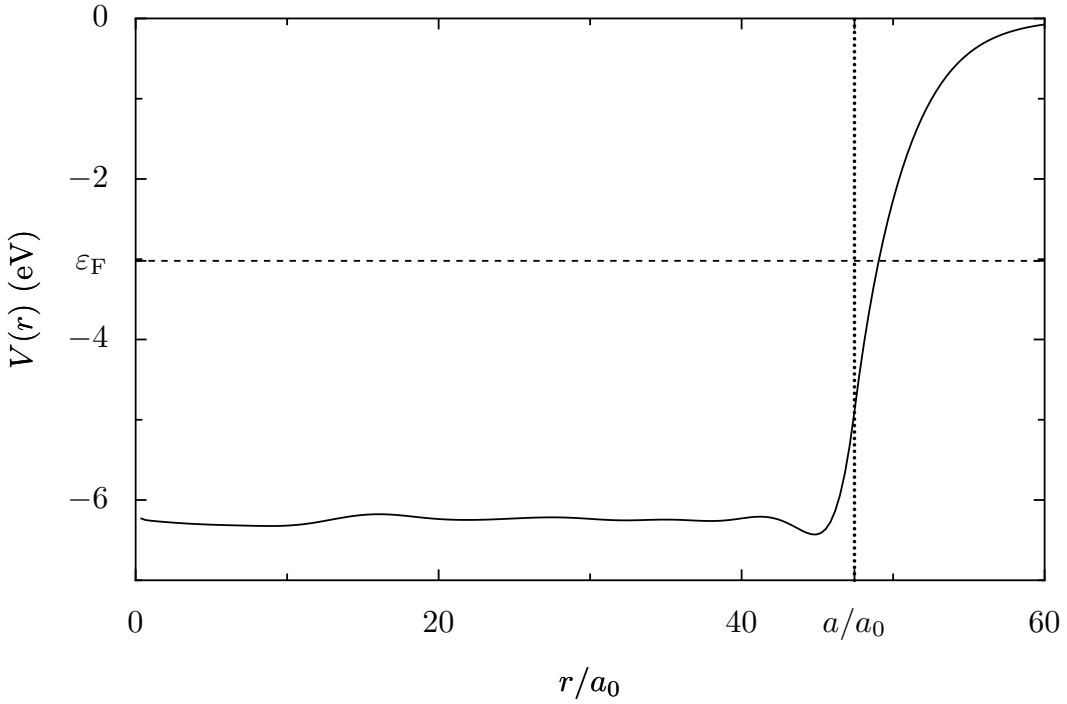

Figure 2.2: Self-consistent mean-field potential V from LDA numerical calculations (at $T = 0$) for a sodium nanoparticle ($r_s = 3.93\,a_0$) in vacuum with $N = 1760$ valence electrons, as a function of the radial coordinate in units of the Bohr radius $a_0 = 0.53\,\text{Å}$. The radius $a \simeq 47.7\,a_0$ is indicated by the dotted vertical line, while the horizontal dashed line indicates the Fermi energy ε_F.

The numerical calculations of the time-dependent local density approximation (TDLDA, see Sec. 1.2.4) within the spherical jellium model at zero temperature are a useful tool to obtain the mean-field potential seen by the electrons [26, 27, 58, 69]. Within this approximation, one can compute the response of the electronic system to an external time-dependent perturbation like, e.g., an electrical field. Basically, in its static counterpart (LDA), this approximation replaces the many-electron Hamiltonian (2.1) by a self-consistent Hamiltonian

$$H_{\text{sc}} = \frac{\mathbf{p}^2}{2m_e} + V(\mathbf{r}), \tag{2.32}$$

where the mean-field potential $V(\mathbf{r})$ is a local function which contains exchange and correlation terms. The self-consistent single-particle wave functions are found according to

$$H_{\text{sc}}\psi_\alpha(\mathbf{r}) = \varepsilon_\alpha\psi_\alpha(\mathbf{r}) \tag{2.33}$$

where ε_α is the eigenenergy of the state $|\alpha\rangle$. Since we consider spherical nanoparticles, the self-consistent potential entering (2.32) has radial symmetry, $V(\mathbf{r}) = V(r)$.[3] In

[3]We use a numerical implementation of the TDLDA which is based on the code JELLYRPA by

Fig. 2.2, we show the self-consistent potential V as a function of the radial coordinate r, for a typical sodium nanoparticle of radius $a = r_{\mathrm{s}} N^{1/3}$, with $r_{\mathrm{s}} = (3/4\pi n_{\mathrm{e}})^{1/3}$ the mean distance between electrons in the nanoparticle [9]. We see that it is relatively flat at the interior of the nanoparticle, and presents a steep increase at the boundary. The potential jump is often approximated for the purpose of analytical calculations by a true discontinuity at $r = a$. However, the details of the self-consistent potential close to the surface may be crucial for some properties, as we show in Sec. 5.1.3 and Chapter 8.

2.2.3 Coupling between center-of-mass and relative-coordinate systems

Inserting (2.9) into the coupling Hamiltonian H_{c} from (2.13), and expressing the Z-coordinate in terms of the annihilation and creation operators of (2.29),

$$Z = \sqrt{\frac{\hbar}{2N m_{\mathrm{e}} \tilde{\omega}_{\mathrm{M}}}} \left(b^{\dagger} + b\right), \tag{2.34}$$

one obtains in second quantization

$$H_{\mathrm{c}} = \Lambda \left(b^{\dagger} + b\right) \sum_{\alpha\beta} d_{\alpha\beta} c_{\alpha}^{\dagger} c_{\beta}, \tag{2.35}$$

where

$$d_{\alpha\beta} = \langle \alpha | \left[z\Theta(a - r) + \frac{z a^3}{r^3} \Theta(r - a) \right] | \beta \rangle \tag{2.36}$$

is the matrix element between two eigenstates of the unperturbed mean-field problem. In (2.35), we have defined the constant

$$\Lambda = \sqrt{\frac{\hbar m_{\mathrm{e}} \omega_{\mathrm{M}}^3}{2N}} \tag{2.37}$$

and we have neglected the spill-out for the calculation of the coupling when we expressed Z in terms of b and $b^{\dagger}$. This assumption is justified a posteriori. Indeed, we have seen in the introduction of this thesis that the spill-out effect leads to a correction of the Mie frequency which goes as $1/a$. As we will see in the sequel, the effect of the coupling on the physical quantities that will be evaluated leads to a scaling behavior which also goes as $1/a$. Thus, restricting ourselves to the first contributing order in $1/a$, we can neglect the spill-out effect in the coupling Hamiltonian H_{c}.

In a quantum many-body approach, the surface plasmon appears as a collective excitation of the electron system. The discrete-matrix random phase approximation (RPA) presented in Sec. 1.2.3 provides a useful representation since the eigenstates of the correlated electron system are expressed as superpositions of particle-hole states built from

G. F. Bertsch [79], which has been modified by R. A. Molina [80, 81] and ourselves. It has been improved in order to get the TDLDA response of large clusters (up to approximately 2000 atoms). Furthermore, with this modified code we are able to consider different dielectric environments.

the Hartree-Fock ground state. Following similar approaches developed for the study of giant resonances in nuclei, Yannouleas and Broglia [30] proposed a partition of the many-body RPA Hilbert space into a low-energy sector (the restricted subspace), generated by particle-hole excitations with low energy, and a high-energy sector (the additional subspace). The surface plasmon arises from a coherent superposition of a large number of basis states of the restricted subspace. Its energy lies in the high-energy sector, and therefore the mixture with particle-hole states of the additional subspace results in the broadening of the collective resonance. Thus, it has to be understood that the sums over α and β in (2.35) are restricted to the additional (high energy) RPA subspace. This separation in disjoint Hilbert spaces allows us to introduce the second quantization for the relative coordinates without falling into problems of double counting. If initially the center of mass is in its first excited state, the coupling H_{c} allows for the decay of the collective excitation into particle-hole pairs in the electronic environment H_{rel}, the so-called *Landau damping* [16, 80, 81].

2.3 External driving field

In this section, we describe the interaction of the nanoparticle with an external (classical) field. The surface plasmon resonance is located in the visible range and thus the size of the nanoparticle is much smaller than the wavelength of the electromagnetic field. Therefore, the external electrical field only couples to the electronic center of mass. In this situation, we can safely assume that the external electric field is independent of the spatial coordinate and monochromatic at the frequency ω_{L},

$$\mathbf{E}(t) = E_0 \cos(\omega_{\mathrm{L}} t)\mathbf{e}_z. \tag{2.38}$$

Therefore, in the dipolar approximation [78], the interaction between the driving field and the center-of-mass system reads

$$H_{\mathrm{F}}(t) = -\mathbf{D} \cdot \mathbf{E}(t) \tag{2.39}$$

where $\mathbf{D} = -eN\mathbf{R}$ is the dipole moment of the center of mass. With (2.34), we then obtain

$$H_{\mathrm{F}}(t) = (b^\dagger + b)\hbar\Omega_{\mathrm{R}} \cos(\omega_{\mathrm{L}} t), \tag{2.40}$$

where the Rabi frequency is defined as [82]

$$\Omega_{\mathrm{R}} = eE_0 \sqrt{\frac{N}{2m_{\mathrm{e}}\hbar\tilde{\omega}_{\mathrm{M}}}}. \tag{2.41}$$

Finally, the time-dependent Hamiltonian of the nanoparticle in presence of the external driving field reads $H + H_{\mathrm{F}}(t)$, where H is the electronic Hamiltonian of (2.14).

2.4 Conclusion for Chapter 2

Starting from the electronic many-body Hamiltonian H within the jellium approximation, we have shown in this chapter that the introduction of center-of-mass and relative coordinates yields a useful decomposition of H. Assuming that the displacement of the center of mass is small compared to the size of the nanoparticle, we have linearized the coupling between center-of-mass and relative-coordinate systems. This coupling arises from the Coulomb part of the single-particle confinement outside the nanoparticle. The Hamiltonian for the center of mass is harmonic, with a frequency redshifted from the classical Mie value by the spill-out effect. The Hamiltonian for the relative coordinates contains the many-body correlations, and therefore is treated within the mean-field approximation.

It has been shown that the coupling Hamiltonian has a simple physical interpretation. It arises from a rigid displacement of the electronic cloud from its equilibrium position, and results in a change of the mean-field potential seen by the electrons. We have shown that in the case of a dielectric mismatch between a noble-metal nanoparticle and the surrounding matrix, the expression for the coupling remains the same as in the case of a alkaline-metal nanoparticle in vacuum, up to a renormalization of the Mie frequency.

The decomposition of the electronic Hamiltonian presented in this chapter shows that the center-of-mass system interacts with an environment or "heat bath" (the relative coordinates) via the coupling Hamiltonian. As we show in the next chapter, this results in dissipation and decoherence of the surface plasmon excitation.

Chapter 3

Dynamics of the surface plasmon excitation

Il n'y a rien d'incompréhensible.

(Comte de Lautréamont, 1846-1870, in Poésies)

In this chapter, our goal is to study the dynamics of the surface plasmon after an excitation by an external driving field, e.g., by a laser. A particularly well-adapted formalism to attain such an objective is the density-matrix formalism that we develop in Sec. 3.1. Under certain approximations, this yields an analytically tractable model to study the dissipation of the collective surface plasmon excitation. In Sec. 3.2, we analyze in detail this dissipative process in terms of a two-level description of the electronic center of mass, a simplification that we discuss in Appendix A.

3.1 Reduced density-matrix description of the electronic center of mass

The advantage of the density-matrix formalism is that one is able, once the dynamical evolution of the system is resolved, to study both, the populations (diagonal part of the density matrix) and the coherences (off-diagonal part) of the system evolving according to a Hamiltonian dynamics. In Sec. 3.1.1, we will consider the free evolution of the system, i.e., without the external driving field whose interaction with the electronic center of mass is described by the Hamiltonian (2.40). In Sec. 3.1.2, we will incorporate the effects of the driving.

3.1.1 Free evolution of the center of mass

The evolution of the whole system in absence of the electromagnetic field is given by the equation of motion of the total density matrix

$$\dot{\rho}_{\mathrm{T}}(t) = -\frac{\mathrm{i}}{\hbar}\left[H, \rho_{\mathrm{T}}(t)\right], \tag{3.1}$$

where the Hamiltonian $H = H_0 + H_{\mathrm{c}}$ of the entire system is given by (2.14), with $H_0 = H_{\mathrm{cm}} + H_{\mathrm{rel}}$. The dot represents the time derivative with respect to t. The coupling Hamiltonian H_{c} between the center-of-mass system and the relative coordinates is assumed to be sufficiently weak so that one can treat it as a small perturbation with respect to H_0. A well-suited representation is therefore the interaction picture, where the evolution of the density matrix is

$$\dot{\tilde{\rho}}_{\mathrm{T}}(t) = -\frac{\mathrm{i}}{\hbar}\left[\tilde{H}_{\mathrm{c}}(t), \tilde{\rho}_{\mathrm{T}}(t)\right], \tag{3.2}$$

with

$$\tilde{\rho}_{\mathrm{T}}(t) = \mathrm{e}^{\mathrm{i}H_0 t/\hbar}\, \rho_{\mathrm{T}}(t)\, \mathrm{e}^{-\mathrm{i}H_0 t/\hbar} \tag{3.3}$$

and

$$\tilde{H}_{\mathrm{c}}(t) = \mathrm{e}^{\mathrm{i}H_0 t/\hbar}\, H_{\mathrm{c}}\, \mathrm{e}^{-\mathrm{i}H_0 t/\hbar}. \tag{3.4}$$

The equation of motion (3.2) can be integrated formally to yield

$$\tilde{\rho}_{\mathrm{T}}(t) = \rho_{\mathrm{T}}(0) - \frac{\mathrm{i}}{\hbar}\int_0^t \mathrm{d}s \left[\tilde{H}_{\mathrm{c}}(s), \tilde{\rho}_{\mathrm{T}}(s)\right]. \tag{3.5}$$

Inserting (3.5) into the equation of motion (3.2) yields the integro-differential equation

$$\dot{\tilde{\rho}}_{\mathrm{T}}(t) = -\frac{\mathrm{i}}{\hbar}\left[\tilde{H}_{\mathrm{c}}(t), \rho_{\mathrm{T}}(0)\right] - \frac{1}{\hbar^2}\int_0^t \mathrm{d}s \left[\tilde{H}_{\mathrm{c}}(t), \left[\tilde{H}_{\mathrm{c}}(s), \tilde{\rho}_{\mathrm{T}}(s)\right]\right]. \tag{3.6}$$

By tracing out the relative coordinates, we obtain the reduced density matrix of the center-of-mass system

$$\rho = \mathrm{Tr}_{\mathrm{rel}}\rho_{\mathrm{T}} = \sum_{\alpha}\langle\alpha|\rho_{\mathrm{T}}|\alpha\rangle, \tag{3.7}$$

where $|\alpha\rangle$ are the eigenstates of the mean-field Hamiltonian H_{rel} given in (2.31). From (3.6), we thus have

$$\dot{\tilde{\rho}}(t) = -\frac{\mathrm{i}}{\hbar}\mathrm{Tr}_{\mathrm{rel}}\left[\tilde{H}_{\mathrm{c}}(t), \rho_{\mathrm{T}}(0)\right] - \frac{1}{\hbar^2}\int_0^t \mathrm{d}s\, \mathrm{Tr}_{\mathrm{rel}}\left[\tilde{H}_{\mathrm{c}}(t), \left[\tilde{H}_{\mathrm{c}}(s), \tilde{\rho}_{\mathrm{T}}(s)\right]\right]. \tag{3.8}$$

Statistical description of the heat bath

In dissipative quantum dynamics the environment is considered to be infinite, i.e., its intrinsic properties like the temperature do not change as a consequence of its coupling to the system [74]. This idealization is particularly stringent in the case of an environment constituted by the relative coordinates. Therefore, we must restrict our analysis to the regime where the electron gas reaches thermal equilibrium at a temperature T determined from the energy balance and from the coupling of the electron system to external degrees of freedom (i.e., lattice vibrations). This is achieved under relatively weak laser excitations (i.e., under the effect of a probe laser field) or after about ten femtoseconds following a strong pump excitation.

We assume that the total system is in a thermal equilibrium at the temperature T at the initial time $t = 0$. Furthermore, we assume weak coupling such that the center-of-mass system and the relative coordinates are initially uncorrelated. Therefore we have

$$\rho_{\mathrm{T}}(0) \approx \rho(0) \otimes \rho_{\mathrm{rel}}, \tag{3.9}$$

with $\rho(0)$ the initial center-of-mass density matrix, and ρ_{rel} the density matrix of the environment.

Since the number of particles is fixed to N, we should work in principle in the canonical ensemble. In order to avoid the difficulty to deal with a fixed number of fermions, we can use the grand-canonical ensemble[1] and then

$$\rho_{\mathrm{rel}} = \frac{\mathrm{e}^{-\beta(H_{\mathrm{rel}}-\mu N)}}{\Xi}, \tag{3.10}$$

where μ is the chemical potential of the electron gas, and where the grand-canonical partition function is

$$\begin{aligned} \Xi &= \mathrm{Tr}_{\mathrm{rel}}\left[\mathrm{e}^{-\beta(H_{\mathrm{rel}}-\mu N)}\right] \\ &= \prod_{\alpha}\left[1+\mathrm{e}^{-\beta(\varepsilon_\alpha-\mu)}\right]. \end{aligned} \tag{3.11}$$

We have defined the inverse temperature as $\beta = (k_{\mathrm{B}}T)^{-1}$, k_{B} being the Boltzmann constant. An implicit assumption in this analysis is that the electronic environment is effectively coupled to a heat reservoir that ensures its thermalization.

As a consequence of the structure of the coupling H_{c} and of the assumption of an uncorrelated initial condition (3.9), the first term on the r.h.s. of (3.8) vanishes. Indeed, by inserting (2.35) and (3.9) we find

$$\mathrm{Tr}_{\mathrm{rel}}\left[\tilde{H}_{\mathrm{c}}(t), \rho(0)\otimes\rho_{\mathrm{rel}}\right] = \mathrm{Tr}_{\mathrm{rel}}\left[H_{\mathrm{c}}, \rho(0)\otimes\rho_{\mathrm{rel}}\right] \tag{3.12a}$$

$$= \Lambda\left[b^\dagger + b, \rho(0)\right]\sum_{\alpha\beta} d_{\alpha\beta}\mathrm{Tr}_{\mathrm{rel}}\left(\rho_{\mathrm{rel}}c_\alpha^\dagger c_\beta\right). \tag{3.12b}$$

[1] This approximation is valid in the thermodynamic limit ($N \gg 1$), where the canonical and grand-canonical ensembles are equivalent [83]. Unlike in the problem of persistent currents in mesoscopic rings [1], nothing subtle will appear with this approximation since we will deal with properties which depend mainly on the smooth density of states (see Appendix B).

To obtain (3.12a), we have used the cyclic invariance of the trace. Now, the trace over the bath coordinates in (3.12b) is only nonvanishing if $\alpha = \beta$, and since $d_{\alpha\alpha} = 0$ because of the dipole selection rules implicit in (2.36),[2] the first term on the r.h.s. of (3.8) vanishes. We therefore have

$$\dot{\tilde{\rho}}(t) = -\frac{1}{\hbar^2}\int_0^t \mathrm{d}s\, \mathrm{Tr}_{\mathrm{rel}}\left[\tilde{H}_{\mathrm{c}}(t), \left[\tilde{H}_{\mathrm{c}}(s), \tilde{\rho}_{\mathrm{T}}(s)\right]\right] \tag{3.13}$$

for the time evolution of the center-of-mass reduced density matrix.

An approximation that is usually done is to assume the weak coupling regime [82]: The perturbation H_{c} does not change significantly the environment, and therefore the relative coordinates remain in the equilibrium state ρ_{rel} during the time evolution of the center of mass. This assumption does not allow to describe the energy relaxation of the electronic heat bath to the phonon heat bath. However, an extension of the present calculation to the case of a time-dependent temperature which takes into account the above-mentioned relaxation process could be possible. Furthermore, we neglect the correlations between the system and the heat bath. Indeed, we assume that those correlations vanish on a timescale τ_{c} which is much smaller than the time t at which we consider the evolution of the system, τ_{c} being the correlation time. Since we disregard the dynamics of the center-of-mass system on the timescale of τ_{c}, we have

$$\tilde{\rho}_{\mathrm{T}}(t) \approx \tilde{\rho}(t) \otimes \rho_{\mathrm{rel}}, \tag{3.14}$$

and thus

$$\dot{\tilde{\rho}}(t) \simeq -\frac{1}{\hbar^2}\int_0^t \mathrm{d}s\, \mathrm{Tr}_{\mathrm{rel}}\left[\tilde{H}_{\mathrm{c}}(t), \left[\tilde{H}_{\mathrm{c}}(s), \tilde{\rho}(s) \otimes \rho_{\mathrm{rel}}\right]\right]. \tag{3.15}$$

Calculation of the correlator

In order to proceed with the evaluation of the correlator appearing in the integrand of (3.15), we now write explicitly the time dependence contained in the interaction picture of H_{c} as defined in (3.4).[3] To this end, we insert (2.35) into (3.4) and arrive at

$$\tilde{H}_{\mathrm{c}}(t) = \Lambda\left[\tilde{b}^\dagger(t) + \tilde{b}(t)\right]\sum_{\alpha\beta} d_{\alpha\beta}\tilde{c}_\alpha^\dagger(t)\tilde{c}_\beta(t). \tag{3.16}$$

The time evolution of any time-independent operator O in the interaction picture is given by

$$\dot{\tilde{O}}(t) = \frac{\mathrm{i}}{\hbar}\mathrm{e}^{\mathrm{i}H_0 t/\hbar}\,[H_0, O]\,\mathrm{e}^{-\mathrm{i}H_0 t/\hbar}. \tag{3.17}$$

For the fermionic operator $\tilde{c}_\alpha$, we thus have

$$\dot{\tilde{c}}_\alpha(t) = \frac{\mathrm{i}}{\hbar}\mathrm{e}^{\mathrm{i}H_0 t/\hbar}\,[H_{\mathrm{rel}}, c_\alpha]\,\mathrm{e}^{-\mathrm{i}H_0 t/\hbar}. \tag{3.18}$$

[2] Those dipole selection rules will appear in (4.10) given in Chapter 4.

[3] By "correlator", we mean the trace over the environment of the double commutator appearing on the r.h.s. of (3.15).

Using (2.31), $[H_{\mathrm{rel}}, c_\alpha] = -\delta_{\alpha\beta} c_\alpha$, and the solution of (3.18) reads

$$\tilde{c}_\alpha(t) = c_\alpha \mathrm{e}^{-\mathrm{i}\omega_\alpha t} \tag{3.19a}$$

with $\omega_\alpha = \varepsilon_\alpha/\hbar$. Likewise,

$$\tilde{c}^\dagger_\alpha(t) = c^\dagger_\alpha \mathrm{e}^{\mathrm{i}\omega_\alpha t}. \tag{3.19b}$$

For the bosonic operators $\tilde{b}$ and $\tilde{b}^\dagger$, a similar derivation yields

$$\tilde{b}(t) = b\mathrm{e}^{-\mathrm{i}\tilde{\omega}_{\mathrm{M}} t}, \tag{3.20a}$$

$$\tilde{b}^\dagger(t) = b^\dagger \mathrm{e}^{\mathrm{i}\tilde{\omega}_{\mathrm{M}} t}. \tag{3.20b}$$

With those results, we thus arrive to the following expression for the correlator of (3.15):

$$\begin{aligned} &\mathrm{Tr}_{\mathrm{rel}}\left[\tilde{H}_{\mathrm{c}}(t), \left[\tilde{H}_{\mathrm{c}}(s), \tilde{\rho}(s)\otimes\rho_{\mathrm{rel}}\right]\right] = \\ &\Lambda^2 \sum_{\alpha\beta\gamma\delta} d_{\alpha\beta} d_{\gamma\delta} \mathrm{e}^{\mathrm{i}(\omega_{\alpha\beta}s + \omega_{\gamma\delta}t)} \Big\{ \left[\tilde{b}^\dagger(t) + \tilde{b}(t), \left(\tilde{b}^\dagger(s) + \tilde{b}(s)\right)\tilde{\rho}(s)\right] \mathrm{Tr}_{\mathrm{rel}}\left(\rho_{\mathrm{rel}} c^\dagger_\gamma c_\delta c^\dagger_\alpha c_\beta\right) \\ &\qquad - \left[\tilde{b}^\dagger(t) + \tilde{b}(t), \tilde{\rho}(s)\left(\tilde{b}^\dagger(s) + \tilde{b}(s)\right)\right] \mathrm{Tr}_{\mathrm{rel}}\left(\rho_{\mathrm{rel}} c^\dagger_\alpha c_\beta c^\dagger_\gamma c_\delta\right) \Big\}, \end{aligned} \tag{3.21}$$

where $\omega_{\alpha\beta} = \omega_\alpha - \omega_\beta$. The two traces of the fermionic operators are given by

$$\mathrm{Tr}_{\mathrm{rel}}\left(\rho_{\mathrm{rel}} c^\dagger_\gamma c_\delta c^\dagger_\alpha c_\beta\right) = \delta_{\alpha\beta}\delta_{\gamma\delta} f(\varepsilon_\alpha) f(\varepsilon_\gamma) + \delta_{\alpha\delta}\delta_{\beta\gamma}\left[1 - f(\varepsilon_\alpha)\right] f(\varepsilon_\beta), \tag{3.22a}$$

$$\mathrm{Tr}_{\mathrm{rel}}\left(\rho_{\mathrm{rel}} c^\dagger_\alpha c_\beta c^\dagger_\gamma c_\delta\right) = \delta_{\alpha\beta}\delta_{\gamma\delta} f(\varepsilon_\alpha) f(\varepsilon_\gamma) + \delta_{\alpha\delta}\delta_{\beta\gamma} f(\varepsilon_\alpha)\left[1 - f(\varepsilon_\beta)\right], \tag{3.22b}$$

where

$$f(\varepsilon) = \frac{1}{\mathrm{e}^{\beta(\varepsilon-\mu)} + 1} \tag{3.23}$$

is the Fermi-Dirac distribution. As it has already been mentioned, the dipole matrix elements satisfy $d_{\alpha\alpha} = 0$, and with (3.22), we obtain for (3.21)

$$\begin{aligned} \mathrm{Tr}_{\mathrm{rel}}\left[\tilde{H}_{\mathrm{c}}(t), \left[\tilde{H}_{\mathrm{c}}(s), \tilde{\rho}(s)\otimes\rho_{\mathrm{rel}}\right]\right] &= C(s-t)\left[\tilde{b}^\dagger(t) + \tilde{b}(t), \left(\tilde{b}^\dagger(s) + \tilde{b}(s)\right)\tilde{\rho}(s)\right] \\ &\quad - C(t-s)\left[\tilde{b}^\dagger(t) + \tilde{b}(t), \tilde{\rho}(s)\left(\tilde{b}^\dagger(s) + \tilde{b}(s)\right)\right]. \end{aligned} \tag{3.24}$$

In the above equation, we have defined the correlation function of the bath as

$$C(\tau) = \sum_{\alpha\beta} \left[1 - f(\varepsilon_\alpha)\right] f(\varepsilon_\beta) \left|\Lambda d_{\alpha\beta}\right|^2 \mathrm{e}^{\mathrm{i}\omega_{\alpha\beta}\tau}. \tag{3.25}$$

It contains the complete information on the time evolution of the relative-coordinate degrees of freedom. It can be shown [82] that the real part of $C(\tau)$ describes the dynamics of the fluctuations of the environment, and that the imaginary part is related to a linear susceptibility.

Inserting the result of (3.24) into (3.15), we then arrive at

$$\begin{aligned} \dot{\tilde{\rho}}(t) = -\frac{1}{\hbar^2}\int_0^t \mathrm{d}\tau \Big\{ &C^*(\tau)\left[\tilde{b}^\dagger(t) + \tilde{b}(t), \left(\tilde{b}^\dagger(t-\tau) + \tilde{b}(t-\tau)\right)\tilde{\rho}(t-\tau)\right] \\ &- C(\tau)\left[\tilde{b}^\dagger(t) + \tilde{b}(t), \tilde{\rho}(t-\tau)\left(\tilde{b}^\dagger(t-\tau) + \tilde{b}(t-\tau)\right)\right] \Big\}. \end{aligned} \tag{3.26}$$

Markovian approximation and perturbative approach

The correlation function (3.25) is a superposition of exponentials oscillating at the eigenfrequencies $\omega_{\alpha\beta}$ of the heat bath. For not too small nanoparticles, the electronic environment described by the Hamiltonian (2.31) contains a large number of degrees of freedom, and its spectrum is therefore a quasi-continuum. Thus, the exponentials in (3.25) interfere in a destructive fashion very rapidly. Therefore, we can assume that the correlation function $C(\tau)$ decreases as a function of τ on a very short timescale τ_{c}, the correlation time. For $\tau > \tau_{\mathrm{c}}$, $C(\tau) \approx 0$. This constitutes the *Markovian approximation* [82, 84]. This allows to replace the upper bound t of the integral in (3.26) by ∞. This implies that we consider the evolution of the center-of-mass system on a timescale $t \gg \tau_{\mathrm{c}}$.[4]

Furthermore, since the coupling between the center-of-mass and the relative-coordinate system is weak, and since the r.h.s. of (3.26) is a second-order term in the coupling Hamiltonian H_{c}, it is reasonable to neglect the evolution of $\tilde{\rho}$ between $t-\tau$ and t. Taking into account this evolution would imply that we actually regard the evolution of the system to a higher order in perturbation theory [82]. Thus we can replace in (3.26) $\tilde{\rho}(t-\tau)$ by $\tilde{\rho}(t)$.

With the Markovian approximation and the perturbative expansion to second order in the coupling Hamiltonian, we then obtain for the evolution of the center-of-mass reduced density matrix (in the interaction picture)

$$\dot{\tilde{\rho}}(t) \approx -\frac{1}{\hbar^2}\int_0^\infty \mathrm{d}\tau \Big\{ C^*(\tau)\left[\tilde{b}^\dagger(t)+\tilde{b}(t), \left(\tilde{b}^\dagger(t-\tau)+\tilde{b}(t-\tau)\right)\tilde{\rho}(t)\right] - C(\tau)\left[\tilde{b}^\dagger(t)+\tilde{b}(t), \tilde{\rho}(t)\left(\tilde{b}^\dagger(t-\tau)+\tilde{b}(t-\tau)\right)\right]\Big\}. \tag{3.27}$$

Within the Markovian approximation, there is no memory effect on a first approximation in the system we are studying.[5] Together with the weak coupling assumption, it yields a time evolution described by (3.27) which is tractable analytically and provides physical insight into the relaxation process of the surface plasmon excitation.

Making explicit the time dependence of the bosonic operators (3.20) in (3.27), we

[4] Note that an explicit evaluation of the correlation function (3.25) could be done either numerically from the knowledge of the single-particle eigenenergies, or analytically by means of the semiclassical expansions that we develop in the remainder of this thesis. As we will see, the Markovian approximation yields valuable results, notably for the surface plasmon linewidth. Thus we can expect this assumption to be reasonable.

[5] However, memory effects on the electron dynamics in metallic nanoparticles have been lately studied numerically, and seem to broaden the surface plasmon resonance [85].

obtain

$$\dot{\tilde{\rho}}(t) = -\frac{1}{\hbar^2}\int_0^\infty \mathrm{d}\tau \Bigg\{ C^*(\tau)\Bigg[\Big[b^\dagger, \tilde{b}(-\tau)\tilde{\rho}(t)\Big] + \Big[b, \tilde{b}^\dagger(-\tau)\tilde{\rho}(t)\Big] + \mathrm{e}^{2\mathrm{i}\tilde{\omega}_\mathrm{M}t}\Big[b^\dagger, \tilde{b}^\dagger(-\tau)\tilde{\rho}(t)\Big] + \mathrm{e}^{-2\mathrm{i}\tilde{\omega}_\mathrm{M}t}\Big[b, \tilde{b}(-\tau)\tilde{\rho}(t)\Big]\Bigg] - C(\tau)\Bigg[\Big[b^\dagger, \tilde{\rho}(t)\tilde{b}(-\tau)\Big] + \Big[b, \tilde{\rho}(t)\tilde{b}^\dagger(-\tau)\Big] + \mathrm{e}^{2\mathrm{i}\tilde{\omega}_\mathrm{M}t}\Big[b^\dagger, \tilde{\rho}(t)\tilde{b}^\dagger(-\tau)\Big] + \mathrm{e}^{-2\mathrm{i}\tilde{\omega}_\mathrm{M}t}\Big[b, \tilde{\rho}(t)\tilde{b}(-\tau)\Big]\Bigg]\Bigg\}. \tag{3.28}$$

In the above expression, the terms proportional to $\mathrm{e}^{\pm 2\mathrm{i}\tilde{\omega}_\mathrm{M}t}$ are highly oscillating ones as a function of t. Thus, once integrated over t to obtain $\tilde{\rho}(t)$, those contributions are almost vanishing and will be neglected in the following. This is the so-called *rotating wave approximation* [82,84]. With the expression (3.25) of the correlation function $C(\tau)$, we then obtain

$$\dot{\tilde{\rho}}(t) \simeq -\frac{1}{\hbar^2}\sum_{\alpha\beta}\left[1-f(\varepsilon_\alpha)\right]f(\varepsilon_\beta)\left|\Lambda d_{\alpha\beta}\right|^2\int_0^\infty \mathrm{d}\tau\Big\{\mathrm{e}^{-\mathrm{i}(\omega_{\alpha\beta}-\tilde{\omega}_\mathrm{M})\tau}\left[b^\dagger, b\tilde{\rho}(t)\right] + \mathrm{e}^{-\mathrm{i}(\omega_{\alpha\beta}+\tilde{\omega}_\mathrm{M})\tau}\left[b, b^\dagger\tilde{\rho}(t)\right] - \mathrm{e}^{\mathrm{i}(\omega_{\alpha\beta}+\tilde{\omega}_\mathrm{M})\tau}\left[b^\dagger, \tilde{\rho}(t)b\right] - \mathrm{e}^{\mathrm{i}(\omega_{\alpha\beta}-\tilde{\omega}_\mathrm{M})\tau}\left[b, \tilde{\rho}(t)b^\dagger\right]\Big\}. \tag{3.29}$$

Now, using

$$\int_0^\infty \mathrm{d}\tau\,\mathrm{e}^{\pm\mathrm{i}\Omega\tau} = \pm\mathrm{i}\mathcal{P}\frac{1}{\Omega} + \pi\delta(\Omega), \tag{3.30}$$

where $\mathcal{P}$ denotes the Cauchy principal value, we obtain by rearranging the commutators in (3.29)

$$\dot{\tilde{\rho}}(t) = \mathrm{i}\delta\left[b^\dagger b, \tilde{\rho}(t)\right] - \frac{\gamma_-}{2}\left[b^\dagger b\tilde{\rho}(t) + \tilde{\rho}(t)b^\dagger b - 2b\tilde{\rho}(t)b^\dagger\right] - \frac{\gamma_+}{2}\left[bb^\dagger\tilde{\rho}(t) + \tilde{\rho}(t)bb^\dagger - 2b^\dagger\tilde{\rho}(t)b\right] \tag{3.31}$$

with

$$\gamma_\pm = \frac{2\pi}{\hbar^2}\sum_{\alpha\beta}\left[1-f(\varepsilon_\alpha)\right]f(\varepsilon_\beta)\left|\Lambda d_{\alpha\beta}\right|^2\delta\left(\tilde{\omega}_\mathrm{M}\pm\omega_{\alpha\beta}\right) \tag{3.32}$$

and

$$\delta = \frac{2}{\hbar^2}\mathcal{P}\sum_{\alpha\beta}\left[1-f(\varepsilon_\alpha)\right]f(\varepsilon_\beta)\left|\Lambda d_{\alpha\beta}\right|^2\frac{\omega_{\alpha\beta}}{\omega_{\alpha\beta}^2-\tilde{\omega}_\mathrm{M}^2}. \tag{3.33}$$

Coming back to the Schrödinger picture, we finally obtain the master equation for the reduced density matrix of the center-of-mass degree of freedom in absence of the external driving field

$$\dot{\rho}(t) = -\mathrm{i}\omega_\mathrm{sp}\left[b^\dagger b, \rho(t)\right] - \frac{\gamma_-}{2}\left[b^\dagger b\rho(t) + \rho(t)b^\dagger b - 2b\rho(t)b^\dagger\right] - \frac{\gamma_+}{2}\left[bb^\dagger\rho(t) + \rho(t)bb^\dagger - 2b^\dagger\rho(t)b\right], \tag{3.34}$$

where

$$\omega_{\rm sp} = \tilde{\omega}_{\rm M} - \delta \tag{3.35}$$

is the renormalized surface plasmon frequency.

Writing (3.34) in the basis of harmonic oscillator states $|n\rangle$, we have for the diagonal part of the center-of-mass density matrix

$$\dot{\rho}_{nn} = -n\gamma_-\rho_{nn} - (n+1)\gamma_+\rho_{n+1,n+1} + n\gamma_+\rho_{n-1,n-1} + (n+1)\gamma_-\rho_{n+1,n+1}. \tag{3.36}$$

If the state $|n\rangle$ is occupied with a certain probability ρ_{nn}, it decays to the state $|n-1\rangle$ with the rate $n\gamma_-$ and raises to the state $|n+1\rangle$ with the rate $(n+1)\gamma_+$. In the mean time, the probability ρ_{nn} is increased by transitions from the states $|n-1\rangle$ and $|n+1\rangle$ with rates $n\gamma_+$ and $(n+1)\gamma_-$, respectively.

Physical meaning of γ_+, γ_-, and δ

As we show here, the expressions of $\gamma_\pm$, and of δ entering (3.34) have simple physical interpretations: γ_+ and γ_- are related to the lifetime of the $n^{\rm th}$ excited state of the harmonic oscillator center-of-mass system, while δ is the frequency shift due to the interaction of the system with the electronic environment.

When the displacement of the center of mass is much smaller than the nanoparticle size, it is possible to linearize the coupling Hamiltonian as it was done in Chapter 2. The weak coupling regime allows to treat $H_{\rm c}$ as a perturbation to the uncoupled Hamiltonian $H_{\rm cm} + H_{\rm rel}$. Assuming that initially the center of mass is in its $n^{\rm th}$ excited state $|n\rangle$, two processes limit the lifetime of $|n\rangle$: (i) the decay into the lower state $|n-1\rangle$ with creation of a particle-hole pair, and (ii) the excitation to the higher state $|n+1\rangle$ of the center of mass caused by the annihilation of a particle-hole pair (see Fig. 3.1). Obviously, this last process is only possible at finite temperatures. Then, Fermi's golden rule [53] yields the linewidth

$$\gamma_n = \frac{2\pi}{\hbar} \sum_{\substack{m \\ F_{\rm rel}, I_{\rm rel}}} P_{I_{\rm rel}} \left|\langle m, F_{\rm rel}|H_{\rm c}|n, I_{\rm rel}\rangle\right|^2 \delta\left((n-m)\hbar\tilde{\omega}_{\rm M} + \varepsilon_{I_{\rm rel}} - \varepsilon_{F_{\rm rel}}\right) \tag{3.37}$$

for the collective state $|n\rangle$. It is related to the lifetime of the center-of-mass state $|n\rangle$ through $\tau_n = 1/\gamma_n$. In the golden rule, $|m\rangle$ and $|F_{\rm rel}\rangle$ are the final states of center-of-mass and relative coordinates, of energy $m\hbar\tilde{\omega}_{\rm M}$ and $\varepsilon_{F_{\rm rel}}$, respectively. The probability of finding the initial state $|I_{\rm rel}\rangle$ occupied is given in the grand-canonical ensemble by the matrix element

$$P_{I_{\rm rel}} = \langle I_{\rm rel}|\rho_{\rm rel}|I_{\rm rel}\rangle \tag{3.38}$$

of the equilibrium density matrix at the temperature T defined in (3.10). Introducing the expression (2.35) of the coupling Hamiltonian, we obtain

$$\gamma_n = n\gamma_- + (n+1)\gamma_+, \tag{3.39}$$

where $\gamma_\pm$ are defined in (3.32). For the linewidth of the surface plasmon excitation, which is the first excited state of the center-of-mass system ($n = 1$), we thus obtain

$$\gamma_1 \equiv \gamma = \gamma_- + 2\gamma_+. \tag{3.40}$$

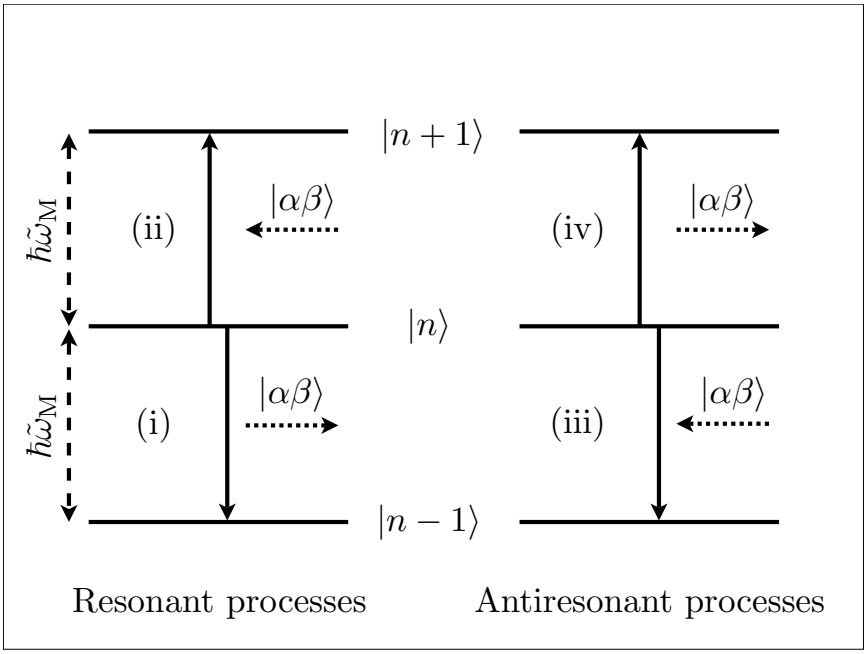

Figure 3.1: The four processes contributing to the linewidth γ_n of the $n^{\rm th}$ center-of-mass state and to the energy shift δ, as discussed in the text. In the figure, $|\alpha\beta\rangle$ stands for a particle-hole pair.

This very important and experimentally relevant quantity will be evaluated in Chapter 4. The first term on the r.h.s. in (3.40) is the rate associated with the spontaneous decay of a plasmon, while the second one is the rate for a plasmon excitation by the thermal environment. The latter mechanism is suppressed at zero temperature.

In the absence of the coupling $H_{\rm c}$, the energy of the $n^{\rm th}$ state of the center-of-mass system is given by the eigenenergies $\mathcal{E}_n^{(0)} = n\hbar\tilde{\omega}_{\rm M}$ of $H_{\rm cm}$ defined in (2.30). The presence of the coupling Hamiltonian (2.35) perturbs the eigenstates of $H_{\rm cm}$. The leading contribution to the resulting shift of the eigenenergies $\mathcal{E}_n^{(0)}$ is determined using perturbation theory in $H_{\rm c}$. While the first order does not contribute due to the selection rules contained in the coupling (2.35), there are four second-order processes involving virtual particle-hole pairs. In addition to the two resonant processes (i) and (ii) mentioned above, one has to take into account (iii) that a plasmon can decay by destroying a particle-hole pair, and (iv) that a plasmon can be excited to a higher collective state by creating a particle-hole pair (see Fig. 3.1). Those two latter processes are antiresonant ones. Taking into account all four mechanisms, to second order in the coupling we obtain

the perturbed energy

$$\mathcal{E}_n^{(2)} = n\hbar\tilde{\omega}_{\mathrm{M}} + \sum_{\substack{m \\ F_{\mathrm{rel}},I_{\mathrm{rel}}}} P_{I_{\mathrm{rel}}} \frac{|\langle m, F_{\mathrm{rel}}|H_{\mathrm{c}}|n, I_{\mathrm{rel}}\rangle|^2}{(n-m)\hbar\tilde{\omega}_{\mathrm{M}} + \varepsilon_{I_{\mathrm{rel}}} - \varepsilon_{F_{\mathrm{rel}}}}. \tag{3.41}$$

Using (2.35) to replace H_{c} in the preceding expression, we obtain

$$\mathcal{E}_n^{(2)} = n\hbar\tilde{\omega}_{\mathrm{M}} - n\hbar\delta_- - (n+1)\hbar\delta_+, \tag{3.42}$$

where

$$\delta_\pm = \frac{1}{\hbar^2}\mathcal{P}\sum_{\alpha\beta}\left[1 - f(\varepsilon_\alpha)\right] f(\varepsilon_\beta) \frac{|\Lambda d_{\alpha\beta}|^2}{\omega_{\alpha\beta} \pm \tilde{\omega}_{\mathrm{M}}}. \tag{3.43}$$

Thus, the energy difference between two adjacent center-of-mass states $|n\rangle$ and $|n+1\rangle$ is independent of n, and is given by

$$\hbar\omega_{\mathrm{sp}} = \mathcal{E}_{n+1}^{(2)} - \mathcal{E}_n^{(2)} = \hbar\tilde{\omega}_{\mathrm{M}} - \hbar\delta, \tag{3.44}$$

where $\delta = \delta_+ + \delta_-$ is defined in (3.33). We thus recover (3.35), and the electronic environment leads to a shift of the harmonic-oscillator frequency as compared to the unperturbed case. As we will see in Chapter 5, the shift δ is positive, and thus we have an additional redshift of the surface plasmon frequency compared to the redshift induced by the spill-out effect which yields the frequency $\tilde{\omega}_{\mathrm{M}}$ given in (1.7). This redshift of the surface plasmon frequency induced by the electronic environment is analogous to the Lamb shift known in atomic physics [82, 84, 86, 87]. If an atom is subject to an electromagnetic field, the interaction with the reservoir of photons induces a shift of its resonance frequency. This effect comes in addition to the hyperfine structure of the atom, and explains for instance the fact that in the hydrogen atom, the $2p_{1/2}$ state is slightly lower in energy than the $2s_{1/2}$ state, resulting in a slight shift of the corresponding spectral line. In our case, the shift δ is induced by the electronic environment which acts on the center-of-mass system.

3.1.2 Effect of the external driving field

In this section, we consider the role of the external driving field whose interaction with the center-of-mass coordinate is described by the time-dependent Hamiltonian $H_{\mathrm{F}}(t)$ (2.40). In a first step, we neglect the coupling Hamiltonian H_{c}. Thus, we do not have any damping mechanism of the surface plasmon excitation, and also no renormalization of the harmonic-oscillator frequency (3.35). In this case, the time-evolution of the density matrix of the whole system is given by

$$\dot{\rho}_{\mathrm{T}}(t) = -\frac{\mathrm{i}}{\hbar}\left[H_{\mathrm{cm}} + H_{\mathrm{rel}} + H_{\mathrm{F}}(t), \rho_{\mathrm{T}}(t)\right]. \tag{3.45}$$

In the absence of the coupling H_{c}, the density matrix of the center-of-mass and of the relative-coordinate system are uncoupled, such that $\rho_{\mathrm{T}}(t) = \rho(t) \otimes \rho_{\mathrm{rel}}$. Tracing out the

relative coordinates, we thus arrive at

$$\dot{\rho}(t) = -\frac{\mathrm{i}}{\hbar}\left[H_{\mathrm{cm}} + H_{\mathrm{F}}(t), \rho(t)\right]. \tag{3.46}$$

Expressing H_{cm} and $H_{\mathrm{F}}(t)$ according to (2.30) and (2.40), respectively, we obtain

$$\dot{\rho}(t) = -\mathrm{i}\tilde{\omega}_{\mathrm{M}}\left[b^{\dagger}b, \rho(t)\right] - \mathrm{i}\Omega_{\mathrm{R}}\cos\left(\omega_{\mathrm{L}}t\right)\left[b^{\dagger} + b, \rho(t)\right] \tag{3.47}$$

which describes the time evolution of a harmonic oscillator driven by an external monochromatic field. The Rabi frequency Ω_{R} is defined in (2.41).

Now, assuming that the driving does not influence the dissipation of the collective surface plasmon excitation, we can add the contributions from H_{c}, i.e., the dissipative part of the reduced density matrix described by the master equation (3.34), and from $H_{\mathrm{F}}(t)$ (see Eq. 3.47) *independently* [82]. This is justified in the following way. The damping rates $\gamma_{\pm}$ and the shift δ are due to the interaction between the center of mass and the relative coordinates via the coupling H_{c}, and not to the interaction with a reservoir of photons. For the nanoparticles we consider, the radiative damping can be neglected compared to the Landau damping. Thus, we can conclude that the external electromagnetic field does not influence the linewidths and shifts of the center-of-mass states.

Finally, the reduced density matrix of the center-of-mass system is governed by the master equation

$$\begin{aligned}\dot{\rho}(t) = &-\mathrm{i}\omega_{\mathrm{sp}}\left[b^{\dagger}b, \rho(t)\right] - \mathrm{i}\Omega_{\mathrm{R}}\cos\left(\omega_{\mathrm{L}}t\right)\left[b^{\dagger} + b, \rho(t)\right] \\ &- \frac{\gamma_{-}}{2}\left[b^{\dagger}b\rho(t) + \rho(t)b^{\dagger}b - 2b\rho(t)b^{\dagger}\right] - \frac{\gamma_{+}}{2}\left[bb^{\dagger}\rho(t) + \rho(t)bb^{\dagger} - 2b^{\dagger}\rho(t)b\right],\end{aligned} \tag{3.48}$$

which is nothing but the well-known master equation for a driven damped harmonic oscillator [82, 84]. Another way to find this master equation would have been to use the optical Bloch equation (3.47), together with the Lindblad theory in order to include the natural damping of the system [88, 89]. Furthermore, we could have used second order perturbation theory to introduce the environment-induced shift of the surface plasmon frequency, as presented above. However, the master-equation method derived in this section provides a self-contained approach which allows to render explicit all the approximation of this simple model.

The matrix representation in the harmonic oscillator basis of (3.48) is given by

$$\begin{aligned}\dot{\rho}_{nm}(t) = &-\mathrm{i}\omega_{\mathrm{sp}}(n-m)\rho_{nm}(t) - \gamma\left[\frac{n+m}{2}\rho_{nm}(t) - \sqrt{(n+1)(m+1)}\rho_{n+1,m+1}(t)\right] \\ &- \mathrm{i}\Omega_{\mathrm{R}}\cos\left(\omega_{\mathrm{L}}t\right)\left[\sqrt{n}\rho_{n-1,m}(t) + \sqrt{n+1}\rho_{n+1,m}(t) - \sqrt{m}\rho_{n,m-1}(t) - \sqrt{m+1}\rho_{n,m+1}(t)\right].\end{aligned} \tag{3.49}$$

In the above equation, we have neglected γ_{+} as compared to γ_{-} and noted $\gamma = \gamma_{-}$. Indeed, it is easy to show from (3.32) that the rate γ_{+} is related to γ_{-} through the detailed-balance relation

$$\gamma_{+} = \mathrm{e}^{-\beta\hbar\tilde{\omega}_{\mathrm{M}}}\gamma_{-}. \tag{3.50}$$

We have $\gamma_+ \ll \gamma_-$ for temperatures up to a few thousand degrees since $\hbar\tilde{\omega}_{\mathrm{M}}$ is of the order of several eV.

3.2 Two-level system approach

We now describe more precisely the time evolution of the center-of-mass degree of freedom under the influence of the external driving field. To this end, we will solve (3.49) under the following assumption: The center-of-mass system which is normally a harmonic oscillator described by the Hamiltonian (2.30) can be approximated by a two-level system. The applicability of such an approximation is discussed in Appendix A. The reasons for this simplifying hypothesis are the following: Except for a very strong driving field, the harmonic oscillator states higher than the first excited state are not significantly populated. Furthermore, the detuning between the frequency of the laser and the resonance frequency of the system plays in favor of the two-level description (for more details, see Appendix A). Moreover, there exists additional damping mechanisms which are not included in our model, like the ionization of the double plasmon state (see Chapter 7), or the radiation damping [11]. Then, the second collective level (the double plasmon) has a width which is significantly larger than the one of the simple surface plasmon, and it is then justified to neglect all excited levels but the first one. In addition to this, the existence of the double-plasmon state has not been clearly identified experimentally, even though indirect observations of such a state have been reported in the experiments of Refs. 72 and 73 on charged sodium clusters in vacuum. In the case of pump-probe experiments on noble-metal nanoparticles embedded in a dielectric medium, interactions with the surrounding matrix provide further decay channels (e.g., via coupling to phonons, localized states, surface states, etc.) For these reasons we will here restrict ourselves to the study of the two-level system.

Writing explicitly the master equation (3.49) for the two collective states $|0\rangle$ and $|1\rangle$ yields the system

$$\dot{\rho}_{00} = -\mathrm{i}\Omega_{\mathrm{R}} \cos(\omega_{\mathrm{L}} t)\,(\rho_{10} - \rho_{01}) + \gamma\rho_{11}, \tag{3.51a}$$

$$\dot{\rho}_{11} = \mathrm{i}\Omega_{\mathrm{R}} \cos(\omega_{\mathrm{L}} t)\,(\rho_{10} - \rho_{01}) - \gamma\rho_{11}, \tag{3.51b}$$

$$\dot{\rho}_{01} = \mathrm{i}\omega_{\mathrm{sp}}\rho_{01} - \mathrm{i}\Omega_{\mathrm{R}} \cos(\omega_{\mathrm{L}} t)\,(\rho_{11} - \rho_{00}) - \frac{\gamma}{2}\rho_{01}, \tag{3.51c}$$

with the conditions $\rho_{00} + \rho_{11} = 1$ and $\rho_{10}^* = \rho_{01}$. Introducing the new variables

$$\rho_{nm} = \hat{\rho}_{nm} \mathrm{e}^{-\mathrm{i}\omega_{\mathrm{L}}(n-m)t} \tag{3.52}$$

and keeping only the terms which significantly contribute close to the resonance $\omega_{\mathrm{L}} \approx \omega_{\mathrm{sp}}$

(rotating wave approximation [82]), one obtains

$$\dot{\hat{\rho}}_{00} = -\mathrm{i}\frac{\Omega_\mathrm{R}}{2}\left(\hat{\rho}_{10} - \hat{\rho}_{01}\right) + \gamma\hat{\rho}_{11}, \tag{3.53a}$$

$$\dot{\hat{\rho}}_{11} = \mathrm{i}\frac{\Omega_\mathrm{R}}{2}\left(\hat{\rho}_{10} - \hat{\rho}_{01}\right) - \gamma\hat{\rho}_{11}, \tag{3.53b}$$

$$\dot{\hat{\rho}}_{01} = -\mathrm{i}\delta_\mathrm{L}\hat{\rho}_{01} - \mathrm{i}\frac{\Omega_\mathrm{R}}{2}\left(\hat{\rho}_{11} - \hat{\rho}_{00}\right) - \frac{\gamma}{2}\hat{\rho}_{01}, \tag{3.53c}$$

where $\delta_\mathrm{L} = \omega_\mathrm{L} - \omega_\mathrm{sp}$ is the detuning between the laser and the resonance frequency.

Introducing a Bloch vector $\mathbf{X} = u\mathbf{e}_u + v\mathbf{e}_v + w\mathbf{e}_w$ with components [82]

$$u = \frac{1}{2}\left(\hat{\rho}_{01} + \hat{\rho}_{10}\right), \tag{3.54a}$$

$$v = \frac{1}{2\mathrm{i}}\left(\hat{\rho}_{01} - \hat{\rho}_{10}\right), \tag{3.54b}$$

$$w = \frac{1}{2}\left(\hat{\rho}_{11} - \hat{\rho}_{00}\right), \tag{3.54c}$$

the Bloch equations (3.53) take the form

$$\dot{\mathbf{X}} = \mathcal{M}\mathbf{X} - \frac{\gamma}{2}\mathbf{e}_w, \tag{3.55}$$

where

$$\mathcal{M} = \begin{pmatrix} -\gamma/2 & \delta_\mathrm{L} & 0 \\ -\delta_\mathrm{L} & -\gamma/2 & -\Omega_\mathrm{R} \\ 0 & \Omega_\mathrm{R} & -\gamma \end{pmatrix}. \tag{3.56}$$

The general solution of (3.55) reads

$$\mathbf{X}(t) = \sum_{i=1}^{3} A_i \mathrm{e}^{\lambda_i t}\mathbf{x}_i + \mathbf{X}_\mathrm{st}, \tag{3.57}$$

where $\mathbf{x}_i$ is the eigenvector associated to the eigenvalue λ_i of the matrix $\mathcal{M}$, while the A_i's are constants of integration determined by the initial conditions. $\mathbf{X}_\mathrm{st} = u_\mathrm{st}\mathbf{e}_u + v_\mathrm{st}\mathbf{e}_v + w_\mathrm{st}\mathbf{e}_w$ is the stationary solution of (3.55) given by $\mathbf{X}_\mathrm{st} = (\gamma/2)\mathcal{M}^{-1}\mathbf{e}_w$, i.e.,

$$u_\mathrm{st} = \frac{\sqrt{2s}\Delta}{1 + s^2 + 4\Delta^2}, \tag{3.58a}$$

$$v_\mathrm{st} = \frac{\sqrt{s/2}}{1 + s^2 + 4\Delta^2}, \tag{3.58b}$$

$$w_\mathrm{st} = \frac{s/2}{1 + s^2 + 4\Delta^2} - \frac{1}{2}. \tag{3.58c}$$

We have defined the so-called *saturation parameter*

$$s = 2\left(\frac{\Omega_\mathrm{R}}{\gamma}\right)^2 \tag{3.59}$$

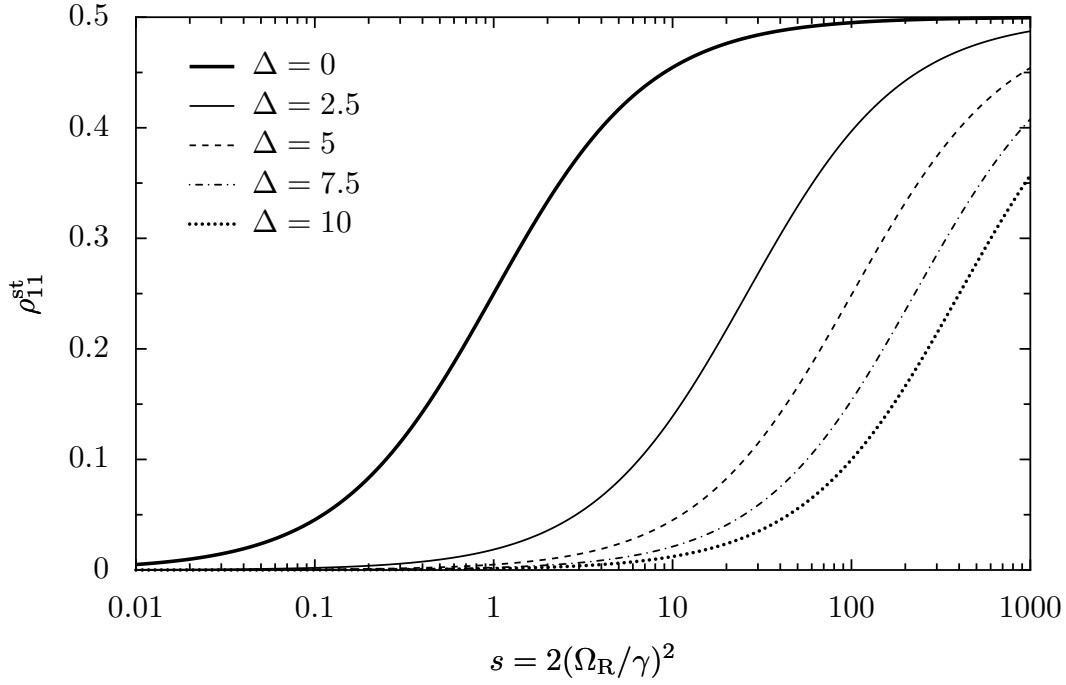

Figure 3.2: Stationary occupation probability ρ_{11}^{st} according to (3.61b) as a function of the saturation parameter s for increasing values of the detuning $\Delta = \delta_{\mathrm{L}}/\gamma$.

which is a measure of the ratio of the field intensity over damping (see the definition of the Rabi frequency, Eq. 2.41), and the scaled detuning

$$\Delta = \frac{\delta_{\mathrm{L}}}{\gamma}. \tag{3.60}$$

With (3.54) and (3.52), this yields the stationary solutions

$$\rho_{00}^{\mathrm{st}} = \frac{1 + s/2 + 4\Delta^2}{1 + s + 4\Delta^2}, \tag{3.61a}$$

$$\rho_{11}^{\mathrm{st}} = \frac{s/2}{1 + s + 4\Delta^2}, \tag{3.61b}$$

$$\rho_{01}^{\mathrm{st}}(t) = \mathrm{e}^{\mathrm{i}\omega_{\mathrm{L}}t} \frac{(2\Delta + \mathrm{i})\sqrt{s/2}}{1 + s + 4\Delta^2}. \tag{3.61c}$$

For $s \gg 1$, both populations ρ_{00}^{st} and ρ_{11}^{st} tend to $1/2$. In this situation, the limitation to two levels is of course questionable. A sufficiently intense excitation thus yields an equal occupation probability of the two collective levels, and hence the name "saturation parameter" for s. In Fig. 3.2, we show the stationary population of the excited state ρ_{11}^{st} as a function of the saturation parameter s for various values of the detuning Δ. For a fixed field intensity, i.e., a fixed saturation parameter, ρ_{11}^{st} decreases as a function of the detuning. Here we should mention that we cannot pretend to correctly describe

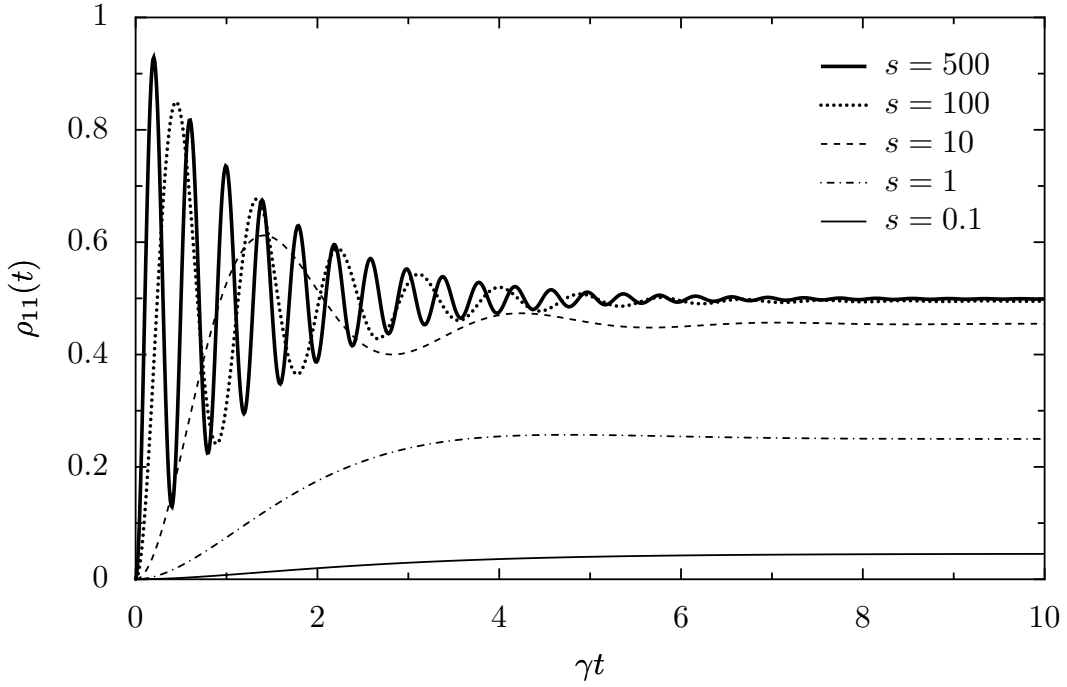

Figure 3.3: Population of the excited state ρ_{11} (3.62) as a function of γt for different values of the saturation parameter s.

the dynamical behavior of the center-of-mass system for a large detuning parameter δ_{L}. Indeed, since we work in the rotating wave approximation, our treatment remains valid for ω_{L} near the resonance frequency ω_{sp}. Thus, the results presented for $\delta_{\mathrm{L}} \sim 10\gamma$ have to be taken with precaution.

3.2.1 Analytical solutions of the Bloch equations without detuning

When the laser field is at resonance with the collective frequency ω_{sp}, i.e., there is no detuning ($\delta_{\mathrm{L}} = 0$), it is possible to solve (3.55) analytically. Assuming that the system is initially at rest, i.e., $\rho_{00}(0) = 1$, the transient solutions are given by

$$\rho_{11}(t) = \frac{s/2}{1+s}\left\{1 - \mathrm{e}^{-3\gamma t/4}\left[\cosh\left(\frac{\gamma t}{4}\sqrt{1-8s}\right) + \frac{3}{\sqrt{1-8s}}\sinh\left(\frac{\gamma t}{4}\sqrt{1-8s}\right)\right]\right\} \tag{3.62}$$

for the population of the excited state, and

$$\rho_{01}(t) = \mathrm{i}\,\mathrm{e}^{\mathrm{i}\omega_{\mathrm{sp}}t}\frac{\sqrt{s/2}}{1+s}\left\{1 - \mathrm{e}^{-3\gamma t/4}\left[\cosh\left(\frac{\gamma t}{4}\sqrt{1-8s}\right) + \frac{1-2s}{\sqrt{1-8s}}\sinh\left(\frac{\gamma t}{4}\sqrt{1-8s}\right)\right]\right\} \tag{3.63}$$

for the coherences. For $\gamma t \gg 1$, (3.62) and (3.63) tend to the stationary solutions (3.61b) and (3.61c), respectively (for $\Delta = 0$).

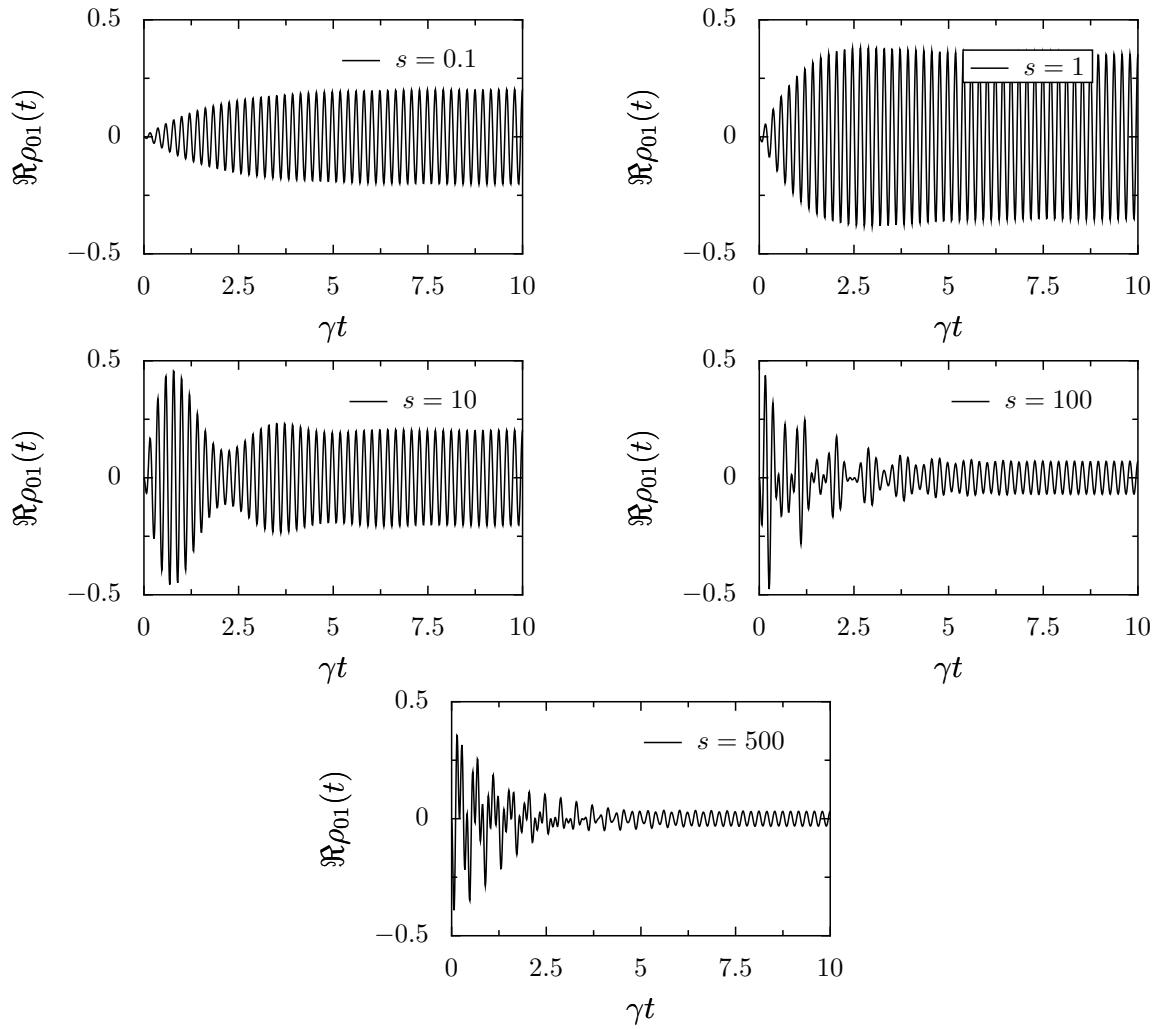

Figure 3.4: Real part of the off-diagonal density matrix element ρ_{01} according to (3.63), proportional to the mean center-of-mass coordinate $\langle Z \rangle$, for increasing values of the saturation parameter s. In the figure, $\omega_{\rm sp}/\gamma = 30$.

In Fig. 3.3, we show the population of the excited state ρ_{11} as a function of time, for increasing values of the saturation parameter. For $s < 1/8$, ρ_{11} smoothly increases as a function of time to reach the stationary value given in (3.61b) (for $\Delta = 0$). For $s \gg 1$, the center-of-mass system experiences damped Rabi oscillations and reaches the steady state on a timescale $\sim \gamma^{-1}$. Note that if the laser field is turned off after a certain time τ, the population of the excited state relaxes to zero according to $\rho_{11}(t) = \rho_{11}(\tau) \exp[-\gamma(t-\tau)]$, while the coherence of the system decreases as $\rho_{01}(t) = \rho_{01}(\tau) \exp[-(\gamma/2 - \mathrm{i}\omega_{\rm sp})(t-\tau)]$.

In Fig. 3.4, we show the real part of (3.63) which is proportional to $\langle Z \rangle = \mathrm{Tr}_{\rm cm}(\rho Z)$,

the mean center-of-mass coordinate (or mean dipole). For $s \ll 1$,

$$\Re\rho_{01}(t) \simeq -\sin(\omega_{\rm sp}t)\sqrt{\frac{s}{2}}\left(1-\mathrm{e}^{-\gamma t/2}\right), \tag{3.64}$$

and the dipole oscillates regularly, while its amplitude increases smoothly as a function of time. In the case of strong saturation parameter $s \gg 1$,

$$\Re\rho_{01}(t) \simeq -\frac{\sin(\omega_{\rm sp}t)}{\sqrt{2s}}\left\{1-\mathrm{e}^{-3\gamma t/4}\left[\cos\left(\gamma t\sqrt{\frac{s}{2}}\right)-\sqrt{\frac{s}{2}}\sin\left(\gamma t\sqrt{\frac{s}{2}}\right)\right]\right\}, \tag{3.65}$$

and an irregular pattern appears for times shorter than a few γ^{-1} (see Fig. 3.4). For $0 \leqslant s \leqslant 1$, the amplitude of $\langle Z\rangle$ increases with s, while for $s > 1$, it goes to zero, as it can be easily seen on the stationary solution (3.61c). Thus, for strong laser excitation, the mean dipole vanishes.

We conclude this section with the following remark: During the time the laser field is applied, one could measure the emission spectrum of the ensemble of nanoparticles. In the limit of an intense laser beam, i.e., of a large saturation parameter, this fluorescent spectrum is [90]

$$S(\omega,\mathbf{r}) = \frac{I(\mathbf{r})}{4\pi}\left\{\frac{\gamma/2}{(\omega-\omega_{\rm sp})^2+(\gamma/2)^2}+\frac{1}{2}\frac{3\gamma/4}{\left[\omega-(\omega_{\rm sp}+\Omega_{\rm R})\right]^2+(3\gamma/4)^2}\right.$$
$$\left.+\frac{1}{2}\frac{3\gamma/4}{\left[\omega-(\omega_{\rm sp}-\Omega_{\rm R})\right]^2+(3\gamma/4)^2}\right\}, \tag{3.66}$$

where

$$I(\mathbf{r}) = \left|\frac{\omega_{\rm sp}^2}{c^2 r}\left(\mathbf{D}\times\frac{\mathbf{r}}{r}\right)\times\frac{\mathbf{r}}{r}\right|^2, \tag{3.67}$$

$\mathbf{D} = -eN\mathbf{R}$ being the dipole moment of the electronic center of mass. We therefore have a fluorescence spectrum consisting of three Lorentzians, a central peak at $\omega = \omega_{\rm sp}$ with a width γ, and two sidebands at $\omega-(\omega_{\rm sp}\pm\Omega_{\rm R})$ with a width $3\gamma/2$ (see Fig. 3.5). The fluorescence spectrum is therefore a good experimental check of a large saturation parameter s as for example in pump-probe experiments [63, 64], since the spectral separation between the central peak and the sidebands provides a measure of the Rabi frequency, while the width of the peaks provides γ. One should scan to this end with a photodetector a region of several eV in order to find the satellites.

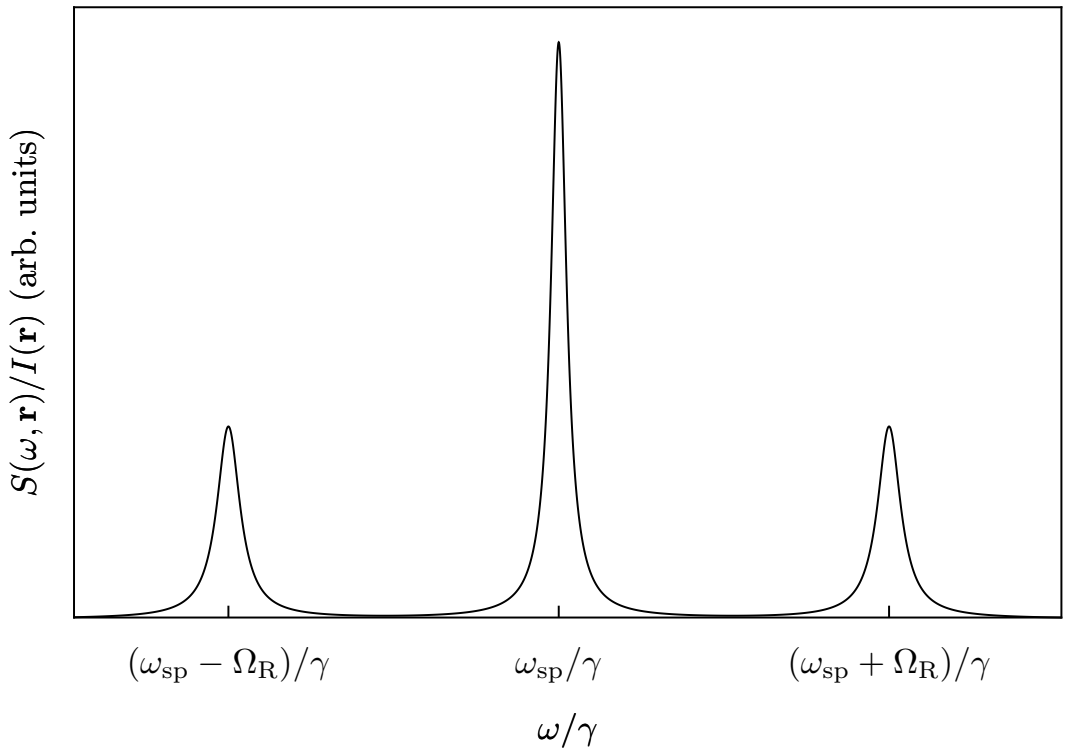

Figure 3.5: Fluorescence spectrum $S(\omega, \mathbf{r})$ from (3.66) in arbitrary units.

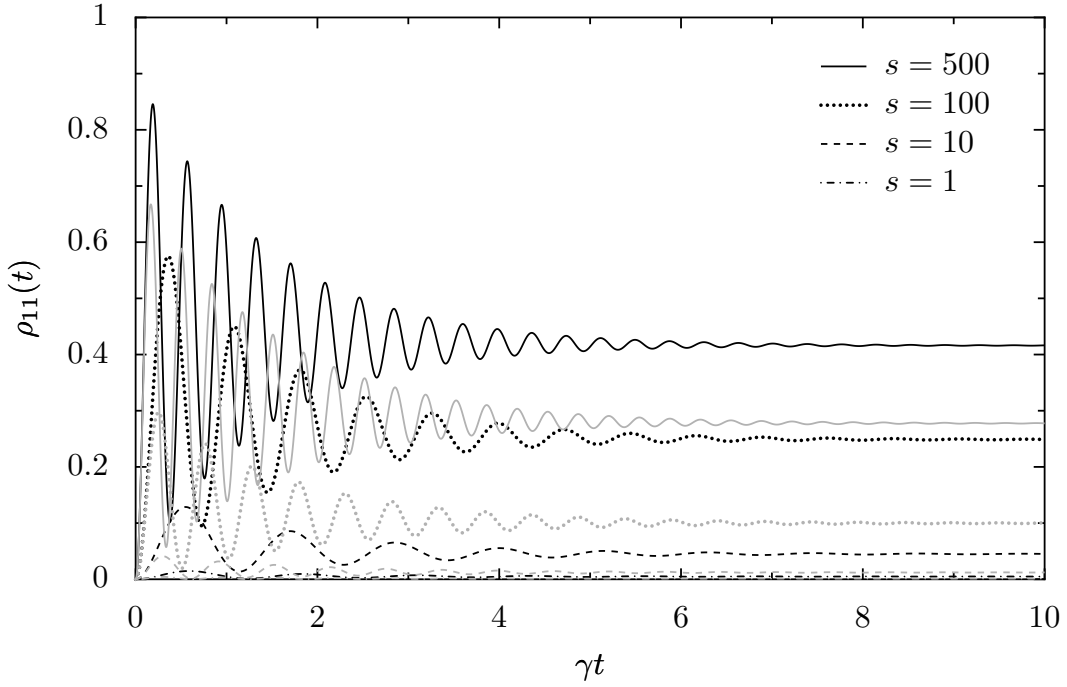

Figure 3.6: Population of the excited center-of-mass state as a function of time for various values of the saturation parameter s. The black curves correspond to $\Delta = 5$, while the gray ones correspond to $\Delta = 10$.

3.2.2 Numerical solutions of the Bloch equations in presence of detuning

When we have a detuning between the frequency of the laser field ω_{L} and the resonance frequency ω_{sp}, i.e., $\delta_{\mathrm{L}} \neq 0$, it is no longer possible to diagonalize the matrix $\mathcal{M}$ of (3.56) analytically. However, in order to understand the role of the detuning on the surface plasmon excitation, we can solve (3.55) numerically. The result for the population ρ_{11} of the collective excited states is presented in Fig. 3.6 for different values of the scaled detuning Δ defined in (3.60). We see that as the detuning increases, the probability to find the first excited state of the center-of-mass system occupied decreases, consistently with the behavior of the stationary solution (3.61b) (see also Fig. 3.2).

For the coherences, the numerical calculations show that for a large saturation parameter, the amplitude of the mean center-of-mass coordinate $\langle Z \rangle \sim \Re\rho_{01}$ increases with the detuning, a result which might be surprising. This feature can be explained in the following way. According to the stationary solution (3.61c), we have

$$\Re\left[\rho_{01}^{\mathrm{st}}(t)\right] = \frac{\sqrt{s/2}}{1+s+4\Delta^2}\left[2\Delta\cos\left(\omega_{\mathrm{L}}t\right) - \mathrm{i}\sin\left(\omega_{\mathrm{L}}t\right)\right]. \tag{3.68}$$

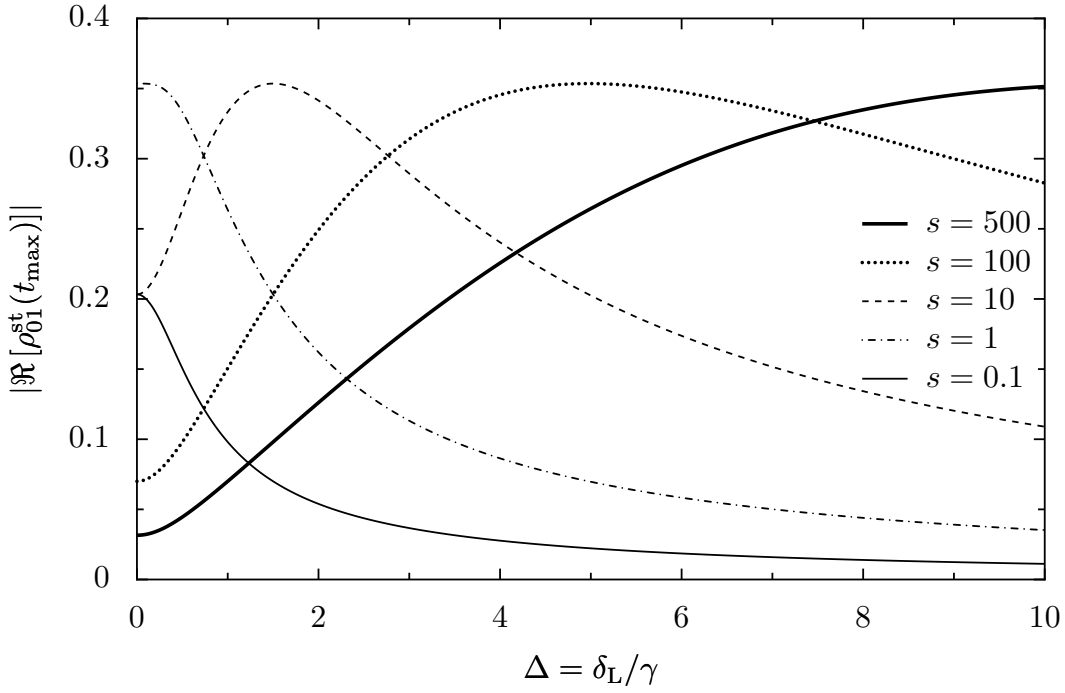

Figure 3.7: Amplitude of the center-of-mass coordinate according to (3.70) as a function of the detuning for different saturation parameters.

The maxima of this equation as a function of time are located at

$$t_{\rm max} = -\frac{1}{\omega_{\rm L}} \arctan\left(\frac{1}{2\Delta}\right) + \frac{n\pi}{\omega_{\rm L}}, \tag{3.69}$$

where n is an integer greater than $\arctan(1/2\Delta)/\pi$. Thus, the amplitude of the center-of-mass coordinate is proportional to

$$\left|\Re\left[\rho_{01}^{\rm st}(t_{\rm max})\right]\right| = \frac{2\sqrt{s/2}}{1+s+4\Delta^2}\sqrt{\Delta^2+\frac{1}{4}}. \tag{3.70}$$

This shows that for $s < 1$, the amplitude of the center-of-mass coordinate decreases with Δ, while for $s > 1$, it increases until it reaches the critical value $\sqrt{(s-1)/2}$ and then decreases as a function of Δ (see Fig. 3.7).

3.2.3 Estimation of the saturation parameter in typical experiments

The study of the preceding sections shows that the saturation parameter of (3.59) is the crucial parameter which determines the dynamics of the surface plasmon excitation in presence of an external driving field.

In typical photoabsorption experiments [10], a weak laser field excites an ensemble of nanoparticles. If the power of the laser is about several mW, the resulting electric field

is of the order of $10^3\,\mathrm{Vm}^{-1}$, and thus the Rabi frequency is no more than several μeV according to (2.41). Since in typical nanoparticles, the surface plasmon linewidth is of the order of less than 1 eV, the resulting saturation parameter $s \ll 1$. The power absorbed by a nanoparticle is $P_{\mathrm{abs}} = \sigma\rho_{00}I - \sigma\rho_{11}I$, where σ is the absorption cross section of the nanoparticle and I the intensity of the driving field. The second term in the above expression accounts for the stimulated emission of photons [82]. With $\rho_{00} = 1 - \rho_{11}$, we have $P_{\mathrm{abs}} = \sigma(1-2\rho_{11})I$. Since the saturation parameter is proportional to Ω_{R}^2, we have according to (2.41) $s \sim E_0^2 \sim I$, and thus for small s, $\rho_{11}^{\mathrm{st}} \sim I$ (see Eq. 3.61b). Therefore, it is only for small values of $\rho_{11} \ll \rho_{00}$ that we are in the linear response regime, i.e., $P_{\mathrm{abs}} \propto I$.

On the contrary, in pump-probe experiments, the nanoparticles are excited by an ultrashort pump laser pulse which is extremely intense. As a generic example, we consider the experiments of Ref. 63 on silver nanoparticles which have an average radius $a = 3.25\,\mathrm{nm}$. These nanoparticles present a broad absorption spectrum around the resonance frequency $\hbar\omega_{\mathrm{sp}} = 2.85\,\mathrm{eV}$. According to TDLDA calculations, the width of this resonance is approximately $\hbar\gamma = 50\,\mathrm{meV}$ (see Chapter 8). The estimation of the Rabi frequency (2.41) requires the knowledge of the electrical field of the pump laser field. The "energy density" $\bar{u}$ being defined as the energy carried by one laser pulse divided by the cross section of the laser beam, we have $\bar{u} = E_0^2 c\tau/8\pi$, where c is the speed of light, and τ the duration of the pulse (typically 100 fs). With $\bar{u} = 1\,\mathrm{Jm}^{-2}$, we get $E_0 = 8.7 \times 10^7\,\mathrm{Vm}^{-1}$. The Rabi frequency is therefore $\hbar\Omega_{\mathrm{R}} \simeq 0.92\,\mathrm{eV}$, which results in a very large saturation parameter $s \simeq 600$. Thus, the population of the excited state equals that of the ground state, $\rho_{00} = \rho_{11} = 1/2$, and we are no longer in the linear response regime.

3.3 Conclusion for Chapter 3

This chapter has been devoted to the study of the surface plasmon dynamics. By means of a reduced-density-matrix formalism, we have established the master equation describing the time evolution of the center-of-mass degree of freedom. To this end, we have made four crucial approximations. First, we have assumed that the electronic environment was in thermal equilibrium. This assumption does not allow us to describe the energy relaxation of the thermal bath, e.g., to the phonon heat bath. Second, we have assumed the weak coupling regime, i.e., the coupling Hamiltonian between the center-of-mass system and the environment of the relative coordinates can be treated as a perturbation to the uncoupled Hamiltonian. Third, we have neglected memory effects and worked within the Markovian approximation. Fourth, we have incorporated the effects of the external driving field and of the environment independently. With those approximations, we have recovered the well-known optical Bloch equation for the evolution of the center-of-mass density matrix.

Two quantities appear as a consequence of the coupling to the environment: the Landau damping rate γ which yields the lifetime of the center-of-mass excited states, and the shift δ which renormalizes the surface plasmon frequency. Those two quantities

will be evaluated in Chapter 4 and 5, respectively.

Assuming that the center-of-mass system can be described by a two-level system, we have solved the corresponding Bloch equations in different situations, i.e., with and without detuning between the frequency of the external field and the surface plasmon resonance frequency. It has appeared that the determining parameter for the dynamical evolution of the center-of-mass degree of freedom is the so-called saturation parameter. It is a measure of the external field intensity over the damping of the system. Increasing it, we go from the linear response regime of typical absorption experiments to the nonlinear regime of pump-probe setups.

Chapter 4

Lifetime of the surface plasmon excitation

> Le temps est un grand maître, il règle bien des choses.
>
> *(Pierre Corneille, 1606-1684, in Sertorius)*

In this chapter, we evaluate the linewidth γ of the surface plasmon excitation (3.40). We will calculate it by means of a semiclassical low-temperature expansion, and focus on its size and temperature dependence. To this end, we introduce the function

$$\Sigma(\omega) = \frac{2\pi}{\hbar^2} \sum_{\alpha\beta} \left[1 - f(\varepsilon_\alpha)\right] f(\varepsilon_\beta) \left|\Lambda d_{\alpha\beta}\right|^2 \delta\left(\omega - \omega_{\alpha\beta}\right). \tag{4.1}$$

In the above expression, $f(\varepsilon)$ is the Fermi-Dirac distribution given in (3.23), Λ the constant defined in (2.37), and $d_{\alpha\beta}$ are the matrix elements of (2.36). The linewidth γ is related to $\Sigma(\omega)$ through

$$\gamma = \Sigma(\tilde{\omega}_{\mathrm{M}}) + 2\Sigma(-\tilde{\omega}_{\mathrm{M}}), \tag{4.2}$$

as it can be seen from (3.32) and (3.40). It is understood that in (4.1), $|\omega_{\alpha\beta}| > \omega_{\mathrm{c}}$ where ω_{c} is some cutoff separating the restricted subspace that builds the coherent superposition of the surface plasmon excitation from the additional subspace at high energy (see Sec. 1.2.3). We have introduced the function $\Sigma(\omega)$ since it is helpful for the evaluation of γ and will also be useful in Chapter 5 when the frequency shift of the surface plasmon induced by the electronic environment (3.33) will be determined. The first term on the r.h.s. in (4.2) is the rate associated with the spontaneous decay of a plasmon [see Fig. 3.1(i)], while the second one is the rate for a plasmon excitation by the thermal environment [see Fig. 3.1(ii)]. The expression (4.1) implies the detailed-balance relation

$$\Sigma(-\omega) = \mathrm{e}^{-\beta\hbar\omega}\Sigma(\omega) \tag{4.3}$$

which allows to write (4.2) as

$$\gamma = \Sigma(\tilde{\omega}_{\mathrm{M}}) \left(1 + 2\mathrm{e}^{-\beta\hbar\tilde{\omega}_{\mathrm{M}}}\right). \tag{4.4}$$

This expression shows that an excitation of the surface plasmon to a higher level is suppressed at low temperatures because no or only few particle-hole pairs are present.

4.1 Dipole matrix element from single-particle self-consistent states

In order to evaluate the plasmon linewidth from (4.1), we need a description of the eigenstates $|\alpha\rangle$ of the mean-field Hamiltonian (2.31). The TDLDA numerical calculations briefly presented in Secs. 1.2.4 and 2.2.2 inform us on the shape of the self-consistent mean field potential $V(r)$, as shown in Fig. 2.2. It suggests that for analytical calculations, $V(r)$ can be approximated by a spherical well of radius a and finite height V_0,

$$V(r) = V_0 \Theta(r - a), \tag{4.5}$$

where $V_0 = \varepsilon_\mathrm{F} + W$, ε_F and W being the Fermi energy and the work function of the considered nanoparticle, respectively. The self-consistent potential of Fig. 2.2 is for an alkaline-metal nanoparticle in vacuum, and as we will see in Chapter 8, the dielectric constants inside and outside the cluster influence the steepness of $V(r)$.

Because of the spherical symmetry of the problem, the one-particle wave functions

$$\psi_{\varepsilon l m}(\mathbf{r}) = \frac{u_{\varepsilon l}(r)}{r} Y_l^m(\theta, \varphi) \tag{4.6}$$

decompose into radial and angular parts given by the spherical harmonics $Y_l^m(\theta, \varphi)$, where l and m are the angular momentum quantum numbers. The radial wave functions $u_{\varepsilon l}(r)$ satisfy the reduced Schrödinger equation

$$\left[-\frac{\hbar^2}{2m_\mathrm{e}} \frac{\mathrm{d}^2}{\mathrm{d}r^2} + \frac{\hbar^2 l(l+1)}{2m_\mathrm{e} r^2} + V(r) \right] u_{\varepsilon l}(r) = \varepsilon u_{\varepsilon l}(r) \tag{4.7}$$

with the conditions $u_{\varepsilon l}(0) = 0$ and $\lim_{r\to\infty} [u_{\varepsilon l}(r)/r] = 0$. This yields the single-particle eigenenergies ε in the mean-field potential $V(r)$ of (4.5). Thus, the matrix elements $d_{\alpha\beta}$ appearing in (4.1) can be separated into an angular part $\mathcal{A}_{l_\alpha l_\beta}^{m_\alpha m_\beta}$ and a radial part $\mathcal{R}_{l_\alpha l_\beta}(\varepsilon_\alpha, \varepsilon_\beta)$,

$$d_{\alpha\beta} = \mathcal{A}_{l_\alpha l_\beta}^{m_\alpha m_\beta} \mathcal{R}_{l_\alpha l_\beta}(\varepsilon_\alpha, \varepsilon_\beta). \tag{4.8}$$

With (2.36), we have

$$\mathcal{A}_{l_\alpha l_\beta}^{m_\alpha m_\beta} = \int_0^\pi \mathrm{d}\theta \sin\theta \int_0^{2\pi} \mathrm{d}\varphi Y_{l_\alpha}^{m_\alpha *}(\theta, \varphi) \cos(\theta) Y_{l_\beta}^{m_\beta}(\theta, \varphi) \tag{4.9}$$

which can be expressed in terms of Wigner-3j symbols [91] as

$$\mathcal{A}_{l_\alpha l_\beta}^{m_\alpha m_\beta} = (-1)^{m_\alpha} \sqrt{(2l_\alpha + 1)(2l_\beta + 1)} \begin{pmatrix} l_\alpha & l_\beta & 1 \\ 0 & 0 & 0 \end{pmatrix} \begin{pmatrix} l_\alpha & l_\beta & 1 \\ -m_\alpha & m_\beta & 0 \end{pmatrix}. \tag{4.10}$$

The Wigner-3j symbols contain the dipole selection rules $l_\alpha = l_\beta \pm 1$ and $m_\alpha = m_\beta$.

For the calculation of the radial part of the matrix elements $d_{\alpha\beta}$, we now closely follow the derivation of Yannouleas and Broglia [30] (see also Ref. 92). In the limit of strong electronic confinement ($V_0 \gg \varepsilon_\mathrm{F}$ in Eq. 4.5), the single-particle wave function vanishes outside the nanoparticle, and we can therefore approximate the radial matrix element (see Eq. 2.36) by

$$\mathcal{R}_{l_\alpha l_\beta}(\varepsilon_\alpha, \varepsilon_\beta) \simeq \int_0^a \mathrm{d}r\, u^*_{\varepsilon_\alpha l_\alpha}(r)\, r\, u_{\varepsilon_\beta l_\beta}(r). \tag{4.11}$$

The commutator of r with the self-consistent Hamiltonian (2.32) reads

$$[r, H_\mathrm{sc}] = \frac{\mathrm{i}\hbar}{m_\mathrm{e}} p_r, \tag{4.12}$$

where p_r is the conjugated momentum to the variable r. Calculating the matrix element of this commutator between two single-particle eigenstates $|\alpha\rangle$ and $|\beta\rangle$ of H_sc then allows to write

$$\langle\alpha|r|\beta\rangle = \frac{\mathrm{i}\hbar}{m_\mathrm{e}\left(\varepsilon_\beta - \varepsilon_\alpha\right)} \langle\alpha|p_r|\beta\rangle. \tag{4.13}$$

Now,

$$[p_r, H_\mathrm{sc}] = -\mathrm{i}\hbar \frac{\mathrm{d}V}{\mathrm{d}r}, \tag{4.14}$$

such that

$$\langle\alpha|p_r|\beta\rangle = -\frac{\mathrm{i}\hbar}{\varepsilon_\beta - \varepsilon_\alpha} \langle\alpha|\frac{\mathrm{d}V}{\mathrm{d}r}|\beta\rangle. \tag{4.15}$$

Inserting this result in (4.13), we have

$$\langle\alpha|r|\beta\rangle = \frac{\hbar^2}{m_\mathrm{e}\left(\varepsilon_\beta - \varepsilon_\alpha\right)^2} \langle\alpha|\frac{\mathrm{d}V}{\mathrm{d}r}|\beta\rangle, \tag{4.16}$$

and then

$$\mathcal{R}_{l_\alpha l_\beta}(\varepsilon_\alpha, \varepsilon_\beta) = \frac{\hbar^2}{m_\mathrm{e}\left(\varepsilon_\beta - \varepsilon_\alpha\right)^2} \int_0^a \mathrm{d}r\, u^*_{\varepsilon_\alpha l_\alpha}(r)\, \frac{\mathrm{d}V}{\mathrm{d}r}\, u_{\varepsilon_\beta l_\beta}(r). \tag{4.17}$$

With (4.5), we thus obtain

$$\mathcal{R}_{l_\alpha l_\beta}(\varepsilon_\alpha, \varepsilon_\beta) = \frac{\hbar^2}{m_\mathrm{e}\left(\varepsilon_\beta - \varepsilon_\alpha\right)^2} V_0 u^*_{\varepsilon_\alpha l_\alpha}(a) u_{\varepsilon_\beta l_\beta}(a). \tag{4.18}$$

For $V_0 \to \infty$ and $r \leqslant a$, the regular solutions of (4.7) satisfying $u_{\varepsilon l}(a) = 0$ are given by (see Appendix C, Sec. C.2.1)

$$u_{\varepsilon l}(r) = \frac{\sqrt{2}}{a^{3/2}} \frac{r j_l(kr)}{j_{l+1}(ka)}, \tag{4.19}$$

where $j_\nu(z)$ are spherical Bessel functions of the first kind [93], and $k = \sqrt{2m_\mathrm{e}\varepsilon}/\hbar$. We have the condition $j_l(ka) = 0$ which yields the quantization of the single-particle

states in the infinitely deep spherical well. Inserting the radial wave functions (4.19) into (4.18), we thus have

$$\mathcal{R}_{l_\alpha l_\beta}(\varepsilon_\alpha, \varepsilon_\beta) = \frac{2\hbar^2}{m_\mathrm{e} a \left(\varepsilon_\beta - \varepsilon_\alpha\right)^2} V_0 \frac{j_{l_\alpha}(k_\alpha a)}{j_{l_\alpha+1}(k_\alpha a)} \frac{j_{l_\beta}(k_\beta a)}{j_{l_\beta+1}(k_\beta a)}. \tag{4.20}$$

Now, for $r \to a^+$, $u_{\varepsilon l}(r) \to 0$ and $V(r) = V_0 \to \infty$, such that the radial Schrödinger equation (4.7) takes the form

$$\left(-\frac{\hbar^2}{2m_\mathrm{e}} \frac{\mathrm{d}^2}{\mathrm{d}r^2} + V_0\right) u_{\varepsilon l}(r) = 0. \tag{4.21}$$

With $k_0 = \sqrt{2m_\mathrm{e}V_0}/\hbar$, the physical solution of this equation is

$$u_{\varepsilon l}(r \to a^+) \sim \mathrm{e}^{-k_0 r}. \tag{4.22}$$

Then,

$$\left.\frac{\mathrm{d}u_{\varepsilon l}}{\mathrm{d}r}\right|_{r\to a^+} = -k_0 u_{\varepsilon l}(r \to a^+), \tag{4.23}$$

and imposing the continuity of the radial wave function and of its derivative with respect to r at $r = a$, we arrive to

$$\left.\frac{\mathrm{d}u_{\varepsilon l}}{\mathrm{d}r}\right|_{r\to a^-} = -k_0 u_{\varepsilon l}(r \to a^-). \tag{4.24}$$

Then, we obtain with (4.19)

$$\lim_{V_0\to\infty} \left[\frac{\sqrt{2m_\mathrm{e}V_0}}{\hbar} j_l(ka)\right] = -\left.\frac{\mathrm{d}j_l(kr)}{\mathrm{d}r}\right|_{r=a} = -k \left.\frac{\mathrm{d}j_l(\eta)}{\mathrm{d}\eta}\right|_{\eta=ka}. \tag{4.25}$$

Using the recurrence relation of the spherical Bessel functions [93]

$$\frac{l}{\eta} j_l(\eta) - \frac{\mathrm{d}j_l}{\mathrm{d}\eta} = j_{l+1}(\eta) \tag{4.26}$$

and the fact that $j_l(\eta) = j_l(ka) = 0$, we finally arrive to the following expression for the radial matrix elements [30, 92]:

$$\mathcal{R}_{l_\alpha l_\beta}(\varepsilon_\alpha, \varepsilon_\beta) = \frac{2\hbar^2}{m_\mathrm{e} a} \frac{\sqrt{\varepsilon_\alpha \varepsilon_\beta}}{\left(\varepsilon_\alpha - \varepsilon_\beta\right)^2}. \tag{4.27}$$

Note that the dipole selection rule $l_\alpha = l_\beta \pm 1$ appearing in the angular matrix element (4.10) implies that $\varepsilon_\alpha \neq \varepsilon_\beta$, and thus (4.27) is nondivergent. Furthermore, it decreases with increasing energy $|\varepsilon_\alpha - \varepsilon_\beta|$ of the dipole transition $|\alpha\rangle \to |\beta\rangle$.

4.2 Semiclassical low-temperature expansion and contribution to the surface plasmon linewidth with smooth size dependence

We now use semiclassical techniques to determine the low-temperature behavior of $\Sigma(\omega)$. In view of the detailed-balance relation (4.3) we can restrict ourselves to positive frequencies ω.

The summations appearing in (4.1) can be replaced by integrals provided one knows the density of states of the single-particle states in the self-consistent potential $V(r)$. Decomposing the density of states as a sum over its fixed angular momentum component,

$$\varrho(\varepsilon) = \sum_{l=0}^{\infty} \sum_{m=-l}^{+l} \varrho_l(\varepsilon), \tag{4.28}$$

we have with (4.8)

$$\Sigma(\omega) = \frac{4\pi}{\hbar} \int_{\hbar\omega}^{\infty} \mathrm{d}\varepsilon F(\varepsilon) \sum_{\substack{l,m \\ l',m'}} \varrho_l(\varepsilon)\varrho_{l'}(\varepsilon - \hbar\omega) \left[\Lambda \mathcal{A}_{ll'}^{mm'} \mathcal{R}(\varepsilon, \varepsilon - \hbar\omega)\right]^2, \tag{4.29}$$

where a factor of 2 accounts for the spin degeneracy. In the above equation, we have introduced the notation

$$F(\varepsilon) = [1 - f(\varepsilon)]\, f(\varepsilon - \hbar\omega). \tag{4.30}$$

Furthermore, we have omitted the subscripts ll' for the radial matrix element $\mathcal{R}$ since (4.27) shows that it actually does not depend on the angular quantum numbers. Performing the sums over l' and m' with the help of the selection rules contained in the angular part (4.10) of the dipole matrix element, namely $l' = l \pm 1$ and $m' = m$, one obtains

$$\begin{aligned}\Sigma(\omega) = \frac{4\pi}{\hbar} \int_{\hbar\omega}^{\infty} \mathrm{d}\varepsilon F(\varepsilon) \left[\Lambda \mathcal{R}(\varepsilon, \varepsilon - \hbar\omega)\right]^2 \\ \times \sum_{lm} \varrho_l(\varepsilon) \left[\left(\mathcal{A}_{l,l+1}^{mm}\right)^2 \varrho_{l+1}(\varepsilon - \hbar\omega) + \left(\mathcal{A}_{l,l-1}^{mm}\right)^2 \varrho_{l-1}(\varepsilon - \hbar\omega)\right].\end{aligned} \tag{4.31}$$

Writing explicitly the Wigner-3j symbols in (4.10), we have

$$\left(\mathcal{A}_{l,l+1}^{mm}\right)^2 = \frac{(l+1-m)(l+1+m)}{(2l+1)(2l+3)}, \tag{4.32a}$$

$$\left(\mathcal{A}_{l,l-1}^{mm}\right)^2 = \frac{(l-m)(l+m)}{(2l+1)(2l-1)}. \tag{4.32b}$$

The summation over m entering (4.31) then yields

$$\sum_{m=-l}^{+l} \left(\mathcal{A}_{l,l+1}^{mm}\right)^2 = \frac{l+1}{3}, \tag{4.33a}$$

$$\sum_{m=-l}^{+l} \left(\mathcal{A}_{l,l-1}^{mm}\right)^2 = \frac{l}{3}, \tag{4.33b}$$

and we obtain for (4.31)

$$\Sigma(\omega) = \frac{4\pi}{3\hbar} \int_{\hbar\omega}^{\infty} \mathrm{d}\varepsilon F(\varepsilon) \left[\Lambda \mathcal{R}(\varepsilon, \varepsilon - \hbar\omega)\right]^2 \sum_{l=0}^{\infty} \varrho_l(\varepsilon) \left[(l+1)\varrho_{l+1}(\varepsilon - \hbar\omega) + l\varrho_{l-1}(\varepsilon - \hbar\omega)\right]. \tag{4.34}$$

We now appeal to a semiclassical approximation for the two densities of states appearing in (4.34) using the Gutzwiller trace formula [94] presented in Appendix B and adapted to the effective radial motion (see Appendix C). The l-fixed density of states is decomposed into a smooth and an oscillating part,

$$\varrho_l(\varepsilon) = \varrho_l^0(\varepsilon) + \varrho_l^{\mathrm{osc}}(\varepsilon), \tag{4.35}$$

with

$$\varrho_l^0(\varepsilon) = \frac{\tau_l(\varepsilon)}{2\pi\hbar} \tag{4.36}$$

and

$$\varrho_l^{\mathrm{osc}}(\varepsilon) = \frac{\tau_l(\varepsilon)}{\pi\hbar} \sum_{\tilde{r}=1}^{\infty} \cos\left[\tilde{r}\left(\frac{S_l(\varepsilon)}{\hbar} - \frac{3\pi}{2}\right)\right]. \tag{4.37}$$

The classical action of the periodic orbit at energy ε is

$$S_l(\varepsilon) = 2\hbar\left[\sqrt{(ka)^2 - (l+1/2)^2} - \left(l + \frac{1}{2}\right)\arccos\left(\frac{l+1/2}{ka}\right)\right], \tag{4.38}$$

while its period is given by

$$\tau_l(\varepsilon) = \frac{\hbar\sqrt{(ka)^2 - (l+1/2)^2}}{\varepsilon}. \tag{4.39}$$

We denote by $\tilde{r}$ the number of repetitions of the periodic orbit. Within the semiclassical approximation, the finite height V_0 of the self-consistent potential is irrelevant since the classical trajectories at a given energy are not sensitive to the shape of the potential above this energy. In this section, we focus on the smooth semiclassical density of states (4.36). As we will see, it yields the dominant $1/a$-dependent component of γ. In Sec. 4.3, we will show that the oscillating component of the density of states gives rise to a nonmonotonic behavior of the surface plasmon linewidth as a function of the size of the nanoparticle. This feature will be shown to be only relevant for small cluster sizes.

Inserting the smooth part (4.36) of the density of states into (4.34), and assuming $l \gg 1$, consistently with the fact that we are interested in leading order contributions in $\hbar$, we obtain the smooth contribution to $\Sigma(\omega)$,

$$\Sigma^0(\omega) = \frac{2}{3\pi\hbar}\int_{\hbar\omega}^{\infty} \mathrm{d}\varepsilon \frac{F(\varepsilon)\left[\Lambda\mathcal{R}(\varepsilon,\varepsilon-\hbar\omega)\right]^2}{\varepsilon(\varepsilon-\hbar\omega)} \times \int_0^{l_{\max}} \mathrm{d}l\, l\sqrt{\frac{2m_\mathrm{e}\varepsilon a^2}{\hbar^2}-l^2}\sqrt{\frac{2m_\mathrm{e}(\varepsilon-\hbar\omega)a^2}{\hbar^2}-l^2}. \tag{4.40}$$

We have approximated the sum over l by an integral and assumed $l \simeq l \pm 1$. Furthermore, $l_{\max} = \sqrt{2m_\mathrm{e}(\varepsilon-\hbar\omega)a^2/\hbar^2}$ is the maximal angular momentum quantum number allowed at the energy $\varepsilon - \hbar\omega$ (see Appendix C). In the above equation, the integral over l can be easily evaluated, and with (4.27) we get

$$\Sigma^0(\omega) = \frac{3v_\mathrm{F}}{8a}\left(\frac{\hbar\omega_\mathrm{M}}{\varepsilon_\mathrm{F}}\right)^3 \frac{\varepsilon_\mathrm{F}}{\hbar\omega}\mathcal{F}(\mu,\hbar\omega). \tag{4.41}$$

Here, we have introduced

$$\mathcal{F}(\mu,\hbar\omega) = \int_{\hbar\omega}^{\infty}\frac{\mathrm{d}\varepsilon}{\hbar\omega}F(\varepsilon)H\left(\frac{\varepsilon}{\hbar\omega}\right), \tag{4.42}$$

where

$$H(x) = (2x-1)\sqrt{x(x-1)} - \ln\left(\sqrt{x}+\sqrt{x-1}\right) \tag{4.43}$$

is a monotonically increasing function. For x close to 1, we have $H(x) \simeq (8/3)(x-1)^{3/2}$. The dependence on the chemical potential μ in (4.42) is via the Fermi functions appearing in this expression.

Integrating (4.42) by parts yields

$$\mathcal{F}(\mu,\hbar\omega) = \int_{\hbar\omega}^{\infty}\mathrm{d}\varepsilon\left(-\frac{\mathrm{d}F}{\mathrm{d}\varepsilon}\right)\mathcal{H}\left(\frac{\varepsilon}{\hbar\omega}\right) \tag{4.44}$$

with

$$\mathcal{H}(x) = \int_1^x \mathrm{d}x' H(x') = \frac{1}{6}\left\{\sqrt{x(x-1)}\left[4x(x-1)+3\right] - 3(2x-1)\ln\left(\sqrt{x}+\sqrt{x-1}\right)\right\}. \tag{4.45}$$

In the low-temperature limit $\hbar\omega \gg k_\mathrm{B}T$, we get according to (4.30)

$$-\frac{\mathrm{d}F}{\mathrm{d}\varepsilon} \approx -\beta\frac{\mathrm{e}^{\beta(\varepsilon-\mu)}}{\left[\mathrm{e}^{\beta(\varepsilon-\mu)}+1\right]^2} + \beta\frac{\mathrm{e}^{\beta(\varepsilon-\hbar\omega-\mu)}}{\left[\mathrm{e}^{\beta(\varepsilon-\hbar\omega-\mu)}+1\right]^2}, \tag{4.46}$$

which corresponds to two peaks of opposite sign centered at $\varepsilon = \mu$ and at $\varepsilon = \mu + \hbar\omega$ (see Fig. 4.1). It is therefore helpful to expand the function $\mathcal{H}$ around $\varepsilon = \mu$ and $\varepsilon = \mu + \hbar\omega$.

As it can be seen from Fig. 4.1, one has to distinguish between three cases: (a) When $\hbar\omega - \mu \gtrsim k_\mathrm{B}T$, only the peak centered at $\varepsilon = \mu + \hbar\omega$ contributes to the integral of (4.44) (Fig. 4.1a). (b) When $\hbar\omega - \mu \lesssim -k_\mathrm{B}T$, the two peaks contribute (Fig. 4.1b). (c) In the special case where $\hbar\omega$ is in a range of order $k_\mathrm{B}T$ around the chemical potential μ (Fig. 4.1c), the nonanalyticity of $\mathcal{H}(x)$ for $x = 1$ has to be properly accounted for, while the peak at $\varepsilon = \mu + \hbar\omega$ yields the same result as in the case (a).

In the case (a), we expand in (4.44) $\mathcal{H}$ around $\varepsilon = \mu + \hbar\omega$ and obtain with (4.46)

$$\mathcal{F}(\mu, \hbar\omega) \simeq \mathcal{H}\left(1 + \frac{\mu}{\hbar\omega}\right) \int_{-\infty}^{+\infty} \mathrm{d}x \frac{\mathrm{e}^x}{(\mathrm{e}^x + 1)^2} + H\left(1 + \frac{\mu}{\hbar\omega}\right) \frac{1}{\beta\hbar\omega} \int_{-\infty}^{+\infty} \mathrm{d}x \frac{x\mathrm{e}^x}{(\mathrm{e}^x + 1)^2} + \frac{1}{2} H'\left(1 + \frac{\mu}{\hbar\omega}\right) \frac{1}{(\beta\hbar\omega)^2} \int_{-\infty}^{+\infty} \mathrm{d}x \frac{x^2\mathrm{e}^x}{(\mathrm{e}^x + 1)^2}, \tag{4.47}$$

where $H'(x)$ denotes the derivative of $H(x)$. Note that the second term on the r.h.s. in (4.47) vanishes since the integrand is an odd function of x. Evaluating the two remaining integrals, we arrive to

$$\mathcal{F}(\mu, \hbar\omega) \simeq \mathcal{H}\left(1 + \frac{\mu}{\hbar\omega}\right) + \frac{\pi^2}{6} \left(\frac{k_\mathrm{B}T}{\hbar\omega}\right)^2 H'\left(1 + \frac{\mu}{\hbar\omega}\right). \tag{4.48}$$

In the case (b) where $\hbar\omega - \mu \lesssim -k_\mathrm{B}T$ (see Fig. 4.1b), one has to take into account the two peaks that present the derivative of $F(\varepsilon)$ to obtain a similar expression. Putting the two cases (a) and (b) together, we obtain for low temperatures and for $|\hbar\omega - \mu| \gtrsim k_\mathrm{B}T$

$$\mathcal{F}(\mu, \hbar\omega) \simeq \mathcal{H}\left(1 + \frac{\mu}{\hbar\omega}\right) - \mathcal{H}\left(\frac{\mu}{\hbar\omega}\right) \Theta(\mu - \hbar\omega) + \frac{\pi^2}{6} \left(\frac{k_\mathrm{B}T}{\hbar\omega}\right)^2 \left[H'\left(1 + \frac{\mu}{\hbar\omega}\right) - H'\left(\frac{\mu}{\hbar\omega}\right) \Theta\left(\mu - \hbar\omega\right)\right]. \tag{4.49}$$

We now come to the special case (c) where $\hbar\omega$ lies in a range $k_\mathrm{B}T$ around μ (Fig. 4.1c). Here, we cannot linearize the function $\mathcal{H}$ given in (4.45) since it is nonanalytical at $x = 1$. However, we can use the behavior of $\mathcal{H}$ near $x = 1$, namely

$$\mathcal{H}(x) \simeq \frac{16}{15} (x - 1)^{5/2}. \tag{4.50}$$

Note that the peak at $\varepsilon = \mu + \hbar\omega \simeq 2\mu$ contributes to $\mathcal{F}(\mu, \hbar\omega)$ like in the case (a) since here, $\mathcal{H}$ can be linearized. Thus, for $\hbar\omega = \mu$, we have with (4.48)

$$\mathcal{F}(\mu, \mu) \simeq \mathcal{H}(2) + \frac{\pi^2}{6} \left(\frac{k_\mathrm{B}T}{\hbar\omega}\right)^2 H'(2) - \underbrace{\frac{16}{15} \int_0^\infty \mathrm{d}x \frac{\mathrm{e}^x x^{5/2}}{(\mathrm{e}^x + 1)^2}}_{\approx 3.07} \left(\frac{k_\mathrm{B}T}{\hbar\omega}\right)^{5/2}. \tag{4.51}$$

In order to pursue the evaluation of (4.49), we need to determine the chemical potential μ. To this end, we employ the Sommerfeld expansion [9] to the second order in T/T_F with T_F the Fermi temperature. This leads to

$$\int_0^\infty \mathrm{d}\varepsilon\, f(\varepsilon) h(\varepsilon) \simeq \int_0^{\varepsilon_\mathrm{F}} \mathrm{d}\varepsilon\, h(\varepsilon) + h(\varepsilon_\mathrm{F})(\mu - \varepsilon_\mathrm{F}) + \frac{\pi^2}{6} h'(\varepsilon_\mathrm{F}) (k_\mathrm{B}T)^2 \tag{4.52}$$

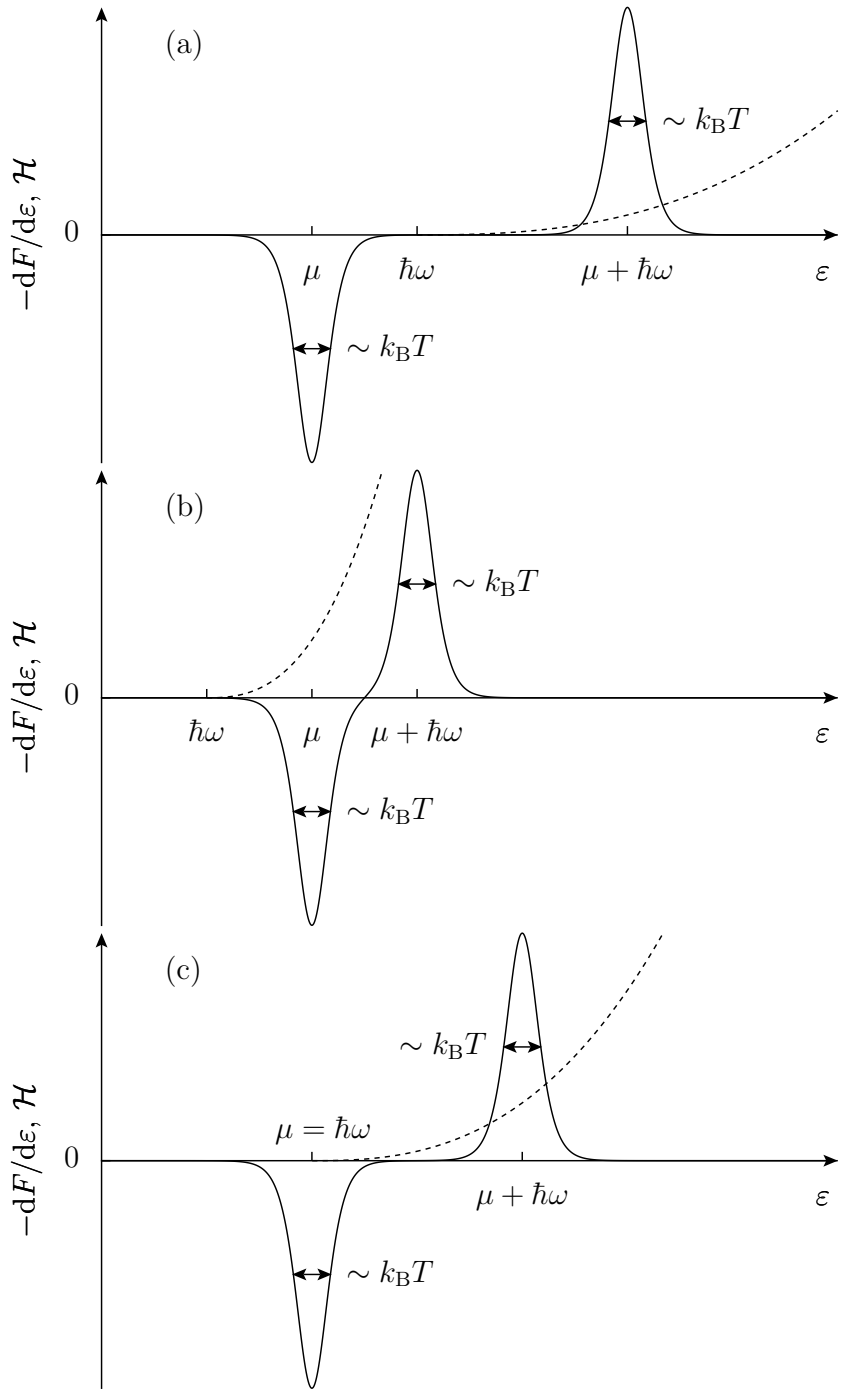

Figure 4.1: Sketch of $-\mathrm{d}F/\mathrm{d}\varepsilon$ from (4.46) (solid line), and of the function $\mathcal{H}$ of (4.45) (dashed line) as a function of ε, for (a) $\hbar\omega-\mu \gtrsim k_\mathrm{B}T$, (b) $\hbar\omega-\mu \lesssim -k_\mathrm{B}T$, and (c) $\hbar\omega=\mu$.

when $h(\varepsilon)$ is a function that varies slowly on scales larger than $k_{\rm B}T$. The first term on the r.h.s. of (4.52) corresponds to the zero-temperature result, while the remaining terms are the finite-temperature corrections. Since the density of states of (4.36), once summed over l and m yields the three-dimensional bulk density of states proportional to $\sqrt{\varepsilon}$ given in (C.28) in Appendix C, we obtain with $h(\varepsilon) = \varrho^0(\varepsilon)$ the standard Sommerfeld expression for the chemical potential of free fermions [9], i.e.,

$$\mu \simeq \varepsilon_{\rm F}\left[1 - \frac{\pi^2}{12}\left(\frac{T}{T_{\rm F}}\right)^2\right]. \tag{4.53}$$

This expression is obtained by requiring that the number of electrons does not depend on temperature. We thus get for (4.49)

$$\begin{aligned}\mathcal{F}(\mu,\hbar\omega) \simeq \int_{\max(\varepsilon_{\rm F},\hbar\omega)}^{\varepsilon_{\rm F}+\hbar\omega} \frac{{\rm d}\varepsilon}{\hbar\omega} H\left(\frac{\varepsilon}{\hbar\omega}\right) \\ + \frac{\pi^2}{6}\frac{\varepsilon_{\rm F}}{\hbar\omega}\left(\frac{T}{T_{\rm F}}\right)^2 \Bigg\{ \frac{\varepsilon_{\rm F}}{\hbar\omega}\Big[H'\left(1+\frac{\varepsilon_{\rm F}}{\hbar\omega}\right) - H'\left(\frac{\varepsilon_{\rm F}}{\hbar\omega}\right)\Theta\left(\varepsilon_{\rm F}-\hbar\omega\right)\Big] \\ - \frac{1}{2}\Big[H\left(1+\frac{\varepsilon_{\rm F}}{\hbar\omega}\right) - H\left(\frac{\varepsilon_{\rm F}}{\hbar\omega}\right)\Theta\left(\varepsilon_{\rm F}-\hbar\omega\right)\Big]\Bigg\}.\end{aligned} \tag{4.54}$$

Inserting the result (4.54) into (4.41), and using the expression (4.43) for H, we finally obtain

$$\Sigma^0(\omega) = \frac{3v_{\rm F}}{4a}\left(\frac{\omega_{\rm M}}{\omega}\right)^3 g\left(\frac{\varepsilon_{\rm F}}{\hbar\omega}, \frac{T}{T_{\rm F}}\right) \tag{4.55}$$

with

$$g\left(x, \frac{T}{T_{\rm F}}\right) = g_0(x) + g_2(x)\left(\frac{T}{T_{\rm F}}\right)^2, \tag{4.56}$$

where [29, 30]

$$\begin{aligned}g_0(x) = \frac{1}{12x^2}\Big\{\sqrt{x(x+1)}\big(4x(x+1)+3\big) - 3(2x+1)\ln\Big(\sqrt{x}+\sqrt{x+1}\Big) \\ - \Big[\sqrt{x(x-1)}\big(4x(x-1)+3\big) - 3(2x-1)\ln\big(\sqrt{x}+\sqrt{x-1}\big)\Big]\Theta(x-1)\Big\}\end{aligned} \tag{4.57}$$

is a monotonically increasing function with $g_0(0) = 0$ and $\lim_{x\to\infty} g_0(x) = 1$, while

$$\begin{aligned}g_2(x) = \frac{\pi^2}{24x}\Big\{\sqrt{x(x+1)}(6x-1) + \ln\Big(\sqrt{x}+\sqrt{x+1}\Big) \\ - \Big[\sqrt{x(x-1)}(6x+1) + \ln\big(\sqrt{x}+\sqrt{x-1}\big)\Big]\Theta(x-1)\Big\}\end{aligned} \tag{4.58}$$

with $g_2(0) = 0$ and $\lim_{x\to\infty} g_2(x) = \pi^2/6$. For x near 1, note that a $T^{5/2}$-correction coming from (4.51) has to be added to (4.56), namely $-1.54(T/T_{\rm F})^{5/2}$.

Eq. 4.4 then yields the size- and temperature-dependent surface plasmon linewidth

$$\gamma^0 = \frac{3v_{\rm F}}{4a} g\left(\frac{\varepsilon_{\rm F}}{\hbar\omega_{\rm M}}, \frac{T}{T_{\rm F}}\right). \tag{4.59}$$

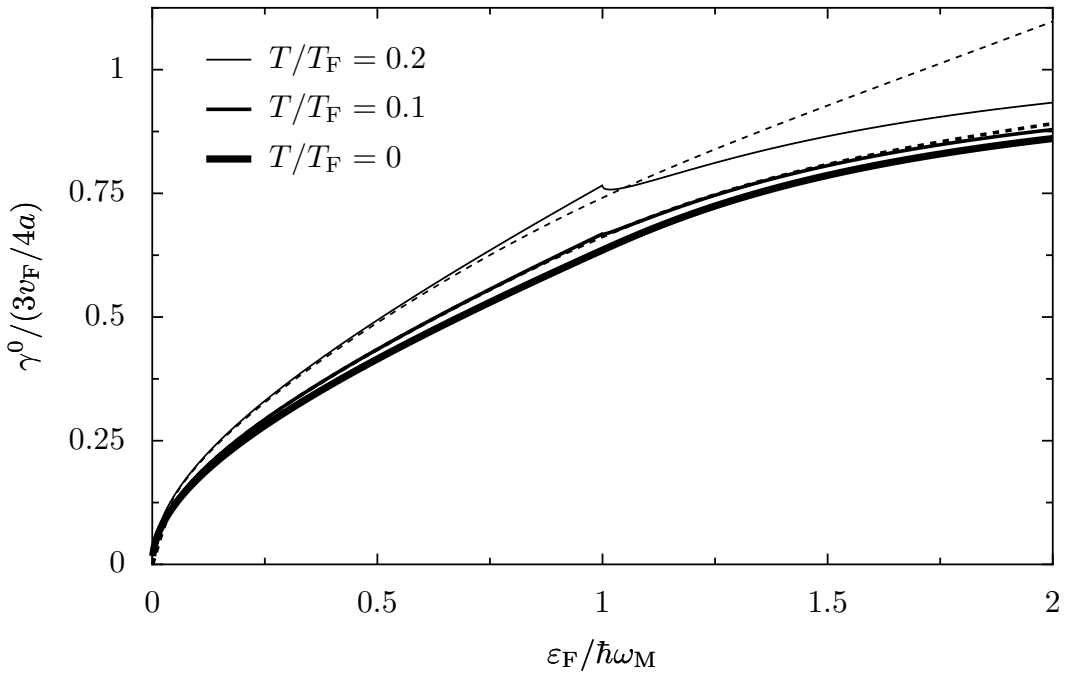

Figure 4.2: Surface plasmon linewidth as a function of $\varepsilon_\mathrm{F}/\hbar\omega_\mathrm{M}$, for different temperatures. Solid lines: low-temperature expansion (4.59). Dashed lines: numerical integration of (4.4) with Eqs. 4.41–4.43. In the figure, the temperature increases from bottom to top.

We denote the smooth component of the surface plasmon linewidth as γ^0 since the smooth semiclassical density of states (4.36) is at the origin of this result. As it will be shown in the next section, the oscillating component (4.37) of the density of states will yield an additional term for the surface plasmon linewidth which oscillates as a function of the size a of the nanoparticle. Note that the exponential factor appearing in (4.4) is irrelevant in our low-temperature expansion. Furthermore, we have replaced $\tilde{\omega}_\mathrm{M}$ by ω_M for the calculation of γ^0. As we will see in Chapter 5, the spill-out correction to the Mie frequency scales as $1/a$ (see also Sec. 1.1.2). Furthermore, (4.59) shows that γ^0 scales also as $1/a$. Thus, incorporating the spill-out correction in the result of (4.59) would yield higher order terms in $1/a$, inconsistently with our semiclassical expansion that we have restricted to the leading order.

At $T = 0$, we recover with (4.59) the well-known $1/a$ size dependence of the surface plasmon linewidth. First found by Kawabata and Kubo [48], this size dependence is due to the confinement of the single-particle states in the nanoparticle (see Sec. 1.2.2). We also recover the zero-temperature frequency dependence found in Refs. 29 and 30. As a function of ε_F, the Landau damping linewidth increases linearly for $\varepsilon_\mathrm{F} \ll \hbar\omega_\mathrm{M}$ and as $\sqrt{\varepsilon_\mathrm{F}}$ for $\varepsilon_\mathrm{F} \gg \hbar\omega_\mathrm{M}$ (see solid line for $T = 0$ in Fig. 4.2). The increase of the linewidth is a consequence of the fact that with increasing Fermi energy the number of particle-hole excitations rises. The behavior for a high Fermi energy when the discreteness of the

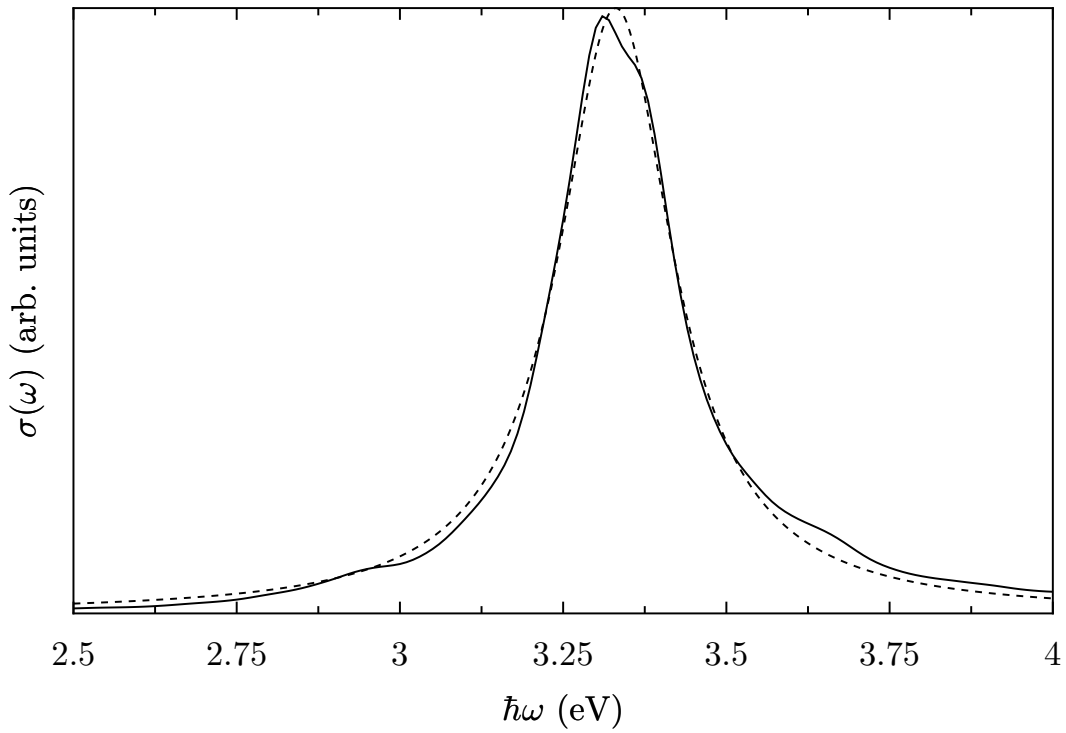

Figure 4.3: TDLDA photoabsorption cross section $\sigma(\omega)$ in arbitrary units for a sodium nanoparticle with $N = 1760$ electrons (solid line). The dashed line is a Lorentzian fit.

quantum levels is negligible can be understood in two ways. Quantum mechanically, the two densities of states in expression (4.34) for the Landau damping rate (4.4) are evaluated nearly at the same energy. Performing the calculations in this limit thus yields $\gamma^0 \sim \sqrt{\varepsilon_{\rm F}}$. Classically, the motion of the electrons is ballistic, and we can think of an effective electronic mean free path limited by the size a of the nanoparticle, such that $\gamma^0 \simeq v_{\rm F}/a \sim \sqrt{\varepsilon_{\rm F}}$ (see Sec. 1.2.1).

In order to confirm the relevance of the result (4.59) at $T = 0$, we can compare it with the TDLDA numerical calculations. From the TDLDA linear response function, one can extract the photoabsorption cross section $\sigma(\omega)$ as defined in (1.15) [79]. It is represented in Fig. 4.3 for a sodium nanoparticle containing $N = 1760$ valence electrons (solid line). A Lorentzian fit then provides the full width at half maximum of the absorption curve $\gamma_{\rm t}(a) = \gamma_{\rm i} + \gamma(a)$ (see dashed line in Fig. 4.3). $\gamma_{\rm i}$ is introduced to smooth the excitation peaks of the TDLDA response function in order to get a continuous curve. It is chosen to be of the order of 0.1 eV, and one has to subtract this quantity from the result of the Lorentzian fit to obtain the size-dependent linewidth $\gamma(a)$. We verified that the precise value of $\gamma_{\rm i}$ does not affect the $\gamma(a)$ that we extract.

The analytical evaluation of γ^0 at $T = 0$ agrees with the TDLDA numerical calculations for the largest nanoparticle sizes (see dashed line of Fig. 4.4). However, we see in Fig. 4.4 that when a decreases, the linewidth extracted from the TDLDA absorption

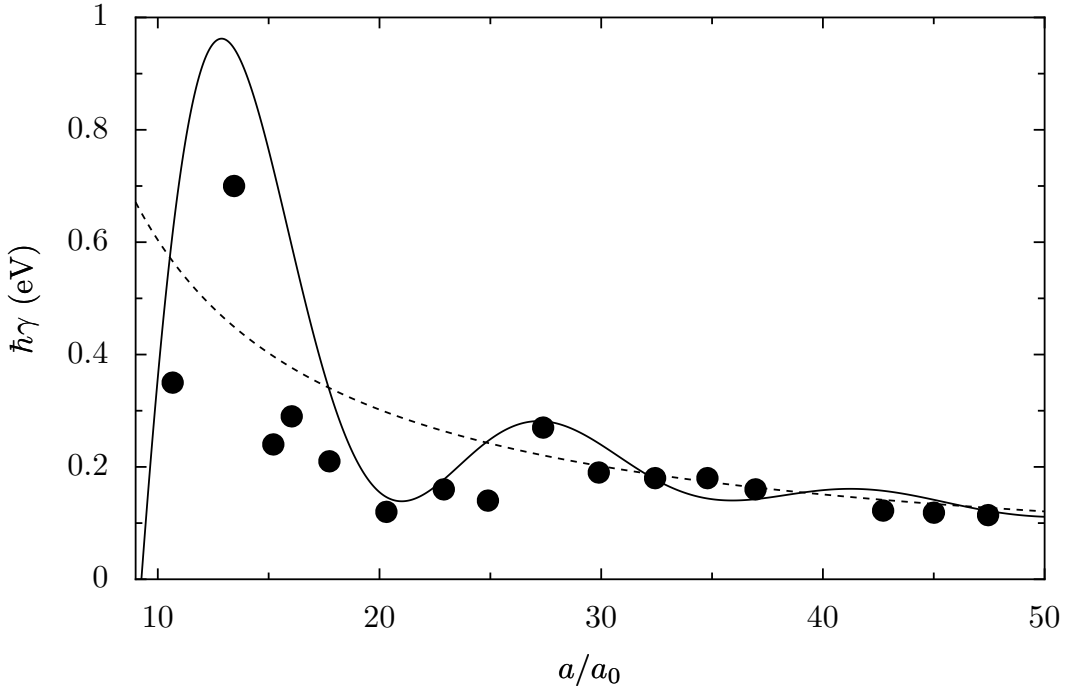

Figure 4.4: Inverse lifetime of the first collective excitation in sodium nanoparticles as a function of the radius a of the cluster for $T = 0$. The dashed line is the smooth part of the single plasmon linewidth (4.59). The full line is the smooth part plus the oscillating contribution from (4.69) for a number of repetitions $\tilde{r} = 1$. This semiclassical result is compared to numerical TDLDA calculations (dots) for clusters with magic numbers of atoms between 20 and 1760, corresponding to $k_{\mathrm{F}}a$ between 5.2 and 23.

cross section presents a nonmonotonic behavior. This will be the subject of the next section. Experiments on charged alkaline clusters with a diameter in the range 1–5 nm in vacuum [18] yield a linewidth of the order of $\hbar\gamma \sim 1\,\mathrm{eV}$. Although the charged character of those clusters used in this experiment might limit the applicability of our model, we note that our calculated value is smaller, but of the same order of magnitude than the experimental one. This difference might be explained by additional contributions to the linewidth present in the experiment.

Since the function g_2 is positive, finite temperatures lead to a broadening of the surface plasmon resonance which to leading order is quadratic. As for $T = 0$, the linewidth decreases with increasing size of the nanoparticle like $1/a$. Based on classical considerations, this has been proposed in Ref. 30, where the authors argued that $\gamma \simeq \bar{v}/a$ with the average speed

$$\bar{v} = \frac{3v_{\mathrm{F}}}{4}\left[1 + \frac{\pi^2}{6}\left(\frac{T}{T_{\mathrm{F}}}\right)^2\right] \tag{4.60}$$

of electrons at the temperature T. The result of Ref. 30 is only relevant in the high

energy limit $\varepsilon_\mathrm{F} \gg \hbar\omega_\mathrm{M}$ where it agrees with our general result (4.59).

In Fig. 4.5, we show the linewidth (4.59) as a function of the temperature, scaled by the zero-temperature linewidth, for different values of the ratio $\varepsilon_\mathrm{F}/\hbar\omega_\mathrm{M}$ (solid lines). In order to confirm the validity of our low temperature expansion, we compare it to the result of a numerical integration (dashed lines) of (4.4) with Eqs. 4.41–4.43.[1] The agreement of the expansion (4.59) with this direct integration is excellent for low temperatures. For fixed T/T_F, the deviation increases with $\varepsilon_\mathrm{F}/\hbar\omega_\mathrm{M}$ since then, the low-temperature condition $\hbar\omega_\mathrm{M} \gg k_\mathrm{B}T$ is less and less fulfilled. This can also be noticed from Fig. 4.2 where we show the result of (4.59) as a function of the ratio $\varepsilon_\mathrm{F}/\hbar\omega_\mathrm{M}$ for different temperatures. Note that the cusp present in our analytical result at finite temperature for $\varepsilon_\mathrm{F} = \hbar\omega_\mathrm{M}$ is unphysical, as confirmed by the numerical integration of (4.4). The cusp comes from the improper treatment of our evaluation of (4.44) when $\hbar\omega_\mathrm{M}$ is in a range of order $k_\mathrm{B}T$ around the Fermi energy ε_F (see Fig. 4.1c).

There are a number of experiments showing a broadening of the surface plasmon linewidth with temperature [46, 47, 95, 96]. Those experimental results on not too small clusters indicate the presence of small corrections to the width of the collective surface plasmon excitation due to finite temperatures, in agreement with our result (4.59). In Ref. 95, absorption measurements on gold nanoparticles with a diameter ranging from 9 to 25 nm in aqueous solution have shown only a weak temperature effect on the surface plasmon linewidth. In Refs. 46 and 47, a weak broadening of the plasmon resonance in silver and gold nanoparticles of sizes $a = 4.25$ to 10 nm is reported, accompanied by a small redshift of the peak position as the temperature increases. In Ref. 96, the temperature dependence of small silver clusters (radius of 1.6 to 10.5 nm) embedded in a glass matrix has been investigated and a rather small broadening of the plasmon line has been reported as the temperature increases from 1.5 to 300 K.

There are also experiments on very small clusters [23,24] showing a strong temperature effect on the surface plasmon linewidth. It has been observed in Ref. 23 that the plasmon width of mercury clusters increases dramatically with temperature. A systematic study of the temperature dependence of the linewidth in small charged sodium nanoparticles

[1] Note that for the purpose of a numerical evaluation of $\gamma^0(T)$, we cannot use the approximate Sommerfeld expression (4.53) for the chemical potential μ. Nevertheless, it can be found by remarking that the number of valence electrons N in the system does not change with temperature. We thus have the self-consistent equation

$$N(T) = \int_0^\infty \mathrm{d}\varepsilon f(\varepsilon)\varrho^0(\varepsilon) = N(T=0)$$

with $f(\varepsilon)$ the Fermi distribution and $\varrho^0(\varepsilon)$ the density of states given in (C.28). The preceding expression can be evaluated and we obtain

$$\left(\frac{T}{T_\mathrm{F}}\right)^{3/2} \mathrm{Li}_{3/2}\left[-\mathrm{e}^{\mu(T)/k_\mathrm{B}T}\right] + \frac{4}{3\sqrt{\pi}} = 0,$$

where $\mathrm{Li}_\nu(z)$ is the polylogarithmic function. This expression can be solved numerically to yield the self-consistent chemical potential μ. We have checked that (4.53) provides a reasonable approximation to μ. For instance, at $T/T_\mathrm{F} = 0.2$, the error of the Sommerfeld result is about 7 %.

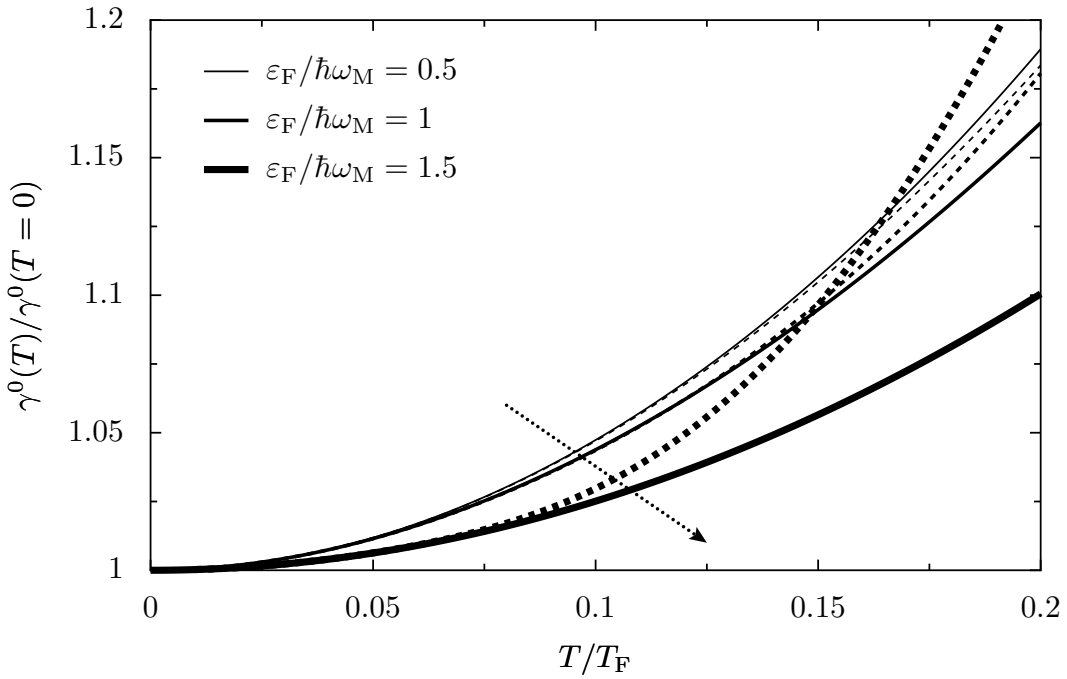

Figure 4.5: Surface plasmon linewidth as a function of the temperature, scaled by the linewidth at $T = 0$, for different ratios $\varepsilon_\mathrm{F}/\hbar\omega_\mathrm{M}$. Solid lines: low-temperature expansion (4.59). For $\varepsilon_\mathrm{F} = \hbar\omega_\mathrm{M}$, we have accounted for the additional $T^{5/2}$-correction to γ^0, see (4.51). Dashed lines: numerical integration of (4.4) with Eqs. 4.41–4.43. The arrow indicates the direction of increasing $\varepsilon_\mathrm{F}/\hbar\omega_\mathrm{M}$.

with $N = 8$, 20, and 40 valence electrons has been carried out in Ref. 24. As the temperature of the cluster is increasing, the authors found a pronounced broadening of the resonance which goes typically as $\sqrt{T}$. This is in apparent contradiction with our result (4.59). However, for very small particle sizes, an additional broadening mechanism not considered in our analysis becomes important, namely the coupling of the surface plasmon to quadrupole surface thermal fluctuations [16, 97, 98].

4.3 Shell effects and nonmonotonic behavior of the plasmon linewidth

In this section, we restrict ourselves to zero temperature. In this case, the function $F(\varepsilon)$ defined in (4.30) and entering (4.34) reads

$$F(\varepsilon) = \Theta(\varepsilon - \varepsilon_\mathrm{F})\Theta(\varepsilon_\mathrm{F} + \hbar\omega - \varepsilon). \tag{4.61}$$

In the expression (4.34), the oscillating part of the density of states (4.35) gives rise to terms of the type $\varrho_l^0 \varrho_{l'}^{\mathrm{osc}}$ as well as $\varrho_l^{\mathrm{osc}} \varrho_{l'}^{\mathrm{osc}}$. The former become negligible (in the

semiclassical limit of small $\hbar$) because one integrates a smooth function multiplied by a highly oscillating one. With the help of (2.37), (4.27) and (4.37), the latter yields

$$\Sigma^{\mathrm{osc}}(\omega) = \frac{24}{\hbar}\left(\frac{\omega_{\mathrm{M}}}{\omega}\right)^3 \frac{\varepsilon_{\mathrm{F}}}{\hbar\omega}\frac{\varepsilon_{\mathrm{F}}}{(k_{\mathrm{F}}a)^7}\int_{\eta_{\min}}^{\eta_{\max}} \mathrm{d}\eta\,\eta \sum_{l,l'=l\pm1} f_{l'}\sqrt{\eta^2-(l+1/2)^2}\sqrt{\eta'^2-(l'+1/2)^2} \times \sum_{\tilde{r},\tilde{r}'\geqslant 1} \cos\left[\tilde{r}\left(\frac{S_l(\eta)}{\hbar}-\frac{3\pi}{2}\right)\right]\cos\left[\tilde{r}'\left(\frac{S_{l'}(\eta')}{\hbar}-\frac{3\pi}{2}\right)\right]. \tag{4.62}$$

We have defined $\eta = ka$ for the particles, $\eta' = \sqrt{\eta^2-(k_{\mathrm{F}}a)^2\hbar\omega/\varepsilon_{\mathrm{F}}}$ for the holes, $\eta_{\min} = k_{\mathrm{F}}a\max(1,\sqrt{\hbar\omega/\varepsilon_{\mathrm{F}}})$, and $\eta_{\max} = k_{\mathrm{F}}a\sqrt{1+\hbar\omega/\varepsilon_{\mathrm{F}}}$. In (4.62), $f_{l'} = l$ for $l' = l-1$ and $f_{l'} = l+1$ for $l' = l+1$. We can expand the product of the two cosines and keep only the contribution in leading order in $\hbar$, neglecting the highly oscillating term as a function of the particle and hole actions. We now write this contribution with the help of the Poisson summation rule (C.29) to obtain

$$\Sigma^{\mathrm{osc}}(\omega) \simeq \frac{24}{\hbar}\left(\frac{\omega_{\mathrm{M}}}{\omega}\right)^3 \frac{\varepsilon_{\mathrm{F}}}{\hbar\omega}\frac{\varepsilon_{\mathrm{F}}}{(k_{\mathrm{F}}a)^7}\int_{\eta_{\min}}^{\eta_{\max}} \mathrm{d}\eta\,\eta \sum_{\tilde{m}=-\infty}^{+\infty}\sum_{\substack{\tilde{r},\tilde{r}'\geqslant 1\\ \sigma=\pm}}\int_{-1/2}^{l_{\max}}\mathrm{d}l \times \sum_{l'=l\pm1} f_{l'}\sqrt{\eta^2-(l+1/2)^2}\sqrt{\eta'^2-(l'+1/2)^2}\;\mathrm{e}^{\sigma\mathrm{i}\phi_l^{\tilde{r}\tilde{r}'\tilde{m}}(\eta)}, \tag{4.63}$$

where we have defined the phase

$$\phi_l^{\tilde{r}\tilde{r}'\tilde{m}}(\eta) = \frac{\tilde{r}S_l(\eta)}{\hbar} - \frac{\tilde{r}'S_{l'}(\eta')}{\hbar} - \frac{3\pi}{2}(\tilde{r}-\tilde{r}') + 2\pi\tilde{m}l. \tag{4.64}$$

Performing a stationary phase approximation (see Appendix B), given by the condition $\partial\phi/\partial l|_{\bar{l}} = 0$ with the stationary points $\bar{l}$, we obtain with (4.38) the stationary phase equation

$$\tilde{r}\arccos\left(\frac{\bar{l}+1/2}{\eta}\right) - \tilde{r}'\arccos\left(\frac{\bar{l}'+1/2}{\eta'}\right) = \pi\tilde{m}. \tag{4.65}$$

The phase of (4.64) indicates that the major contribution to the integral over l in (4.63) will be given by $\tilde{r} = \tilde{r}'$ and $\tilde{m} = 0$. We then select only one point within the full mesh of the stationary points,

$$\frac{\bar{l}+1/2}{\eta} = \frac{\bar{l}'+1/2}{\eta'}. \tag{4.66}$$

Noticing that $\eta' = \sqrt{\eta^2-(k_{\mathrm{F}}a)^2\hbar\omega/\varepsilon_{\mathrm{F}}} < \eta$, we see that in order to satisfy (4.66), we have to set $\bar{l}' = \bar{l}-1$. The stationary point is then given by

$$\bar{l} = \frac{\eta+\eta'}{2(\eta-\eta')}. \tag{4.67}$$

Performing the integral over l in (4.63) with the help of the stationary phase approximation, we get

$$\Sigma^{\rm osc}(\omega) = \frac{48\sqrt{2\pi}}{\hbar}\left(\frac{\omega_{\rm M}}{\omega}\right)^3 \frac{\varepsilon_{\rm F}}{\hbar\omega}\frac{\varepsilon_{\rm F}}{(k_{\rm F}a)^7}\int_{\eta_{\min}}^{\eta_{\max}} {\rm d}\eta\,\eta\bar{l}\sqrt{\eta^2-(\bar{l}+1/2)^2}\sqrt{\eta'^2-(\bar{l}-1/2)^2}$$
$$\times\sum_{\tilde{r}=1}^{\infty}\left|\frac{\partial^2\phi_l^{\tilde{r},\tilde{r},0}(\eta)}{\partial l^2}\right|_{l=\bar{l}}\Bigg|^{-1/2}\cos\left\{\phi_{\bar{l}}^{\tilde{r},\tilde{r},0}(\eta)+\frac{\pi}{4}{\rm sign}\left[\frac{\partial^2\phi_l^{\tilde{r},\tilde{r},0}(\eta)}{\partial l^2}\Bigg|_{l=\bar{l}}\right]\right\}. \quad (4.68)$$

After a lengthly but straightforward calculation, this finally provides the following result for the oscillating part of the first plasmon linewidth, $\gamma^{\rm osc} = \Sigma^{\rm osc}(\omega_{\rm M})$:

$$\gamma^{\rm osc} = \frac{6\sqrt{\pi}}{\hbar}\frac{\varepsilon_{\rm F}}{\xi(k_{\rm F}a)^5}\int_{\max(1,\sqrt{\xi})}^{\sqrt{1+\xi}} {\rm d}\beta\frac{\beta+\beta'}{(\beta-\beta')^4}\beta^{5/2}\beta'^{3/2}\left[(k_{\rm F}a)^2(\beta-\beta')^2-1\right]^{5/4} \quad (4.69)$$
$$\times\sum_{\tilde{r}=1}^{\infty}\frac{1}{\sqrt{\tilde{r}}}\cos\left\{2\tilde{r}\left[\sqrt{(k_{\rm F}a)^2(\beta-\beta')^2-1}-\arccos\left(\frac{1}{k_{\rm F}a(\beta-\beta')}\right)\right]-\frac{\pi}{4}\right\},$$

where $\beta' = \sqrt{\beta^2-\xi}$ and $\xi = \hbar\omega_{\rm M}/\varepsilon_{\rm F}$. The remaining integral over β can be performed numerically (solid line, Fig. 4.4). Assuming that $k_{\rm F}a \gg 1$, using that $\beta-\beta' \sim 1$ and that the sum over the number of repetitions is dominated by the first term, we see that the argument of the cosine is close to $2k_{\rm F}a$ and

$$\gamma^{\rm osc} \sim \frac{\varepsilon_{\rm F}}{\hbar(k_{\rm F}a)^{5/2}}\cos(2k_{\rm F}a). \quad (4.70)$$

Therefore the linewidth of the single surface plasmon excitation has a nonmonotonic behavior as a function of the size a of the metallic cluster. This is due to the density-density particle-hole correlation appearing in (4.34). Let us mention that the result of (4.69) is slightly different from the one of the previous work of Ref. 80. This is due to the fact that we have used here a more rigorous treatment of the semiclassical radial problem, as presented in Appendix C. As in Ref. 80, we have to set a phase shift in our analytical prediction of (4.69) to map the TDLDA numerical points in Fig. 4.4. This is due to the fact that we have taken only one stationary point (see Eq. 4.66) and neglected all the other contributions coming from the full mesh of stationary points which influence the phase appearing in (4.63).

A nonmonotonic behavior of the surface plasmon linewidth has also been observed experimentally in the case of charged lithium clusters [18]. Our numerical TDLDA calculations confirm the presence of size-dependent oscillations for alkaline metals. In Refs. 29, 99, and 100, some numerical evidences of such oscillations have also been reported. Our semiclassical approach also predicts a nonmonotonous behavior of γ for noble metal clusters, in agreement with recent experimental results [101]. However, the presence of different dielectric constants inside and outside the cluster renders the problem more involved. This issue is discussed in Chapter 8.

4.4 Conclusion for Chapter 4

In this chapter, we have evaluated the Landau damping linewidth resulting from the coupling of the surface plasmon to particle-hole excitations. Assuming that the self-consistent states are perfectly confined by the mean field, the size and temperature dependence of the linewidth of the surface plasmon has been investigated by means of a semiclassical evaluation, together with a low-temperature expansion.

In addition to the well-known $1/a$ size dependence, we have shown that for the smallest sizes, the surface plasmon linewidth presents oscillations as a function of the size of the nanoparticle. These oscillations arise from electron-hole density-density correlations. These results are in good agreement with numerical time-dependent local density approximation calculations, and consistent with experiments on free alkaline nanoparticles. The development of the spectroscopy for individual nano-objects [38–44], which gets rid of the inhomogeneous broadening, will certainly allow in a near future to quantitatively confront our prediction of the oscillating behavior of the surface plasmon linewidth with measurements.

Furthermore, we have demonstrated in this chapter that an increase in temperature leads to an increasing width of the resonance. The effect of the temperature has been found to be weak, in qualitative agreement with the experimental results and with the previous theory of Ref. 30.

Chapter 5

Frequency of the surface plasmon excitation

Quand je n'ai pas de bleu, je mets du rouge.

(Pablo Picasso, 1881-1973, cited by Paul Éluard in Donner à voir)

In this chapter we turn to the evaluation of the redshift of the surface plasmon frequency with respect to the classical Mie value ω_{M}. The experimentally observed surface plasmon frequencies are smaller than the Mie frequency ω_{M} [10, 22, 25], and this is qualitatively captured by TDLDA calculations since the position of the maximum of the absorption curve ω_{sp} is smaller than ω_{M} (see Fig. 5.1). This redshift is usually attributed to the so-called *spill-out effect* [10,11,13]. As presented in Sec. 1.1.2, the origin of this quantum effect is a nonzero probability to find electrons outside the nanoparticle, which results in a reduction of the effective frequency for the center-of-mass coordinate. If a fraction N_{out}/N of the electrons is outside the geometrical boundaries of the nanoparticle, we can expect that the electron density within the nanoparticle is reduced accordingly and the frequency of the surface plasmon is given by (1.7). We have seen in Chapter 2 that such an estimation can be formalized considering the form of the single-particle confining potential (2.5).

It has been known for a long time [11] that ω_{sp} is even smaller than the Mie frequency corrected by the spill-out effect $\tilde{\omega}_{\mathrm{M}}$. Therefore the spill-out effect is not sufficient to explain the redshift of the surface plasmon frequency as illustrated in Fig. 5.1. Recently, the coupling to the electronic environment has been invoked as an additional source of frequency shift [60, 102]. This has been formalized in Chapter 3, where the expression (3.33) for the environment-induced shift δ has been established. In this chapter we provide an estimation of such a contribution (analogous to the Lamb shift of atomic physics [82]) and its parametric dependence on the particle size and electron temperature (see Sec. 5.2). Despite the fact that we have to make drastic approximations, we find that this additional shift implies a reduction of the surface plasmon frequency, thus approaching the TDLDA result. However it is known [11] that the experimental resonance

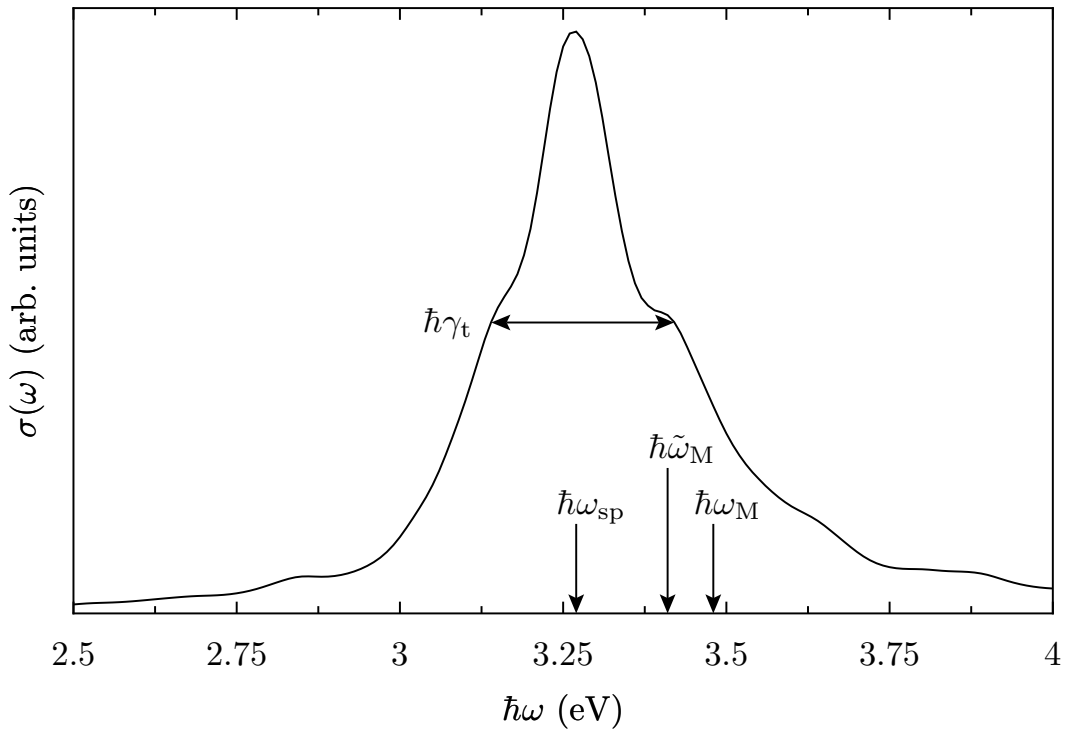

Figure 5.1: Absorption cross section $\sigma(\omega)$ in arbitrary units extracted from TDLDA calculations for a sodium cluster containing $N = 832$ valence electrons. The classical Mie frequency is ω_M, while $\tilde{\omega}_M$ is the frequency of the surface plasmon resonance taking into account the spill-out effect, Eq. 1.7. It has been obtained with the LDA self-consistent ground-state density as explained in Sec. 5.1.3. The frequency ω_{sp} corresponds to the position of the maximum of the absorption curve.

frequency is even lower than the TDLDA prediction within the jellium approximation. This could be due to the ionic degrees of freedom.

In Sec. 5.1, we calculate one of the contributions affecting the resonance frequency according to (1.7), namely the spill-out effect, while in Sec. 5.2, we will calculate the additional frequency shift induced by the electronic environment (3.33).

5.1 Spill-out-induced frequency shift

5.1.1 Mean-field approximation

Within the mean-field approximation, the electronic degrees of freedom are treated in the self-consistent one-particle potential $V(r)$ shown in Fig. 2.2, and the number of

electrons outside of the nanoparticle is given by

$$N_{\text{out}} = 2\int_0^\infty \mathrm{d}\varepsilon \sum_{lm} \varrho_l(\varepsilon) f(\varepsilon) \int_{(r>a)} \mathrm{d}^3\mathbf{r}\, |\psi_{\varepsilon lm}(\mathbf{r})|^2 \,. \tag{5.1}$$

Here, $\varrho_l(\varepsilon)$ is the density of states restricted to a fixed angular momentum l from (4.35), while $f(\varepsilon)$ is the Fermi-Dirac distribution defined in (3.23). The factor of 2 accounts for the spin degeneracy. Because of the spherical symmetry of the problem, the one-particle wave functions separate into radial and angular parts according to (4.6). The radial wave functions $u_{\varepsilon l}(r)$ satisfy the reduced Schrödinger equation (4.7) which yields the single-particle eigenenergies ε in the mean-field potential $V(r)$, that we approximate by the step-like potential of (4.5).

The Fermi function in (5.1) suppresses contributions to the energy integral from values higher than ε_{F} plus a few $k_{\text{B}}T$. For low temperatures $k_{\text{B}}T \ll W$, the states in the continuum do not contribute and we restrict our evaluation to the bound states with $\varepsilon < V_0$.[1] Defining $k = \sqrt{2m_{\text{e}}\varepsilon}/\hbar$ and $\chi = \sqrt{2m_{\text{e}}(V_0-\varepsilon)}/\hbar$, we find for the regular solutions of (4.7)

$$u_{\varepsilon l}(r) = \sqrt{\frac{r}{a}} \begin{cases} A_{kl}\sqrt{k} J_{l+\frac{1}{2}}(kr), & r \leqslant a, \\ B_{kl}\sqrt{\chi} K_{l+\frac{1}{2}}(\chi r), & r > a, \end{cases} \tag{5.2}$$

where $J_\nu(z)$ are Bessel functions of the first kind and $K_\nu(z)$ are modified Bessel functions. The normalization constants A_{kl} and B_{kl} are given by

$$A_{kl} = \sqrt{\frac{2}{kaC_{kl}}}, \tag{5.3a}$$

$$B_{kl} = \sqrt{\frac{2}{\chi a C_{kl}}} \frac{J_{l+\frac{1}{2}}(ka)}{K_{l+\frac{1}{2}}(\chi a)}, \tag{5.3b}$$

with

$$C_{kl} = \left[\frac{J_{l+\frac{1}{2}}(ka)}{K_{l+\frac{1}{2}}(\chi a)}\right]^2 K_{l-\frac{1}{2}}(\chi a) K_{l+\frac{3}{2}}(\chi a) - J_{l-\frac{1}{2}}(ka) J_{l+\frac{3}{2}}(ka). \tag{5.4}$$

We therefore obtain for the integral in (5.1)

$$\int_{(r>a)} \mathrm{d}^3\mathbf{r}\, |\psi_{\varepsilon lm}(\mathbf{r})|^2 = \frac{J^2_{l+\frac{1}{2}}(ka)}{C_{kl}} \left[\frac{K_{l-\frac{1}{2}}(\chi a) K_{l+\frac{3}{2}}(\chi a)}{K^2_{l+\frac{1}{2}}(\chi a)} - 1\right]. \tag{5.5}$$

The summation of this expression over all one-particle states required to obtain N_{out} according to (5.1) cannot be done analytically. We therefore use a semiclassical approximation which provides additional physical insight into the spill-out effect.

[1] The energy required to ionize the nanoparticle is the work function W plus the charging energy. This corresponds to a temperature of several 10^5 K. Therefore, nanoparticles cannot be thermoionized at reasonable temperatures.

5.1.2 Semiclassical low-temperature expansion for the number of spill-out electrons

The integral of the electronic density (5.5) increases with the energy. Combined with the increasing density of states in (5.1) and the Fermi function providing an energy cutoff, this allows to conclude that the spill-out is dominated by the energies near the Fermi level. In addition, in most of the metallic nanoparticles, we have $\varepsilon_\mathrm{F} \sim W \gg \Delta$, where Δ is the mean single-particle level spacing. The semiclassical limit, in which ka and χa must be much larger than one, then applies. In this limit, we obtain[2] for the integral (5.5) of the density outside of the nanoparticle

$$\int_{(r>a)} \mathrm{d}^3\mathbf{r}\, |\psi_{\varepsilon lm}(\mathbf{r})|^2 \simeq \frac{\varepsilon}{\chi a V_0}, \tag{5.6}$$

to first order in $1/ka$ and $1/\chi a$. Since this result for a single state does not depend on the angular momentum quantum numbers l and m, the total density of states $\varrho(\varepsilon) = \sum_{lm} \varrho_l(\varepsilon)$ is sufficient to determine the number of spill-out electrons. Restricting ourselves to the smooth semiclassical density of states $\varrho^0(\varepsilon)$ given in (C.28),[3] and inserting (5.6) into (5.1) then yields

$$N_\mathrm{out} \simeq \frac{4m_\mathrm{e}a^2}{3\pi\hbar^2 V_0} \int_0^{V_0} \mathrm{d}\varepsilon\, f(\varepsilon) h(\varepsilon) \tag{5.7}$$

with

$$h(\varepsilon) = \frac{\varepsilon^{3/2}}{\sqrt{V_0 - \varepsilon}}. \tag{5.8}$$

Applying the low-temperature Sommerfeld expansion (4.52) with the chemical potential (4.53), we obtain

$$N_\mathrm{out} = \frac{(k_\mathrm{F}a)^2}{6\pi} \zeta\left(\frac{\varepsilon_\mathrm{F}}{V_0}, \frac{T}{T_\mathrm{F}}\right) \tag{5.9}$$

with

$$\zeta\left(x, \frac{T}{T_\mathrm{F}}\right) = \zeta_0(x) + \zeta_2(x) \left(\frac{T}{T_\mathrm{F}}\right)^2, \tag{5.10}$$

where

$$\zeta_0(x) = \frac{1}{x}\left[-\sqrt{x(1-x)}(2x+3) + 3\arcsin\sqrt{x}\right] \tag{5.11}$$

[2] To obtain this result, we have used the asymptotic behavior of the Bessel functions

$$J_\nu(z) \simeq \sqrt{\frac{2}{\pi z}} \cos\left(z - \frac{\nu\pi}{2} - \frac{\pi}{4}\right),$$
$$K_\nu(z) \simeq \sqrt{\frac{\pi}{2z}} \mathrm{e}^{-z},$$

for $z \gg 1$ [93].

[3] The oscillating component (C.37) of the density of states does not contribute to N_out. Indeed, integrating (5.1) with (5.6) and (C.37) leads to an averaging-out.

and

$$\zeta_2(x) = \frac{\pi^2}{3}\left(\frac{x}{1-x}\right)^{3/2}(2-x). \tag{5.12}$$

Note that the upper bound of the integral over the energy in (5.7) has been replaced by V_0 since we neglect exponentially suppressed contributions from higher energies. Therefore our Sommerfeld expansion is reliable for temperatures $T/T_\mathrm{F} \lesssim 1 - \varepsilon_\mathrm{F}/V_0$.

At zero temperature the number of spill-out electrons increases smoothly with increasing Fermi energy, reaching its maximal value $(k_\mathrm{F}a)^2/4$ at $\varepsilon_\mathrm{F} = V_0$. According to (5.9) and (5.10), the number of spill-out electrons increases with temperature. This is expected since the evanescent part of the wave function increases with the energy of the occupied states.

Scaling the result (5.9) with the total number of electrons in the nanoparticle, $N = 4(k_\mathrm{F}a)^3/9\pi$, we obtain

$$\frac{N_\mathrm{out}}{N} = \frac{3}{8k_\mathrm{F}a}\zeta\left(\frac{\varepsilon_\mathrm{F}}{V_0}, \frac{T}{T_\mathrm{F}}\right). \tag{5.13}$$

This relative spill-out scales to first order as $1/a$, and becomes less important for large particles. Since the work function W depends on the size of the nanoparticle through $W = W_\infty + \alpha/a$,[4] the number of spill-out electrons (5.13) acquires, via the dependence on V_0, higher-order corrections to the $1/a$ scaling. We neglect these terms because they are of the same order as the ones neglected in our semiclassical expansion. Therefore we approximate W by its bulk value W_∞. The dependence of (5.13) on a can be interpreted by observing that the spill-out is a surface effect so that N_out increases only with a^2. Inserting (5.13) into (1.7), one can calculate the spill-out-induced redshift of the surface plasmon resonance. This redshift increases for decreasing sizes and for increasing temperatures, in qualitative agreement with experiments [18, 22, 46, 47, 96].

One can define a spill-out length as the depth

$$l_\mathrm{s} = \frac{1}{3}\frac{N_\mathrm{out}}{N}a \tag{5.14}$$

of the spill-out layer. Inserting (5.13) into (5.14) yields the size-independent spill-out length

$$k_\mathrm{F}l_\mathrm{s} = \frac{1}{8}\zeta\left(\frac{\varepsilon_\mathrm{F}}{V_0}, \frac{T}{T_\mathrm{F}}\right), \tag{5.15}$$

which is represented in Fig. 5.2 as a function of the ratio $\varepsilon_\mathrm{F}/V_0$ for different temperatures. The result is compared with the results of a numerical integration of (5.7) with (5.8) (dashed lines). This confirms our expectations about the validity of our results, namely for low temperatures and for small ratios $\varepsilon_\mathrm{F}/V_0$.

[4] α is a constant which includes quantum mechanical corrections. See, e.g., Ref. 103.

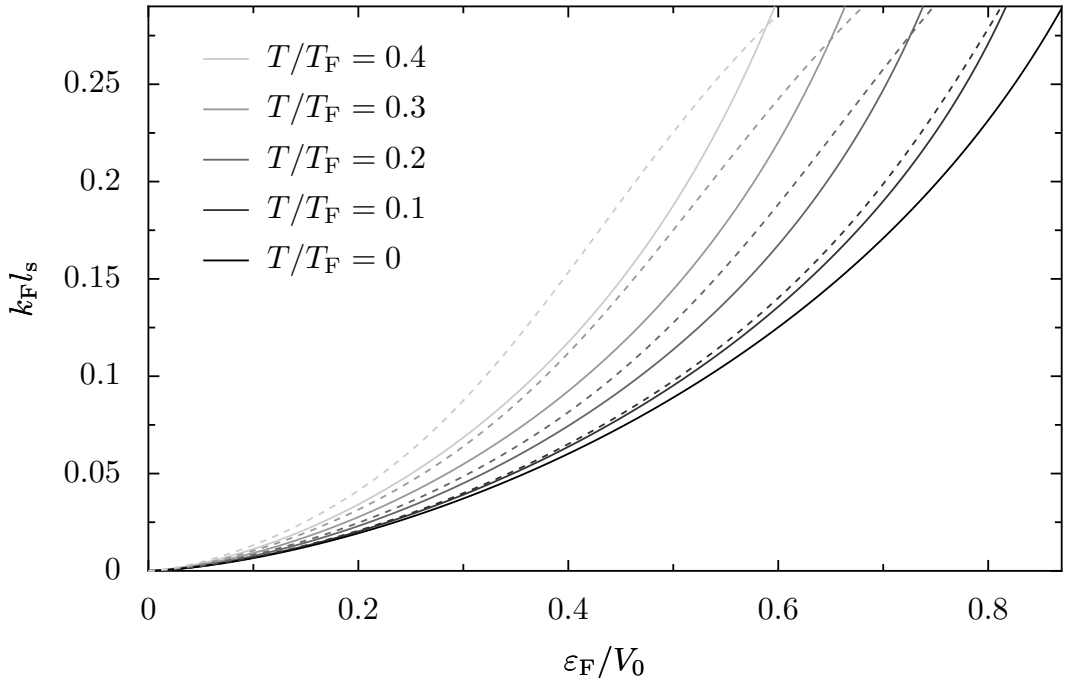

Figure 5.2: $k_\mathrm{F} l_\mathrm{s}$ from (5.15) as a function of $\varepsilon_\mathrm{F}/V_0$ at zero temperature (black line) and for finite temperatures (solid gray lines). The dashed lines result from the numerical integration of (5.7) with (5.8). In the figure, T/T_F increases from bottom to top.

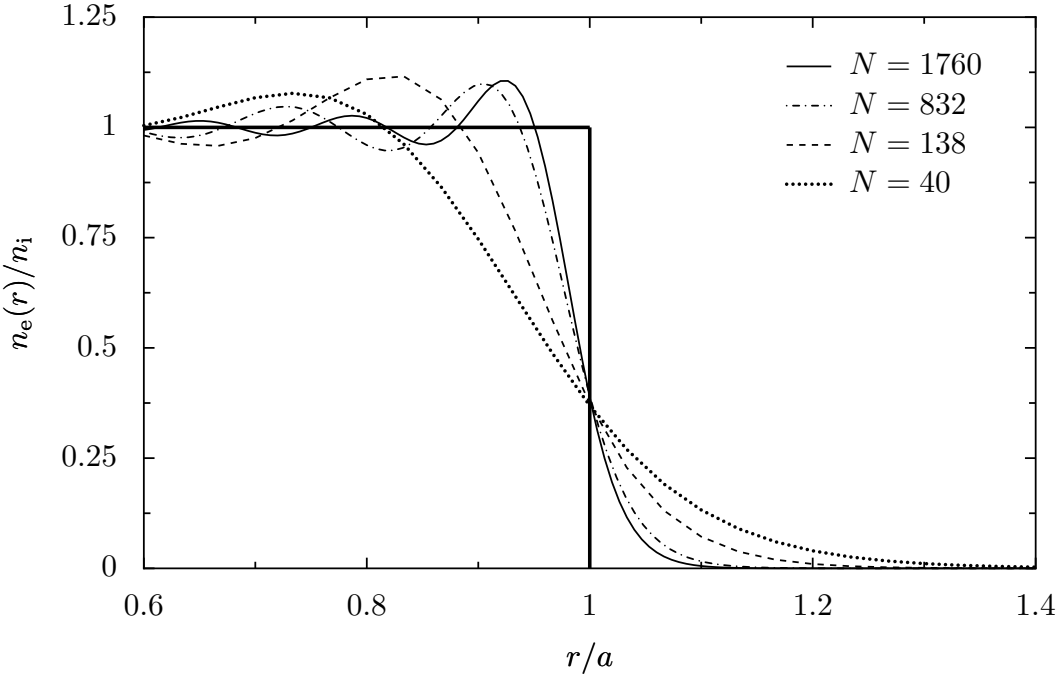

Figure 5.3: LDA ground-state self-consistent electronic density n_e as a function of the radial coordinate r scaled by the radius a, for various nanoparticle sizes ($r_s = 3.93\,a_0$, corresponding to sodium). The square profile (thick solid line) represents the abrupt jellium density decreasing from its value n_i inside the nanoparticle to zero at $r = a$.

5.1.3 Number of spill-out electrons: semiclassics vs. LDA

In this section, we compare our semiclassical evaluation of the spill-out effect at zero temperature with LDA calculations for spherical sodium nanoparticles. One possible way to estimate N_{out} is to use the LDA, which allows to compute the spherically symmetric self-consistent electronic ground-state density for nanoparticles with closed electronic shells (see Fig. 5.3). Integrating the density outside the nanoparticle then yields an approximation to N_{out}, and thus to l_s according to (5.14). An estimation of the spill-out length from (5.15) by means of our semiclassical theory at zero temperature gives $l_s \simeq 0.2\,a_0$ for sodium nanoparticles, while Madjet and collaborators obtained on the basis of Kohn-Sham and Hartree-Fock calculations l_s around $0.55\,a_0$ for clusters of size $N = 8$–196 [31]. With our LDA calculations, we obtain l_s of the order of $0.45\,a_0$ for all sizes between $N = 8$ and $N = 1760$ (see the squares in Fig. 5.4).

The fact that the semiclassical spill-out length is significantly smaller than that of LDA is a consequence of our assumption of a step-like potential for $V(r)$. Indeed, the LDA self-consistent potential $V(r)$ shown in Fig. 5.5 deviates from the form $V(r) = V_0\Theta(r-a)$ that we have used. As one can see in Fig. 5.5, the Fermi level does not coincide with $V(a)$. Defining the effective radius of the nanoparticle for the spill-out effect by means

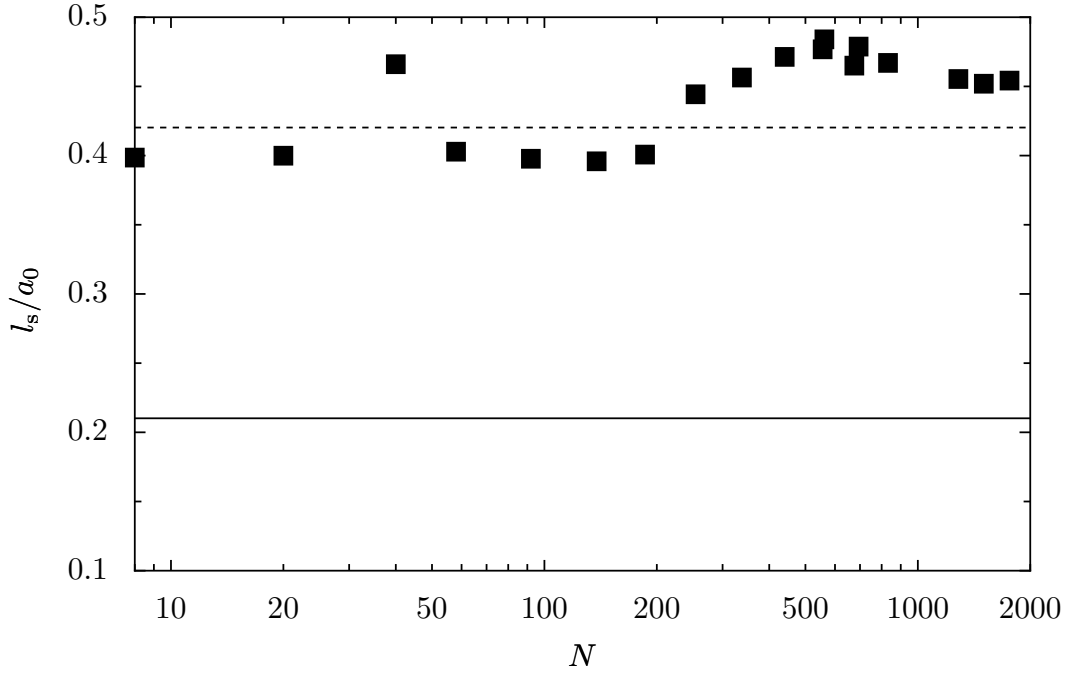

Figure 5.4: Spill-out length l_s at $T = 0$ from (5.15) in units of the Bohr radius a_0 as a function of the total number of electrons N (solid line) for sodium nanoparticles. The dashed line is twice the result of (5.15), and is obtained considering the effective radius a_{eff} for the approximated self-consistent potential, namely $V(r) = V_0\Theta(r - a_{\text{eff}})$. The squares result from LDA calculations.

of $V(a_{\text{eff}}) = \varepsilon_F$, it seems appropriate to approximate the self-consistent potential by $V(r) = V_0\Theta(r - a_{\text{eff}})$. An estimation from our LDA calculations gives $a_{\text{eff}} \simeq a + l_s$ for all sizes between $N = 8$ and $N = 1760$. Using this effective radius in (5.9) does not change our results for N_{out} and l_s since $a \gg l_s$. However, the spill-out length is defined from the geometrical radius a of the ionic jellium background of the nanoparticle. Since $a_{\text{eff}} \simeq a + l_s$, it actually yields an effective spill-out length $l_s^{\text{eff}} \approx 2l_s$ and approximately doubles our result for N_{out}. The improved $T = 0$ result for the spill-out length is represented by the dashed line in Fig. 5.4. It yields good agreement with the spill-out length as deduced from the LDA calculations (squares in Fig. 5.4). Note that there is no need to consider an effective radius of the nanoparticle in the calculation of the resonance width presented in Chapter 4. Indeed, the linewidth γ scales to leading order as $1/a$. Replacing a by an effective radius for the linewidth γ would thus lead to higher-order corrections.

5.1.4 Redshift of the surface plasmon resonance

We now examine the redshift of the surface plasmon resonance by means of TDLDA calculations. In Fig. 5.6, we show the frequencies deduced from the LDA number of

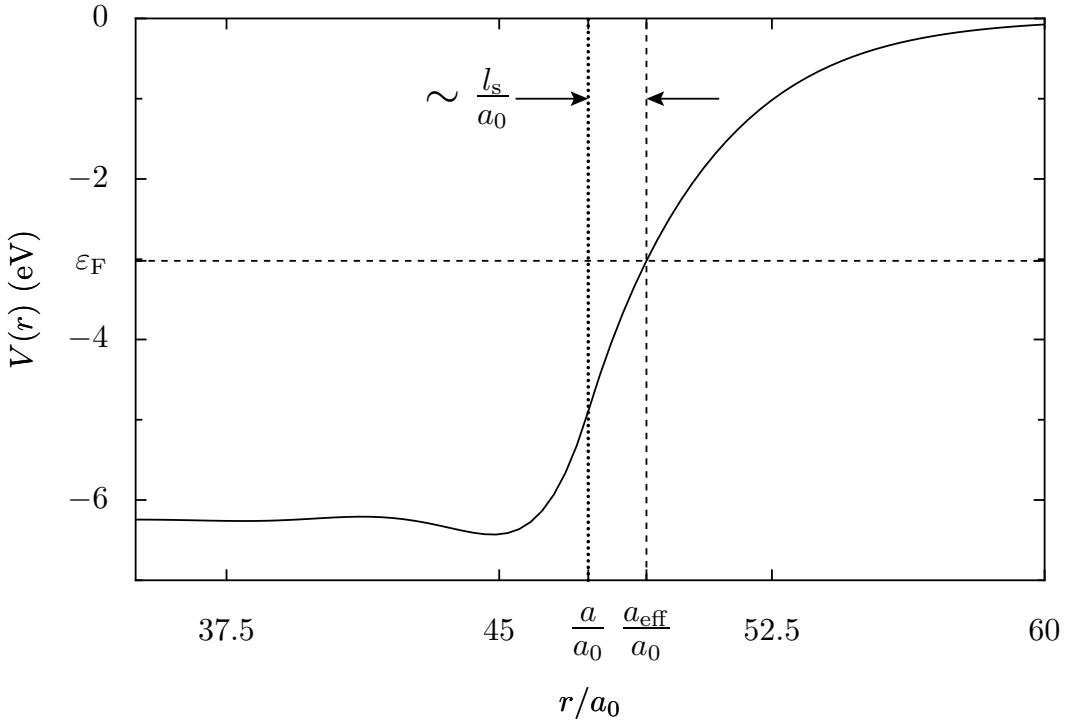

Figure 5.5: LDA self-consistent potential V as a function of the radial coordinate r for a sodium nanoparticle containing $N = 1760$ valence electrons. The radius a is indicated by the vertical dotted line, and the effective radius defined by $V(a_{\rm eff} \simeq a + l_{\rm s}) = \varepsilon_{\rm F}$ is indicated by the dashed line. The Fermi level corresponds to the horizontal dashed line.

spill-out electrons for various closed-shell nanoparticle sizes between $N = 8$ and $N = 1760$, where $N_{\rm out}$ is incorporated according to (1.7) (squares). The dashed line is our semiclassical result from (5.13) with (1.7), where we have taken into account the effective radius for the self-consistent potential, as discussed in the preceding section. We see that our analytical expression for the spill-out is in a good agreement with the LDA calculations, and that the redshift is increasing with decreasing size as predicted by (5.13).

Alternatively the resonance frequency can be extracted directly from the absorption cross section $\sigma(\omega)$ defined in (1.15) and calculated from the TDLDA response function (see Fig. 5.1). An upper bound for the resonance energy is given by the root mean square [11, 104]

$$\sqrt{\langle\omega^2\rangle} = \sqrt{\frac{\int_0^\infty {\rm d}\omega\ \omega^2\sigma(\omega)}{\int_0^\infty {\rm d}\omega\ \sigma(\omega)}}, \tag{5.16}$$

providing a lower bound for the redshift of the surface plasmon frequency from the Mie value. In the spherical jellium model, the frequency deduced from (5.16) coincides with $\tilde{\omega}_{\rm M}$ [11, 105], the Mie frequency redshifted by the spill-out effect (1.7). We have checked

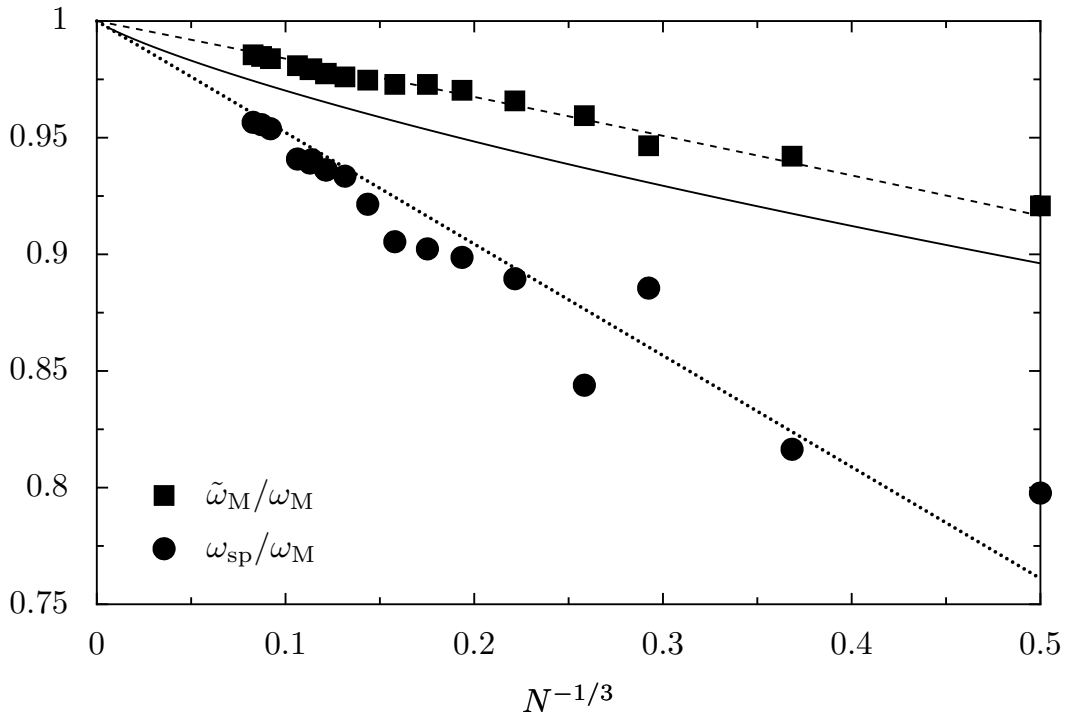

Figure 5.6: Surface plasmon frequency as a function of the number N of valence electrons in the nanoparticle. Squares: $\tilde{\omega}_{\rm M}/\omega_{\rm M}$, frequencies deduced from the LDA number of spill-out electrons according to (1.7). Dashed line: semi-classical evaluation of (5.13) with (1.7). Dots: $\omega_{\rm sp}/\omega_{\rm M}$, frequencies obtained by fitting the TDLDA absorption curves with a Mie-type cross section [10]. Dotted line: linear fit to the dots. Solid line: sum of the spill-out effect (dashed line) and the environment-induced redshift of the resonance (5.27). All results shown here are at zero temperature for the case of sodium. The points shown represent all closed shell sizes between $N = 8$ and $N = 1760$.

with our TDLDA calculations that the frequencies deduced from $N_{\rm out}$, i.e., from the electronic ground-state self-consistent density, correspond to the frequencies obtained from (5.16), up to the numerical error. At zero temperature, the TDLDA thus fulfills the sum rule [11] $\sqrt{\langle\omega^2\rangle} = \tilde{\omega}_{\rm M}$ within less than 1 % for sizes N larger than 254, and within 1–4 % for the smaller sizes up to $N = 8$.

The dots in Fig. 5.6 represent the maxima $\omega_{\rm sp}$ of the absorption curves obtained by fitting the TDLDA results with a Mie-type cross section [10]. It is clear from Fig. 5.6 that the frequency obtained by (1.7) from the number of spill-out electrons (squares) overestimates the resonance frequency $\omega_{\rm sp}$ (see also Fig. 5.1).[5] It has been noticed in

[5]Within the jellium model, the LDA is not responsible for any underestimation of the number of spill-out electrons, as it has been shown using Hartree-Fock and RPA calculations [11]. Our results show that the frequency shift induced by the electronic environment has to be taken into account in order to explain the above-mentioned discrepancy.

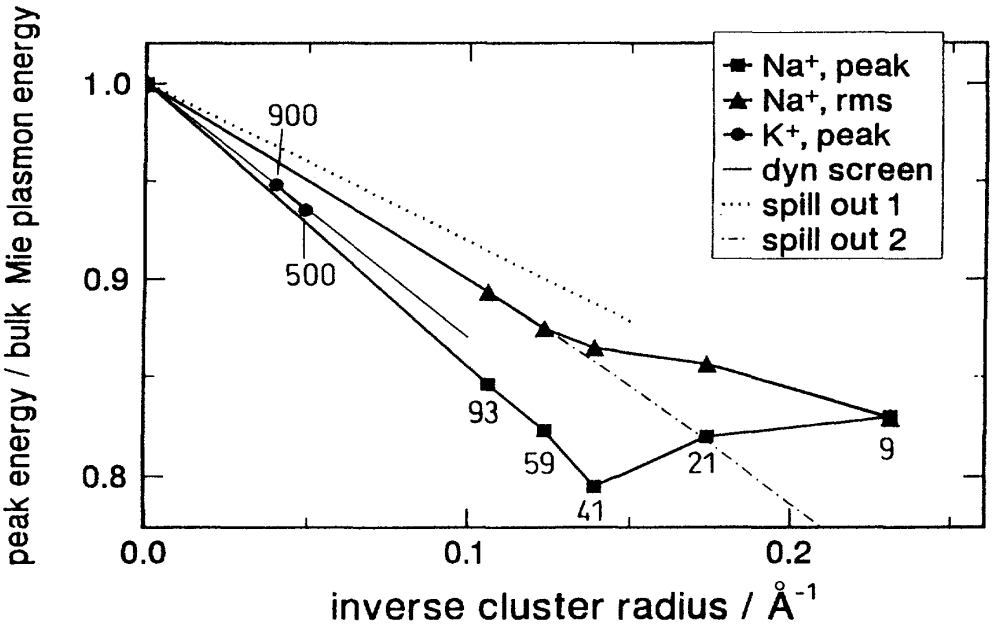

Figure 5.7: Measured peak positions for singly-ionized spherical sodium clusters Na_A^+ (squares) and large potassium nanoparticles K_A^+ (dots). The number of atoms $A = N + 1$ is indicated in the figure (N is the number of valence electrons). The triangles represent the measured root mean square of (5.16) for the sodium clusters. The straight lines are deduced from various theories of the spill-out and of the dynamic screening of surface science (see Ref. 25 and references therein). (Reproduced from Ref. 25.)

Ref. 25 that the spill-out effect is not sufficient to describe the experimentally observed resonance frequency (see Fig. 5.7).

In the following section, we propose to interpret the discrepancy between $\omega_{\rm sp}$ given by the TDLDA and $\tilde{\omega}_{\rm M}$ deduced from the spill-out by means of the coupling of the surface plasmon mode to electron-hole excitations. This coupling results in a shift of the surface plasmon frequency which adds to the effect of the spill-out.

5.2 Environment-induced frequency shift

We now evaluate the redshift δ defined in (3.33) which comes in addition to the spill-out contribution, as stated in (3.35).

According to (4.1) and (3.33), the energy shift δ is related to the function $\Sigma(\omega)$ through the Kramers-Kronig relation

$$\delta = \frac{1}{\pi}\mathcal{P}\int_{-\infty}^{+\infty} \mathrm{d}\omega \frac{\omega\Sigma(\omega)}{\omega^2 - \tilde{\omega}_{\rm M}^2}. \tag{5.17}$$

In what follows, we focus on the smooth size-dependent function $\Sigma^0(\omega)$ given in (4.55) which will yield the smooth component δ^0 of the environment-induced redshift of the surface plasmon frequency. Thus, in (5.17), the frequency $\tilde{\omega}_{\rm M}$ appearing in the denominator can be replaced by $\omega_{\rm M}$. Indeed, the function $\Sigma^0(\omega)$ of (4.55) is proportional to $1/k_{\rm F}a$. Thus, taking into account the spill-out effect in the evaluation of δ would yield higher order terms in powers of $1/k_{\rm F}a$, that we neglect in the semiclassical limit. Furthermore, we have to restrict the integral over the frequency ω by introducing the cutoff $\omega_{\rm c}$ discussed in Chapter 4. It arises from the fact that the particle-hole pairs that participate to δ in (3.33) belong to the high-energy sector of the RPA Hilbert space, while the surface plasmon excitation is the superposition of particle-hole pairs of the restricted low-energy subspace (see Secs. 1.2.3 and 2.2.3). The TDLDA absorption cross section shows a large excitation peak at the frequency $\omega_{\rm sp}$ which supports almost all of the dipole strength. This peak is surrounded by particle-hole excitations that become noticeable for frequencies larger than $\sim \omega_{\rm M} - \eta\gamma$, where η is a constant of the order of unity. Thus for the purpose of calculating the integral (5.17) we can take the cutoff at $\omega_{\rm M} - \eta\gamma$ and approximate

$$\delta^0 \simeq \frac{1}{\pi}\mathcal{P}\int_{\omega_{\rm M}-\eta\gamma}^{+\infty} {\rm d}\omega \frac{\omega\Sigma^0(\omega)}{\omega^2-\omega_{\rm M}^2}. \tag{5.18}$$

For frequencies ω larger than $\omega_{\rm M} - \eta\gamma$, the function g appearing in (4.55) can be replaced by its asymptotic expansion for $\varepsilon_{\rm F} \ll \hbar\omega$,

$$g\left(x, \frac{T}{T_{\rm F}}\right) \simeq \left[\frac{8}{15} + \frac{2\pi^2}{9}\left(\frac{T}{T_{\rm F}}\right)^2\right]\sqrt{x}. \tag{5.19}$$

Inserting (4.55) with (5.19) into (5.18), we arrive at

$$\delta^0 = \frac{3v_{\rm F}}{4\pi a}\left[\frac{8}{15} + \frac{2\pi^2}{9}\left(\frac{T}{T_{\rm F}}\right)^2\right] I\left(\frac{\hbar\omega_{\rm M}}{\varepsilon_{\rm F}}, \frac{\eta\gamma}{\varepsilon_{\rm F}}\right), \tag{5.20}$$

where we have defined

$$I(\xi,\alpha) = \xi^3\mathcal{P}\int_{\xi-\alpha}^{\infty} \frac{{\rm d}x}{x^{5/2}\left(x^2-\xi^2\right)}. \tag{5.21}$$

This integral can be split into two parts, namely

$$I_1(\xi,\alpha) = \xi^3\mathcal{P}\int_{\xi-\alpha}^{\xi+\alpha} \frac{{\rm d}x}{x^{5/2}\left(x^2-\xi^2\right)} \tag{5.22}$$

and

$$I_2(\xi,\alpha) = \xi^3\int_{\xi+\alpha}^{\infty} \frac{{\rm d}x}{x^{5/2}\left(x^2-\xi^2\right)}. \tag{5.23}$$

I_1 yields a vanishing contribution to the shift δ^0. Indeed, the linewidth $\hbar\gamma$ is of the order of $\sim$0.1–0.2 eV (see Chapter 4), while the Mie energy is of several eV. Thus we

have $\gamma \ll \omega_{\rm M}$, and expanding I_1 in the limit $\alpha \ll \xi$, we obtain a contribution which goes as γ, i.e., $\sim 1/a$. Inserting this result into (5.20) therefore yields a term proportional to $1/a^2$, that we can neglect in our semiclassical expansion. The remaining integral I_2 can be evaluated exactly, and we have

$$I(\xi,\alpha) \simeq \frac{1}{\sqrt{\xi}}\left[-\frac{\pi}{2} - \frac{2}{3}\left(\frac{\xi}{\xi+\alpha}\right)^{3/2} + \arctan\left(\sqrt{1+\frac{\alpha}{\xi}}\right) - \frac{1}{2}\ln\left(\frac{\sqrt{\xi+\alpha}-\sqrt{\xi}}{\sqrt{\xi+\alpha}+\sqrt{\xi}}\right)\right]. \tag{5.24}$$

In the limit $\alpha \ll \xi$, it reduces to

$$I(\xi,\alpha) \simeq \frac{1}{\sqrt{\xi}}\left[\frac{1}{2}\ln\left(\frac{4\xi}{\alpha}\right) - \frac{\pi}{4} - \frac{2}{3}\right], \tag{5.25}$$

and inserting this result into (5.20), we obtain in the semiclassical limit $k_{\rm F}a \gg 1$

$$\delta^0 \simeq \frac{3v_{\rm F}}{4a}\sqrt{\frac{\varepsilon_{\rm F}}{\hbar\omega_{\rm M}}}\left[\ln\left(\frac{4\omega_{\rm M}}{\eta\gamma}\right) - \frac{\pi}{2} - \frac{4}{3}\right]\left[\frac{4}{15\pi} + \frac{\pi}{9}\left(\frac{T}{T_{\rm F}}\right)^2\right]. \tag{5.26}$$

We remark that the dependence of this result on the cutoff is only logarithmic.

Inserting our expression (4.59) for the linewidth γ,[6] we obtain to second order in $T/T_{\rm F}$

$$\delta^0 = \frac{3v_{\rm F}}{4a} j\left(\frac{\varepsilon_{\rm F}}{\hbar\omega_{\rm M}}, \frac{T}{T_{\rm F}}\right) \tag{5.27}$$

where

$$j\left(x, \frac{T}{T_{\rm F}}\right) = j_0(x) + j_2(x)\left(\frac{T}{T_{\rm F}}\right)^2, \tag{5.28}$$

with

$$j_0(x) = \frac{4\sqrt{x}}{15\pi}\left[\ln\left(\frac{8k_{\rm F}a}{3\eta x g_0(x)}\right) - \frac{\pi}{2} - \frac{4}{3}\right] \tag{5.29}$$

and

$$j_2(x) = \frac{\pi\sqrt{x}}{9}\left[\ln\left(\frac{8k_{\rm F}a}{3\eta x g_0(x)}\right) - \frac{\pi}{2} - \frac{4}{3} - \frac{12}{5\pi^2}\frac{g_2(x)}{g_0(x)}\right]. \tag{5.30}$$

The functions g_0 and g_2 are defined in (4.57) and (4.58), respectively. While the linewidth (4.59) goes as $1/a$, the frequency shift scales as $1/a$ up to a logarithmic factor. This redshift increases with temperature and adds to the redshift arising from the spill-out effect discussed in Sec. 5.1.

The importance of the shift δ^0 can be seen in Fig. 5.6. There, the position of the surface plasmon resonance peak for sodium clusters calculated from TDLDA (dots) is in qualitative agreement with our semiclassical result (solid line) taking into account the shift δ^0 and the spill-out (see Eqs. 1.7 and 5.13).[7] In Fig. 5.6, we have used $\eta =$

[6] We neglect here the oscillating component (4.69) which yields higher order corrections.

[7] We can compare the semiclassical and numerical results since both approaches are based on the many-body Hamiltonian (2.1), and thus contain the same physical ingredients.

1/2 for the frequency cutoff in (5.18). Our approximate expression for δ^0 does not permit us to obtain a quantitative agreement with the position $\omega_{\rm sp}$ of the resonance frequency shown by the dots. This is not surprising considering the approximations needed in order to derive an analytical result. First, the expression for δ^0 is based on our result (4.55) for $\Sigma^0(\omega)$ which was derived under the assumption of perfectly confined electronic states. Thus, the delocalized self-consistent single-particle states have not been treated accurately in the calculation of δ^0. Second, the cutoff introduced above is a rough estimate of the energy beyond which particle-hole excitations couple to the surface plasmon. Despite those approximations, our estimate implies an increase of the redshift beyond that caused by the spill-out (dashed line in Fig. 5.6). Comparing the two effects leading to a redshift of the surface plasmon frequency, we find that they have the same parametric size and temperature dependence, and are of the same order of magnitude. Therefore, one has to take into account both contributions in quantitative descriptions of the surface plasmon frequency.

For zero temperature, the shift δ has also been considered in Refs. 60 and 102. The authors of Ref. 60 have used the separation of the collective center-of-mass motion from the relative coordinates. Their coupling between the two subsystems which is only nonvanishing outside the nanoparticle leads to a shift that they have numerically evaluated by means of the RPA plus exchange in the case of small charged sodium clusters. In Ref. 102, the authors assumed a certain expression for the coupling, and a variational RPA calculation was used to obtain an analytical expression of the environment-induced redshift. In contrast to our findings, Refs. 60 and 102 obtained a shift δ proportional to the number of spill-out electrons.

For very small clusters (N between 8 and 92), a nonmonotonic behavior of the resonance frequency as a function of the size of the nanoparticle has been observed experimentally [25] (see Fig. 5.7). This behavior is consistent with our numerical calculations (see dots in Fig. 5.6) and can be understood in the following way. We have shown in Chapter 4 that the linewidth of the surface plasmon resonance presents oscillations as a function of the size of the nanoparticle. Furthermore, we have shown in this section that the linewidth and the environment-induced shift are related through the Kramers-Kronig transform (5.17). Thus, the shift δ should also present oscillations as a function of the size of the cluster. This is in contrast to the spill-out effect discussed in Sec. 5.1 where the oscillating character of the density of states leads to a vanishing contribution, as confirmed by the LDA calculations (see squares in Fig. 5.6). Those significantly different behaviors could allow to distinguish between the two mechanisms contributing to the redshift of the surface plasmon frequency with respect to the classical Mie value.

Using temperature-dependent TDLDA calculations, Hervieux and Bigot [67] have recently found a nonmonotonic behavior of the energy shift of the surface plasmon frequency as a function of the temperature for a given nanoparticle size (see Fig. 5.8). They observed a redshift of the surface plasmon resonance up to a certain critical temperature (e.g., 1000 K and 2500 K for Na_{138} and Na^+_{139}, respectively), followed by a blueshift of the resonance at higher temperatures. This behavior is not present in our theory. The authors of Ref. 67 attribute the nonmonotonic temperature dependence to the coupling of the surface plasmon to bulklike extended states in the continuum, which causes a

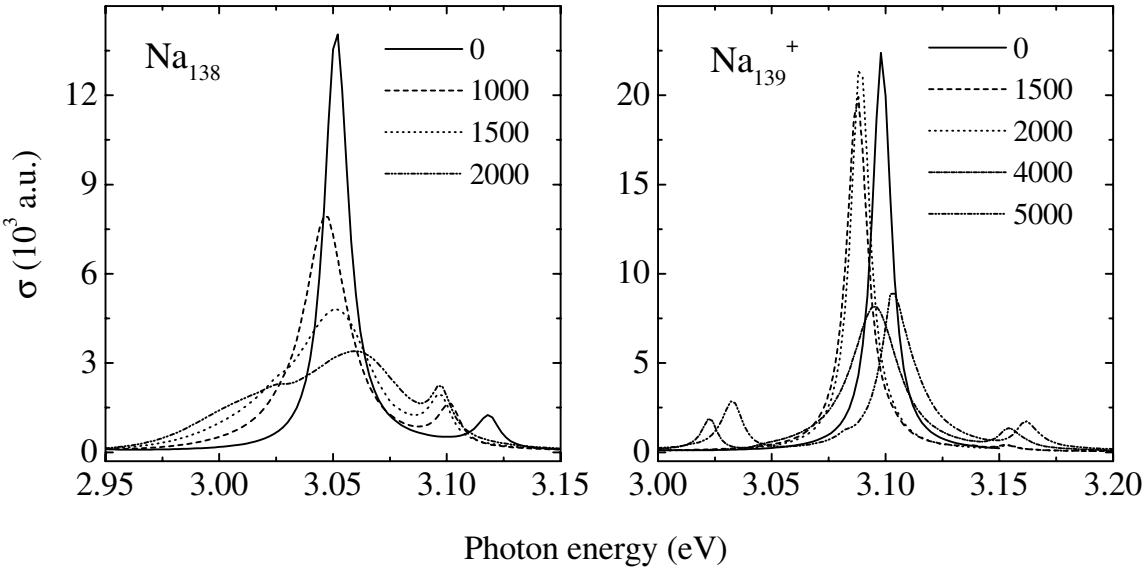

Figure 5.8: TDLDA photoabsorption cross sections (in atomic units) of Na_{138} and Na^{+}_{139} as a function of the photon energy for different values of the electronic temperature. (Reproduced from Ref. 67.)

blueshift, as one can expect for a bulk metal. However, we have restricted ourselves to low temperatures compared to the work function of the nanoparticle, where we can neglect those extended states in the evaluation of the spill-out. The critical temperature of a thousand degrees is much smaller than the Fermi temperature for metals, such that our treatment should remain a good approximation.

5.3 Conclusion for Chapter 5

In this chapter, we have focused on the surface plasmon resonance frequency. There are two effects which lead to a redshift of this frequency with respect to the classical Mie frequency: the well-known electronic spill-out and the coupling of the collective surface plasmon excitation to the electronic environment.

We have analyzed the spill-out effect arising from the electron density outside the nanoparticle. Our semiclassical analysis has led to a good agreement with local density approximation calculations. In order to achieve this, it was necessary to introduce an effective radius of the nanoparticle which accounts for the details of the self-consistent mean-field potential. The ratio of spill-out electrons over the total number as well as the resulting redshift of the surface plasmon frequency scale inversely with the size of the nanoparticle. The spill-out-induced redshift was shown, by means of a Sommerfeld expansion, to increase quadratically with the temperature.

We have demonstrated that the coupling between the electronic center of mass and the

relative coordinates results in an additional redshift of the surface plasmon frequency. This effect is of the same order as the redshift induced by the spill-out effect and presents a similar size and temperature dependence. Thus it has to be taken into account in the description of numerical and experimental results. Our semiclassical theory predicts that for the smallest sizes of nanoparticles, the environment-induced redshift should exhibit a nonmonotonic behavior as a function of the size. This is confirmed by numerical calculations. Since such oscillations do not occur in the contribution to the redshift caused by the spill-out effect, one should be able to distinguish the two effects.

Chapter 6

Time evolution of the optical transmission in a pump-probe configuration

Inutile d'employer un thermomètre de haute précision pour prendre la température d'un fantôme.

(Jean Rostand 1894-1977, in Carnet d'un biologiste)

We now discuss the experimental consequences of the temperature dependence of the Landau damping linewidth (4.59) and of the energy shifts induced by the spill-out (Eqs. 1.7 and 5.13) and by the electronic environment (5.27).

We focus on the absorption cross section defined in (1.15). Assuming it to be of the Breit-Wigner form, we have

$$\sigma(\omega, T) = s(a) \frac{\gamma(T)/2}{\left[\omega - \omega_{\mathrm{sp}}(T)\right]^2 + \left[\gamma(T)/2\right]^2}, \tag{6.1}$$

where $\omega_{\mathrm{sp}}(T)$ is the temperature-dependent resonance frequency of the surface plasmon excitation given in (3.35) and $s(a)$ is a size-dependent normalization prefactor. For the spill-out-caused redshift included in ω_{sp}, we consider the effective radius discussed in Sec. 5.1.3 which doubles the result of (5.13).

Unfortunately, to the best of our knowledge, systematic experimental investigations of the shape of the absorption cross section as a function of temperature are not available. However, an indirect approach is offered by pump-probe experiments [61–65], where the nanoparticles are excited by an intense laser pulse, i.e., the pump laser field (see Sec. 1.3). After a given time delay, the system is probed with a weak laser field, measuring the transmission $\mathcal{T}$ of the nanoparticles. After the excitation of a surface plasmon, its energy is transferred on the femtosecond timescale to the electronic environment, resulting in

the heating of the latter. On a much longer timescale of typically a picosecond, the equilibration of the electrons with the phonon heat bath results in the decrease of the temperature of the electronic system with time. Such a process is not treated in our theory.

An experimentally accessible quantity [61–65] is the differential transmission $\Delta\mathcal{T}/\mathcal{T} = (\mathcal{T}_{\rm on} - \mathcal{T}_{\rm off})/\mathcal{T}_{\rm off}$, i.e., the normalized difference of transmissions with and without the pump laser field. It is defined as $\Delta\mathcal{T}/\mathcal{T} = -\Delta\alpha L$ where $L = 2a$ is the sample thickness (here, the diameter of the nanoparticle) and $\Delta\alpha$ is the pump-induced absorption change [66]. Since the absorption coefficient α is related to the photoabsorption cross section through $\sigma = \alpha\mathcal{V}$, $\mathcal{V}$ being the volume of the nanoparticle, we have

$$\frac{\Delta\mathcal{T}}{\mathcal{T}}(\omega, T) = -\frac{3}{2\pi a^2}\left[\sigma(\omega, T) - \sigma(\omega, T_{\rm amb})\right], \tag{6.2}$$

$T_{\rm amb}$ being the ambient temperature. The relation (6.2) between transmission and absorption holds provided that the reflectivity of the sample can be neglected, which is the case in most of the experimental setups. The differential transmission can be viewed in two different ways. For a fixed time delay between the pump and the probe pulses, it is sensitive to the energy provided by the pump laser which is transferred to the electronic environment via the surface plasmon, and thus to the temperature of the heat bath. Alternatively, for a given pump intensity, increasing the time delay between the pump and the probe scans the relaxation process of the electronic system as the bath temperature decreases.

In order to obtain an estimate of the electronic temperature just after the excitation of the nanoparticle by the pump laser field, we assume that the cluster absorbs resonantly a photon of energy $E_{\rm ph} \simeq \hbar\omega_{\rm M}$. This results in an increase of the internal energy $E(T)$ of the nanoparticle compared to the ambient temperature according to $E_{\rm ph} = E(T) - E(T_{\rm amb})$. The Sommerfeld theory of metals yields for the electronic energy of a Fermi gas at a temperature $T \ll T_{\rm F}$ [9]

$$E(T) \simeq E(T=0) + \frac{\pi^2}{6}\left(k_{\rm B}T\right)^2 \varrho(\varepsilon_{\rm F}), \tag{6.3}$$

where $\varrho(\varepsilon_{\rm F})$ is the density of states at the Fermi energy $\varepsilon_{\rm F}$. Consistently with our semiclassical expansions, we take for the density of states the Weyl term (C.28), and including the spin degeneracy, we obtain

$$k_{\rm B}T \simeq \left[\frac{9E_{\rm ph}}{\pi\sqrt{\varepsilon_{\rm F}}}\left(\frac{\hbar^2}{2m_{\rm e}a^2}\right)^{3/2} + \left(k_{\rm B}T_{\rm amb}\right)^2\right]^{1/2} \tag{6.4}$$

for the initial electronic temperature just after the excitation by the pump pulse.[1]

[1] As an example, if we consider a sodium nanoparticle consisting of $N = 138$ electrons, we obtain with (6.4) an initial temperature of approximately 2400 K after the excitation by the pump laser field. This is consistent with the result of 2000 K obtained in Ref. 67 using a two-temperature model (see Fig. 3a in Ref. 67).

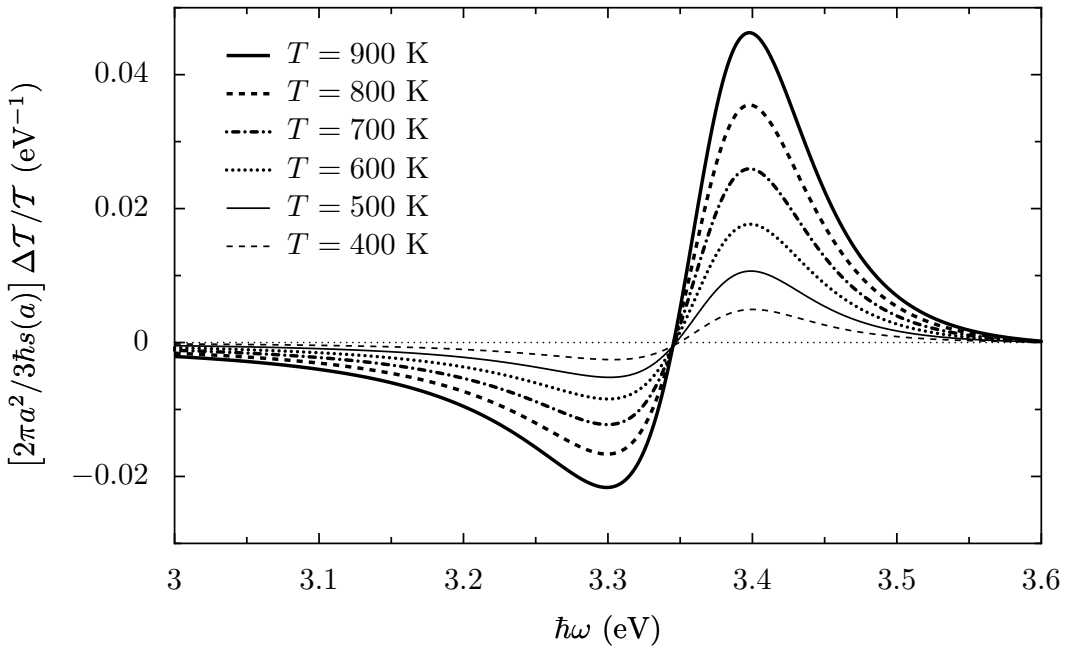

Figure 6.1: Differential transmission $\Delta\mathcal{T}/\mathcal{T}$ as a function of the probe energy $\hbar\omega$ for increasing temperatures, resulting from increasing pump intensities and a fixed delay between pump and probe (or by decreasing the time delay at a fixed pump intensity). The presented results are for a sodium nanoparticle with a radius $a = 2\,\mathrm{nm}$.

In Fig. 6.1, we present the differential transmission of (6.2) for a sodium nanoparticle of radius $a = 2\,\mathrm{nm}$, which has a strong surface plasmon resonance around $\hbar\omega_{\mathrm{sp}}(T = 300\,\mathrm{K}) \simeq 3.37\,\mathrm{eV}$ according to our semiclassical calculations. From (6.4), the resonant absorption of one photon heats the electronic system to a temperature of approximately 900 K. We see that as the temperature of the electronic system increases, $\Delta\mathcal{T}/\mathcal{T}$ becomes more and more pronounced since both, the linewidth and the redshift of the resonance frequency in (6.1) increase with temperature. Similar results are observed in experiments [61–65], where the amplitude of $\Delta\mathcal{T}/\mathcal{T}$ is observed to decrease as a function of the time delay between the pump and the probe laser fields (see Fig. 6.2). This is accompanied by the blueshift of the crossing of the differential transmission curves with the zero line as the time delay increases. This blueshift comes from the fact that, as the time delay increases, the temperature of the electronic system decreases, and thus the surface plasmon frequency is shifted to higher energies. This could explain the slowing of the relaxation process noticed in Ref. 61 when the probe frequency is in the vicinity of the surface plasmon resonance (see Fig. 1.10). Moreover, the asymmetry of $\Delta\mathcal{T}/\mathcal{T}$ is observed in the experiments (see Figs. 1.9 and 6.2) and obtained in our calculations.

Our results could provide a possibility to fit the experimental results on metallic nanoparticles excited by a pump laser field in order to extract the temperature, and thus could assist in analyzing the relaxation process. The possibility of fitting the dif-

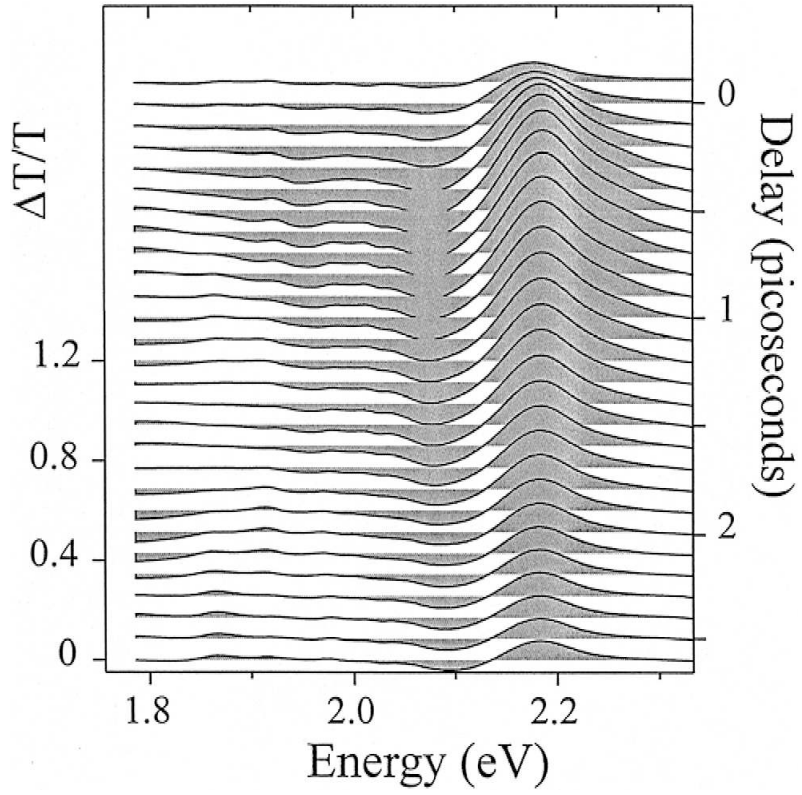

Figure 6.2: Measured differential transmission as a function of the probe energy for increasing delay times between the pump and the probe pulses for copper nanoparticles with a radius $a = 5\,\text{nm}$. (Reproduced from Ref. 63).

ferential transmission using a well-defined temperature would allow to determine the thermalization time following the pump laser excitation and the surface plasmon decay. This initial period is very difficult to describe theoretically given its nonequilibrium character.[2] In the timescale of picoseconds, the two-temperature model, in which the electrons and lattice vibrations (phonons) are considered as two interacting systems at different temperatures, can be used. From the time dependence of the electron temperature, important informations can be extracted, like the electron-phonon coupling strength [63].

[2] A useful tool to describe nonequilibrium phenomena is however Keldysh's formalism. See, e.g., Ref. 106.

Chapter 7

Double plasmon excitation and ionization in metallic clusters

> Ce qui n'est pas, c'est ce qui ne pouvait être.
>
> *(André Gide, 1869-1951, in Journal)*

In this chapter we address the lifetime of the second collective excitation level in metallic nanoparticles. This second excited level will be called "double plasmon" in the sequel. Although there is no clear direct experimental observation of a double plasmon in metallic clusters, the development of femtosecond spectroscopy will certainly allow for detailed studies in the near future. Recent experiments observed the ionization of the charged cluster Na_{93}^{+} by a femtosecond laser pulse and claimed it was a consequence of the excitation of the second plasmon state [72]. However, the analysis of the distribution of photoelectrons yielded a thermal distribution and therefore the relevance of the double plasmon for this experiment is not yet settled [73]. On the other hand, it is clear that a strong-enough laser pulse will excite the second collective state (see Appendix A). Such an excitation will be a well-defined resonance only if its linewidth is small compared with other scales of the photoabsorption spectrum (like for instance ω_{M}).

Second collective excitations have been widely analyzed in the context of giant dipolar resonances in nuclei [6,7,107,108]. The anharmonicities were found to be relatively small, making it possible to observe this resonance [109]. The theoretical tools developed in nuclear physics have been adapted to the study of the double plasmon in metallic clusters [110, 111]. In particular, a variational approach [111] showed that the difference between the energy of the double plasmon and $2\hbar\omega_{\mathrm{M}}$ decreases as $N^{-4/3}$ with the size of the nanoparticle. In our calculations, we will assume that the double-plasmon energy is exactly twice the Mie energy.

For most of the clusters of experimental interest, $2\hbar\omega_{\mathrm{M}} > W > \hbar\omega_{\mathrm{M}}$, where W is the work function. Ionization then appears as an additional decay channel of the double plasmon that adds to the Landau damping, while it is not possible if only the single

plasmon is excited.[1]

In the remaining of this chapter, we will neglect the spill-out effect that redshifts the frequency of the surface plasmon from the classical Mie value according to (1.7). As it was previously the case for instance in our derivation of the single surface plasmon linewidth in Chapter 4, the spill-out correction to the Mie frequency yields higher-order terms for the double plasmon linewidth that we can neglect consistently with our semiclassical expansions. Thus, we will approximate $\tilde{\omega}_{\rm M}$ by $\omega_{\rm M}$. Furthermore, we will restrict ourselves to zero temperature.

7.1 Second plasmon decay: Landau damping

In this section, we consider processes which do not lead to ionization, that is, the final particle energies verify $\varepsilon_p < V_0 = \varepsilon_{\rm F} + W$. A sufficiently strong laser excitation gives rise to a non-negligible occupation probability of the second harmonic oscillator state $|2\rangle$ (see Appendix A). The second plasmon state can then decay by two distinct Landau damping processes (see the sketch of Fig. 7.1). A first-order process, with a rate $\gamma_{2\to 1}$, results from the transition of $|2\rangle$ (double plasmon) into $|1\rangle$ (single plasmon). The corresponding matrix element of the perturbation $H_{\rm c}$ between these two states is a factor of $\sqrt{2}$ larger than the one worked out in Chapter 4, and then $\gamma_{2\to 1} = 2\gamma$ [where γ is the single-plasmon linewidth given by (4.2) and calculated under certain approximations in Chapter 4]. Thus, the contribution of the first-order process to the linewidth is just twice the value found for the single plasmon, and shows the same nonmonotonic features superposed to a $1/a$ size-dependence.

The other mechanism one has to take into account is the second-order process, where the double plasmon decays directly into the center-of-mass ground state. It is shown by the dashed arrow in Fig. 7.1. This is possible provided that $V_0 > 2\hbar\omega_{\rm M}$. In order to simplify the calculation we assume, for the remainder of this section, that $V_0 \to \infty$. At zero temperature, the corresponding linewidth $\gamma_{2\to 0}$ is given by the Fermi golden rule in second order perturbation theory (see Appendix D, Eq. D.9, and Ref. 71):

$$\gamma_{2\to 0} = \frac{2\pi}{\hbar} \sum_{F_{\rm rel}} \left| \sum_{F'_{\rm rel}} \frac{\langle 0, F_{\rm rel}|H_{\rm c}|1, F'_{\rm rel}\rangle\langle 1, F'_{\rm rel}|H_{\rm c}|2, I_{\rm rel}\rangle}{\hbar\omega_{\rm M} + \varepsilon_{I_{\rm rel}} - \varepsilon_{F'_{\rm rel}}} \right|^2 \delta(2\hbar\omega_{\rm M} + \varepsilon_{I_{\rm rel}} - \varepsilon_{F_{\rm rel}}). \quad (7.1)$$

Here we have used the same notations as in Sec. 3.1.1. Making explicit the perturbation $H_{\rm c}$ of (2.35) and restricting ourselves to the random phase approximation which allows only one particle-one hole transitions [54], we obtain at zero temperature

$$\gamma_{2\to 0} = \frac{4\pi}{\hbar} \sum_{ph} |K_{ph}|^2 \, \delta(2\hbar\omega_{\rm M} - \varepsilon_p + \varepsilon_h), \quad (7.2)$$

with

$$K_{ph} = \Lambda^2 \sum_{i\neq p,h} \frac{d_{pi} d_{ih}}{\hbar\omega_{\rm M} - \varepsilon_i + \varepsilon_h}. \quad (7.3)$$

[1] However, for $\hbar\omega_{\rm M} > W$, the ionization through a single-plasmon process is a relevant channel [112].

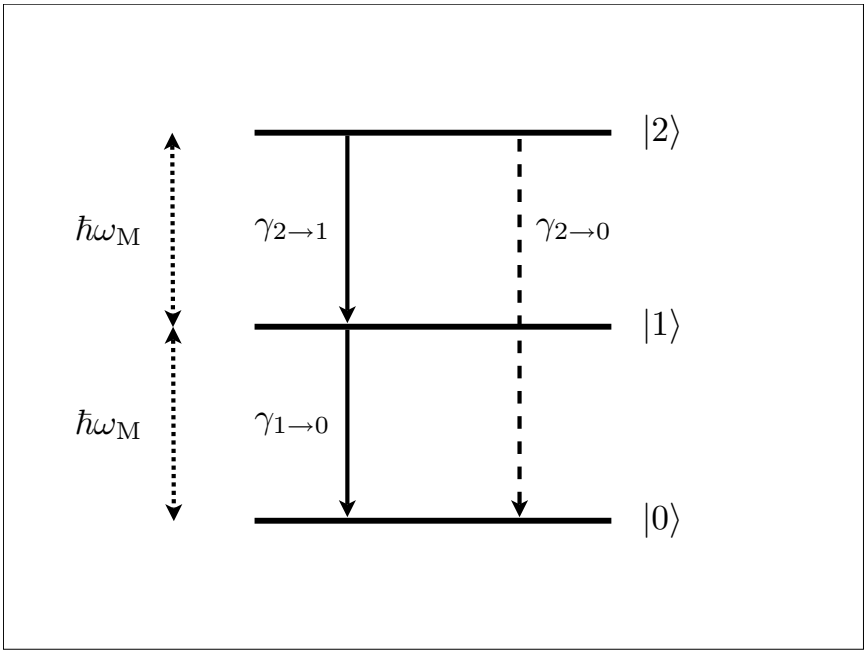

Figure 7.1: Sketch of the decay of the double plasmon state. The first-order decay mechanisms are indicated by solid arrows (rates $\gamma_{2\to1}$ and $\gamma_{1\to0}$), while the second-order process is shown by a dashed arrow (rate $\gamma_{2\to0}$).

In (7.2) and (7.3), p and h denote particle and hole states, respectively. The sum over i in (7.3) runs over all the virtual intermediate states. We use the same notations as in Chapter 4 and replace the sums over particle and hole states by integrals over the energy with the appropriate density of states, which is approximated by its semiclassical counterpart (4.35).

As in the case of the single plasmon, we work in the limit $l_p \gg 1$ in order to find the smooth size-dependent contribution $\gamma^0_{2\to0}$ (and the corresponding K^0_{ph}). Using the expression of the matrix elements $d_{\alpha\beta}$ (see Eqs. 4.8, 4.10 and 4.27), the dipole selection rules, and the smooth part of the semiclassical density of states (4.36), we have

$$K^0_{ph} = 9\left(\frac{\hbar\omega_{\mathrm{M}}}{\varepsilon_{\mathrm{F}}}\right)^3 (k_{\mathrm{F}}a)^3 \sqrt{\varepsilon_p\varepsilon_h}\delta_{m_pm_h}\Big[\mathcal{A}^{m_pm_p}_{l_pl_p+1}\mathcal{A}^{m_pm_p}_{l_p+1l_h} I_{l_p+1}(\eta_p,\eta_h)(\delta_{l_hl_p}+\delta_{l_h,l_p+2}) \\ +\mathcal{A}^{m_pm_p}_{l_pl_p-1}\mathcal{A}^{m_pm_p}_{l_p-1l_h} I_{l_p-1}(\eta_p,\eta_h)(\delta_{l_hl_p}+\delta_{l_h,l_p-2})\Big]. \tag{7.4}$$

Here, we have defined the integral

$$I_{l_i}(\eta_p,\eta_h) = \int_{l_i+1/2}^{\infty} \mathrm{d}\eta_i \frac{\eta_i\sqrt{\eta_i^2-(l_i+1/2)^2}}{(\xi\eta_{\mathrm{F}}^2-\eta_i^2+\eta_h^2)\left[(\eta_i^2-\eta_p^2)(\eta_i^2-{\eta_h}^2)\right]^2} \tag{7.5}$$

with $\eta = ka$, $\eta_{\rm F} = k_{\rm F}a$, and $\xi = \hbar\omega_{\rm M}/\varepsilon_{\rm F}$.

By inserting the semiclassical oscillating density of states (4.37) in the expression of K_{ph} (7.3), we obtain a negligible contribution $K_{ph}^{\rm osc}$ since one has to integrate smooth energy-dependent functions multiplied by the oscillating density of states $\varrho_{l_i}^{\rm osc}(\varepsilon_i)$ of the intermediate states in the well.

Inserting (7.4) into expression (7.2), replacing the sum over l_p by an integral, we find

$$\gamma_{2\to 0}^{0} = \frac{324}{5\pi\hbar}\left(\frac{\hbar\omega_{\rm M}}{\varepsilon_{\rm F}}\right)^{6}\varepsilon_{\rm F}\,(k_{\rm F}a)^{4}\int_{\eta_{\rm F}\max(1,\sqrt{2\xi})}^{\eta_{\rm F}\sqrt{1+2\xi}}\mathrm{d}\eta_p\;\eta_p \times\int_{0}^{\eta_h}\mathrm{d}l_p\;2l_p\sqrt{\eta_p^2-l_p^2}\sqrt{{\eta_h}^2-l_p^2}\left[I_{l_p}(\eta_p,\eta_h)\right]^2, \tag{7.6}$$

where a factor of 2 accounts for the spin degeneracy. We have introduced $\eta_h = (\eta_p^2 - 2\eta_{\rm F}^2\xi)^{1/2}$. With the change of variables $z = \eta_p^2/\eta_{\rm F}^2$, $y = l_p^2/\eta_{\rm F}^2$, and $x = \eta_i^2/\eta_{\rm F}^2$, we obtain

$$\gamma_{2\to 0}^{0} = \frac{81}{10\pi\hbar}\left(\frac{\hbar\omega_{\rm M}}{\varepsilon_{\rm F}}\right)^{6}\frac{\varepsilon_{\rm F}}{(k_{\rm F}a)^{4}}\int_{\max(1,2\xi)}^{1+2\xi}\mathrm{d}z\int_{0}^{z-2\xi}\mathrm{d}y\sqrt{z-y}\sqrt{z-y-2\xi}\,J^2(y,z,\xi), \tag{7.7}$$

with

$$J(y,z,\xi) = \int_{y}^{\infty}\mathrm{d}x\frac{\sqrt{x-y}}{(x+\xi-z)\left[(x-z)(x-z+2\xi)\right]^2}. \tag{7.8}$$

The integral J possesses three singularities. This comes from the fact that, to evaluate K_{ph}, we have approximated the discrete sum over intermediate states i by an integral over the energy ε_i. However, in (7.3), i must be different from a particle (p) or a hole (h) state. The divergences occurs for

$$x = z-\xi \;\Leftrightarrow\; \varepsilon_i = \varepsilon_p - \hbar\omega_{\rm M}, \tag{7.9a}$$

$$x = z \;\Leftrightarrow\; \varepsilon_i = \varepsilon_p, \tag{7.9b}$$

$$x = z-2\xi \;\Leftrightarrow\; \varepsilon_i = \varepsilon_h. \tag{7.9c}$$

The function J is therefore dominated by those divergences. Changing the variable x to $x' = x - z + \xi$, we obtain by expanding the integral around the three singularities

$$J(y,z,\xi) \approx \frac{1}{4\xi^3}\left[\sqrt{z-y}\int_{-\infty}^{+\infty}\mathrm{d}x'\frac{1}{(x'-\xi)^2} - \sqrt{z-y-2\xi}\int_{-\infty}^{+\infty}\mathrm{d}x'\frac{1}{(x'+\xi)^2}\right], \tag{7.10}$$

which can be rewritten, introducing the appropriate cutoffs α_ξ and $\alpha_{-\xi}$, as

$$\begin{aligned} J(y,z,\xi) &= \frac{1}{2\xi^3}\left[\sqrt{z-y}\int_{\alpha_\xi/2}^{+\infty}\frac{\mathrm{d}\alpha}{\alpha^2} - \sqrt{z-y-2\xi}\int_{\alpha_{-\xi}/2}^{+\infty}\frac{\mathrm{d}\alpha}{\alpha^2}\right] \\ &= \frac{1}{\xi^3}\left(\frac{\sqrt{z-y}}{\alpha_\xi} - \frac{\sqrt{z-y-2\xi}}{\alpha_{-\xi}}\right). \end{aligned} \tag{7.11}$$

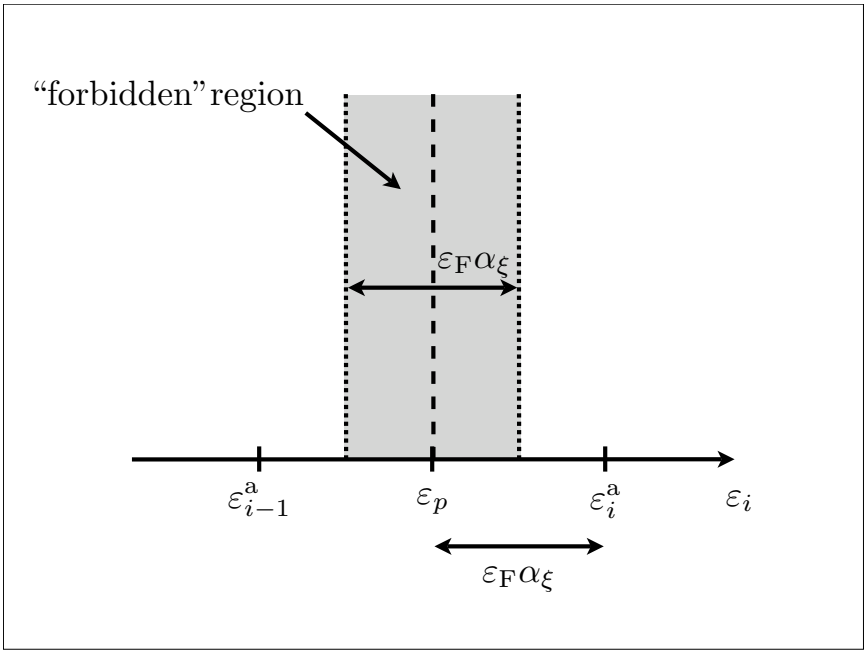

Figure 7.2: Sketch of the region of integration over the intermediate state of energy ε_i. The width of the forbidden region (shown in gray) is taken as the mean level spacing in the system. ε_i^a is the energy of the quantum level just above $\varepsilon_i = \varepsilon_p$ which determines the cutoff α_ξ.

Let us now detail the estimation of the cutoff α_ξ at $\varepsilon_i = \varepsilon_p$: With our notations, it is given by

$$\alpha_\xi = \frac{\varepsilon_i^{\mathrm{a}} - \varepsilon_p}{\varepsilon_{\mathrm{F}}} \tag{7.12}$$

where $\varepsilon_i^{\mathrm{a}}$ is the allowed energy of the (discrete) state i just after the divergence point for which $\varepsilon_i = \varepsilon_p$ (see Fig. 7.2). Using the semiclassical quantization in the infinite spherical well[2]

$$ka = \frac{l\pi}{2} + n\pi \tag{7.13}$$

with n a positive integer, we obtain

$$\alpha_\xi = \frac{1}{(k_{\mathrm{F}}a)^2}\left[\frac{(l_i^{\mathrm{a}} - l_p)\,\pi}{2} + (n_i^{\mathrm{a}} - n_p)\pi\right]\left[\frac{(l_i^{\mathrm{a}} + l_p)\,\pi}{2} + (n_i^{\mathrm{a}} + n_p)\pi\right]. \tag{7.14}$$

Now, the dipole selection rules dictate that $l_i^{\mathrm{a}} = l_p \pm 1$. If $l_i^{\mathrm{a}} = l_p + 1$ ($l_i^{\mathrm{a}} = l_p - 1$), the next allowed quantum level just after the state p has $n_i^{\mathrm{a}} = n_p$ ($n_i^{\mathrm{a}} = n_p + 1$). Thus, in

[2]It is obtained by expanding the spherical Bessel function $j_l(ka)$ for $ka \gg 1$.

the limit $k_{\mathrm{F}}a \gg 1$, we finally obtain

$$\alpha_{\xi} = \frac{\pi\sqrt{z}}{k_{\mathrm{F}}a}. \tag{7.15}$$

A similar calculation yields the cutoff

$$\alpha_{-\xi} = \frac{\pi\sqrt{z-2\xi}}{k_{\mathrm{F}}a} \tag{7.16}$$

for the divergence at $\varepsilon_i = \varepsilon_h$. Thus, we get for (7.11)

$$J(y,z,\xi) \simeq \frac{k_{\mathrm{F}}a}{\pi\xi^3}\left(\sqrt{\frac{z-y}{z}} - \sqrt{\frac{z-y-2\xi}{z-2\xi}}\right). \tag{7.17}$$

With this result, we finally obtain for the Landau damping rate of the second-order decay process (7.7)

$$\gamma^0_{2\to 0} \simeq \frac{81}{10\pi^3\hbar}\frac{\varepsilon_{\mathrm{F}}}{(k_{\mathrm{F}}a)^2}h\left(\frac{\hbar\omega_{\mathrm{M}}}{\varepsilon_{\mathrm{F}}}\right), \tag{7.18}$$

where the function h of the parameter $\xi = \hbar\omega_{\mathrm{M}}/\varepsilon_{\mathrm{F}}$ is defined as

$$h(\xi) = \int_{\max(1,2\xi)}^{1+2\xi} \mathrm{d}z \int_0^{z-2\xi} \mathrm{d}y \sqrt{z-y}\sqrt{z-y-2\xi}\left(\sqrt{\frac{z-y}{z}} - \sqrt{\frac{z-y-2\xi}{z-2\xi}}\right)^2. \tag{7.19}$$

When the remaining two-dimensional integral is evaluated numerically we obtain an increasing function of the parameter ξ, with $h(0) = 0$ as shown in Fig. 7.3. This function has the asymptotic limit $\lim_{\xi\gg 1} h(\xi) = \infty$. We see that when the double-plasmon state is too high in energy, the linewidth diverges to infinity and this resonance is no longer well-defined (the double-plasmon state has a lifetime equal to zero in this condition).

The total linewidth of the Landau damped second plasmon is the sum of the first- and second-order processes: $\gamma_{\mathrm{dp}} = \gamma_{2\to 1} + \gamma_{2\to 0}$ (see Fig. 7.1). The different (smooth) size dependence of both processes [v_{F}/a for the former and $(k_{\mathrm{F}}a)^{-1}v_{\mathrm{F}}/a$ for the latter] implies that, except for the smallest clusters, the second-order process gives a negligible contribution to the linewidth of the double plasmon (in comparison with that of the first order). We might ask the question of whether the inclusion of the oscillating components of both linewidths can affect the above conclusion in this range of particle sizes. An extension of the calculations presented in Chapter 4 shows that the oscillating part of the second-order channel of the double plasmon is given by

$$\gamma^{\mathrm{osc}}_{2\to 0} \sim \frac{\varepsilon_{\mathrm{F}}}{\hbar(k_{\mathrm{F}}a)^{11/2}}\cos(2k_{\mathrm{F}}a). \tag{7.20}$$

As indicated before, $\gamma^{\mathrm{osc}}_{2\to 1}$ is given by twice the result of (4.69), therefore these nonmonotonic contributions cannot lead to a significant modification of our conclusion about the irrelevance of the second-order term for the sizes of physical interest. We also notice

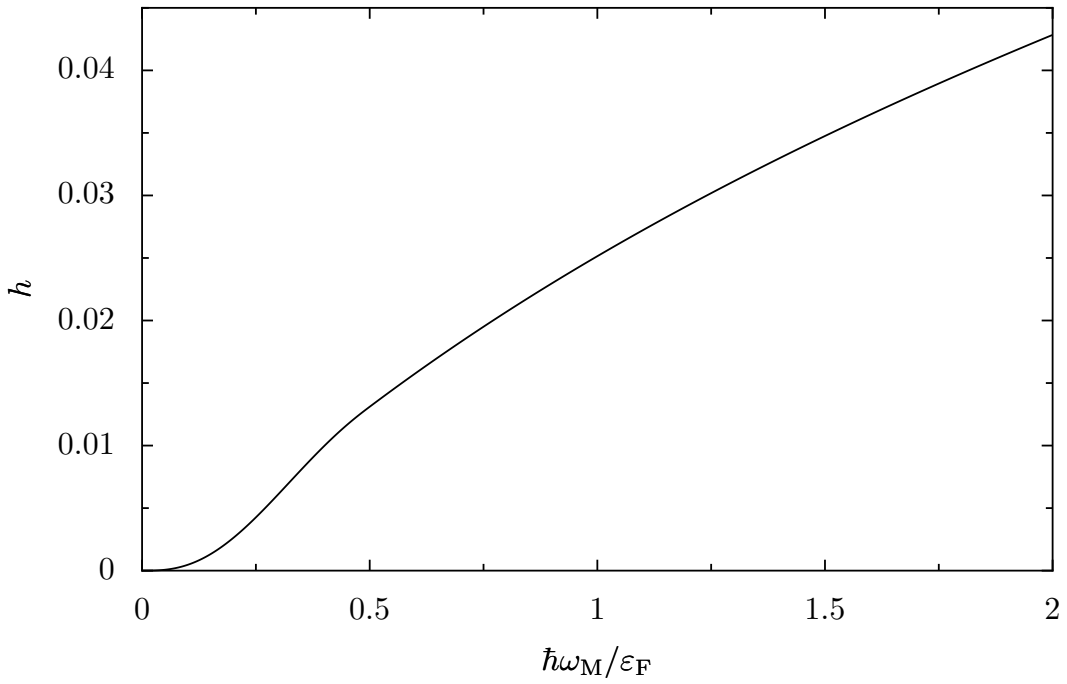

Figure 7.3: Frequency dependence of the double-plasmon Landau damping rate, given by the function h of $\hbar\omega_{\mathrm{M}}/\varepsilon_{\mathrm{F}}$.

that $\gamma_{\mathrm{dp}} \ll \omega_{\mathrm{M}}$, since for typical nanoparticles, $\varepsilon_{\mathrm{F}} \sim \hbar\omega_{\mathrm{M}}$ and $k_{\mathrm{F}}a \gg 1$. Therefore, the Landau damping is not capable of ruling out the second plasmon as a well-defined resonance.

The lifetime of the second plasmon for the Landau damping processes is simply $\gamma_{\mathrm{dp}}^{-1}$. To determine the time it takes for the doubly excited state of the center-of-mass system to return to its ground state, we also have to take into account the decay of the first plasmon into the ground-state $\gamma_{1\to 0}$. If we assume that the recombination of particle-hole pairs (created by the decay of the double plasmon into the single plasmon) is very fast as compared to other timescales, we have $\gamma_{1\to 0} = \gamma$. Due to the fact that lifetimes are additive, we have for this sequential decay a lifetime $\tau_{2\to 1\to 0} = 3/2\gamma$.

7.2 Second plasmon decay and ionization

We now examine the last decay channel of the second plasmon state: the relaxation of this collective excitation by ejecting an electron from the nanoparticle (ionization, see Fig. 7.4). We now need to determine the particle and hole states in the self-consistent field $V(r) = V_0\Theta(r-a)$ which has a finite height V_0, since the ionization process requires an appropriate treatment of the states of the continuum. For simplicity, we will neglect the Coulomb tail seen for $r > a$ by electrons with an energy $\varepsilon_p > V_0$.

In order to determine the particle and hole states, we close the system into a spherical

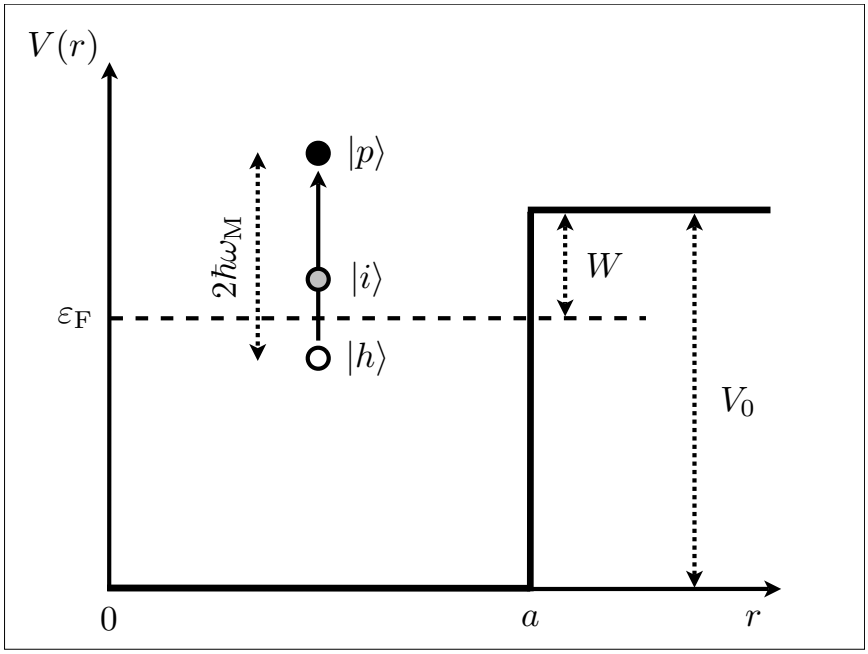

Figure 7.4: Scheme of the ionization process of the double-plasmon state which decays by creating a particle-hole pair of energy $2\hbar\omega_{\mathrm{M}}$, via the intermediate state $|i\rangle$. Since the energy of the particle is such that $\varepsilon_p > V_0$, ionization occurs.

box of radius $L \gg a$ to quantize the states above the well and take the limit of $L \to \infty$ at the end of our calculations. Obviously we need to do some approximations in order to simplify this difficult problem. First, in the high energy limit, we assume that $kr \gg 1$, and then use the asymptotic expansions of the quantum mechanical single-particle states inside and outside the well. Even though this approximation strongly affects the wave functions near $r = 0$, its impact on the dipole matrix elements is very small.[3] Second, for the states with energy $\varepsilon < V_0$, we neglect the exponential decay of the wave function for $r > a$. Finally, in the spirit of the scattering theory, we use a simplified expression for the normalization of the free states above the well. The above assumptions result in the following radial wave functions inside the well ($\varepsilon < V_0$)

$$u_{\varepsilon l}^{<}(r) \simeq \begin{cases} \sqrt{\dfrac{2}{a}} \sin\left(kr - l\pi/2\right), & r \leqslant a, \\ 0, & r > a. \end{cases} \tag{7.21}$$

The wavevector $k = \sqrt{2m_{\mathrm{e}}\varepsilon}/\hbar$ is given by the quantization condition $ka = l\pi/2 + n\pi$,

[3] As a test of consistency, we checked that this approximation leads in the case of the single plasmon to a linewidth at $T = 0$ given by (4.59) for $\hbar\omega_{\mathrm{M}}/\varepsilon_{\mathrm{F}} = 0$. For $\hbar\omega_{\mathrm{M}}/\varepsilon_{\mathrm{F}} \neq 0$, we obtain a slightly different frequency-dependence, but with the same decreasing features.

with n a non-negative integer. For energies $\varepsilon > V_0$, we have

$$u^{>}_{\varepsilon l}(r) \simeq \sqrt{\frac{2}{L}} \begin{cases} \alpha_l(k) A(k) \sin(kr - l\pi/2), & r \leqslant a, \\ \sin[\kappa(r-L)], & r > a, \end{cases} \tag{7.22}$$

with $\kappa = \sqrt{k^2 - 2m_e V_0/\hbar^2}$. We have introduced the notations

$$\alpha_l(k) = \text{sign}\left\{ \frac{\sin[\kappa(a-L)]}{\sin(ka - l\pi/2)} \right\}, \tag{7.23}$$

$$A(k) = \sqrt{\sin^2[\kappa(a-L)] + \left(\frac{\kappa}{k}\right)^2 \cos^2[\kappa(a-L)]}. \tag{7.24}$$

The ionization rate of the double-plasmon state γ_{ion} is given by (7.2) in the case where the final particle states p of the sum are in the continuum. Since the effective (second-order) matrix element K_{ph} (7.3) is given by a sum over intermediate states $|i\rangle$, we now have contributions from cases where the energy of $|i\rangle$ lies either in the well or in the continuum.

When i represents a state in the well, using the angular momentum selection rules, we can write in the limit $kr \gg 1$ the radial part of the matrix elements (4.8) as

$$\mathcal{R}_{l_i l_h}(\varepsilon_i, \varepsilon_h) = \frac{(-1)^{n_i - n_h}}{\Delta k_{ih}^2 a} \delta_{l_i, l_h \pm 1}, \tag{7.25}$$

and

$$\mathcal{R}_{l_p l_i}(\varepsilon_p, \varepsilon_i) = \pm \sqrt{\frac{a}{L}} \frac{\alpha_{l_p}(k_p) A(k_p)}{\Delta k_{pi}} \left[\cos(\Delta k_{pi} a) - \frac{\sin(\Delta k_{pi} a)}{\Delta k_{pi} a} \right] \delta_{l_i, l_p \pm 1}, \tag{7.26}$$

where $\Delta k_{\alpha\beta} = k_\alpha - k_\beta$ $(\alpha, \beta = p, h, i)$.

When i represents a state in the continuum, $\mathcal{R}_{l_i l_h}(\varepsilon_i, \varepsilon_h)$ can be obtained by exchanging $(p \leftrightarrow i)$ and $(i \leftrightarrow h)$ in (7.26). For the remaining case, we have

$$\begin{aligned} \mathcal{R}_{l_p l_i}(\varepsilon_p, \varepsilon_i) = {} & \frac{a}{L} \frac{\alpha_{l_p}(k_p) \alpha_{l_p+1}(k_i) A(k_p) A(k_i)}{\Delta k_{pi}} \left[\cos(\Delta k_{pi} a) - \frac{\sin(\Delta k_{pi} a)}{\Delta k_{pi} a} \right] \delta_{l_i, l_p \pm 1} \\ & + B(k_p, k_i) \delta_{l_i, l_p \pm 1}, \end{aligned} \tag{7.27}$$

where

$$\begin{aligned} B(k_p, k_i) = \frac{a^2}{L} \Big\{ & \cos(\Delta\kappa_{pi} L) - \sin(\Delta\kappa_{pi} L) \text{ci}(|\Delta\kappa_{pi}| a) \\ & + \Delta\kappa_{pi} a \big[\cos(\Delta\kappa_{pi} L) \text{sign}(\Delta\kappa_{pi}) \text{si}(|\Delta\kappa_{pi}| a) \big] \Big\}, \end{aligned} \tag{7.28}$$

with $\text{si}(x)$ and $\text{ci}(x)$ the sine and cosine integral functions [113].

The semiclassical l-fixed smooth density of states can be approximated by

$$\varrho_l^0(\varepsilon) \simeq \frac{1}{2\pi\varepsilon_0} \begin{cases} \dfrac{\sqrt{(ka)^2-(l+1/2)^2}}{(ka)^2}, & \varepsilon < V_0, \\ \dfrac{\sqrt{(\kappa L)^2-(l+1/2)^2}}{(\kappa a)^2}, & \varepsilon > V_0, \end{cases} \tag{7.29}$$

with $\varepsilon_0 = \hbar^2/2m_{\rm e}a^2$.

There is an obvious divergence that occurs in the sum of (7.3) for $\varepsilon_i = \varepsilon_h$, as it can be seen on the matrix element (7.25). However, a careful analysis shows that the contribution around that divergence vanishes because of the alternating sign when one integrates over n_i. For $\varepsilon_i = \varepsilon_p$, there is no divergence in (7.27). Therefore the dominant contribution to K_{ph} is given by the divergence of the term $1/(\hbar\omega_{\rm M} - \varepsilon_i + \varepsilon_h)$ that occurs for $\varepsilon_i < V_0$ in the regime we are interested in ($\hbar\omega_{\rm M} < W < 2\hbar\omega_{\rm M}$). We then have for the ionization rate

$$\gamma_{\rm ion} \simeq 2\Lambda^4 \frac{4\pi}{\hbar} \sum_{\substack{p>V_0 \\ h<\varepsilon_{\rm F}}} \sum_{i,j<V_0} \frac{d_{pi}d_{ih}}{\hbar\omega_{\rm M} - \varepsilon_i + \varepsilon_h} \frac{d_{pj}d_{jh}}{\hbar\omega_{\rm M} - \varepsilon_j + \varepsilon_h} \delta(2\hbar\omega_{\rm M} - \varepsilon_p + \varepsilon_h), \tag{7.30}$$

where the factor of 2 accounts for the two spin channels and the $d_{\alpha\beta}$ are given by (4.8) with the approximations (7.25) and (7.26) for the radial matrix elements. Furthermore, we can distinguish in the above equation two contributions: off-diagonal terms ($i \neq j$) which have divergences of the principal value type and that we neglect here, and diagonal terms ($i = j$) yielding divergences which determine $\gamma_{\rm ion}$. We smooth out the energy ε_i appearing in the denominator by introducing an imaginary part of the order of the mean level-spacing

$$\Delta = \frac{3\pi\varepsilon_0^{3/2}}{\sqrt{\hbar\omega_{\rm M} + \varepsilon_h}} \tag{7.31}$$

at an energy $\hbar\omega_{\rm M} + \varepsilon_h$. Δ is just the inverse of the Weyl density of states taken at the above-mentioned energy. This standard procedure of smoothing the divergences is of critical importance, and that is why in Ref. 71 the final result is presented as a function of Δ. Summing over l_i and m_i, the remaining sum over the radial quantum numbers n_i can be done in the following way. Defining

$$X = \sum_{n_i} \frac{1}{\left(\hbar\omega_{\rm M} - \varepsilon_i + \varepsilon_h\right)^2} \tag{7.32}$$

and

$$x = \frac{\hbar\omega_{\rm M} + \varepsilon_h}{\pi^2\varepsilon_0}, \tag{7.33}$$

and using the quantization

$$\varepsilon_i = \varepsilon_0 \left(\frac{l_i\pi}{2} + n_i\pi\right)^2, \tag{7.34}$$

we have

$$X = \frac{1}{\pi^4 \varepsilon_0^2} \sum_{n_i} \frac{1}{\left[(n_i - n_i^-)(n_i - n_i^+)\right]^2}. \tag{7.35}$$

In the above equation, we have defined $n_i^+ = -l_i/2 + \sqrt{x}$ and $n_i^- = -l_i/2 - \sqrt{x}$. Since n_i has to be positive, $n_i^- < 0$ cannot be a singularity. Thus we have

$$X \approx \frac{1}{\pi^4 \varepsilon_0^2} \frac{1}{(n_i^+ - n_i^-)^2} \sum_{n_i} \frac{1}{(n_i - n_i^+)^2}. \tag{7.36}$$

Now, using the definitions of $n_i^\pm$ and x, replacing the sum over n_i by an integral and introducing the imaginary part Δ, we obtain

$$X \approx \frac{1}{4\pi^2 \varepsilon_0} \frac{1}{\hbar\omega_\mathrm{M} + \varepsilon_h} \int_{-\infty}^{+\infty} \frac{\mathrm{d}y}{(y - n_i^+ - \mathrm{i}\bar{\Delta})(y - n_i^+ + \mathrm{i}\bar{\Delta})}, \tag{7.37}$$

with $\bar{\Delta} = \Delta/\pi^2\varepsilon_0$. Performing the remaining integral in the complex plane, we finally obtain

$$\sum_{n_i} \frac{1}{\left|\hbar\omega_\mathrm{M} - \varepsilon_i + \varepsilon_h + \mathrm{i}\Delta\right|^2} \approx \frac{\pi}{4\Delta} \frac{1}{\hbar\omega_\mathrm{M} + \varepsilon_h}. \tag{7.38}$$

Inserting the result (7.38) into (7.30), we arrive at

$$\gamma_\mathrm{ion} \simeq \frac{\pi^2 a (\hbar\omega_\mathrm{M})^6 \varepsilon_0}{120 \hbar N^2 L} \sum_{l_p} l_p \int_{\max(V_0, 2\hbar\omega_\mathrm{M})}^{\varepsilon_\mathrm{F} + 2\hbar\omega_\mathrm{M}} \mathrm{d}\varepsilon_p \frac{\varrho_{l_p}^0(\varepsilon_p)\varrho_{l_p}^0(\varepsilon_h)}{\Delta} \times \frac{[A(k_p)]^2}{(\hbar\omega_\mathrm{M} + \varepsilon_h)(\sqrt{\hbar\omega_\mathrm{M} + \varepsilon_h} - \sqrt{\varepsilon_h})^4 (\sqrt{\varepsilon_p} - \sqrt{\hbar\omega_\mathrm{M} + \varepsilon_h})^2}, \tag{7.39}$$

with $\varepsilon_h = \varepsilon_p - 2\hbar\omega_\mathrm{M}$.

Taking the limit of $L \to \infty$, we finally obtain

$$\gamma_\mathrm{ion} \simeq \frac{3\pi}{160} \frac{v_\mathrm{F}}{a} q(\xi, \zeta), \tag{7.40}$$

where $\xi = \hbar\omega_\mathrm{M}/\varepsilon_\mathrm{F}$ and $\zeta = W/\varepsilon_\mathrm{F}$. The function q of the two variables ξ and ζ is defined as

$$q(\xi, \zeta) = \left(\frac{\xi}{2}\right)^6 \int_{\max(2\xi, 1+\zeta)}^{1+2\xi} \mathrm{d}z \frac{(2z - 1 - \zeta)\sqrt{z - 2\xi}}{z\sqrt{(z - \xi)(z - 1 - \zeta)}} \times \frac{1}{(\sqrt{z - \xi} - \sqrt{z - 2\xi})^4 (\sqrt{z} - \sqrt{z - \xi})^2}. \tag{7.41}$$

Since our approach is valid when $\hbar\omega_\mathrm{M} \leqslant W \leqslant 2\hbar\omega_\mathrm{M}$, the function $q(\xi, \zeta)$ is defined for $\xi \leqslant \zeta \leqslant 2\xi$. It can be integrated numerically. The result is shown in Fig. 7.5. The function $q(\xi, \zeta)$ is not very sensitive to the value of $\zeta/\xi = W/\hbar\omega_\mathrm{M}$ in the presented

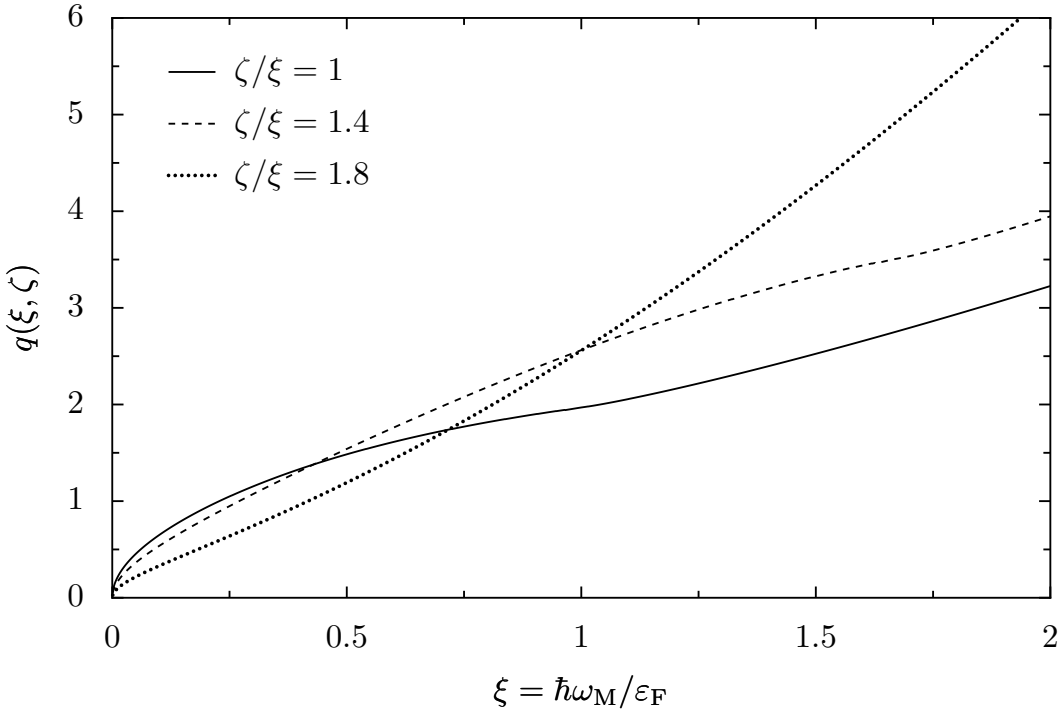

Figure 7.5: Function $q(\xi, \zeta)$ from (7.41). It is represented as a function of ξ for different values of ζ/ξ, with $\zeta = W/\varepsilon_{\rm F}$.

interval. However, it vanishes at the upper limit $W = 2\hbar\omega_{\rm M}$, since in this case particle states cannot be in the continuum and $\gamma_{\rm ion} = 0$.

The size scaling of $\gamma_{\rm ion}$ is mainly given by a $1/a$-dependence of the prefactor (Fig. 7.6), despite the fact that the work function W appearing in the parameter ζ is size dependent and scales (for a neutral cluster) as [103] $W = W_\infty + 3e^2/8a$ where W_∞ is the work function of the bulk material.

Using the work function $W = 4.65\,\text{eV}$ and the experimental value of $\hbar\omega_{\rm M} = 2.75\,\text{eV}$ for the charged Na_{93}^+ clusters of Refs. 72 and 73, Eq. 7.40 yields $\hbar\gamma_{\rm ion} \simeq 0.1\,\text{eV}$, which corresponds to an ionization lifetime of the second plasmon of 6.6 fs. This value is of the same order of magnitude as the experimentally reported lifetime of 10 fs. It is also in rough agreement with the estimation yielded by the numerical calculations of Ref. 71 based on a separable residual interaction (10 to 20 fs). Therefore, despite the approximations we have been forced to make in our analytical calculations, we believe that we kept the essential ingredients of this complicated problem. The lifetimes obtained by the different procedures consistently establish the second plasmon as a well-defined resonance in metallic clusters, at least in charged ones where the work function is larger than for the case of neutral nanoparticles. While the numerical calculations of Ref. 71 have been performed for just one size, our results exhibit a clear size dependence that can be tested in future experiments.

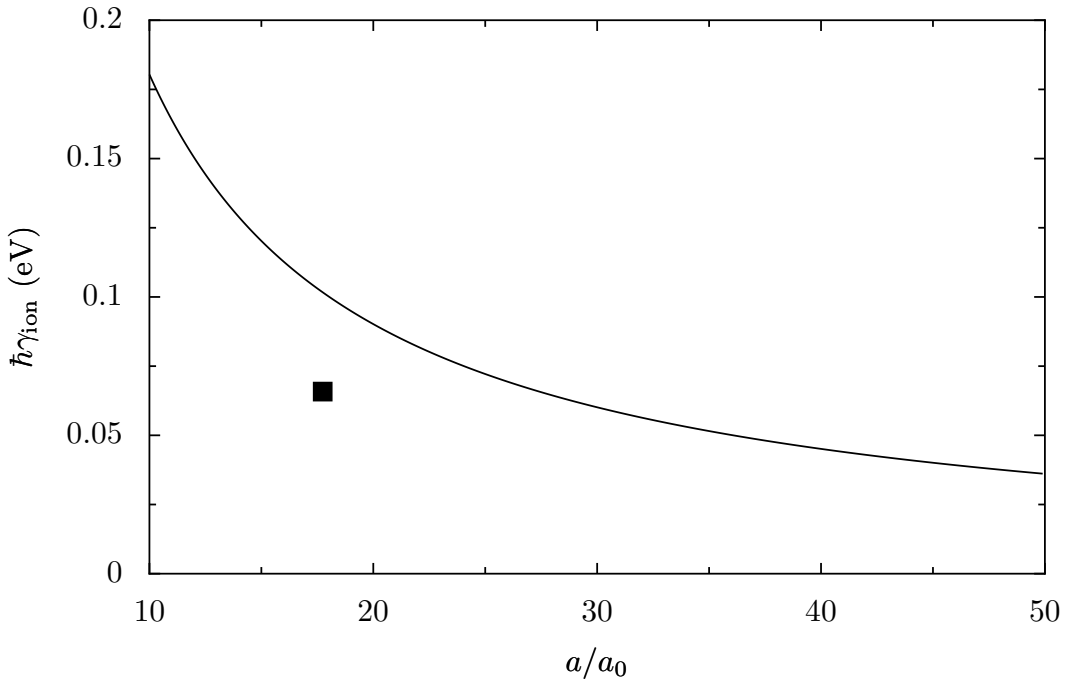

Figure 7.6: Ionization linewidth of the second plasmon state as a function of the nanoparticle radius for singly charged Na clusters. Square: experimental value for Na_{93}^+ taken from Refs. 72, 73. We have assumed a constant work function $W = 4.65\,\text{eV}$ and took the experimental surface plasmon frequency of $2.75\,\text{eV}$ for $\omega_{\rm M}$.

7.3 Conclusion for Chapter 7

In this chapter, the physical relevance of the second surface plasmon collective state has been analyzed in terms of different decay channels: Landau damping and particle ionization. For the Landau damping, we have shown that there exist two decay mechanisms: the decay of the second collective state to the first one, a process whose associated linewidth scales as $1/a$ with superimposed size-oscillations, and the direct decay to the collective ground state leading to an additional linewidth scaling as $1/a^2$. The latter is therefore negligible compared to the first-order decay process. The linewidth associated with the ionization of the nanoparticle has been shown, by means of a semiclassical expansion, to scale with the inverse size of the cluster. In this case, the delocalized self-consistent states play a crucial role, and make the calculations more involved.

We have shown that both processes, Landau damping and particle ionization, are relevant, but they do not preclude the existence of the resonance. The comparison of our semiclassical calculation with the existing numerical and experimental results is reasonably good, despite the various approximations of our model.

Our theoretical results concerning the different decay mechanisms of the second collective excitation of metallic clusters should be important for the analysis of the electron

dynamics following short and strong laser excitations. Indeed, a sufficiently strong excitation could lead to a non-negligible occupation probability of the second collective state. It could then be necessary to take it into account when discussing the dynamics of the surface plasmon excitation.

Chapter 8

Surface plasmon linewidth with an inhomogeneous dielectric environment

> Notre esprit est fait d'un désordre, plus un besoin de mettre en ordre.
>
> *(Paul Valéry, 1871-1945, in Mauvaises Pensées et autres)*

In this chapter, we go back to the problem of the single surface plasmon lifetime in the experimentally relevant case of noble-metal nanoparticles embedded in a surrounding matrix. In those nanoparticles, the screening of the s-electrons by the d-electrons can be modeled by a dielectric constant $\epsilon_{\rm d}$, and the dielectric matrix by a constant $\epsilon_{\rm m}$. The two dielectric constants affect the classical Mie frequency $\omega_{\rm M}$ according to (1.5). However, a generalization of the derivation of Chapter 4 shows that, as long as we work with the hypothesis of a steep potential (4.5), the smooth part of γ at zero temperature is still given by

$$\gamma^0(T=0) = \frac{3v_{\rm F}}{4a} g_0\left(\frac{\varepsilon_{\rm F}}{\hbar\omega_{\rm M}}\right), \tag{8.1}$$

g_0 being defined in (4.57). For a silver nanoparticle ($\epsilon_{\rm d} \simeq 3.7$) embedded in an argon matrix ($\epsilon_{\rm m} \simeq 1.7$) [114], using (8.1) yields a value of γ^0 about three times larger than the TDLDA calculations [80, 81], themselves in good agreement with existing experiments [115] (see Fig. 8.1). This discrepancy quoted by Molina *et al.* in Refs. 80 and 81 makes the more systematic study of the dependence of the plasmon lifetime on $\epsilon_{\rm d}$ and $\epsilon_{\rm m}$ presented in this chapter necessary. In the sequel of this chapter, we show that this discrepancy can be understood regarding the details of the mean-field self-consistent potential that has been approximated by a step-like function in Chapter 4.

In Fig. 8.2 we present the surface plasmon linewidth obtained from TDLDA calculations for several particle sizes between $N = 138$ and 1760, taking $\epsilon_{\rm d} = 4$ and $\epsilon_{\rm m} = 2$ and the electron density of silver ($r_{\rm s} = 3.03\,a_0$). As in the case of Fig. 4.4, we see that for

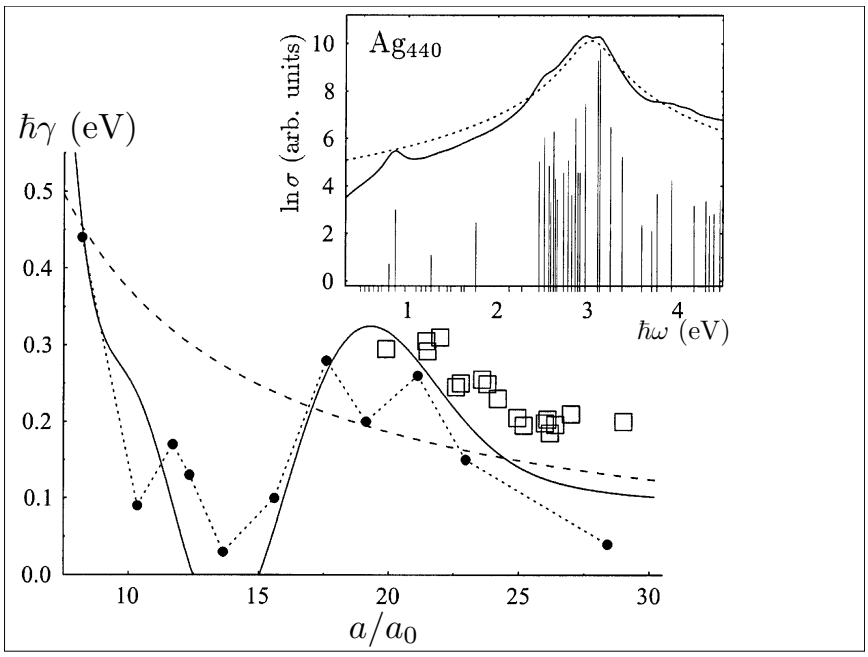

Figure 8.1: Linewidth at zero temperature as a function of the radius (in units of the Bohr radius a_0) for silver nanoparticles in an argon matrix calculated within TDLDA (full circles) together with the experimental results of Ref. 115 (empty squares). The dotted line through the numerical points is a guide-to-the-eye. The dashed and the solid lines represent, respectively, $\hbar\gamma^0$ and $\hbar\gamma = \hbar(\gamma^0 + \gamma^{\rm osc})$ according to (4.59) and (4.69) (with a reduction factor of 3 as discussed in the text). Inset: TDLDA absorption cross section (in logarithmic scale) for Ag_{440} ($a = 2.2\,a_0$), showing the pronounced surface plasmon resonance, fitted by a Lorentzian (dotted line). The many-body states are indicated by tick marks and their oscillation strengths given by the height of the vertical lines. (Reproduced from Ref. 81.)

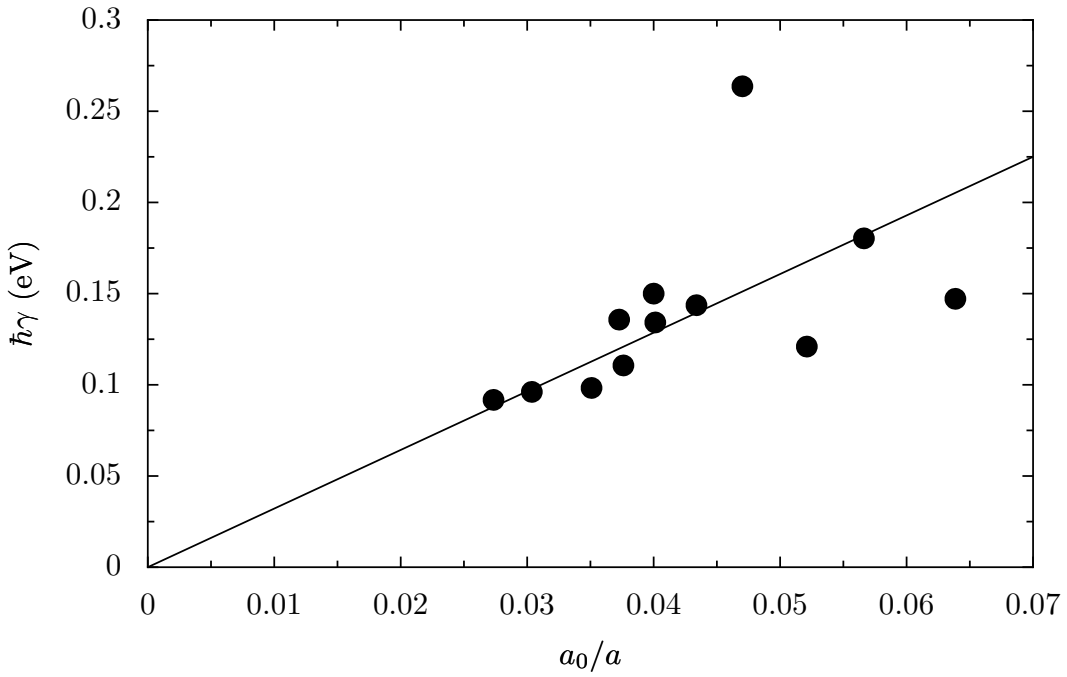

Figure 8.2: Surface plasmon linewidth from the TDLDA as a function of the inverse radius for the example of $\epsilon_\mathrm{d} = 4$ and $\epsilon_\mathrm{m} = 2$ (dots). The straight line is a linear fit $\hbar\gamma^0 = C/(a/a_0)$ with $C = 3.21\,\mathrm{eV}$. In the figure, $r_\mathrm{s} = 3.03\,a_0$.

relatively large radii the linewidth can be approximated by

$$\hbar\gamma^0 = \frac{C}{a/a_0} \tag{8.2}$$

while for smaller radii a, superimposed oscillations become noticeable. As shown in Figs. 8.3 and 8.4 when plotting the coefficients C as a function of ϵ_d and ϵ_m, we see that the numerical results are at odds with the simple prediction of (8.1) (upward continuous curves).

The increase of γ^0 with ϵ_d and ϵ_m in the latter case arises from the fact that the function g_0 is increasing with $\varepsilon_\mathrm{F}/\hbar\omega_\mathrm{M}$ and the Mie frequency $\omega_\mathrm{M} = \omega_\mathrm{p}/\sqrt{\epsilon_\mathrm{d} + 2\epsilon_\mathrm{m}}$ is redshifted when ϵ_d or ϵ_m is increasing. Calculations performed for the electronic density of sodium ($r_\mathrm{s} = 3.93\,a_0$) give the same kind of discrepancy between (8.1) and TDLDA results, as shown in Fig. 8.4. The discrepancy in Fig. 8.3 for $\epsilon_\mathrm{d} = \epsilon_\mathrm{m} = 1$ between (8.1) and the TDLDA is due to the uncertainty of the fitting procedure. For $r_\mathrm{s} = 3.93\,a_0$ (see Fig. 8.4), both points are in good agreement.

The discrepancy between the numerics and (8.1) shows that a direct application of the analytical approach presented in Chapter 4 does not reproduce the TDLDA results. As we will see in the following, the discrepancy is caused by approximating the electronic self-consistent potential by a square well.

The LDA calculations show that the shape of the self-consistent potential is modified

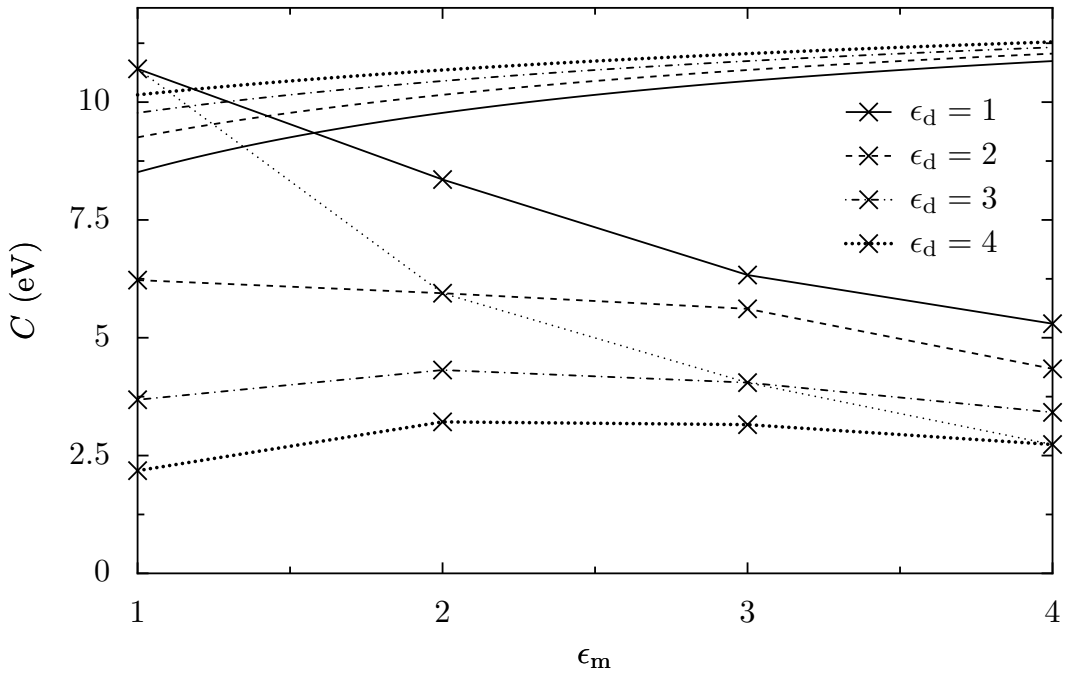

Figure 8.3: Prefactor C of the smooth $1/a$ size-dependent component of the surface plasmon linewidth $\hbar\gamma^0$ as a function of ϵ_m for ϵ_d between 1 and 4. The crosses connected by straight lines (guide-to-the-eye) represent the TDLDA calculations, while the increasing curves in the upper part of the figure depict the analytical expression (8.1). The thin dotted line is for $\epsilon_d = \epsilon_m$. The results presented in the figure are for the electronic density of silver ($r_s = 3.03\,a_0$).

when one increases the dielectric constants ϵ_d or ϵ_m. In Fig. 8.5 we present the self-consistent potential of a nanoparticle consisting of $N = 832$ atoms ($r_s = 3.03\,a_0$) for various values of $\epsilon = \epsilon_d = \epsilon_m$. This choice does not correspond to a physical realization, but it is useful for the interpretation of the analytical work, as it merely represents a renormalization of the electronic charge. The main effect of increasing ϵ is the decrease of the slope of the potential near the boundary $r = a$. This indicates that our approximation of a square-well potential becomes less valid as the dielectric constant is increased. The dependence of γ^0 on ϵ in this case is obtained by moving along the (thin dotted) line $\epsilon_d = \epsilon_m$ in Figs. 8.3 and 8.4.

In the following we refine the calculation of the radial dipole matrix element (4.17) in order to take into account the behavior of the slope of the self-consistent potential. The finite value of the slope of the self-consistent potential is often ignored. But here, it is necessary to go beyond the hypothesis of infinitely steep potential walls (see Eq. 4.5) in order to make progress. As it can be seen from (4.17), the dipole matrix element is proportional to the matrix element of the derivative of the potential V with respect to r. In the sequel, we show that below a certain value, the dipole matrix element is directly

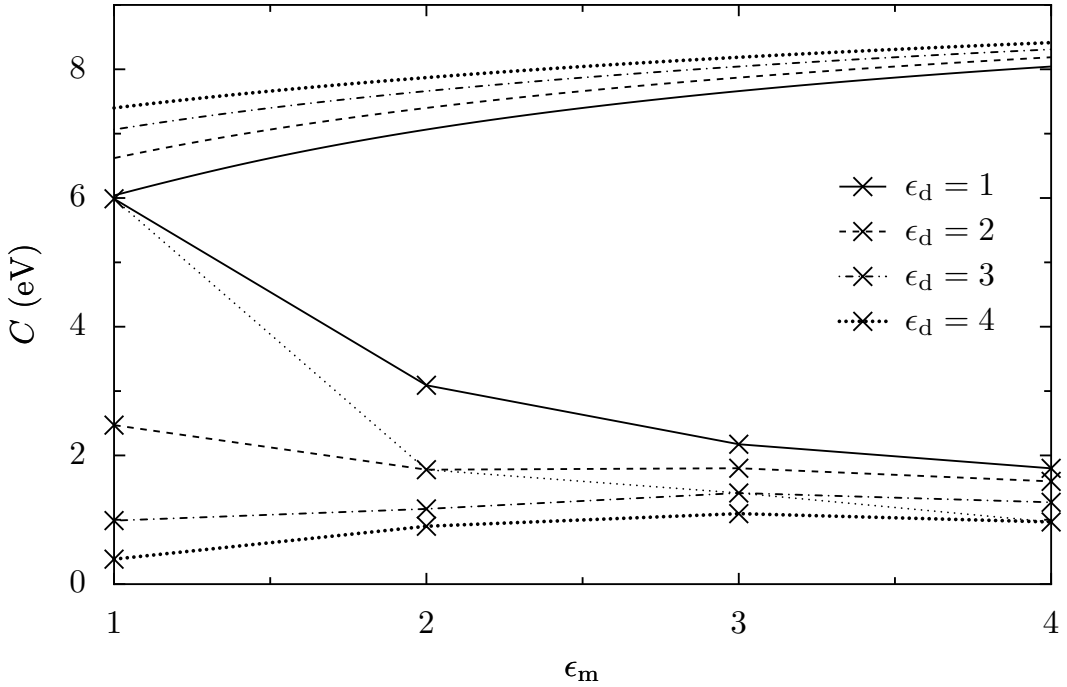

Figure 8.4: Same as in Fig. 8.3 for the electronic density of sodium ($r_{\mathrm{s}} = 3.93\, a_0$).

proportional to the slope of the self-consistent potential near the interface and estimate the slope from a simple Thomas-Fermi model. Since the linewidth is proportional to the square of the dipole matrix element, we see that γ decreases with the slope, and thus with the increase of the dielectric constant.

8.1 Surface plasmon linewidth with a soft self-consistent potential

In all the forthcoming derivations, we restrict ourselves to zero temperature. In order to improve our understanding of the role of a dielectric mismatch to the surface plasmon linewidth, we now need to come back to the evaluation of the surface plasmon linewidth at $T = 0$,

$$\gamma = \frac{2\pi}{\hbar} \sum_{ph} |\Lambda d_{ph}|^2 \, \delta(\hbar\omega_{\mathrm{M}} - \varepsilon_p + \varepsilon_h), \tag{8.3}$$

without making the approximation of an infinitely steep well for the self-consistent potential. In (8.3), p and h denote particle and hole states, respectively. A simplified way

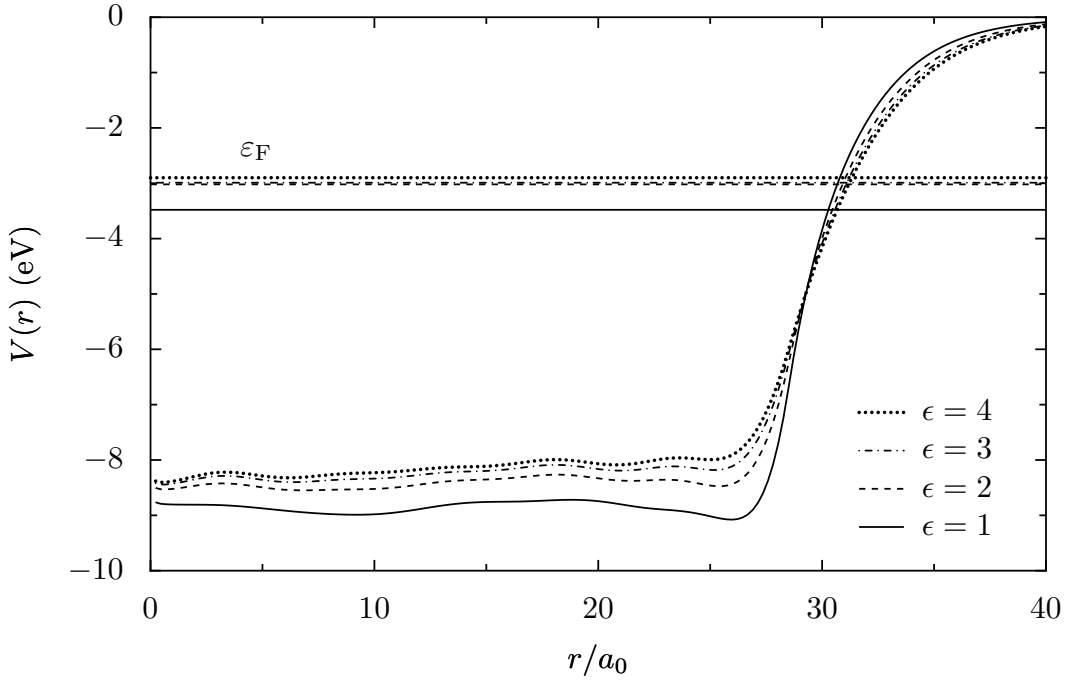

Figure 8.5: Self-consistent potential as a function of the radial coordinate (in units of the Bohr radius a_0) from the LDA calculations for a 832-atom nanoparticle with mean distance between electrons $r_s = 3.03\,a_0$, corresponding to $a \simeq 28.5\,a_0$. The different curves are for $\epsilon = \epsilon_d = \epsilon_m$ between 1 and 4, showing that the slope of the potential decreases with increasing values of ϵ. The corresponding Fermi levels are indicated by horizontal lines.

of taking into account the noninfinite slope of $V(r)$ is to change (4.5) by

$$V(r) = \begin{cases} 0, & 0 \leqslant r < a - \dfrac{d_s}{2}, \\ s\left(r - a - \dfrac{d_s}{2}\right) + V_0, & a - \dfrac{d_s}{2} \leqslant r \leqslant a + \dfrac{d_s}{2}, \\ V_0, & r > a + \dfrac{d_s}{2}, \end{cases} \tag{8.4}$$

where the distance d_s on which the slope $s = V_0/d_s$ is nonvanishing is assumed to be small as compared to the nanoparticle radius a. We first need an approximation for the dipole matrix element between particle and hole states in that potential. As explained in the following section, this can be done semiclassically using the limit in which particle and hole states are close in energy:

$$\frac{\varepsilon_p - \varepsilon_h}{\varepsilon_F} = \frac{\hbar\omega_M}{\varepsilon_F} \ll 1. \tag{8.5}$$

This semiclassical approximation relates the dipole matrix element to the Fourier components of the classical trajectory in the one-dimensional effective potential $V_l^{\text{eff}}(r)$ given

in (C.7).

8.1.1 Semiclassical dipole matrix element with spherical symmetry

In this section we focus on the semiclassical evaluation of the dipole matrix element for the case of a spherically symmetric system, and extend the well-known result which relates in the one-dimensional case the dipole matrix element to the Fourier components of the classical motion of the particle [116, 117].

The spherical symmetry permits us to separate the dipole matrix element $\langle nlm|z|n'l'm'\rangle$ into two parts: an angular part $\mathcal{A}_{ll'}^{mm'}$ given in (4.10) and a radial part

$$\mathcal{R}_{nn'}^{ll'} = \int_0^\infty \mathrm{d}r\; u_{nl}(r)^*\, r\, u_{n'l'}(r), \tag{8.6}$$

where the radial wave functions $u_{nl}(r)$ satisfy the reduced Schrödinger equation (4.7). Here, n denotes the radial quantum number. According to (4.13), and expressing the conjugated momentum to r as $p_r = -\mathrm{i}\hbar\mathrm{d}/\mathrm{d}r$, we have

$$\mathcal{R}_{nn'}^{ll'} = \frac{\hbar^2}{m_\mathrm{e}(\varepsilon_{n'l'} - \varepsilon_{nl})} \int_0^\infty \mathrm{d}r\; u_{nl}(r) \frac{\mathrm{d}}{\mathrm{d}r} u_{n'l'}(r). \tag{8.7}$$

Next, we restrict ourselves to the classical region in the effective potential $V_l^\mathrm{eff}(r)$ given in (C.7) between the two turning points (r_-, r_+) and use the WKB approximation to express the radial wave functions as (see Eq. B.27 in Appendix B)

$$u_{nl}(r) = \frac{2\cos\left\{1/\hbar \int_{r_-}^{r} \mathrm{d}r' \sqrt{2m_\mathrm{e}\left[\varepsilon_{nl} - V_l^\mathrm{eff}(r')\right]} - \pi/4\right\}}{\sqrt{\tau_l}\left\{2\left[\varepsilon_{nl} - V_l^\mathrm{eff}(r)\right]/m_\mathrm{e}\right\}^{1/4}}. \tag{8.8}$$

In (8.8), τ_l is the period of the periodic orbit trajectory at energy ε_{nl} in the effective potential $V_l^\mathrm{eff}(r)$. In order to pursue the evaluation of (8.7), we need to evaluate the derivative of (8.8) with respect to r. In the high energy limit ($\varepsilon_{nl} \gg \left|V_l^\mathrm{eff}\right|$), we obtain to leading order in $\hbar$

$$\frac{\mathrm{d}}{\mathrm{d}r} u_{nl}(r) \simeq -\frac{2}{\hbar\sqrt{\tau_l}} \left\{2m_\mathrm{e}^3\left[\varepsilon_{nl} - V_l^\mathrm{eff}(r)\right]\right\}^{1/4} \sin\left[\frac{1}{\hbar} S_l(r_-, r; \varepsilon_{nl}) - \frac{\pi}{4}\right], \tag{8.9}$$

where we have defined

$$S_l(r_-, r; \varepsilon_{nl}) = \int_{r_-}^{r} \mathrm{d}r' \sqrt{2m_\mathrm{e}\left[\varepsilon_{nl} - V_l^\mathrm{eff}(r')\right]}. \tag{8.10}$$

We now assume that $l \simeq l'$ (this is justified because the dipole selection rules dictate that $l' = l \pm 1$ and we are looking at the high energy limit) and that the energies involved in the dipole matrix element are sufficiently close to each other, i.e., both trajectories

at the energies ε_{nl} and $\varepsilon_{n'l'}$ have the same classically allowed region. Inserting (8.8) and (8.9) into (8.7), we thus obtain

$$\mathcal{R}^{ll'}_{nn'} \simeq -\frac{2\hbar}{\tau_l(\varepsilon_{n'l'}-\varepsilon_{nl})}\int_{r_-}^{r_+} \mathrm{d}r \left\{ \sin\left[\frac{S_{l'}(r,r_-;\varepsilon_{n'l'}) - S_l(r,r_-;\varepsilon_{nl})}{\hbar}\right] + \sin\left[\frac{S_{l'}(r,r_-;\varepsilon_{n'l'}) + S_l(r,r_-;\varepsilon_{nl})}{\hbar}\right]\right\}. \tag{8.11}$$

In the above equation, we neglect the last term since it is highly oscillating (in the limit "$\hbar \to 0$"). Moreover, we have for $l \simeq l'$ and $\varepsilon_{nl} \simeq \varepsilon_{n'l'}$

$$S_{l'}(r,r_-;\varepsilon_{n'l'}) - S_l(r,r_-;\varepsilon_{nl}) \approx \frac{\partial S_l}{\partial \varepsilon_{nl}}(\varepsilon_{n'l'}-\varepsilon_{nl}). \tag{8.12}$$

Note that $\partial S_l/\partial\varepsilon_{nl} = t_l(r,\varepsilon_{nl})$ is the time it takes to the particle to go from r_- to r with the energy ε_{nl} in the effective potential $V_l^{\mathrm{eff}}(r)$. Next, we use the semiclassical quantization condition (see Appendix B)

$$S_l(\varepsilon_{nl}) = 2\pi\hbar\left(n + \frac{\nu_\mathrm{c}}{4} + \frac{\nu_\mathrm{r}}{2}\right), \tag{8.13}$$

where ν_c and ν_r are the number of conjugated and reflection points in the effective radial potential, respectively. It yields

$$\frac{\partial\varepsilon_{nl}}{\partial n} = \frac{\partial\varepsilon_{nl}}{\partial S_l}\frac{\partial S_l}{\partial n} = \frac{2\pi\hbar}{\tau_l}. \tag{8.14}$$

Thus,

$$\varepsilon_{n'l'} - \varepsilon_{nl} \approx \frac{2\pi\hbar\Delta n}{\tau_l}, \tag{8.15}$$

with $\Delta n = n' - n$. With those approximations, we have for (8.11)

$$\mathcal{R}^{ll'}_{nn'} \simeq -\frac{1}{\pi\Delta n}\int_{r_-}^{r_+} \mathrm{d}r \sin\left(2\pi\Delta n\frac{t_l}{\tau_l}\right), \tag{8.16}$$

and changing the spatial coordinate r to the time t_l, we obtain

$$\mathcal{R}^{ll'}_{nn'} = -\frac{1}{\pi\Delta n}\int_0^{\tau_l/2} \mathrm{d}t\, \dot{r}(t) \sin\left(2\pi\Delta n\frac{t}{\tau_l}\right). \tag{8.17}$$

Integrating by parts, we finally obtain, to leading order in $\hbar$

$$\mathcal{R}^{ll'}_{nn'} = \frac{2}{\tau_l}\int_0^{\tau_l/2} \mathrm{d}t\; r(t) \cos\left(2\pi\Delta n\frac{t}{\tau_l}\right), \tag{8.18}$$

where $r(t)$ represents the classical trajectory in the effective potential. Thus we see that, as in the one-dimensional case, the dipole matrix element is related to the Fourier transform of the trajectory of the classical motion [116].

Example of application: Spherical hard wall potential

As a check of consistency, we apply this semiclassical analysis to the hard-wall potential (of radius a) involved in our evaluation of the surface-plasmon lifetime. This analysis is only possible in the limit $\varepsilon_{\rm F} \gg \hbar\omega_{\rm M}$: The approximation of (8.18) is valid if we assume that the energy of the particle is close to the one of the hole. This energy difference is, because of the conservation of energy appearing in the Fermi golden rule (8.3), simply $\hbar\omega_{\rm M}$.

At a given energy ε, the periodic trajectory in the effective potential obeys the conservation of energy

$$\varepsilon = \frac{1}{2} m_{\rm e} \dot{r}^2 + \frac{\hbar^2 (l+1/2)^2}{2 m_{\rm e} r^2}, \tag{8.19}$$

i.e.,

$$\dot{r} = \sqrt{\frac{2}{m_{\rm e}} \left[\varepsilon - \frac{\hbar^2 (l+1/2)^2}{2 m_{\rm e} r^2} \right]}. \tag{8.20}$$

Since we have a periodic motion, the initial position of the particle can be chosen everywhere in the classically allowed region, and we choose $r(t=0) = r_-$. Using

$$\int_0^t {\rm d}t' = \int_{r_-}^{r} \frac{{\rm d}r'}{\dot{r}'}, \tag{8.21}$$

we obtain

$$t = \frac{1}{\varepsilon} \sqrt{\frac{m_{\rm e}}{2} \varepsilon r^2 - \frac{\hbar^2 (l+1/2)^2}{4}}, \tag{8.22}$$

which can be inverted to yield the trajectory

$$r(t) = \sqrt{\frac{2\varepsilon}{m_{\rm e}} t^2 + \frac{\hbar^2 (l+1/2)^2}{2 m_{\rm e} \varepsilon}} \ , \ 0 \leqslant t \leqslant \frac{\tau_l}{2}. \tag{8.23}$$

The period of the effective radial motion being $\tau_l = \sqrt{2 m_{\rm e} \varepsilon a^2 - \hbar^2 (l+1/2)^2}/\varepsilon$, we verify that $r(\tau_l/2) = a$.

Substituting the above expression of the classical trajectory in (8.18), and integrating twice by parts, we have

$$\mathcal{R}^{ll'}_{nn'} = \frac{\tau_l \varepsilon}{2 (\pi \Delta n)^2 m_{\rm e}} \left\{ (-1)^{\Delta n} \frac{\tau_l}{a} - \hbar^2 \left(l + \frac{1}{2} \right)^2 \sqrt{m_{\rm e}} \int_0^{\tau_l/2} \frac{\cos\left(2\pi \Delta n t/\tau_l\right)}{\left[2\varepsilon t^2 + \hbar^2 (l+1/2)^2/2\varepsilon \right]^{3/2}} \right\}. \tag{8.24}$$

By continuing to integrate by parts, we will obtain an even series in $1/(\Delta n)^{2q}$, with q an integer. But, in the semiclassical limit, we are interested in a range of energies where $\varepsilon_{\rm F} \gg \hbar\omega_{\rm M} \gg \Delta$, with Δ the mean level spacing in the nanoparticle. Making the expansion in $1/\Delta n$ (proportional to $1/\hbar\omega_{\rm M}$, see Eq. 8.15), we obtain the leading order term (up to an irrelevant phase factor)

$$\mathcal{R}_{l_\alpha l_\beta}(\varepsilon_\alpha, \varepsilon_\beta) = \frac{2\hbar^2}{m_{\rm e} a} \frac{\varepsilon_\alpha}{\left(\varepsilon_\alpha - \varepsilon_\beta\right)^2}, \tag{8.25}$$

which agrees with (4.27) in the limit $\varepsilon_\alpha \approx \varepsilon_\beta$. We notice that this semiclassical dipole matrix element leads to the correct result for the smooth part γ^0 of the single-plasmon linewidth in the limit $\varepsilon_\mathrm{F}/\hbar\omega_\mathrm{M} \to \infty$ of (8.1).

8.1.2 Surface plasmon rate with a slope for the self-consistent field

In this section, we apply the semiclassical calculation of the dipole matrix element depicted in Sec. 8.1.1 to the case of the self-consistent potential with a finite slope (8.4). As a simplifying approximation, we neglect the centrifugal part of the effective potential $V_l^\mathrm{eff}(r)$ above $r > a - d_s/2$. With this assumption, valid in the semiclassical limit $k_\mathrm{F}a \gg 1$, we have

$$V_l^\mathrm{eff}(r) \simeq \begin{cases} \dfrac{\hbar^2(l+1/2)^2}{2m_\mathrm{e}r^2}, & 0 \leqslant r < a - \dfrac{d_s}{2}, \\ \tilde{s}\left(r - a - \dfrac{d_s}{2}\right) + V_0, & a - \dfrac{d_s}{2} \leqslant r \leqslant a + \dfrac{d_s}{2}, \\ V_0, & r > a + \dfrac{d_s}{2}, \end{cases} \tag{8.26}$$

where $\tilde{s} = s - \hbar^2(l+1/2)^2/2m_\mathrm{e}d_s(a-d/2)^2$. The effective radial potential from (8.26) is represented in Fig. 8.6.

Integrating the classical equation of motion, we obtain periodic trajectories for $\varepsilon < V_0$ given by

$$r(t) = \begin{cases} \sqrt{\dfrac{2\varepsilon}{m_\mathrm{e}}t^2 + \dfrac{\hbar^2(l+1/2)^2}{2m_\mathrm{e}\varepsilon}}, & 0 \leqslant t \leqslant t_\mathrm{c}, \\ -\dfrac{\tilde{s}}{2m_\mathrm{e}}\left(\dfrac{\tau_l}{2} - t\right)^2 + a + \dfrac{d_s}{2} - \dfrac{V_0 - \varepsilon}{\tilde{s}}, & t_\mathrm{c} < t \leqslant \dfrac{\tau_l}{2}, \end{cases} \tag{8.27}$$

with $r(t_\mathrm{c}) = a - d_s/2$. We can now evaluate the dipole matrix element using the semiclassical Eq. 8.18, neglecting the acceleration of the particle for $r - a + d_s/2 \to 0^-$ and approximating $\tilde{s}$ by s (justified for $a \gg d_s$). An expansion in $1/\Delta n$ (where Δn is the difference between the radial quantum number of the particle and of the hole) gives, up to an irrelevant phase factor,

$$\mathcal{R}_{l_p l_h}(\varepsilon_p, \varepsilon_h) \simeq \frac{s}{m_\mathrm{e}}\frac{2}{\tau_{l_p}}\frac{\hbar^3}{(\varepsilon_p - \varepsilon_h)^3}\sin\left(\pi\Delta n\frac{\delta t}{t_\mathrm{c}}\right), \tag{8.28}$$

with $\delta t = \tau_{l_p}/2 - t_\mathrm{c}$ the time spent by the particle in the region where the slope is nonvanishing.

An estimation of the argument of the sine gives $(\hbar\omega_\mathrm{M}/\Delta)(d_s/a)$, with Δ the mean level spacing. Typical values give $\hbar\omega_\mathrm{M}/\Delta \sim 10^4 \gg 1$. In the limit of a very large slope, d_s/a tends to zero. Then, the argument of the sine is very small compared to one, and we recover the semiclassical evaluation of (8.25) with an infinite slope. On the contrary, if we assume that d_s is of the order of the spill-out length l_s ($\sim a_0$, see Chapter 5), the

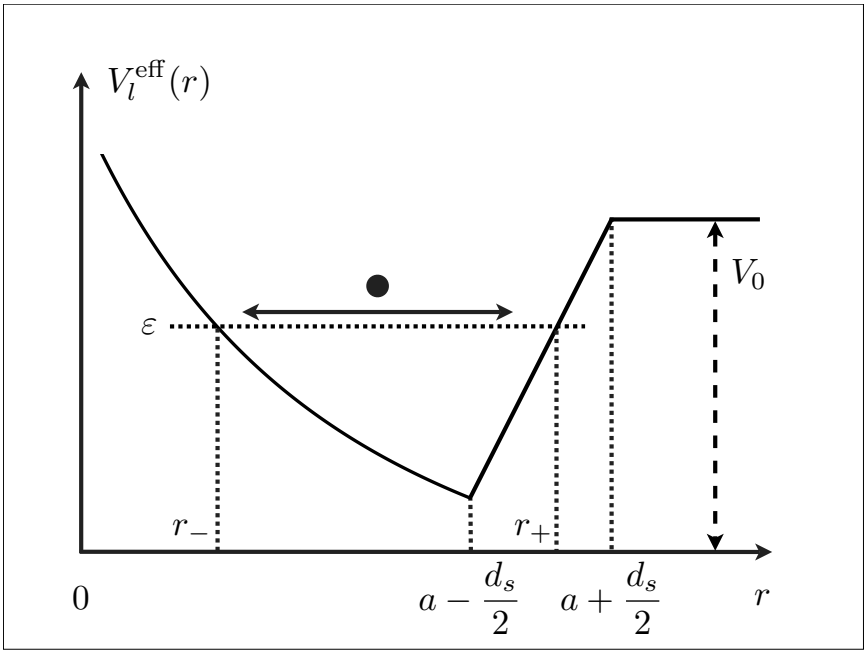

Figure 8.6: Sketch of the effective radial potential $V_l^{\text{eff}}(r)$ from (8.26). We denote by r_- and r_+ the turning points on the left and on the right of the classically allowed region of the potential, respectively.

argument of the sine is much greater than one. Inserting (8.28) into (8.3), we obtain with (4.36)

$$\gamma^0 = \frac{2s^2}{\pi\hbar^2\omega_{\text{M}}^3 N m_{\text{e}}} \int_{\varepsilon_{\text{F}}}^{\varepsilon_{\text{F}}+\hbar\omega_{\text{M}}} \mathrm{d}\varepsilon_p \sum_{\substack{l_p,m_p \\ l_h,m_h}} \left(\mathcal{A}_{l_p l_h}^{m_p m_h}\right)^2 \sin^2\left(\pi\Delta n \frac{\delta t}{t_{\text{c}}}\right). \tag{8.29}$$

Averaging the highly oscillating sine (squared) by 1/2 gives for the surface plasmon linewidth in the limit $\hbar\omega_{\text{M}} \ll \varepsilon_{\text{F}}$

$$\gamma^0 \simeq \frac{3s^2}{4\hbar} \frac{1}{m_{\text{e}}\omega_{\text{M}}^2} \frac{1}{k_{\text{F}} a}. \tag{8.30}$$

We then see that in the case of a soft self-consistent potential, the surface plasmon linewidth is proportional to the square of the slope s of that potential. When one increases the dielectric constant of the medium, the slope decreases (see Fig. 8.5) and therefore γ^0 decreases. We also notice that the smooth $1/a$ size dependence of the surface plasmon linewidth remains valid even for a finite slope.

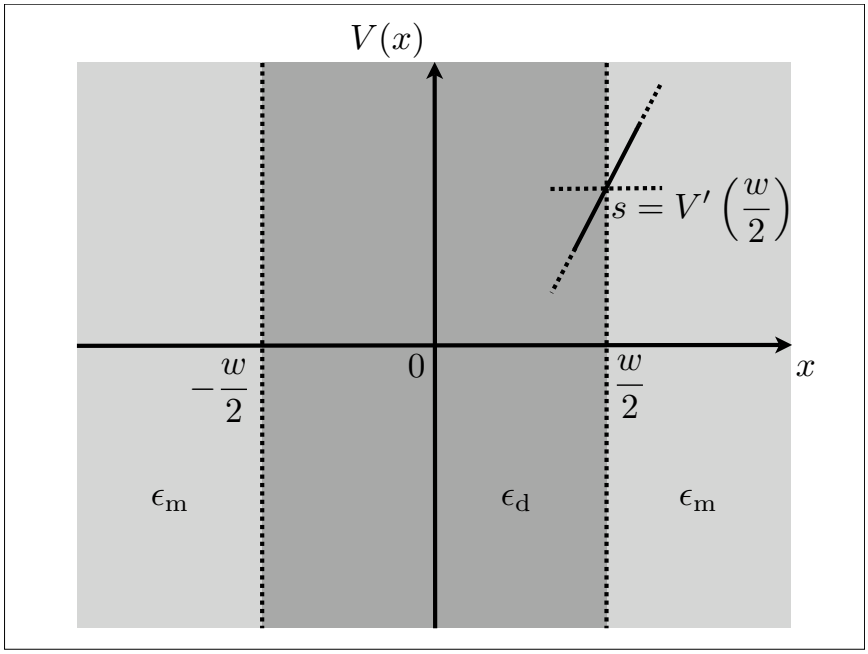

Figure 8.7: Sketch of the metallic slab used to determine the slope s of the self-consistent potential V in presence of a dielectric mismatch $(\epsilon_\mathrm{d}, \epsilon_\mathrm{m})$.

8.2 Steepness of the self-consistent potential with a dielectric mismatch

In order to estimate the slope of the self-consistent potential, we consider the simpler geometry of a metallic slab of dielectric constant ϵ_d, bounded by two interfaces at $x = \pm w/2$ and with an infinite extension in the (y, z) plane, surrounded by a dielectric medium with a constant ϵ_m (see Fig. 8.7). This geometry allows us to simplify the problem to an effective one-dimensional system. It can be expected to provide a good approximation for the shape of the potential near the interface for the sphere geometry. Indeed, it seems reasonable that the effects of the curvature of the sphere on the potential are negligible close to the surface.

We make the jellium approximation for the ionic density $n_\mathrm{i}(x) = n_\mathrm{i}\Theta(w/2 - |x|)$ and work within the Thomas-Fermi approach, writing the local energy in the electrostatic potential $\phi(x)$ as

$$\varepsilon = \frac{\mathbf{p}^2(x)}{2m_\mathrm{e}} - e\phi(x). \tag{8.31}$$

For the electrons, we assume the Fermi-Dirac distribution

$$f(x,\mathbf{p}) = \frac{1}{\exp\left\{\beta\left[\frac{\mathbf{p}^2(x)}{2m_\mathrm{e}} - e\phi(x) - \mu\right]\right\}+1} \tag{8.32}$$

yielding the electronic density (at zero temperature)

$$\begin{aligned} n_\mathrm{e}(x) &= \int \mathrm{d}^3\mathbf{p}\, f(x,\mathbf{p}) \\ &= \begin{cases} \dfrac{1}{3\pi^2}\left(\dfrac{2m_\mathrm{e}}{\hbar^2}\right)^{3/2}\left[\mu + e\phi(x)\right]^{3/2}, & \mu \geqslant -e\phi(x), \\ 0, & \mu < -e\phi(x), \end{cases} \end{aligned} \tag{8.33}$$

with μ the chemical potential. The mean-field potential will simply be given by $V(x) = -e\phi(x)$. The Thomas-Fermi approach to surfaces is known to have serious shortcomings [118] (for instance, it predicts a vanishing work function). However, it will be useful for our estimation of the slope of the mean field seen by the charge carriers. The self-consistency is achieved through the Poisson equation

$$\frac{\mathrm{d}^2\phi}{\mathrm{d}x^2} = \begin{cases} \dfrac{4\pi e}{\epsilon_\mathrm{d}}\left[n_\mathrm{e}(x) - n_\mathrm{i}\right], & |x| < \dfrac{w}{2}, \\ \dfrac{4\pi e}{\epsilon_\mathrm{m}} n_\mathrm{e}(x), & |x| > \dfrac{w}{2}. \end{cases} \tag{8.34}$$

In the following, we first consider, for pedagogical reason, the case where $\epsilon_\mathrm{d} = \epsilon_\mathrm{m} = \epsilon = 1$, i.e., there is neither dielectric mismatch, nor a renormalization of the electronic charge. In a second part, we consider the case where $\epsilon_\mathrm{d} = \epsilon_\mathrm{m} = \epsilon$, that is, just a renormalization of e. Finally, we consider the realistic realization of a dielectric mismatch $(\epsilon_\mathrm{d}, \epsilon_\mathrm{m})$.

8.2.1 First case: $\epsilon_\mathrm{d} = \epsilon_\mathrm{m} = \epsilon = 1$

Inserting the electronic density (8.33) into the Poisson equation (8.34) in the case where both, the dielectric constant characterizing the d-electrons and the dielectric constant of the matrix are equal to one, we have

$$\varphi''(x) = \begin{cases} \alpha_1\varphi^{3/2}(x) - \beta_1, & |x| < w/2, \\ \alpha_1\varphi^{3/2}(x), & |x| > w/2. \end{cases} \tag{8.35}$$

In the above equation, we have defined

$$\varphi(x) = \mu + e\phi(x), \tag{8.36a}$$

$$\alpha_1 = \frac{4e^2}{3\pi}\left(\frac{2m_\mathrm{e}}{\hbar^2}\right)^{3/2}, \tag{8.36b}$$

$$\beta_1 = 4\pi e^2 n_\mathrm{i}. \tag{8.36c}$$

Imposing that there are no electrons at $x = \infty$, i.e., $\lim_{x\to\infty} n_{\mathrm{e}}(x) = 0^+$, we have $\lim_{x\to\infty} \varphi(x) = 0^+$ according to (8.33), and then $\lim_{x\to\infty} \varphi'(x) = 0^-$. Thus there is no electric field far away from the metallic slab. Furthermore, by imposing the charge neutrality of the system slab plus matrix, we have $\varphi'(0) = 0$.

Integrating once (8.35), we obtain with the boundary conditions just exposed

$$\varphi'(x) = \begin{cases} -\sqrt{\dfrac{4\alpha_1}{5}\left[\varphi^{5/2}(x) - \mu^{5/2}\right] - 2\beta_1\left[\varphi(x) - \mu\right]}, & |x| < w/2, \\ -\sqrt{\dfrac{4\alpha_1}{5}\varphi^{5/2}(x)}, & |x| > w/2. \end{cases} \tag{8.37}$$

The continuity of the electrical field at $x = w/2$ translates with our notations into $\varphi'(w^-/2) = \varphi'(w^+/2)$, which allows to obtain

$$s = -\varphi'\left(\frac{w}{2}\right) = \sqrt{\frac{4\alpha_1}{5}}\mu^{5/4}\left(1 - \frac{2\alpha_1}{5\beta_1}\mu^{3/2}\right)^{5/4}. \tag{8.38}$$

With the definitions (8.36), we have for the slope of the self-consistent field $V(x)$ at the boundary

$$s = \frac{4e}{\sqrt{15\pi}}\left(\frac{2m_{\mathrm{e}}}{\hbar^2}\right)^{3/4}\mu^{5/4}\left[1 - \frac{2}{5}\left(\frac{\mu}{\varepsilon_{\mathrm{F}}}\right)^{3/2}\right]^{5/4}, \tag{8.39}$$

where ε_{F} is the Fermi energy of the free electron gas.

8.2.2 Second case: $\epsilon_{\mathrm{d}} = \epsilon_{\mathrm{m}} = \epsilon \neq 1$

The calculations in this case are similar to the ones in the preceding section, up to a replacement of the constants α_1 and β_1 by $\alpha_\epsilon = \alpha_1/\epsilon$ and $\beta_\epsilon = \beta_1/\epsilon$. We thus obtain

$$s = \frac{4e}{\sqrt{15\pi}}\left(\frac{2m_{\mathrm{e}}}{\hbar^2}\right)^{3/4}\frac{\mu^{5/4}}{\epsilon^{1/2}}\left[1 - \frac{2}{5}\left(\frac{\mu}{\varepsilon_{\mathrm{F}}}\right)^{3/2}\right]^{5/4}. \tag{8.40}$$

The chemical potential is fixed by the consistency condition

$$\sqrt{\frac{\epsilon\mu}{8\pi e^2 n_{\mathrm{i}}}}\int_{1-\frac{2}{5}\left(\frac{\mu}{\varepsilon_{\mathrm{F}}}\right)^{3/2}}^{1}\frac{\mathrm{d}u}{\sqrt{\frac{2}{5}\left(\frac{\mu}{\varepsilon_{\mathrm{F}}}\right)^{3/2}(u^{5/2}-1) - (u-1)}} = \frac{w}{2}. \tag{8.41}$$

This consistency equation is obtained by integrating twice the Poisson equation between 0 and $w/2$. If we do not have any dielectric constant (i.e., $\epsilon = 1$), the same equation is obtained but without the prefactor $\sqrt{\epsilon}$. The integral in (8.41) is clearly dominated by its prefactor. Then, assuming that the integral appearing in this equation does not change appreciably when we have a dielectric constant, we find the scaling $\mu \approx \mu_1/\epsilon$ with μ_1 the chemical potential in the case where $\epsilon = 1$. Thus, we obtain for (8.40)

$$s = \frac{4e}{\sqrt{15\pi}}\left(\frac{2m_{\mathrm{e}}}{\hbar^2}\right)^{3/4}\frac{\mu_1^{5/4}}{\epsilon^{7/4}}\left[1 - \frac{2}{5\epsilon^{3/2}}\left(\frac{\mu_1}{\varepsilon_{\mathrm{F}}}\right)^{3/2}\right]^{5/4}. \tag{8.42}$$

Therefore, we see with (8.42) that the slope at the interface is decreasing with increasing values of the dielectric constant ϵ, a feature confirmed by our LDA calculations (see Fig. 8.5).

8.2.3 Third case: $\epsilon_\mathrm{d} \neq \epsilon_\mathrm{m}$

In the case where we have a dielectric mismatch between the metallic slab and the environment, the continuity of the normal component of the displacement field $\mathbf{D}$ gives the condition

$$\epsilon_\mathrm{d}\varphi'\left(\frac{w^-}{2}\right) = \epsilon_\mathrm{m}\varphi'\left(\frac{w^+}{2}\right) \tag{8.43}$$

Perturbatively, in the limit $|\epsilon_\mathrm{d} - \epsilon_\mathrm{m}| \to 0$, we obtain

$$\begin{aligned} s = \frac{4e}{\sqrt{15\pi}}\left(\frac{2m_\mathrm{e}}{\hbar^2}\right)^{3/4} \frac{\mu_1^{5/4}}{\epsilon_\mathrm{m}^{1/2}\epsilon_\mathrm{d}^{5/4}}\left[1 - \frac{2}{5\epsilon_\mathrm{d}^{3/2}}\left(\frac{\mu_1}{\varepsilon_\mathrm{F}}\right)^{3/2}\right]^{5/4} \\ \times\left\{1 + \frac{\epsilon_\mathrm{d} - \epsilon_\mathrm{m}}{2\epsilon_\mathrm{d}^{5/2}}\left(\frac{\mu_1}{\varepsilon_\mathrm{F}}\right)^{3/2}\left[1 - \frac{2}{5\epsilon_\mathrm{d}^{3/2}}\left(\frac{\mu_1}{\varepsilon_\mathrm{F}}\right)^{3/2}\right]\right\}, \end{aligned} \tag{8.44}$$

with the scaling $\mu \approx \mu_1/\epsilon_\mathrm{d}$, which can be justified in the same manner as for the case of a single dielectric constant. The only difference is that in the case of a dielectric mismatch, we obtain (8.41), up to a change of ϵ into ϵ_d. We then see that the slope s of the confining mean-field potential at the interface is decreasing either with ϵ_d or ϵ_m (for small $|\epsilon_\mathrm{d} - \epsilon_\mathrm{m}|$), in agreement with the LDA calculations.

This Thomas-Fermi approach to the mean-field potential of a metallic slab then provides an estimate of the slope of the potential near the interface between the slab and the surrounding environment. It can be expected that these results are also applicable to the more involved problem of the metallic sphere, up to some geometrical prefactors. In the following section, we will incorporate our estimate of the self-consistent potential slope in our evaluation of the surface plasmon lifetime.

8.3 Surface plasmon linewidth with a dielectric mismatch

We can now use our estimate (8.44) for the slope of the self-consistent potential in our evaluation (8.30) of the surface plasmon linewidth. In order to do that, we assume that the chemical potential μ_1 for $\epsilon = 1$ is the Fermi energy ε_F of a free electron gas.

In the case where we have a charge renormalization (i.e., $\epsilon_\mathrm{d} = \epsilon_\mathrm{m} = \epsilon$), we obtain by inserting (8.42) into (8.30)

$$\gamma^0 \simeq \frac{9v_\mathrm{F}}{10a}\frac{1}{\epsilon^{5/2}}\left(1 - \frac{2}{5\epsilon^{3/2}}\right)^{5/2}. \tag{8.45}$$

This result qualitatively reproduces the decrease obtained from TDLDA for $\hbar\gamma^0\, a/a_0$ as a function of the dielectric constant ϵ as it can be seen on Figs. 8.3 and 8.4 (thin dotted line). We notice that for $\epsilon = 1$, we have $\gamma^0 \approx v_\mathrm{F}/2a$ in the limit of large $\varepsilon_\mathrm{F}/\hbar\omega_\mathrm{M}$, which has to be compared with (8.1) giving $3v_\mathrm{F}/4a$. This small discrepancy is not surprising, regarding the various approximations we made here.

In the case where we have a dielectric mismatch, by inserting (8.44) into (8.30) and making the expansion for small $\Delta\epsilon = \epsilon_\mathrm{d} - \epsilon_\mathrm{m}$, we obtain

$$\gamma^0 \simeq \gamma^0_{(\Delta\epsilon=0)} + A(\epsilon_\mathrm{d})\Delta\epsilon \tag{8.46}$$

for fixed ϵ_d and

$$\gamma^0 \simeq \gamma^0_{(\Delta\epsilon=0)} - B(\epsilon_\mathrm{m})\Delta\epsilon \tag{8.47}$$

for fixed ϵ_m. In the above two equations, A and B are two positive coefficients given by

$$A(\epsilon_\mathrm{d}) = \frac{3v_\mathrm{F}}{10a}\frac{1}{\epsilon_\mathrm{d}^{7/2}}\left(1-\frac{2}{5\epsilon_\mathrm{d}}\right)^{5/2}\left[1+\frac{3}{\epsilon_\mathrm{d}^{3/2}}\left(1-\frac{2}{5\epsilon_\mathrm{d}^{3/2}}\right)\right], \tag{8.48a}$$

$$B(\epsilon_\mathrm{m}) = \frac{9v_\mathrm{F}}{10a}\frac{1}{\epsilon_\mathrm{m}^{7/2}}\left[\frac{13}{6}-\frac{3}{2\left(\epsilon_\mathrm{m}^{3/2}-2/5\right)}-\frac{1}{\epsilon_\mathrm{m}^{3/2}}\left(1-\frac{2}{5\epsilon_\mathrm{m}^{3/2}}\right)\right], \tag{8.48b}$$

and $\gamma^0_{(\Delta\epsilon=0)}$ is given by (8.45). These results confirm the behavior of the TDLDA calculations depicted on Figs. 8.3 and 8.4 around $\Delta\epsilon = 0$ (thin dotted line). For instance, if we are at ϵ_m fixed, we see that when $\Delta\epsilon > 0$, (8.47) predicts that $\hbar\gamma^0\, a/a_0$ decreases for increasing values of ϵ_d.

8.4 Conclusion for Chapter 8

In this chapter, we have analyzed the surface plasmon linewidth in the case of noble-metal nanoparticles embedded (or not) in a dielectric matrix. For such a situation, the role of the d-electrons of the metal cannot be ignored, since they lead to a dielectric mismatch between the nanoparticle and the surrounding matrix. We have shown that the well-known Kubo formula for the surface plasmon linewidth predicts an increase of this linewidth as the dielectric constants increase, a result in contradiction with the numerical calculations of the time-dependent local density approximation. Furthermore, the analytical prediction (8.1) overestimates the linewidth as deduced from experiments on noble-metal clusters.

We have shown how to take into account the inhomogeneous dielectric environment in our semiclassical model through the corrections in the slope of the mean-field potential. Evaluating the slope with a simple Thomas-Fermi model, the resulting improved theory is in qualitative agreement with the TDLDA calculations, themselves in good agreement with existing experiments [115]. The use of semiclassical expansions and drastic approximation has allowed us to clarify the main physical ingredients in the surface plasmon

decay rate for the experimentally relevant case of noble-metal nanoparticles embedded in inert dielectric matrices.

The case of noninert environments, where the matrix provides conduction electronic states, is more complicated. In this situation, the conduction band of the matrix provides additional decay channels, and the linewidth of the surface plasmon is increased (i.e., its lifetime is decreased), still presenting oscillations as a function of the size of the cluster [81].

A possible experimental check of our prediction concerning the decrease of the surface plasmon linewidth with increasing dielectric constants could be the following. Taking noble-metal nanoparticles of a given size and of a given metal (i.e., of a given dielectric constant ϵ_{d}) in a colloidal suspension (e.g., sugared water), one could significantly change the index of refraction and thus ϵ_{m} by changing the sugar concentration of the solution. For each concentration, one could measure the photoabsorption cross section of the sample and then deduces the linewidth.

Chapter 9

Concluding remarks and outlook

A moins d'être un crétin, on meurt toujours dans l'incertitude de sa propre valeur et de ses œuvres.

(Gustave Flaubert, 1821-1880, in Correspondance)

9.1 Summary

In this thesis we have studied collective excitations in metallic nanoparticles, the so-called surface plasmons. More specifically, we have focused on the quantum dissipation and decoherence of such excitations. We have chosen as a specific example the study of spherical nanoparticles which have closed angular momentum shells, i.e., a "magic" number of atoms.

Within the spherical jellium model, where the ionic structure of the nanoparticle is replaced by a homogeneous positively charged background, we have decomposed, by introducing the electronic center-of-mass and relative coordinates, the many-body electronic Hamiltonian into three terms. A first term contains only the center-of-mass degree of freedom, which is the natural coordinate to describe the oscillations of the electronic cloud around its equilibrium position created by an external driving field. The Hamiltonian for the center of mass is harmonic at a frequency redshifted by the spill-out effect as compared to the classical Mie value. A second term is associated only with the relative coordinates, and contains the electron-electron interaction that we have treated within the mean-field approximation. Finally, a coupling appears between the center-of-mass and relative-coordinate subsystems. We have linearized this coupling assuming that the displacement of the center of mass is small compared to the size of the nanoparticle. The coupling Hamiltonian arises from the Coulomb part of the single-particle confinement created by the jellium background at the exterior of the cluster. The coupling between the center of mass and the relative coordinates can be obtained in a different manner, regarding the change in the electronic mean-field potential created by a

displacement of the electronic cloud [16]. This approach has allowed us to generalize the expression of the coupling to the case of a noble-metal nanoparticle (where the screening of the s-electrons by the d-electrons has to be taken into account) possibly embedded in a surrounding matrix. It turns out that the coupling Hamiltonian remains the same, up to a renormalization of the classical Mie frequency by the dielectric constants of the nanoparticle and of the matrix.

The decomposition of the electronic Hamiltonian presented in Chapter 2 is archetypal of quantum dissipative systems: The system under study (the center of mass) is subject to an environment (the relative coordinates) and dissipates its energy due to the coupling to the environment. In our case, the environment is peculiar in the sense that it is not an external but an *internal* environment: The environmental degrees of freedom belong to the nanoparticle itself and moreover are finite in number. The coupling causes dissipation and decoherence of the collective excitation by a Landau damping mechanism: The surface plasmon decays by creating particle-hole excitations in the environment.

We have developed a density-matrix formalism to study the decoherence of the surface plasmon excitation. By eliminating the environmental degrees of freedom, we obtained the evolution of the reduced density matrix of the center of mass in presence of an external driving field. This has been done under the following assumptions. The coupling between system and environment has been assumed to be weak, rendering possible a perturbative expansion of the reduced density matrix. Furthermore, since the environment contains a large number of degrees of freedom, we have supposed that the dynamics of the center of mass is Markovian, neglecting potential memory effects. We have also added the influences of the environment and of the external driving field independently. Those approximations have provided a tractable master equation for the dynamical evolution of the surface plasmon excitation. Two parameters have appeared in the master equation: the Landau damping rate γ, and the shift δ which renormalize the surface plasmon frequency, an effect analogous to the Lamb shift in atomic systems. Thus, the electronic environment has two effects. First, it yields a finite lifetime for the surface plasmon excitation. Second, a redshift with respect to the classical Mie frequency appears in addition to the one caused by the well-known spill-out effect.

The obtained master equation for the reduced density matrix of the center of mass is the one of a driven damped harmonic oscillator. We have restricted ourselves only to two levels for the description of the dynamics of the surface plasmon excitation. The important parameter determining the temporal evolution of the center of mass is the so-called saturation parameter. This is a measure of the ratio of the external field intensity over natural damping of the system. In the case of a weak external driving field, like it is for instance the case in photoabsorption experiments, we have shown that the description in terms of only two levels is valid. However, when the saturation parameter becomes large, we enter the nonlinear regime, and the two-level system approach might be questionable, especially when the frequency of the laser field is at resonance with the surface plasmon frequency. Thus, the double plasmon, which is the second collective excited state of the center-of-mass system, may play a role in the context of pump-probe experiments where the intensity of the pump laser field is particularly intense.

By means of a semiclassical expansion, we have evaluated the surface plasmon linewidth.

To this end, we have assumed that the single-particle self-consistent states are perfectly confined in a step-like mean-field potential. This particularly simple approximation appears to yield reliable results in the case of an alkaline-metal nanoparticle in vacuum. At zero temperature, taking only into account the smooth semiclassical density of states of the particles and of the holes, we have recovered the well-known size dependence of the surface plasmon linewidth first found by Kawabata and Kubo [48]. The linewidth scales with the inverse size of the nanoparticle, this due to the confinement of the self-consistent states. Furthermore, we have recovered for the linewidth the frequency dependence of Refs. 29 and 30. Taking into account the semiclassical oscillating density of states, we have shown that the surface plasmon linewidth exhibits a nonmonotonic behavior as a function of the size of the nanoparticle. This comes in addition to the smooth inverse-size scaling. This oscillatory behavior is non-negligible for the smallest cluster sizes. Comparing our semiclassical result for the surface plasmon linewidth with the numerical calculations of the time-dependent local density approximation (TDLDA), we have obtained a quantitative agreement. Furthermore, this oscillating feature is consistent with experiments [18, 101]. We have also extended our semiclassical expansion to the case of finite temperature. By means of a low-temperature expansion, we have shown that finite temperatures lead to a broadening of the surface plasmon resonance. This effect has been found to be weak, consistently with the experiments [46, 47, 95, 96].

The spill-out effect arising from the electronic density outside the nanoparticle has been analyzed. With the help of a semiclassical expansion, we have shown that the ratio of spill-out electrons over the total number scales as the inverse size of the nanoparticle. Thus, the resulting redshift of the classical Mie frequency induced by the electronic spill-out scales also with the inverse size of the cluster, in qualitative agreement with the experiments. Introducing in our semiclassical expansion an effective radius for the nanoparticle which takes into account the details of the self-consistent mean-field potential near the jellium edge, we have obtained good agreement with LDA calculations. By means of a Sommerfeld low-temperature expansion of the number of spill-out electrons, we have shown that the redshift induced by the spill-out increases with increasing temperature.

Comparing the surface plasmon resonance frequency deduced from the LDA number of spill-out electrons with the maximum of the TDLDA absorption curve, we have concluded that the spill-out effect is not sufficient to describe the redshift of the surface plasmon resonance. This has been noticed experimentally a long time ago [11, 25], and the failure of the local density approximation has been invoked to explain this discrepancy. In this thesis, we have tested a mechanism which leads to an additional redshift of the resonance frequency, namely the coupling of the surface plasmon excitation with the electronic environment. This effect has been suggested in Refs. 60 and 102. We have calculated the environment-induced redshift, and shown that it is of the same order of magnitude as the spill-out-induced redshift. Thus, it has to be taken into account in the description of the numerical and experimental results. With our semiclassical expansion, we have demonstrated that this shift scales with the inverse size of the nanoparticle, and is increased by the temperature, similarly to the shift induced by the spill-out effect. Despite the various approximations of our model, our result implies an increase of the

redshift of the surface plasmon frequency beyond the one caused by the spill-out effect. However, we have not obtained a quantitative agreement compared to the calculated resonance frequency within the TDLDA. Our semiclassical theory predicts that for the smallest sizes of nanoparticles, the shift induced by the environment should present a nonmonotonic behavior as a function of the size. This is confirmed by the numerical calculations. No oscillations are expected for the redshift caused by the spill-out effect. Thus we have two qualitatively different behaviors which could permit to distinguish between both effects.

Our theory of the thermal broadening of the surface plasmon linewidth, together with the temperature dependence of the resonance frequency, has permitted us to qualitatively explain the differential transmission curves measured in time-resolved pump-probe experiments. Our findings could open the possibility to analyze relaxation processes in excited nanoparticles.

We have addressed the question of the relevance and of the existence of the second collective state in metallic nanoparticles (the double plasmon). We have neglected the anharmonic effects which become noticeable for very small clusters [60, 111], and determined the lifetime of this second collective state. Depending on the physical situation, the double plasmon state can decay by two distinct mechanisms: Landau damping and particle ionization. For the Landau damping, there are two processes of the first and second order which leads to the decay of such a collective state. The first-order process yields a linewidth which is twice the linewidth of the single surface plasmon state. Extending our semiclassical expansions to the nonlinear case, we have shown that the linewidth associated to the second-order process can be neglected. Calculating the linewidth induced by the ionization of the nanoparticle, we have obtained good agreement with existing theoretical [71] and experimental works [72, 73], despite the approximation we have been forced to make in order to address this difficult problem. Our semiclassical calculations show that the double plasmon state is a well-defined excitation, and an experimental observation of such a state could be in principle possible, provided one can excite this state with a sufficiently strong laser excitation.

Exploring the effects of an inhomogeneous dielectric environment on the single surface plasmon excitation (like it is for instance the case in embedded noble-metal nanoparticles), we have shown that the simple analytical prediction implies an increase of the surface plasmon linewidth with the dielectric constants, while the TDLDA calculations predict a decrease of the same quantity. We have seen that this discrepancy is due to the approximation of an infinitely steep self-consistent potential. As the LDA calculations show, the slope of the self-consistent potential decreases as the dielectric constants increase. This has been confirmed with the help of a simple Thomas-Fermi model for a metallic slab. Refining our semiclassical calculation of the linewidth by taking into account the steepness of the mean-field potential, we have been able to obtain a qualitative agreement with the TDLDA calculations, themselves in accordance with existing experiments.

9.2 Outlook and future perspectives

In this section we present an outlook of the work presented in this thesis, as well as possible further improvements.

All our analytical derivations have been carried out within the mean-field approximation. Furthermore, the numerical calculations have been based on the local density approximation. Those two different approximations are reliable for relatively large nanoparticles. For very small clusters, they become questionable. A way to test those approximations is to use an "exact" diagonalization of the many-body electronic Hamiltonian. From the numerical diagonalization, one obtains the many-body eigenstates and eigenenergies of the correlated system, and therefore can deduce the absorption spectrum of the nanoparticle. Thus, one can extract for instance the linewidth and the resonance frequency of the surface plasmon excitation. This is also a way to check if the surface plasmon state is mainly a superposition of one particle-one hole excitations as described in the random phase approximation, or if one has to consider more excitations to well describe this collective state. Such an exact diagonalization approach has been carried out in different works [119–123], adapting the nuclear shell model [6, 7] to the case of metallic nanoparticles. It was shown that the surface plasmon remains a well defined excitation even in very small clusters with a very small number of atoms (between 8 and 20). During this thesis, we also have performed such exact-diagonalization calculations.[1] Restricting ourselves to spinless fermions, we have observed that the surface plasmon excitation is indeed well-defined, already for only four interacting electrons. Furthermore, the surface plasmon peak supports almost all the oscillator strength and its frequency is redshifted with respect to the classical Mie value. It could be interesting to extend these calculations to larger clusters, including the spin of the electron. This could be a way to test our prediction concerning the oscillatory behavior of the surface plasmon linewidth. However, even with the most modern computers, we are restricted to quite small nanoparticles because of the very large number of Slater determinants required in such an approach.

Our description of the dynamics of the surface plasmon excitation in terms of a reduced density matrix approach has been based on several approximations. The Markovian approximation has been used with the only justification that the environment contains a large number of degrees of freedom. The fact that the dynamics is Markovian could be tested by quantitatively evaluating the correlation function of the environment (3.25), either numerically or with the help of semiclassical expansions as used in this thesis. A preliminary semiclassical calculation shows that the correlation function decreases when the size of the cluster increases. This is quite natural, since the size is of course related to the number of electrons in the nanoparticle, and thus to the number of degrees of freedom of the environment. However, the relevant dependence which is useful to assess that we deal with a Markov process is the time dependence of the correlation function. But there exists good indications that we deal with a Markov process. Indeed, within this approximation, the obtained expression for the linewidth of the surface plasmon (that

[1] Not included in this thesis.

one can equivalently obtained by virtue of Fermi's golden rule) is in agreement with the numerical calculations of the TDLDA. If the dynamics were radically non-Markovian, this would not be the case.

The solutions of the master equation have been obtained, within a two-level approach, with the help of the rotating wave approximation which assumes that the frequency of the external driving field is close to the resonance energy of the system. We have seen in this context that the detuning between the two above-mentioned frequencies plays a role on the surface plasmon dynamics. However, we cannot pretend to describe accurately this dynamics if we are far from resonance. The accuracy of the rotating wave approximation could then be tested by solving numerically the master equation without appealing to this assumption.

An improvement of our density matrix formalism could be to consider a dynamical environment. Indeed, in our approach, we have assumed that the environment is in a thermal equilibrium and does not evolve with time. Thus, it does not permit to account for the cooling of the electronic temperature of the heat bath after an excitation by a laser pulse. This would be of great interest for the description of pump-probe experiments, where, as we have shown, the electronic temperature plays a crucial role in the interpretation of the measured differential transmission curves. A time dependence of the density matrix of the environment could be introduced via a time-dependent electronic temperature which decreases as a function of time (as described, e.g., in the two-temperature model). However, we expect that the introduction of a dynamical environment renders the density-matrix approach much more involved than in the case of a static environment.

Our prediction for the oscillatory behavior of the surface plasmon linewidth as a function of the size of the nanoparticle has been restricted to the case of zero temperature, where the calculations are already quite involved. We expect that for increasing temperature, this nonmonotonic behavior should be smoothed out because of the thermal fluctuations. However, a quantitative estimate could be carried out to confirm our expectation.

In our semiclassical evaluation of the environment-induced redshift of the surface plasmon frequency, we have not obtained a quantitative agreement with the resonance frequency deduced from the TDLDA calculations. This could be due to the fact that we have not accurately taken into account the single-particle self-consistent states of the continuum which, contrarily to the linewidth, could presumably play a role. Such an assumption has been done in order to simplify this difficult problem. An improvement of the present calculations thus could be obtained by considering those extended states. However, the inclusion of the states of the continuum in this calculation is quite difficult analytically, considering the complexity of the dipole matrix elements in this case (see our analysis of the decay of the double plasmon via ionization of an electron in Sec. 7.2). A direct numerical calculation of the environment-induced redshift of the surface plasmon frequency within the mean-field approximation could provide a way to test the role of the extended states.

Finally, in all this thesis we have restricted ourselves to the case of spherical nanoparticles. The spherical symmetry has allowed us to significantly simplify our approach by

separating the angular and radial motions. In some sense, it represents an ideal theoretical framework. An extension of the present calculations to the case of nonspherical nanoparticles could be of relevance, both for theoretical and experimental purposes.

Appendix A

Three-level system

L'art de persuader consiste autant en celui d'agréer qu'en celui de convaincre.

(Blaise Pascal, 1632-1662, in De l'esprit géométrique)

In this appendix, we discuss under which conditions the center-of-mass system, whose Hamiltonian is given in (2.30), can be described by a two-level system. To show that the two level approach can be relevant, the strategy is as follows. We consider a three level system, including damping mechanisms in addition to the Landau damping. The Landau damping linewidth is for the n^{th} level of the harmonic oscillator at zero temperature $\gamma_n = n\gamma$ according to (3.39), $\gamma = \gamma_-$ being the width of the first excited state that we calculate in Chapter 4. The additional damping mechanisms can be of two kinds: (i) First order decay processes which lead to the decay of the second collective state into the first one, as for instance the radiation damping [10, 11], or the coupling to the surrounding matrix, and (ii) second order decay processes which result in the direct decay from the second excited state to the ground state, like it is the case for example for the ionization of an electron due to the intense laser field (see Chapter 7). These two decay channels are illustrated on Fig. A.1.

In the following we denote by γ_1 the width resulting from the additional first-order damping mechanisms, and by γ_2 the second order ones. We then write the master equation (3.49) for the three levels, and we include the additional decay channels according to the Lindblad theory [88, 89]:

$$\begin{aligned}\dot{\rho}_{nm}(t) = &-\mathrm{i}\omega_{\mathrm{sp}}(n-m)\rho_{nm}(t) - \gamma\left[\frac{n+m}{2}\rho_{nm}(t) - \sqrt{(n+1)(m+1)}\rho_{n+1,m+1}(t)\right]\\ &- \mathrm{i}\Omega_{\mathrm{R}}\cos(\omega_{\mathrm{L}}t)\left[\sqrt{n}\rho_{n-1,m}(t) + \sqrt{n+1}\rho_{n+1,m}(t) - \sqrt{m}\rho_{n,m-1}(t) - \sqrt{m+1}\rho_{n,m+1}(t)\right]\\ &+ \langle n|\sum_{a=1,2}\gamma_a\left(L_a\rho L_a^\dagger - \frac{1}{2}L_a^\dagger L_a\rho - \frac{1}{2}\rho L_a^\dagger L_a\right)|m\rangle, \end{aligned} \tag{A.1}$$

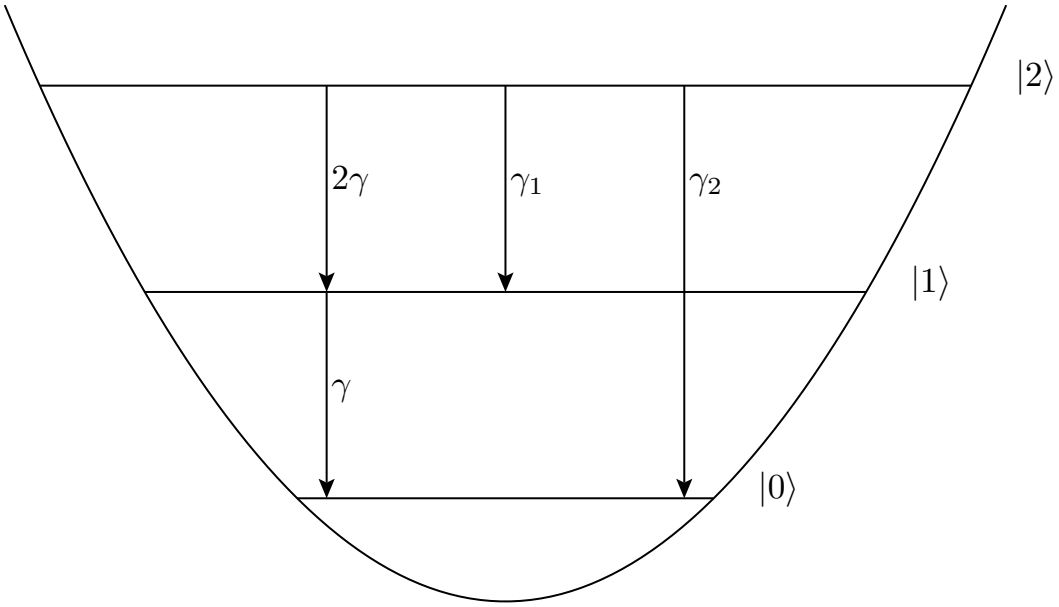

Figure A.1: Schematics of the three-level system with additional damping mechanisms. γ is the Landau damping linewidth resulting from the coupling to the electronic environment, while γ_1 and γ_2 accounts for additional damping mechanisms of the first and second order, respectively.

where Ω_R is the Rabi frequency defined in (2.41). We choose the Lindblad operators as $L_1 = |1\rangle\langle 2|$ and $L_2 = |0\rangle\langle 2|$, which leads to transitions between the center-of-mass states $|2\rangle$ and $|1\rangle$, and $|2\rangle$ and $|0\rangle$, respectively (see Fig. A.1). We then obtain in the rotating wave approximation the following set of coupled differential equations:

$$\dot{\hat{\rho}}_{00} = -\mathrm{i}\frac{\Omega_\mathrm{R}}{2}\left(\hat{\rho}_{10} - \hat{\rho}_{01}\right) + \gamma\hat{\rho}_{11} + \gamma_2\hat{\rho}_{22}, \tag{A.2a}$$

$$\dot{\hat{\rho}}_{11} = -\mathrm{i}\frac{\Omega_\mathrm{R}}{2}\left[\hat{\rho}_{01} - \hat{\rho}_{10} + \sqrt{2}\left(\hat{\rho}_{21} - \hat{\rho}_{12}\right)\right] - \gamma\hat{\rho}_{11} + (2\gamma + \gamma_1)\hat{\rho}_{22}, \tag{A.2b}$$

$$\dot{\hat{\rho}}_{22} = -\mathrm{i}\frac{\Omega_\mathrm{R}}{2}\sqrt{2}\left(\hat{\rho}_{12} - \hat{\rho}_{21}\right) - \left(2\gamma + \sum_{a=1,2}\gamma_a\right)\hat{\rho}_{22}, \tag{A.2c}$$

$$\dot{\hat{\rho}}_{01} = -\mathrm{i}\delta_\mathrm{L}\hat{\rho}_{01} - \mathrm{i}\frac{\Omega_\mathrm{R}}{2}\left(\hat{\rho}_{11} - \hat{\rho}_{00} - \sqrt{2}\hat{\rho}_{02}\right) - \frac{\gamma}{2}\hat{\rho}_{01} + \sqrt{2}\gamma\hat{\rho}_{12}, \tag{A.2d}$$

$$\dot{\hat{\rho}}_{12} = -\mathrm{i}\delta_\mathrm{L}\hat{\rho}_{12} - \mathrm{i}\frac{\Omega_\mathrm{R}}{2}\left[\hat{\rho}_{02} + \sqrt{2}\left(\hat{\rho}_{22} - \hat{\rho}_{11}\right)\right] - \frac{1}{2}\left(3\gamma + \sum_{a=1,2}\gamma_a\right)\hat{\rho}_{12}, \tag{A.2e}$$

$$\dot{\hat{\rho}}_{02} = -2\mathrm{i}\delta_\mathrm{L}\hat{\rho}_{02} - \mathrm{i}\frac{\Omega_\mathrm{R}}{2}\left(\hat{\rho}_{12} - \sqrt{2}\hat{\rho}_{01}\right) - \frac{1}{2}\left(2\gamma + \sum_{a=1,2}\gamma_a\right)\hat{\rho}_{02}. \tag{A.2f}$$

As in Chapter 3, we have used the notation $\rho_{nm} = \hat{\rho}_{nm}\mathrm{e}^{-\mathrm{i}\omega_\mathrm{L}(n-m)t}$, while $\delta_\mathrm{L} = \omega_\mathrm{L} - \omega_\mathrm{sp}$ is the detuning between the frequency of the external driving field and the surface plasmon

frequency.

A.1 Rabi oscillations of a three-level system

As a first insight into the three-level system, we consider here the case where there is no damping at all, i.e., $\gamma = \gamma_1 = \gamma_2 = 0$ in (A.2). The system therefore experiences Rabi oscillations between the ground state and the two excited states due to the laser field which is switched on at $t = 0$.

In the case where there is no detuning between the laser and surface plasmon frequencies, it is possible to solve (A.2) analytically. Assuming that at $t = 0$, the system is in its ground state, i.e., $\rho_{00}(0) = 1$, $\rho_{11}(0) = \rho_{22}(0) = 0$, and all the coherences are equal to 0, we obtain for the populations

$$\rho_{00}(t) = \frac{1}{18}\left[9 + 8\cos\left(\frac{\sqrt{3}}{2}\Omega_{\mathrm{R}}t\right) + \cos\left(\sqrt{3}\Omega_{\mathrm{R}}t\right)\right], \tag{A.3a}$$

$$\rho_{11}(t) = \frac{1}{6}\left[1 - \cos\left(\sqrt{3}\Omega_{\mathrm{R}}t\right)\right], \tag{A.3b}$$

$$\rho_{22}(t) = \frac{1}{9}\left[3 - 4\cos\left(\frac{\sqrt{3}}{2}\Omega_{\mathrm{R}}t\right) + \cos\left(\sqrt{3}\Omega_{\mathrm{R}}t\right)\right]. \tag{A.3c}$$

We present the result of (A.3) in Fig. A.2. It is interesting to notice that the probability to find the ground state unoccupied is never zero, while the second excited state cannot be found occupied with a probability of one. The fact that the first excited state is, in average, the less probable state comes from the fact that it is related via dipole matrix elements to two states (namely $|0\rangle$ and $|2\rangle$), while the two other states are connected only once. This feature is peculiar to the three-level system without any damping. In the case of an infinite number of levels, all the excited states are connected twice.

When $\delta_{\mathrm{L}} \neq 0$, one can solve easily the system (A.2) with $\gamma = \gamma_1 = \gamma_2 = 0$ numerically. In Fig. A.3, we show the population ρ_{22} of the second excited state for different values of the detuning (scaled by the Rabi frequency Ω_{R}). We see that as the detuning is increased, the probability to find the state $|2\rangle$ occupied is in average lowered. The detuning therefore plays a crucial role, and one might argue that for a reasonable value of δ_{L}, one can neglect the second excited state. In experiments, there exists in most of the cases a detuning between the surface plasmon frequency and the frequency of the laser field. Thus it seems reasonable to approximate the center of mass by a two-level system. Moreover, as it will be seen in the following section, the damping mechanisms decrease the probability to find the second collective state occupied.

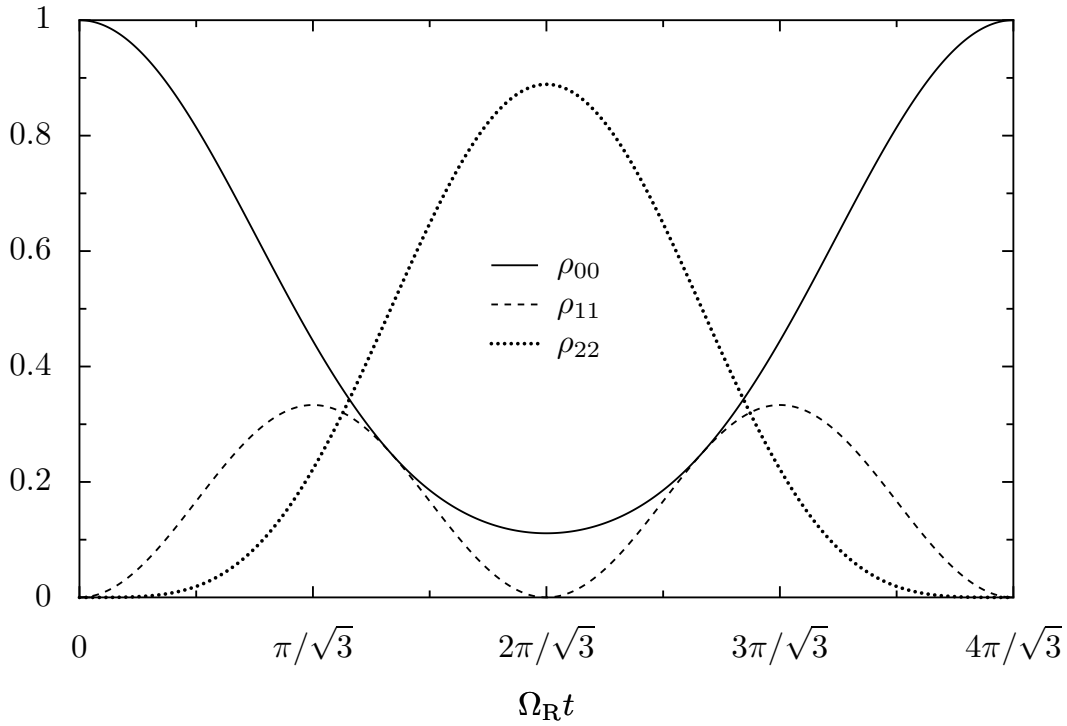

Figure A.2: Population of the ground state ρ_{00} and of the two excited states ρ_{11} and ρ_{22} as a function of time for $\delta_{\mathrm{L}} = 0$ (no detuning) and $\gamma = \gamma_1 = \gamma_2 = 0$ (no damping).

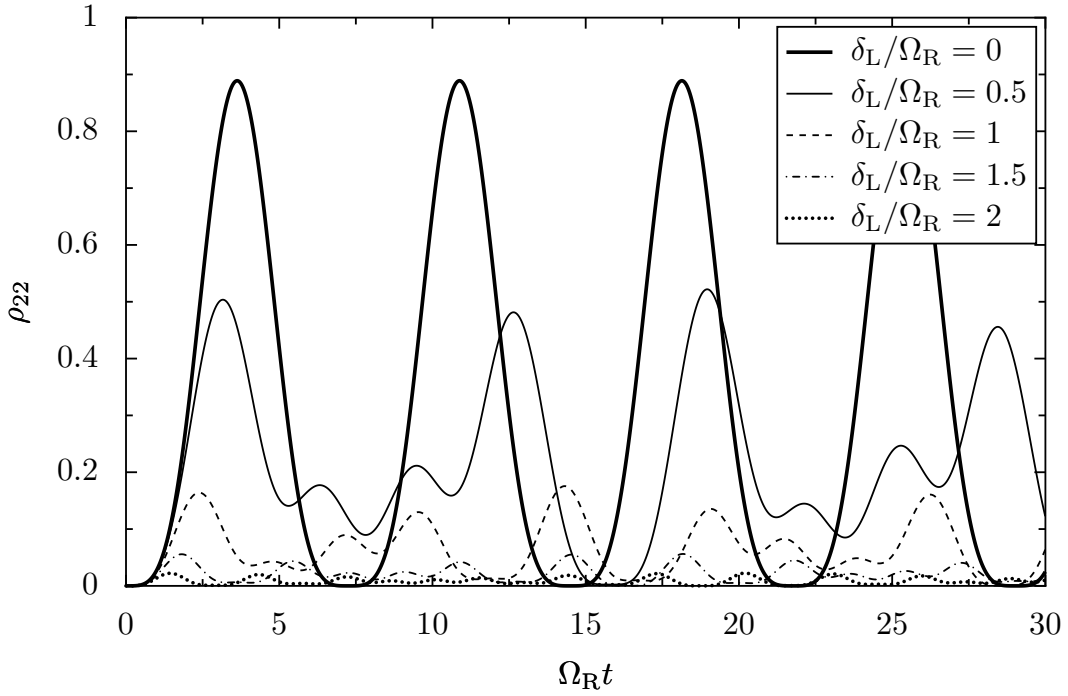

Figure A.3: Population of the second excited state ρ_{22} as a function of time for different values of the detuning δ_L. There is no damping ($\gamma = \gamma_1 = \gamma_2 = 0$).

A.2 Three-level system with additional damping mechanisms

We now consider the three-level system depicted in Fig. A.1 in presence of damping mechanisms. In Sec. A.2.1, we consider the case where there is no additional damping constant ($\gamma_1 = \gamma_2 = 0$), while in Sec. A.2.2, we move on to the description of the complete model that we consider here.

A.2.1 Stationary solutions for the case $\gamma_1 = \gamma_2 = 0$ (no additional damping constants)

For $\gamma_1 = \gamma_2 = 0$, the stationary populations of (A.2) are given by

$$\rho_{00}^{\mathrm{st}} = \frac{s(s+2) + 8 + 8\Delta^2(s+8) + 128\Delta^4}{3s(s+2) + 8 + 8\Delta^2(3s+8) + 128\Delta^4}, \tag{A.4a}$$

$$\rho_{11}^{\mathrm{st}} = \frac{s(s+4+16\Delta^2)}{3s(s+2) + 8 + 8\Delta^2(3s+8) + 128\Delta^4}, \tag{A.4b}$$

$$\rho_{22}^{\mathrm{st}} = \frac{s^2}{3s(s+2) + 8 + 8\Delta^2(3s+8) + 128\Delta^4}, \tag{A.4c}$$

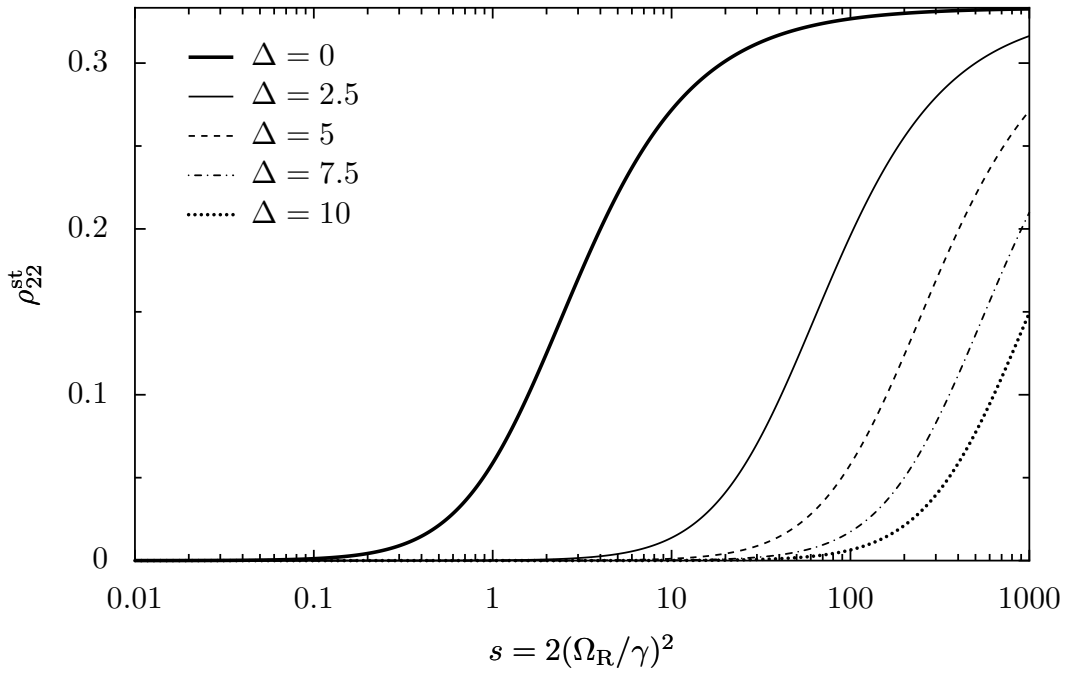

Figure A.4: ρ_{22}^{st} according to (A.4c) as a function of the saturation parameter s for increasing values of the detuning $\Delta = \delta_{\mathrm{L}}/\gamma$.

where the saturation parameter s is defined in (3.59) and where the scaled detuning Δ is given by (3.60). In Fig. A.4, we show ρ_{22}^{st} as a function of s for increasing values of Δ. The population of the second excited state increases with s for a fixed detuning. Thus, as the intensity of the laser field increases, the two-level system approach might be less and less valid. However, the population of the second excited state decreases with increasing detuning. As it is the case for the free Rabi oscillations (i.e., when there is no damping at all, see Sec. A.1), we see that the detuning plays in favor of a description of the center of mass by a two-level system.

A.2.2 Stationary solutions for the three-level system with additional dampings

We now consider the case where γ_1 and γ_2 are finite in (A.2). As a simplifying hypothesis, we assume that the two additional damping constants are equal, i.e., $\gamma_1 = \gamma_2 = \gamma_{\mathrm{add}}$. In Fig. A.5, we show the stationary solution of (A.2) for the population of the second excited state ρ_{22}^{st} as a function of $\gamma_{\mathrm{add}}/\gamma$ for different values of the detuning Δ. The figure presents the case of a large saturation parameter ($s = 100$). It shows that for $\Delta \gtrsim 5$, the probability to find the second collective state occupied is less than 10 % and is almost constant as a function γ_{add}. In the case $\Delta < 5$, ρ_{22}^{st} decreases with γ_{add} but is still quite important. There, the assumption of a two-level system to describe the surface plasmon dynamics might be questionable.

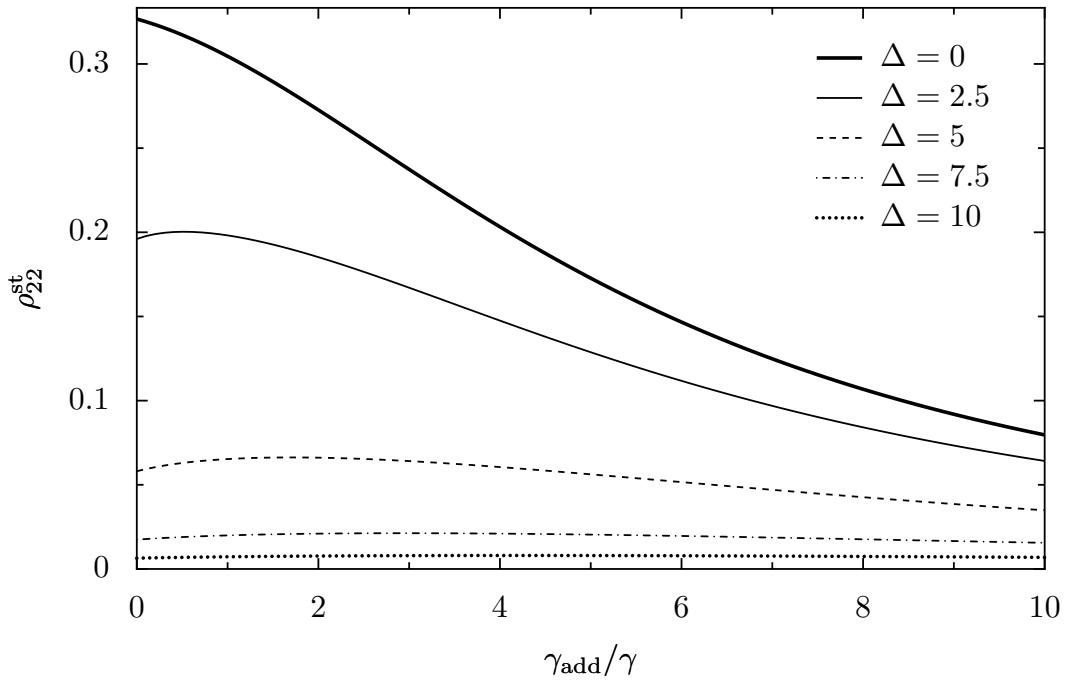

Figure A.5: Stationary solution of (A.2) for the population of the second excited state as a function of the additional damping constant γ_{add} and for various values of the detuning Δ. In the figure, the saturation parameter is $s = 100$.

In conclusion, we have shown in this appendix that for a rather small saturation parameter, i.e., for a weak external laser field, the second collective state can be neglected for the description of the surface plasmon dynamics. In the case of a large saturation parameter, as it is for example the case in pump-probe experiments, this second collective state can be neglected for finite values of the detuning between the frequency of the pump laser and the resonance frequency. However, at resonance, the description in terms of only two levels might be questionable even in presence of additional damping mechanisms. Thus, the double plasmon state might play a role on the dynamics of the surface plasmon excitation.

Appendix B

Semiclassical physics

Chaque homme doit inventer
sont chemin.

(Jean-Paul Sartre, 1905-1980, in Les Mouches)

The semiclassical approximation has been developed since the early stages of the quantum theory in the 1920's in order to solve problems that are too complex to treat in a fully quantum mechanical fashion. These are, for instance, the determination of the quantum spectrum of a particle in a complicated potential, the scattering properties of a particle moving against a potential barrier, etc. In the 1970's, a renewal of the interest in the semiclassical theory occurred with the advent of quantum chaos.[1] A chaotic system is characterized by the sensibility of the classical trajectories to the initial conditions (e.g., a particle bouncing in a stadium billiard) [94]. In such a system, the trajectory of the particle diverges exponentially from its original path if the initial conditions are changed even slightly. It turns out that the spectral properties of a complex quantum system (for example a heavy nucleus) can be explained in terms of the features of a generic classically chaotic system, using, e.g., the random matrix theory. It appeared at that time that the spectral properties of "chaotic" quantum systems are universal [94]. More recently, the concepts of the semiclassical theory has been applied to the case of mesoscopic systems [126], like the transport properties of quantum dots [127], or the many-particle properties of nanoparticles [11, 124].

[1] Quantum chaos is the theory studying the quantum properties — especially the spectrum — of *classically* chaotic systems [4, 94, 124, 125]. Rigorously, this denomination does not have much sense since it seems to imply the existence of trajectories in quantum mechanics. This goes against Heisenberg's uncertainty principle. As we will see in the sequel of this appendix, this name is more justified when one employs the semiclassical formalism, where trajectories are meaningful.

B.1 Quantum propagator

The quantum propagator plays a key role in quantum mechanics. This object is important since it draws a link between quantum and classical mechanics [128] within the formalism of Feynman's path integrals [129].

One of the main problem of quantum mechanics is to solve the time-dependent Schrödinger equation

$$\mathrm{i}\hbar\frac{\partial}{\partial t}|\psi\rangle = H|\psi\rangle, \tag{B.1}$$

where the state of the system $|\psi\rangle$ evolves in time under the influence of the Hamiltonian H. We assume in the following that we have a conservative system, i.e., the Hamiltonian is time-independent. The formal solution of (B.1) is

$$|\psi(t)\rangle = \mathrm{e}^{-\mathrm{i}H(t-t_0)/\hbar}|\psi(t_0)\rangle, \tag{B.2}$$

where t_0 is the initial time. We can interpret this result as follows: Starting with the initial state $|\psi(t_0)\rangle$, the state of the system at a future time t is given by an evolution operator acting on the initial state. This operator then contains all the information on the time evolution of the system. Writing (B.2) in position representation, one obtains

$$\psi(\mathbf{r},t) = \int \mathrm{d}^d\mathbf{r}_0 K(\mathbf{r},\mathbf{r}_0;t-t_0)\psi(\mathbf{r}_0,t_0), \tag{B.3}$$

with the propagator[2]

$$K(\mathbf{r},\mathbf{r}_0;t) = \langle\mathbf{r}|\mathrm{e}^{-\mathrm{i}Ht/\hbar}|\mathbf{r}_0\rangle. \tag{B.4}$$

This quantity is the matrix element (in position representation) of the evolution operator. Then the knowledge of the initial state and of the propagator provides the state of the system at a later time.

B.2 Feynman's path integrals

Feynman's formalism of quantum mechanics [129] is equivalent to the ones of Schrödinger and Heisenberg. It permits to interpret the quantum propagator in terms of trajectories, by virtue of the so-called *path integrals* or functional integrals. Within this formalism, the propagator (B.4) reads [4, 129, 130]

$$K(\mathbf{r},\mathbf{r}_0;t) = \int \mathcal{D}[\mathbf{r}]\mathrm{e}^{\mathrm{i}R[\mathbf{r}]/\hbar}, \tag{B.5}$$

where

$$R(\mathbf{r},\mathbf{r}_0;t) = \int_0^t \mathrm{d}t' L\left(\dot{\mathbf{r}}(t'),\mathbf{r}(t'),t'\right) \tag{B.6}$$

[2] d is the dimension of the real space.

is the Hamilton principal function.[3] The Lagrangian of the system is $L = T - V$ where T and V are the kinetic and potential energies, respectively, and $\mathbf{r}(t)$ stands for a trajectory. The symbol $\mathcal{D}[\mathbf{r}]$ represents the measure of the functional integral, and this quantity is extremely difficult to evaluate in the general case. However one can interpret the result (B.5) obtained in 1948 by Feynman in the following way: The propagator is the sum over all possible trajectories between $\mathbf{r}_0$ and $\mathbf{r}$ of the exponential of a phase given by the Hamilton principal function divided by the Planck constant $\hbar$. We will see in the next section that one can evaluate the quantum fluctuations around the classical paths, and that the classical contributions dominate in the limit "$\hbar \to 0$": This is the semiclassical approximation.

B.3 Semiclassical approximation of the propagator and of the Green function

We are now interested in the semiclassical limit of the propagator (B.5). This means that we are concerned with leading order in $1/\hbar$ contributions, for "$\hbar \to 0$", this statement becoming meaningful in the sequel.

B.3.1 Free propagator and van Vleck's approximation

For the sake of clarity, let us first examine the propagator of a free particle, that is when $V = 0$. One can easily show [124] that the exact quantum propagator of a free particle of mass μ is

$$K_{\text{free}}(\mathbf{r}, \mathbf{r}_0; t) = \left(\frac{\mu}{2\pi \mathrm{i}\hbar t}\right)^{d/2} \mathrm{e}^{(\mathrm{i}\mu/2\hbar t)(\mathbf{r}-\mathbf{r}_0)^2}. \tag{B.7}$$

Now, the quantity appearing in the exponential is exactly $\mathrm{i}/\hbar$ times the Hamilton principal function of a free particle, $R_{\text{free}}(\mathbf{r}, \mathbf{r}_0; t)$. Furthermore if one calculates the determinant of the second (negative) variation of R_{free}, one obtains

$$\det\left(-\frac{\partial^2 R_{\text{free}}}{\partial \mathbf{r} \partial \mathbf{r}_0}\right) = \left(\frac{\mu}{t}\right)^d. \tag{B.8}$$

Then, one can write the propagator (B.7) as

$$K_{\text{free}}(\mathbf{r}, \mathbf{r}_0; t) = \left(\frac{1}{2\pi \mathrm{i}\hbar}\right)^{d/2} \sqrt{\det\left(-\frac{\partial^2 R_{\text{free}}}{\partial \mathbf{r} \partial \mathbf{r}_0}\right)}\ \mathrm{e}^{\mathrm{i}R_{\text{free}}(\mathbf{r},\mathbf{r}_0;t)/\hbar}. \tag{B.9}$$

Van Vleck proposed in 1928 the following prescription in order to obtain an approximate propagator of a particle moving in the potential V [128]: replace R_{free} in (B.9) by

[3] We reserve the name of *action* to the quantity $S(\varepsilon) = R + \varepsilon t = \int \mathrm{d}\mathbf{r} \cdot \mathbf{p}$, Legendre transform of the Hamilton principal function at fixed energy.

R, the Hamilton principal function of a particle in the potential V. He then obtained the following expression:

$$K_{\text{vanVleck}}(\mathbf{r}, \mathbf{r}_0; t) = \left(\frac{1}{2\pi \mathrm{i}\hbar}\right)^{d/2} \sqrt{\det C}\ \mathrm{e}^{\mathrm{i}R(\mathbf{r},\mathbf{r}_0;t)/\hbar}, \tag{B.10}$$

with C the matrix defined by its elements

$$C_{ij}(\mathbf{r}, \mathbf{r}_0; t) = -\frac{\partial^2 R}{\partial r_i \partial r_{0,j}},\ \forall (i,j) = 1, ..., d. \tag{B.11}$$

As we will see in the sequel, Gutzwiller [94] added some important phases of quantum origin to van Vleck's result (B.10) to obtain the semiclassical propagator.

B.3.2 Gutzwiller's approximation to the propagator and the Green function — Semiclassical expansions

In the following we only present the principal ideas of the approximation due to Gutzwiller. His work in the 1970's was principally inspired by van Vleck's previous idea. The integrand in Feynman's expression of the propagator (B.5) is a highly oscillating functional in the space of trajectories since, in general, the variations of R are much larger than $\hbar$. It is then appropriate to use the stationary phase approximation that we briefly present in the next paragraph.

The stationary phase approximation

The stationary phase approximation is maybe the most widely used approximation in semiclassical physics. Let us here present this method for the simpler case of an ordinary integration [130]: Consider the following one-dimensional integral

$$I(\alpha) = \int_a^b \mathrm{d}x g(x) \mathrm{e}^{\mathrm{i}\alpha f(x)} \tag{B.12}$$

in the limit of a large parameter α. The function $g(x)$ is assumed to be sufficiently smooth compared to the term in the exponential. The principal idea of this approximation is that the integral $I(\alpha)$ is dominated by the region of integration where the phase $f(x)$ is stationary. Outside this region, the phase oscillates very rapidly and consequently the contribution to the total integral is negligible to the leading order in α.

In the following we suppose that there is only one stationary point $\bar{x}$ — given by the condition $f'(\bar{x}) = 0$ — and that this point belongs to the interval $]a, b[$. We can therefore expand the function $f(x)$ around the stationary point $\bar{x}$ as

$$f(x) \simeq f(\bar{x}) + \frac{1}{2} f''(\bar{x})(x - \bar{x})^2, \tag{B.13}$$

and replace $g(x)$ by $g(\bar{x})$ in (B.12). Therefore the integral (B.12) has the approximate expression

$$I(\alpha) \simeq g(\bar{x}) \mathrm{e}^{\mathrm{i}\alpha f(\bar{x})} \int_a^b \mathrm{d}x \ \mathrm{e}^{\mathrm{i}\alpha f''(\bar{x})(x-\bar{x})^2/2}. \tag{B.14}$$

Since one restricts the expansion of the function $f(x)$ up to the quadratic order, one can reasonably replace the boundaries of the integral by $\pm\infty$ [4] and one has only to evaluate the Gaussian integral given by

$$\int_{-\infty}^{+\infty} \mathrm{d}x \ \mathrm{e}^{\mathrm{i}ax^2} = \sqrt{\frac{\pi}{|a|}} \mathrm{e}^{\mathrm{i}\pi \mathrm{sign}(a)/4}. \tag{B.15}$$

Within the stationary phase approximation, one thus obtains

$$I(\alpha) \simeq \sqrt{\frac{2\pi}{|\alpha f''(\bar{x})|}} g(\bar{x}) \ \mathrm{e}^{\mathrm{i}\{\alpha f(\bar{x}) + \mathrm{sign}[\alpha f''(\bar{x})]\pi/4\}}. \tag{B.16}$$

This method is also extended to functions of several variables $f(x_1, \cdots, x_d)$. In this case, one has to be aware that it is necessary to diagonalize the terms of order 2 in the development of the function f, in order to get d Gaussian integrals.

Gutzwiller's semiclassical derivation

We are now able to apply the stationary phase approximation in our case of interest, i.e., when the variations of Hamilton's principal function R are much larger than $\hbar$.[5] Consequently, regarding (B.5), the trajectories that contribute the most to the path integral are those for which the first variation of R vanishes, $\delta R = 0$. These are, by virtue of the Hamilton-Jacobi principle [131, 132], the *classical paths* which contribute the most to the quantum propagator. The quantum fluctuations are of higher order in $\hbar$. Gutzwiller [94, 125] then arrived to the following conclusion: One has to sum the propagator of (B.5) over all the classically allowed paths between $\mathbf{r}_0$ and $\mathbf{r}$, but taking into account the following subtlety: It can occur that the determinant of the matrix C defined in (B.11) vanishes at certain points, the so-called *conjugated points*, the physical meaning of that type of points becoming clearer in the sequel, and consequently the stationary phase approximation is no longer valid. This has the consequence to introduce an additional phase factor in the exponential appearing in the expression of the propagator. Finally, the semiclassical propagator is

$$\mathcal{K}(\mathbf{r}, \mathbf{r}_0; t) = \left(\frac{1}{2\pi \mathrm{i}\hbar}\right)^{d/2} \sum_{\lambda} \sqrt{|\det C_\lambda|} \ \mathrm{e}^{\mathrm{i}\mathcal{R}_\lambda(\mathbf{r},\mathbf{r}_0;t)/\hbar - \mathrm{i}\kappa_\lambda \pi/2}, \tag{B.17}$$

[4] This is not the case when the stationary point coincides with one of the two boundaries ($\bar{x} = a$ or b). If so, one has to treat specifically this point.

[5] Note that the stationary phase method can only be used here by an adequate parametrization of the paths in the functional integral, which leads to an ordinary multidimensional integral [94].

where λ stands for the classical trajectories, and where κ_λ counts the number of conjugated points for the trajectory λ. $\mathcal{R}_\lambda$ is the classical Hamilton principal function, which means that one takes only into account the classical trajectories between $\mathbf{r}_0$ and $\mathbf{r}$. One shows easily that

$$C_\lambda = -\frac{\partial^2 \mathcal{R}_\lambda}{\partial \mathbf{r} \partial \mathbf{r}_0} = \left(\frac{\partial \mathbf{r}}{\partial \mathbf{p}_0} \right)_\lambda^{-1}, \tag{B.18}$$

with $\mathbf{p}_0 = -\partial \mathcal{R}_\lambda / \partial \mathbf{r}_0$ the initial momentum of the particle. Consequently, a conjugated point, defined by the fact that $\det C_\lambda = 0$, is a point for which several trajectories with different initial momenta attain this same point in the same trajectory time t.

The next stage, which will provide us the so-called *Gutzwiller trace formula* for the semiclassical density of states, is to switch from a fixed-time representation to a fixed-energy representation. Indeed, most of the physical systems that one studies are conservative systems, and it is then more appropriate to work at constant energy than at a fixed time. In other words, one is now interested in a semiclassical approximation for the retarded Green function which is the Fourier transform of the propagator (B.4) for positive times, namely

$$G(\mathbf{r}, \mathbf{r}_0; \varepsilon) = -\frac{\mathrm{i}}{\hbar} \int_0^\infty \mathrm{d}t \ \mathrm{e}^{\mathrm{i}\varepsilon t/\hbar} K(\mathbf{r}, \mathbf{r}_0; t) \tag{B.19a}$$

$$= \sum_{\mathbf{n}} \frac{\psi_{\mathbf{n}}(\mathbf{r}) \psi_{\mathbf{n}}^*(\mathbf{r}_0)}{\varepsilon - \varepsilon_{\mathbf{n}} + \mathrm{i}0^+}. \tag{B.19b}$$

In the above expression, $\varepsilon_{\mathbf{n}}$ is the single-particle eigenenergies associated to the wave function $\psi_{\mathbf{n}}(\mathbf{r})$, while $\mathbf{n} = (n_1, n_2, \cdots)$ are the quantum numbers of the system. Inserting the semiclassical propagator (B.17) into (B.19a), one obtains

$$\mathcal{G}(\mathbf{r}, \mathbf{r}_0; \varepsilon) = \frac{2\pi}{(2\pi \mathrm{i}\hbar)^{d/2+1}} \sum_\lambda \mathrm{e}^{-\mathrm{i}\kappa_\lambda \pi/2} \int_0^\infty \mathrm{d}t \sqrt{|\det C_\lambda|} \, \mathrm{e}^{\mathrm{i}[\mathcal{R}_\lambda(\mathbf{r}, \mathbf{r}_0; t) + \varepsilon t]/\hbar}. \tag{B.20}$$

One then sees appearing in the exponential the classical action

$$S_\lambda(\mathbf{r}, \mathbf{r}_0; \varepsilon) = \mathcal{R}_\lambda(\mathbf{r}, \mathbf{r}_0; t) + \varepsilon t = \int_{\mathbf{r}_0}^{\mathbf{r}} \mathrm{d}\mathbf{q}.\mathbf{p}. \tag{B.21}$$

In order to be coherent with the approximation which was done previously for the propagator, one has now to evaluate the integral over the time t with the help of the stationary phase method. Then, if $\bar{t}$ is the time for which the phase is stationary, one obtains the following condition:

$$\frac{\partial}{\partial t} \left[\mathcal{R}_\lambda(\mathbf{r}, \mathbf{r}_0; t) + \varepsilon t \right] \Big|_{t=\bar{t}} = -\varepsilon_{\bar{t}} + \varepsilon = 0, \tag{B.22}$$

that is $\bar{t}$ is the time taken by the system to go from $\mathbf{r}_0$ to $\mathbf{r}$ along the particular trajectory $\mathbf{q}(t)$ where its energy is $\varepsilon = \varepsilon_{\bar{t}}$. Finally, after this approximation, one obtains for the semiclassical retarded Green function the result [94, 125]

$$\mathcal{G}(\mathbf{r}, \mathbf{r}_0; \varepsilon) = \frac{2\pi}{(2\pi \mathrm{i}\hbar)^{(d+1)/2}} \sum_\lambda \sqrt{|D_\lambda|} \, \mathrm{e}^{\mathrm{i}S_\lambda(\mathbf{r}, \mathbf{r}_0; \varepsilon)/\hbar - \mathrm{i}\sigma_\lambda \pi/2}. \tag{B.23}$$

Here D_λ is the determinant of a $(d+1)\times(d+1)$ matrix, and is given by

$$D_\lambda(\mathbf{r},\mathbf{r}_0;\varepsilon) = (-1)^d \frac{\partial^2 S_\lambda}{\partial \varepsilon^2} \det C_\lambda = \begin{vmatrix} \dfrac{\partial^2 S_\lambda}{\partial \mathbf{r}_0 \partial \mathbf{r}} & \dfrac{\partial^2 S_\lambda}{\partial \mathbf{r}_0 \partial \varepsilon} \\ \dfrac{\partial^2 S_\lambda}{\partial \varepsilon \partial \mathbf{r}} & \dfrac{\partial^2 S_\lambda}{\partial^2 \varepsilon} \end{vmatrix}, \tag{B.24}$$

for all classical paths λ. σ_λ counts the number of conjugated points at the fixed energy ε for the trajectory λ.

General results in one-dimensional systems

Before we pursue with Gutzwiller's trace formula, let us apply the approximations detailed here for the case of a one-dimensional system. As an example, we consider a particle confined in a well $V(x)$ which can have arbitrary shape, except that we exclude in the present discussion the presence of one or several hard walls [125].

The momentum of the particle is written as $p(x) = \sqrt{2\mu[\varepsilon - V(x)]}$. Let x_- and x_+ be the classical turning points, respectively on the left and on the right of the classically accessible region, solutions of $\varepsilon = V(x_\pm)$: These are the only and unique conjugated points in this one-dimensional problem. In the following we assume that $x_- < x_0 < x < x_+$. The classical trajectories between x_0 and x are of four types, i.e., there are four different ways to travel between these two points:

1. $x_0 \longrightarrow x$;
2. $x_0 \longrightarrow x_- \longrightarrow x$;
3. $x_0 \longrightarrow x_+ \longrightarrow x$;
4. $x_0 \longrightarrow x_- \longrightarrow x_+ \longrightarrow x$.

Each of these trajectories contains its fundamental trajectory plus all the repetitions of closed orbits. In (B.23), the prefactor D_λ is reduced in this one-dimensional motion simply to the product $[p(x_0)/\mu^2]^{-1/2}[p(x)/\mu^2]^{-1/2}$ for the four families of trajectories. The indices σ_λ are for each family

1. $\sigma = 2\tilde{r}$;
2. $\sigma = 2\tilde{r} + 1$;
3. $\sigma = 2\tilde{r} + 1$;
4. $\sigma = 2\tilde{r} + 2$,

where $\tilde{r}$ if the number of repetitions of the closed orbit. The summation in (B.23) pertains only to the four families, just as to the number of repetitions $\tilde{r}$ running from 1

to ∞. The summation over $\tilde{r}$ leads to a geometrical series, and finally one obtains for $x_0 < x$

$$\mathcal{G}(x, x_0; \varepsilon) = -\frac{2\cos\left[1/\hbar \int_{x_-}^{x_0} \mathrm{d}x' p(x') - \pi/4\right] \cos\left[1/\hbar \int_{x}^{x_+} \mathrm{d}x' p(x') - \pi/4\right]}{\hbar [p(x_0)/\mu^2]^{1/4} [p(x)/\mu^2]^{1/4} \cos\left[1/\hbar \int_{x_-}^{x_+} \mathrm{d}x' p(x')\right]}. \tag{B.25}$$

From (B.19b), the poles of (B.25) give the semiclassical spectrum ε_n. Setting the cosine in the denominator to zero, one then has the condition

$$S(\varepsilon) = \oint \mathrm{d}x\, p(x) = 2\int_{x_-}^{x_+} \mathrm{d}x\, p(x) = 2\pi\hbar\left(n + \frac{1}{2}\right), \tag{B.26}$$

with n a positive integer,[6] and one recovers the well-known quantization condition of Wentzel, Kramers and Brillouin (WKB quantization) [53]. Let us notice that these poles are directly related to the phases at the classical turning points.

In order to find the residues, and in order to check that the poles of the Green function are really simple poles, one expands the cosine of the denominator in (B.25) in powers of $\varepsilon - \varepsilon_n$, and finally, to the first leading order in $1/\hbar$, one finds for the semiclassical wave function, and this because of (B.19b),

$$\psi_n^{\mathrm{sc}}(x) = \frac{2\cos\left\{1/\hbar \int_{x_-}^{x} \mathrm{d}x' \sqrt{2\mu\left[\varepsilon_n - V(x'))\right]} - \pi/4\right\}}{\sqrt{\tau}\left\{2\left[\varepsilon_n - V(x)\right]/\mu\right\}^{1/4}}, \tag{B.27}$$

with $\tau = \partial S/\partial\varepsilon$ the period of the closed orbit. Once again, this result is exactly the one given by the WKB theory, except that we have only here the wave functions in the classical accessible region, while the WKB wave functions also exist in the two forbidden classical regions (on the left and on the right hand side of the well) by virtue of the connection formulae [53]. We notice that the WKB theory fails to correctly describe the quantum system in the vicinity of the classical turning points where the momentum vanishes and consequently the wave functions diverge. We also point out that the wave functions (B.27) are automatically normalized, this due to the square root of the period τ appearing in the denominator, which is not the case in the standard WKB theory.

B.4 Semiclassical density of states: Gutzwiller's trace formula

We now return to the more general case of a d-dimensional space. In order to obtain a semiclassical approximation to the density of states, we are now interested in the trace of the Green function (B.23). Indeed, from the definition of the density of states $\varrho(\varepsilon) = \sum_{\mathbf{n}} \delta(\varepsilon - \varepsilon_{\mathbf{n}})$, and from the expression (B.19b) of the Green function, we have

$$\varrho(\varepsilon) = -\frac{1}{\pi}\Im\mathrm{Tr}\; G = -\frac{1}{\pi}\Im \int \mathrm{d}^d\mathbf{r} G(\mathbf{r}, \mathbf{r}; \varepsilon), \tag{B.28}$$

[6] The classical action is a positive definite quantity. Consequently, n can only be a positive integer.

where $\Im$ represents the imaginary part and Tr the trace.

Instead of detailing the whole derivation that one can find in the references already cited, we highlight here the crucial points of the development in order to obtain the semiclassical density of states $\varrho(\varepsilon) = -1/\pi \Im \mathrm{Tr} \mathcal{G}$. First of all, the trace of the semiclassical retarded Green function is evaluated by virtue of the stationary phase approximation. Thence one imposes that the first variation of S with respect to $\mathbf{r}$ vanishes:

$$\left[\frac{\partial S(\mathbf{r}, \mathbf{r}_0; \varepsilon)}{\partial \mathbf{r}} + \frac{\partial S(\mathbf{r}, \mathbf{r}_0; \varepsilon)}{\partial \mathbf{r}_0}\right]_{\mathbf{r}=\mathbf{r}_0=\mathbf{r}'} = \mathbf{p} - \mathbf{p}_0 = \mathbf{0}. \tag{B.29}$$

This means that the classical trajectories which contribute to the density of states are those with the same initial and final momentum at the same point $\mathbf{r}'$, i.e., *only the periodic trajectories contribute to the density of states.*

One shows afterwards that the semiclassical density of states is decomposed into a smooth and an oscillating part,

$$\varrho(\varepsilon) = \varrho^0(\varepsilon) + \varrho^{\mathrm{osc}}(\varepsilon), \tag{B.30}$$

where $\varrho^0(\varepsilon)$ is the Thomas-Fermi term [124], that is the available volume in phase space

$$\varrho^0(\varepsilon) = \int \frac{\mathrm{d}^d\mathbf{p}\mathrm{d}^d\mathbf{r}}{h^d} \delta(\varepsilon - H(\mathbf{r}, \mathbf{p})). \tag{B.31}$$

We remark that in the semiclassical theory, this smooth density of states comes from the zero-length trajectories. The oscillating part of the density of states is given by the Gutzwiller trace formula [94, 125]

$$\varrho^{\mathrm{osc}}(\varepsilon) = \frac{1}{\pi\hbar} \sum_{\lambda \in \mathrm{ppo}} \sum_{\tilde{r}=1}^{\infty} \frac{\tau_\lambda}{\sqrt{|\det\left(M_\lambda - I_{2d-2}\right)|}} \cos\left[\tilde{r}\left(\frac{S_\lambda}{\hbar} - \nu_\lambda \frac{\pi}{2}\right)\right], \tag{B.32}$$

where ppo means primitive periodic orbits, $\tilde{r}$ being the number of repetitions. $\tau_\lambda = \partial S_\lambda / \partial \varepsilon$ is the period of the primitive periodic orbit λ associated to the classical action S_λ and ν_λ is the Maslov index, which is equal to the sum $\sigma_\lambda + \phi_\lambda$, with σ_λ the number of conjugated points at fixed energy, and ϕ_λ comes from the stationary phase approximation in the transverse directions to the motion. M_λ is the stability matrix of the trajectory and I_{2d-2} is the identity matrix in $(2d-2)$ dimensions. As its name indicates, M_λ measures the stability of an orbit, i.e., the sensibility of the trajectory to a modification of the initial conditions of the motion. In other words, the stability matrix measures the degree of instability of a given orbit. Notice that in one dimension, the determinant appearing in the trace formula (B.32) is equal to one.

Gutzwiller's trace formula is only valid for *isolated* orbits, that is for *nondegenerate* ones, in the sense that there are not several trajectories with the same classical action. For instance, in a disk with hard walls (disk billiard), the diametral trajectory is infinitely degenerate due to the continuous axial symmetry of the disk. Different works have permitted to extend this semiclassical formalism to systems presenting continuous symmetries, notably the works of Balian and Bloch [133] and also of Berry and

Tabor [134, 135]. In this extended theory, the summations are not any more over the trajectories, since their number is infinite, but over a torus in the action-angle space, canonical transforms of the variables in phase space [131, 132]. We emphasize the fact that in one dimension, there does not exist any system presenting degenerated trajectories: All the periodic orbits are isolated.

Finally, the semiclassical approximation to the density of states (B.30) is remarkable in the sense that it provides, for all systems without classically degenerated orbits, a valuable approximation of the density of states. This is one of the great successes of this approach. We emphasize as well a critical point of this approximation, namely the convergence of the infinite series appearing in (B.32). Indeed, the series does not necessarily converge. But one notices in practice that it is sufficient to perform a partial summation, the first repetitions $\tilde{r}$ of the primitive periodic orbits sufficing to give a rather good approximation to the density of states. In mesoscopic physics [1, 2], the trajectory cutoff is implemented through the factor $\exp\left(-L_{\mathrm{ppo}}/L_{\varphi}\right)$, with L_{φ} the phase coherence length and L_{ppo} the length of the primitive periodic orbit. The physical justification for such an approach arises from the consideration of environmental degrees of freedom that introduce further scattering mechanisms for timescales (or lengths L_{φ}) larger than the typical ones imposed by the Hamiltonian we are considering [127].

Appendix C

Semiclassics with radial symmetry

> Tous les moyens sont bons
> quand ils sont efficaces.
>
> *(Jean-Paul Sartre, 1905-1980, in Les Mains sales)*

As it has been mentioned in Appendix B, the Gutzwiller trace formula (B.32) is only applicable when the classical trajectories in the potential are not organized in families degenerate in action. For a system having circular or spherical symmetry (like for instance the disk billiard), we cannot use (B.32) to determine the semiclassical spectrum of the considered system. Since it is an integrable problem the quantization can be readily done from the WKB scheme, and the resulting density of states can be obtained from the Berry-Tabor approach [124, 134, 135].

As an alternative route in the case of problems with radial symmetry, like the one we treat in this work, it is tempting to take advantage of the separability into radial and angular coordinates in order to reduce the dimensionality of the trajectories contributing to the semiclassical expansions. However there are technical difficulties introduced by the singularity at the origin of the centrifugal potential, and this is probably the reason why the radial symmetry is often not fully exploited in semiclassical expansions. On the other hand, the well-known Langer modification [136] is a prescription to avoid the above-mentioned difficulties and provides a route to the semiclassical quantization of spherically symmetric systems (which has been recently extended to higher orders [137]).

In this appendix, we start from the Langer modification in order to obtain the partial (or angular momentum dependent) density of states $\varrho_l(\varepsilon)$ that we need for instance in our evaluation of the surface plasmon lifetime (see Chapter 4). As a check of consistency, we verify in a few simple examples that when $\varrho_l(\varepsilon)$ is summed (in a semiclassical way) over the angular momentum quantum number l and its projection along the quantization axis m, we recover the well-known Berry-Tabor formula for the total density of states [133–135].

C.1 Langer modification and partial density of states

We consider a system presenting spherical symmetry, where the natural coordinates are the spherical coordinates $\mathbf{r} = (r, \theta, \varphi)$. For a central potential $V(r)$, the Schrödinger equation is separable into angular and radial parts. The wave function can be written as

$$\psi_{klm}(\mathbf{r}) = \frac{u_{kl}(r)}{r} Y_l^m(\theta, \varphi), \tag{C.1}$$

where $Y_l^m(\theta, \varphi)$ are the spherical harmonics, and where $u_{kl}(r)$ satisfies

$$\left[-\frac{\hbar^2}{2\mu} \frac{\mathrm{d}^2}{\mathrm{d}r^2} + \frac{\hbar^2 l(l+1)}{2\mu r^2} + V(r) \right] u_{kl}(r) = \varepsilon_{kl} u_{kl}(r), \tag{C.2}$$

with the conditions $u_{kl}(0) = 0$ and $\lim_{r\to\infty} u_{kl}(r)/r = 0$. In the radial Schrödinger equation, μ is the mass of the particle. It is important to notice that the variable r is limited to positive values and that the centrifugal potential possesses a singularity at $r = 0$. This significant difference between (C.2) and a standard one-dimensional Schrödinger equation prevents us from a naïve application of the WKB approximation to treat this radial problem.

The change of variables

$$x = \ln r, \tag{C.3a}$$

$$\chi_{kl}(x) = \mathrm{e}^{x/2} u_{kl}(r) \tag{C.3b}$$

in (C.2) results in the one-dimensional Schrödinger equation

$$\left[\frac{\mathrm{d}^2}{\mathrm{d}x^2} + \Pi_l^2(x) \right] \chi_{kl}(x) = 0, \tag{C.4}$$

with

$$\Pi_l^2(x) = \frac{2\mu}{\hbar^2} \mathrm{e}^{2x} \left[\varepsilon_{kl} - V\left(\mathrm{e}^x\right) \right] - \left(l + \frac{1}{2} \right)^2. \tag{C.5}$$

Using the WKB approximation for $\chi_{kl}(x)$ amounts to change the centrifugal potential in (C.2) according to the Langer modification [136, 138]

$$l(l+1) \Longrightarrow \left(l + \frac{1}{2} \right)^2. \tag{C.6}$$

The modified effective radial potential thus reads

$$V_l^{\mathrm{eff}}(r) = \frac{\hbar^2 (l+1/2)^2}{2\mu r^2} + V(r) \tag{C.7}$$

for a three-dimensional system. The resulting WKB quantization provides for instance the exact spectrum for the hydrogen atom, as well as for the three-dimensional isotropic harmonic oscillator.

The same kind of considerations in two-dimensional systems with a circular symmetry lead to the following substitution in the centrifugal potential [124, 138]:

$$\left(m - \frac{1}{4}\right)^2 \Longrightarrow m^2, \tag{C.8}$$

with m the eigenvalue of the L_z operator. This substitution yields an exact WKB spectrum for the cases of the isotropic harmonic oscillator as well as for the hydrogen atom in two dimensions. In this two-dimensional case, the semiclassical radial potential is then

$$V_m^{\text{eff}}(r) = \frac{\hbar^2 m^2}{2\mu r^2} + V(r). \tag{C.9}$$

As it has been explained in Appendix B, the semiclassical approximation provides a method to calculate the leading $\hbar$ contributions to the density of states in the limit of large quantum numbers, and decomposes the density of states into a smooth and an oscillating part. The smooth term is simply the Weyl contribution [124] and the oscillating term is given, in the case where the periodic orbits are not degenerate in action, by the Gutzwiller trace formula (B.32) as a sum over the primitive periodic orbits.

In the case of multidimensional integrable systems, the periodic orbits belonging to a torus of the phase space are degenerate, and the oscillating part of the density of states is given by the Berry-Tabor formula as a sum over rational tori [134, 135]. In one-dimensional problems, or in the radial coordinate of a spherically symmetric case, the trajectories are not degenerate, and therefore the semiclassical approximation to the density of states at fixed angular momentum l is given by

$$\varrho_l(\varepsilon) = \varrho_l^0(\varepsilon) + \varrho_l^{\text{osc}}(\varepsilon), \tag{C.10}$$

with

$$\varrho_l^0(\varepsilon) = \frac{\tau_l(\varepsilon)}{2\pi\hbar}, \tag{C.11a}$$

$$\varrho_l^{\text{osc}}(\varepsilon) = \frac{\tau_l(\varepsilon)}{\pi\hbar} \sum_{\tilde{r}=1}^{\infty} \cos\left[\tilde{r}\left(\frac{S_l(\varepsilon)}{\hbar} - \nu_{\text{c}}\frac{\pi}{2} - \nu_{\text{r}}\pi\right)\right], \tag{C.11b}$$

where S_l and $\tau_l = \partial S_l/\partial\varepsilon$ are the action and period referring to the motion in the effective (l-dependent) radial potential; ν_{c} (ν_{r}) is the number of classical turning points of the primitive periodic orbits against the smooth (hard) walls, while $\tilde{r}$ is the number of repetition of the periodic orbit.

We note the essential difference between conjugated and reflection points, as it appears in the phase of the trace formula (C.11b). For this effective one-dimensional problem, the conjugated points are the classical turning points in the effective potential $V_l^{\text{eff}}(r)$, *except* when the potential is a hard wall. For the conjugated points, the momentum of the particle vanishes at those locations, and thus acquires a phase of $\pi/2$. For the reflection points, the momentum of the particle just changes its sign, the particle acquiring then a phase of π.

C.2 Total density of states and Berry-Tabor formula for systems with radial symmetry

Using the selection rules for the decay of the surface plasmon, its lifetime can be expressed in terms of the partial density of states $\varrho_l(\varepsilon)$ whose semiclassical expression is given by (C.10) and (C.11). It is then important to verify that the semiclassical sum over angular momenta (that we use throughout our calculations), when applied to $\varrho_l(\varepsilon)$, is able to reproduce the total density of states. Rather than working the most general case, we perform our test for three particular examples: the three dimensional billiard (like the one we treat in the text), the disk billiard (where the calculations are particularly simple), and the isotropic spherical harmonic oscillator (where the semiclassical spectrum coincides with the exact one).

C.2.1 Spherical billiard

A spherical billiard is defined by its radial potential

$$V(r) = \begin{cases} 0, & r < a, \\ \infty, & r \geqslant a, \end{cases} \tag{C.12}$$

where a is the radius of the sphere. First, we determine the exact quantum mechanical spectrum of this system, while in a second part, we calculate the corresponding semiclassical spectrum. As we will show, the semiclassical approximation is very accurate, provided that one uses the Langer modification for the radial effective potential (C.7). At the end of this section, we will show how it is possible to recover the total density of states (Berry-Tabor formula) from the knowledge of the angular momentum restricted density of states $\varrho_l(\varepsilon)$.

Exact spectrum

For $r \leqslant a$, the radial Schrödinger equation (C.2) reads with the radial potential (C.12)

$$\left[\frac{\mathrm{d}^2}{\mathrm{d}r^2} - \frac{l(l+1)}{r^2} + k^2\right] u_{kl}(r) = 0, \tag{C.13}$$

where the wavenumber is defined as $k = \sqrt{2\mu\varepsilon_{kl}}/\hbar$. Since the radial potential is infinite outside of the sphere, the radial wave functions must satisfy $u_{kl}(r \geqslant a) = 0$. The general solution of (C.13) reads [93]

$$u_{kl}(r) = \sqrt{r}\left[AJ_{l+\frac{1}{2}}(kr) + BY_{l+\frac{1}{2}}(kr)\right], \tag{C.14}$$

where $J_\nu(z)$ and $Y_\nu(z)$ are the Bessel functions of the first and second kind, respectively, and where A and B are normalizing constants. The boundary condition $u_{kl}(0) = 0$ leads

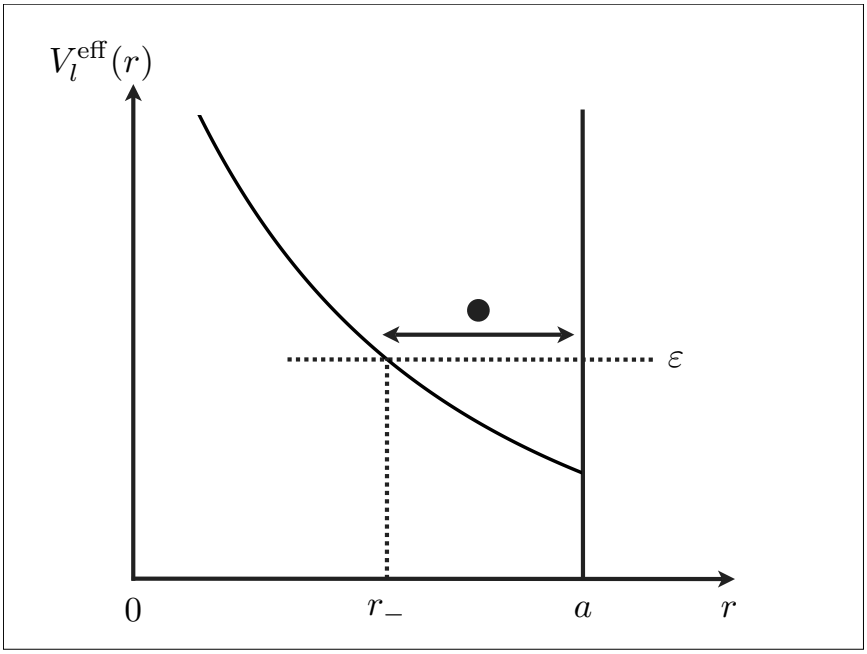

Figure C.1: Effective, l-fixed, radial potential V_l^{eff} of the spherical cavity as a function of the radial coordinate r.

to the elimination of the solution $Y_{l+\frac{1}{2}}(kr)$ which diverges at the origin. Furthermore, the condition of continuity at $r = a$ ensures that

$$J_{l+\frac{1}{2}}(ka) = 0. \tag{C.15}$$

The quantum mechanical spectrum of the spherical billiard is thus given by the zeros of Bessel functions of the first kind, which are not known analytically, except in some asymptotic limits. If one wants the exact spectrum of this system, one has to resort to some numerical search of zeros. This was not necessarily easy in the 1960's, and the semiclassical quantization of Keller and Rubinow [139] was thus a great success at that time, since it provides a route to the semiclassical quantization of integrable systems.

Semiclassical spectrum

The determination of the trace formula (see Eqs. C.10 and C.11) requires the knowledge of two classical quantities, namely the classical action of the periodic orbit in the effective, l-fixed radial potential, and the corresponding period of the classical periodic motion. In order to determine the action, one has to know the classical turning points. The turning point on the left of the classically allowed region is given by the condition $V_l^{\text{eff}}(r_-) = \varepsilon$, i.e., $r_- = \hbar(l + 1/2)/\sqrt{2\mu\varepsilon}$. On the right of the classical region, we have a reflection point at $r = a$ (see Fig. C.1).

The classical action at energy ε is given by

$$S_l(\varepsilon) = 2\int_{r_-}^{a} \mathrm{d}r \sqrt{2\mu\left[\varepsilon - V_l^{\mathrm{eff}}(r)\right]}. \tag{C.16}$$

The integrand of the above integral is simply the conjugated momentum to the variable r, i.e., p_r. With (C.7) and (C.12), we obtain

$$S_l(\varepsilon) = 2\hbar\left[\sqrt{(ka)^2 - \left(l+\frac{1}{2}\right)^2} - \left(l+\frac{1}{2}\right)\arccos\left(\frac{l+1/2}{ka}\right)\right]. \tag{C.17}$$

The period of the classical motion at energy ε is thus given by $\tau_l = \partial S_l/\partial\varepsilon$, i.e.,

$$\tau_l(\varepsilon) = \frac{\hbar\sqrt{(ka)^2 - (l+1/2)^2}}{\varepsilon}. \tag{C.18}$$

We now determine the WKB quantization condition, which is modified by the presence of the hard wall at $r = a$: Since the radial potential $V_l^{\mathrm{eff}}(r)$ is infinite at this point, the semiclassical wave function (B.27) vanishes and thus

$$\cos\left\{\frac{1}{\hbar}\int_{r_-}^{a} \mathrm{d}r' \sqrt{2\mu\left[\varepsilon_{nl} - V_l^{\mathrm{eff}}(r')\right]} - \frac{\pi}{4}\right\} = 0, \tag{C.19}$$

that is

$$\frac{S_l(\varepsilon)}{2\hbar} - \frac{\pi}{4} = \frac{\pi}{2} + n\pi, \tag{C.20}$$

with n a positive integer, which is the number of nodes of the wave function of the quantum level $|n,l,m\rangle$. Rearranging the above equation, we obtain the WKB quantization in presence of a hard wall:

$$S_l(\varepsilon) = 2\pi\hbar\left(n + \frac{3}{4}\right). \tag{C.21}$$

More generally, one shows [124, 134, 135, 139] that the quantization condition for a potential having ν_{c} conjugated points and ν_{r} reflection points reads

$$S(\varepsilon) = 2\pi\hbar\left(n + \frac{\nu_{\mathrm{c}}}{4} + \frac{\nu_{\mathrm{r}}}{2}\right). \tag{C.22}$$

In the case of the spherical billiard, we find with (C.17) and (C.21)

$$\sqrt{(ka)^2 - \left(l+\frac{1}{2}\right)^2} - \left(l+\frac{1}{2}\right)\arccos\left(\frac{l+1/2}{ka}\right) = \pi\left(n+\frac{3}{4}\right). \tag{C.23}$$

This result is the one found by Keller and Rubinow in Ref. 139. It has to be compared with the exact quantization condition (C.15). We first note that it is numerically much easier to find the roots of (C.23) than the zeros of Bessel functions. Second, in Fig. C.2, one can remark the accuracy of the Keller and Rubinow quantization condition: We show as a function of ka the absolute error between the exact spectrum from (C.15) and the semiclassical one (C.23) for different values of the angular momentum l. The error is decreasing with increasing energy, as it is expected from the semiclassical approximation (high energy limit).

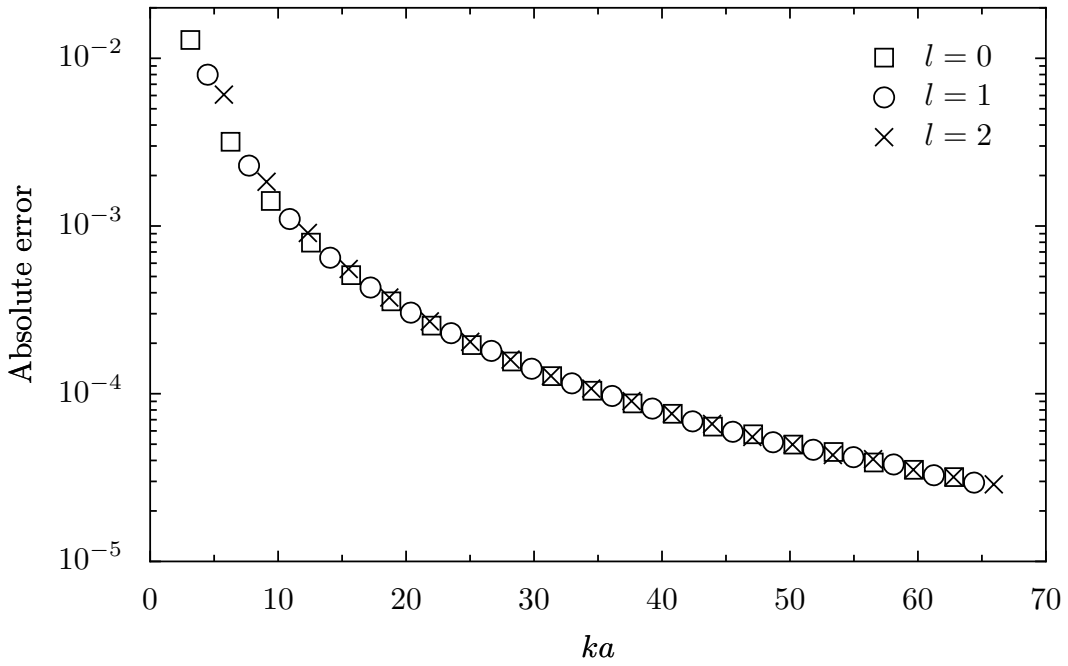

Figure C.2: Absolute error between the exact spectrum of the spherical billiard (C.15) and the semiclassical spectrum (C.23) as a function of ka, for $l = 0, 1, 2$.

Berry-Tabor formula for the density of states

In this paragraph, we will show how it is possible to recover the full (three-dimensional) density of states from the knowledge of the density restricted to a fixed angular momentum l. To this end, we sum the semiclassical density of states from (C.10) over the angular momentum quantum numbers,

$$\varrho(\varepsilon) = \sum_{l=0}^{l_{\max}} \sum_{m=-l}^{+l} \varrho_l(\varepsilon). \tag{C.24}$$

In the above equation, $l_{\max}$ is the maximal angular momentum quantum number allowed at the energy ε. It is given by the condition $V^{\text{eff}}_{l_{\max}}(a) = \varepsilon$, i.e., $l_{\max} = ka - 1/2$.

With (C.11a), the smooth part of the full density of states is given by

$$\varrho^0(\varepsilon) = \frac{1}{2\pi\hbar} \sum_{l=0}^{l_{\max}} (2l+1)\tau_l(\varepsilon). \tag{C.25}$$

For $l_{\max} = ka - 1/2 \gg 1$ (high energy limit), we can replace the summation over l by an integral to obtain

$$\varrho^0(\varepsilon) = \frac{1}{2\pi\hbar} \int_{-1/2}^{ka-1/2} \mathrm{d}l (2l+1)\tau_l(\varepsilon). \tag{C.26}$$

Replacing the period τ_l by its expression (C.18), we obtain

$$\varrho^0(\varepsilon) = \frac{2\mu k a^3}{3\pi\hbar^2}, \tag{C.27}$$

which reads

$$\varrho^0(\varepsilon) = \frac{1}{4\pi^2}\left(\frac{2\mu}{\hbar^2}\right)^{3/2}\sqrt{\varepsilon}\,\mathcal{V}, \tag{C.28}$$

with $\mathcal{V} = 4\pi a^3/3$ the volume of the sphere. We thus recover with this resummation procedure the Thomas-Fermi term, which corresponds to the first term of the Weyl expansion, of order $1/\hbar^2$ [124].

In order to find the oscillating term of the density of states, we use the Poisson summation rule [140]

$$\sum_{l=a}^{b} f_l = \sum_{\tilde{m}=-\infty}^{+\infty} \int_{a-1/2}^{b+1/2} \mathrm{d}l\, \mathrm{e}^{2\pi \mathrm{i}\tilde{m}l} f_l. \tag{C.29}$$

With (C.11b), we thus have

$$\varrho^{\mathrm{osc}}(\varepsilon) = \frac{1}{\pi\hbar}\sum_{\tilde{m}=-\infty}^{+\infty}\sum_{\tilde{r}=1}^{\infty}\int_{-1/2}^{ka-1/2}\mathrm{d}l\,\mathrm{e}^{2\pi\mathrm{i}\tilde{m}l}(2l+1)\tau_l(\varepsilon)\cos\left[\tilde{r}\left(\frac{S_l(\varepsilon)}{\hbar}-\frac{3\pi}{2}\right)\right], \tag{C.30}$$

where we have used the fact that we have $\nu_{\mathrm{c}} = 1$ conjugated point in r_- and $\nu_{\mathrm{r}} = 1$ hard wall at the boundary a. Note that the upper bound of the integral over l should be ka according to the Poisson summation rule. However, the integrand is not defined for $l > ka - 1/2$, since the semiclassical Green function at a given energy vanishes outside of the classically allowed region of the effective radial potential. We can rewrite (C.30) as

$$\varrho^{\mathrm{osc}}(\varepsilon) = \frac{1}{2\pi\hbar}\sum_{\tilde{m}=-\infty}^{+\infty}\sum_{\tilde{r}=1}^{\infty}\sum_{\sigma=\pm}\int_{-1/2}^{ka-1/2}\mathrm{d}l\,(2l+1)\tau_l(\varepsilon)\mathrm{e}^{\mathrm{i}\phi_{l,\sigma}^{\tilde{m}\tilde{r}}(\varepsilon)} \tag{C.31}$$

with the phases

$$\phi_{l,\pm}^{\tilde{m}\tilde{r}}(\varepsilon) = 2\pi\tilde{m}l \pm \tilde{r}\left(\frac{S_l(\varepsilon)}{\hbar}-\frac{3\pi}{2}\right). \tag{C.32}$$

The integral over l is evaluated by virtue of the stationary phase approximation explained in Appendix B.3.2. The stationarity condition

$$\left.\frac{\partial\phi_{l,\pm}^{\tilde{m}\tilde{r}}(\varepsilon)}{\partial l}\right|_{\bar{l}_\pm} = 0 \tag{C.33}$$

implies, using (C.17), that

$$\arccos\left(\frac{\bar{l}_\pm + 1/2}{ka}\right) = \pm\frac{\pi\tilde{m}}{\tilde{r}}. \tag{C.34}$$

Since the inverse cosine function is positive, the above expression imposes that $m \geqslant 0$ and $m \leqslant 0$ for the two families of stationary points $\bar{l}_+$ and $\bar{l}_-$, respectively. Inverting (C.34) gives the stationary points

$$\bar{l}_\pm = ka\cos\varphi_{\tilde{r}\tilde{m}} - \frac{1}{2}, \tag{C.35}$$

with $\varphi_{\tilde{r}\tilde{m}} = \pi\tilde{m}/\tilde{r}$. The stationarity condition is then only valid if the stationary points belong to the interval of integration, i.e., $\bar{l}_\pm \in]-1/2, ka - 1/2[$. Imposing that condition, we find that $\tilde{r} > 2\,|\tilde{m}|$ for the two families of stationary points.

The stationarity condition (C.35) reads $\hbar(\bar{l}_\pm + 1/2) = pa\cos\varphi_{\tilde{r}\tilde{m}}$, p being the momentum of the particle of mass μ. This guarantees that the trajectories selected by the stationary phase approximation are the *classical* trajectories inside the spherical billiard. Indeed, it is easy to show that the only possible trajectories in the billiard are such that $\tilde{r} > 2\,|\tilde{m}|$ with $\tilde{r}$ the number of instance that the particle bounces against the surface of the sphere, and $\tilde{m}$ the winding number around the center of the sphere. Moreover, $pa\cos\varphi_{\tilde{r}\tilde{m}}$ is precisely the classical kinetic momentum associated with the trajectory $(\tilde{r}, \tilde{m})$, and $\varphi_{\tilde{r}\tilde{m}}$ is the bisection of the angle formed by the polygons $(\tilde{r}, \tilde{m})$. We note also that $L_{\tilde{r}\tilde{m}} = 2\tilde{r}a\sin\varphi_{\tilde{r}\tilde{m}}$ is the length of the orbit labeled with the indices $(\tilde{r}, \tilde{m})$, that we have thus identified with Berry-Tabor's topological indices [134, 135].

Coming back to (C.31), we obtain with the stationary phase approximation

$$\begin{aligned}\varrho^{\rm osc}(\varepsilon) = {} & \frac{1}{2\pi\hbar}\sum_{\tilde{m}=1}^{\infty}\sum_{\tilde{r}>2\tilde{m}}(2\bar{l}_+ + 1)\tau_{\bar{l}_+}(\varepsilon)\mathrm{e}^{\mathrm{i}\phi^{\tilde{m}\tilde{r}}_{\bar{l}_+,+}(\varepsilon)}\int_{-\infty}^{+\infty}\mathrm{d}l\,\exp\left(\frac{\mathrm{i}}{2}\left.\frac{\partial^2\phi^{\tilde{m}\tilde{r}}_{l,+}(\varepsilon)}{\partial l^2}\right|_{\bar{l}_+} l^2\right) \\ & + \frac{1}{2\pi\hbar}\sum_{\tilde{m}=-\infty}^{-1}\sum_{\tilde{r}>-2\tilde{m}}(2\bar{l}_- + 1)\tau_{\bar{l}_-}(\varepsilon)\mathrm{e}^{\mathrm{i}\phi^{\tilde{m}\tilde{r}}_{\bar{l}_-,-}(\varepsilon)}\int_{-\infty}^{+\infty}\mathrm{d}l\,\exp\left(\frac{\mathrm{i}}{2}\left.\frac{\partial^2\phi^{\tilde{m}\tilde{r}}_{l,-}(\varepsilon)}{\partial l^2}\right|_{\bar{l}_-} l^2\right),\end{aligned} \tag{C.36}$$

where we have used the change of variables $(l - \bar{l}_\pm) \to l$. Evaluating the two Gaussian integrals, rearranging the sum over $\tilde{m}$ in the second term on the r.h.s. of the above expression, and calculating explicitly all terms, we finally obtain

$$\varrho^{\rm osc}(\varepsilon) = \frac{2\mu a^2}{\hbar^2}\sqrt{\frac{ka}{\pi}}\sum_{\substack{\tilde{m}\geqslant 1\\ \tilde{r}>2\tilde{m}}}(-1)^{\tilde{m}}\sin(2\varphi_{\tilde{r}\tilde{m}})\sqrt{\frac{\sin\varphi_{\tilde{r}\tilde{m}}}{\tilde{r}}}\cos\Phi_{\tilde{r}\tilde{m}} \tag{C.37}$$

with $\Phi_{\tilde{r}\tilde{m}} = kL_{\tilde{r}\tilde{m}} + \pi/4 - 3\tilde{r}\pi/2$. $L_{\tilde{r}\tilde{m}}$ and $\hbar k L_{\tilde{r}\tilde{m}}$ are the length and the action of the classical trajectory $(\tilde{r}, \tilde{m})$, respectively. With our resummation technique of the angular momentum restricted density of states, we thus recover the well-known Berry-Tabor formula for the oscillating part of the density of states of a spherical billiard [124,134,135].

In Fig. C.3, we show the oscillating component (C.37) of the density of states as a function of ka. We have only retained the triangular and the square trajectories $(3, 1)$ and $(4, 1)$: These are the major contributions to the oscillating density of states [124]. Indeed, those trajectories have, in the Fourier spectrum in real space, the largest amplitudes. When $\tilde{r}$ and $\tilde{m}$ increase, the amplitudes become negligible. The beating pattern in Fig. C.3 is due to the interferences that occur between the triangular and square trajectories, as it has been shown in Ref. 133 by Balian and Bloch.

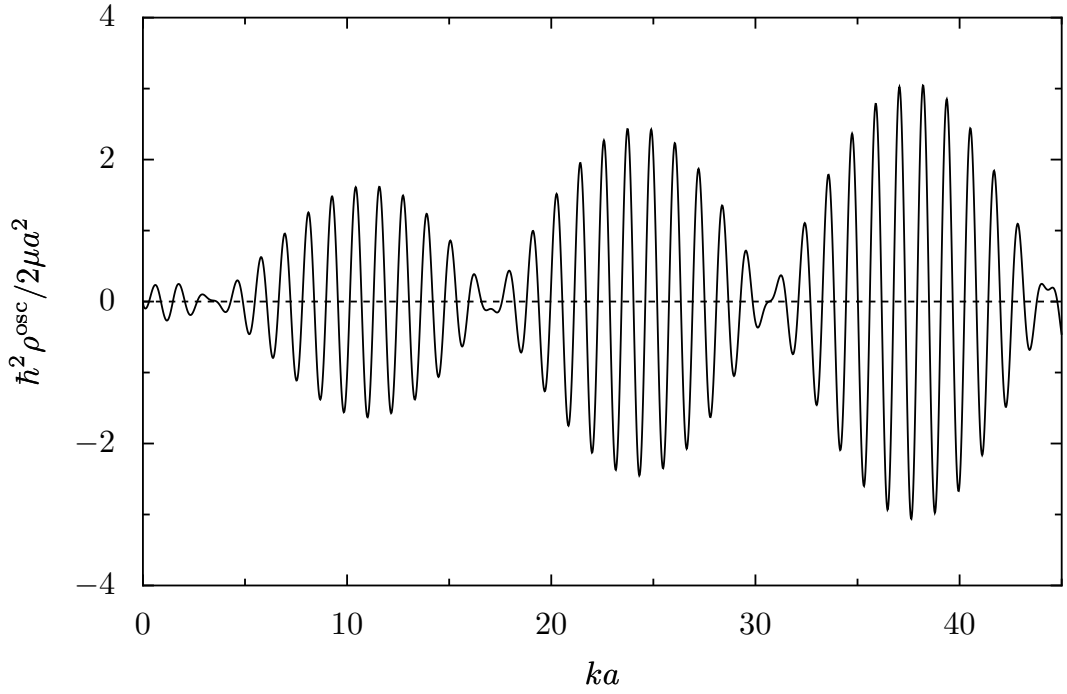

Figure C.3: Oscillating component of the density of states of a spherical billiard as a function of ka. We have only retained the trajectories $(3,1)$ and $(4,1)$.

C.2.2 Disk billiard

A disk billiard is defined by the radial potential (C.12) in the two-dimensional case. The effective radial motion is governed by the potential given in (C.9). The classical primitive periodic orbits have $\nu_{\rm c} = \nu_{\rm r} = 1$ since there is one turning point at the (smooth) kinetic barrier and another at the (hard) wall for $r = a$. For a given energy ε we have $m_{\max} = \sqrt{2\mu\varepsilon}a/\hbar = ka$. Since the calculations are very similar to those performed in the case of the spherical cavity, Sec. C.2.1, we will not give all the details of the derivation leading to the Berry-Tabor formula for the density of states of the disk billiard.

The action and period of the periodic orbit with energy ε and angular momentum m are given by

$$S_m(\varepsilon) = 2\hbar\left[\sqrt{(ka)^2 - m^2} - m\arccos\left(\frac{m}{ka}\right)\right], \tag{C.38a}$$

$$\tau_m(\varepsilon) = \frac{\hbar\sqrt{(ka)^2 - m^2}}{\varepsilon}, \tag{C.38b}$$

respectively. The smooth part of the density of states is

$$\varrho^0(\varepsilon) = \sum_{m=-m_{\max}}^{+m_{\max}} \varrho_m^0(\varepsilon) = \frac{1}{4\pi}\left(\frac{2\mu}{\hbar^2}\right)\mathcal{A}, \tag{C.39}$$

with $\mathcal{A} = \pi a^2$ being the disk area. We have replaced the sum by an integral and obtained the Weyl part of the density of states. For the oscillating part we make use of the Poisson

summation rule and write

$$\varrho^{\rm osc}(\varepsilon) = \frac{1}{2\pi\hbar} \sum_{\tilde{m}=-\infty}^{+\infty} \sum_{\substack{\tilde{r}\geqslant 1 \\ \sigma=\pm}} \int_0^{m_{\max}} {\rm d}m \tau_m(\varepsilon)\, {\rm e}^{\sigma {\rm i} \phi_m^{\tilde{m}\tilde{r}}(\varepsilon)} \tag{C.40}$$

with the phase

$$\phi_m^{\tilde{m}\tilde{r}}(\varepsilon) = 2\pi\tilde{m}m + \tilde{r}\left(\frac{S_m(\varepsilon)}{\hbar} - \frac{3\pi}{2}\right). \tag{C.41}$$

Consistently with the semiclassical expansions, we perform a stationary phase approximation. The stationary points are given by $\bar{m} = ka\cos\varphi_{\tilde{r}\tilde{m}}$, with $\varphi_{\tilde{r}\tilde{m}} = \pi\tilde{m}/\tilde{r}$ and the condition $\tilde{r} \geqslant 2\tilde{m} > 0$, which yields just the classical angular momenta of the periodic orbits labeled by the topological indices $(\tilde{r}, \tilde{m})$. We then recover for the oscillating density of states the well-known result [133–135]

$$\varrho^{\rm osc}(\varepsilon) = \frac{2\mu a^2}{\hbar^2} \frac{1}{\sqrt{\pi ka}} \sum_{\tilde{m}=1}^{\infty} \sum_{\tilde{r}\geq 2\tilde{m}} f_{\tilde{r}\tilde{m}} \frac{\sin^{3/2}\varphi_{\tilde{r}\tilde{m}}}{\sqrt{\tilde{r}}} \cos\Phi_{\tilde{r}\tilde{m}}, \tag{C.42}$$

where $f_{\tilde{r}\tilde{m}} = 1$ if $\tilde{r} = 2\tilde{m}$ and $f_{\tilde{r}\tilde{m}} = 2$ if $\tilde{r} > 2\tilde{m}$, $\Phi_{\tilde{r}\tilde{m}} = kL_{\tilde{r}\tilde{m}} - 3r\pi/2 + \pi/4$ and $L_{\tilde{r}\tilde{m}} = 2\tilde{r}a\sin\varphi_{\tilde{r}\tilde{m}}$ is the length of the orbit $(\tilde{r}, \tilde{m})$. The oscillating component (C.42) of the density of states is represented in Fig. C.4 as a function of ka. Here, we have retained the diametral trajectory $(2, 1)$ which gives the major contribution, plus the triangle and square trajectories, as in the case of the spherical billiard.

We also notice that the quantization of the radial problem leads to the well-known Keller and Rubinow condition [139]

$$\sqrt{(ka)^2 - m^2} - m\arccos\left(\frac{m}{ka}\right) = \pi\left(n + \frac{3}{4}\right), \tag{C.43}$$

from which the Berry-Tabor formula can be readily obtained. It has to be compared with the exact spectrum given by the zeros of $J_m(ka)$. As in the case of the spherical billiard, (C.43) is a very good approximation to the exact quantum mechanical spectrum.

C.2.3 Isotropic spherical harmonic oscillator

The isotropic harmonic oscillator in three dimensions is an integrable system without hard wall boundaries and therefore the Berry-Tabor quantization is very difficult to implement. The radial approach that we develop clearly overcomes this difficulty. The effective potential is

$$V_l^{\rm eff}(r) = \frac{\hbar^2(l+1/2)^2}{2\mu r^2} + \frac{1}{2}\mu\omega^2 r^2, \tag{C.44}$$

where ω is the frequency of the harmonic confinement. At a given ε, we have $l_{\max} = -1/2 + \varepsilon/\hbar\omega$. The classical action is given by $S_l(\varepsilon) = \varepsilon\pi/\omega - \pi\hbar(l+1/2)$ and the period

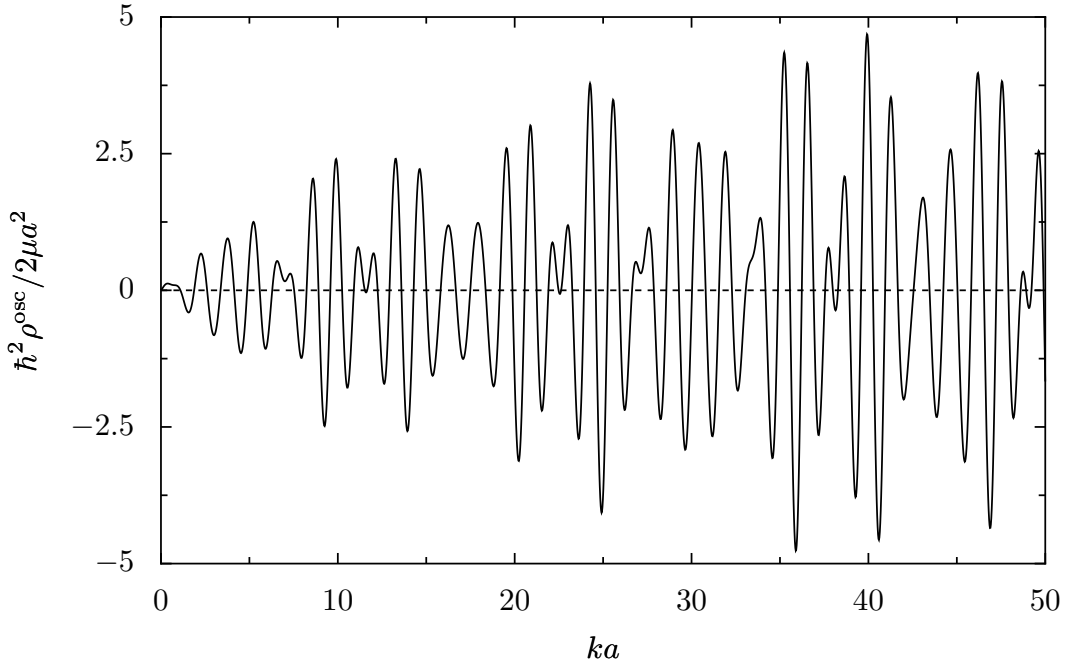

Figure C.4: Oscillating component of the density of states of a disk billiard as a function of ka. We have only retained the trajectories $(2,1)$, $(3,1)$ and $(4,1)$.

is $\tau = \pi/\omega$. Using (C.10) with $\nu_{\rm c} = 2$ and $\nu_{\rm r} = 0$ (no hard wall) gives the density of states at fixed orbital momentum

$$\varrho_l(\varepsilon) = \frac{1}{2\hbar\omega}\left\{1 + 2\sum_{\tilde{r}=1}^{\infty}\cos\left[\pi\tilde{r}\left(\frac{\varepsilon}{\hbar\omega} - l - \frac{3}{2}\right)\right]\right\} \tag{C.45}$$

For the smooth part of the density of states, the sum over l can be performed exactly, but to be consistent with the semiclassical approximation we have to take the limit $\varepsilon/\hbar\omega \gg 1$: $\varrho^0(\varepsilon) \simeq \varepsilon^2/2(\hbar\omega)^3$. Writing the Poisson summation rule for the oscillating part and performing a stationary phase approximation, we have the condition on topological indices $\tilde{r} = 2\tilde{m}$ and $\tilde{m} \geqslant 1$. Finally we obtain for the total density of states the trace formula [141]

$$\varrho(\varepsilon) = \frac{\varepsilon^2}{2(\hbar\omega)^3}\left[1 + 2\sum_{\tilde{m}=1}^{\infty}(-1)^{\tilde{m}}\cos\left(2\pi\tilde{m}\frac{\varepsilon}{\hbar\omega}\right)\right], \tag{C.46}$$

which has to be compared with the exact trace formula given in Ref. 124, where the prefactor is shifted by the quantity $-1/8\hbar\omega$, negligible at the (high energy) semiclassical limit. One also notices that the WKB quantization rule yields the exact quantum spectrum of the harmonic oscillator: $\varepsilon_{nl} = \hbar\omega(2n + l + 3/2)$.

In Fig. C.5, we show the number of single-particle states having an energy below ε,

$$\mathcal{N}(\varepsilon) = \int_0^{\varepsilon} {\rm d}\varepsilon'\varrho(\varepsilon'). \tag{C.47}$$

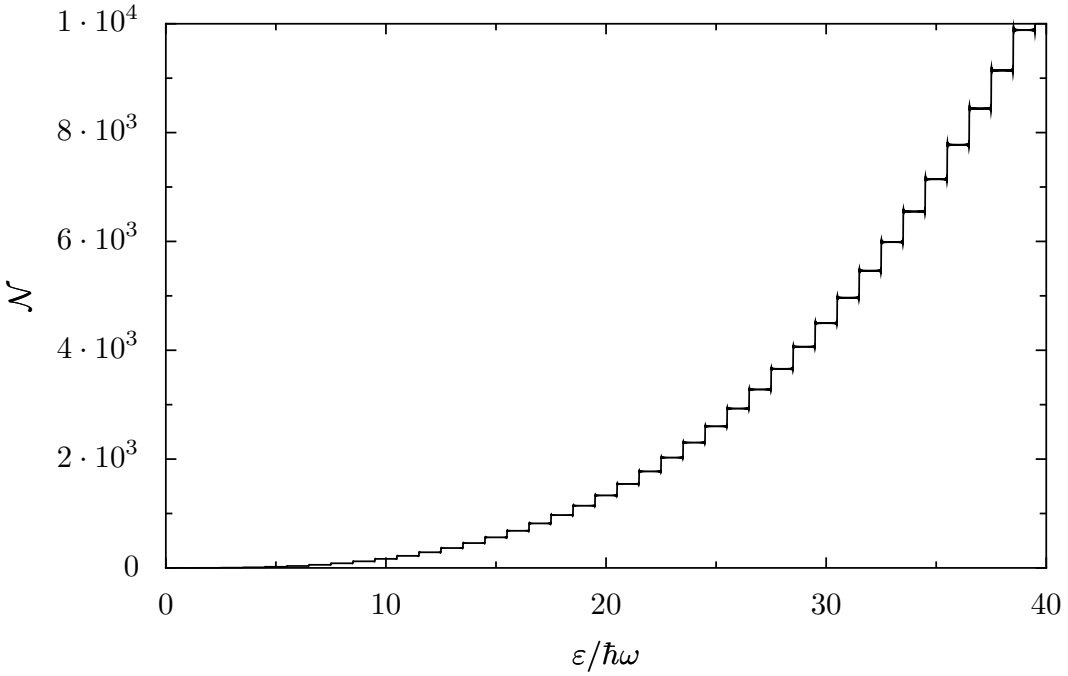

Figure C.5: Number $\mathcal{N}$ of single-particle states of a three-dimensional harmonic oscillator having an energy smaller than ε, as a function of $\varepsilon/\hbar\omega$. It is plotted for m up to $m_{\max} = 50$.

With (C.46), we have

$$\mathcal{N}(\varepsilon) = \frac{1}{6}\left(\frac{\varepsilon}{\hbar\omega}\right)^3 + \sum_{\tilde{m}=1}^{\infty} \frac{(-1)^{\tilde{m}}}{4(\pi\tilde{m})^3}\left\{2\pi\tilde{m}\frac{\varepsilon}{\hbar\omega}\cos\left(2\pi\tilde{m}\frac{\varepsilon}{\hbar\omega}\right) + \left[2\left(\pi\tilde{m}\frac{\varepsilon}{\hbar\omega}\right)^2 - 1\right]\sin\left(2\pi\tilde{m}\frac{\varepsilon}{\hbar\omega}\right)\right\}. \tag{C.48}$$

It reproduces very accurately the quantum mechanical spectrum of the three-dimensional isotropic harmonic oscillator. As expected, the single-particle states are separated by an energy $\hbar\omega$. Moreover, the semiclassical trace formula (C.46) reproduces the degeneracy of a state $|n, l, m\rangle$ of the spherical harmonic oscillator in three dimensions.

In this appendix, we have demonstrated the usefulness of the radial decomposition for the semiclassical expansion of the density of states. Even in the case of degenerate classical periodic trajectories, one is able to find the semiclassical density of states by using the appropriate symmetry of the system, without requiring the action-angle quantization of Berry and Tabor.

Appendix D

Second-order perturbation theory: Fermi's golden rule

Je cherche l'or du temps.

(André Breton, 1896-1966, in Discours sur le peu de réalité)

In this appendix, we present the second order perturbation theory that we use in our determination of the linewidth of the double plasmon, as well as for the ionization rate via the second surface plasmon state in Chapter 7. The second order time-dependent perturbation theory will yield the Fermi golden rule of (7.1).

Our goal is here to solve approximately the time-dependent Schrödinger equation

$$\mathrm{i}\hbar|\dot{\psi}(t)\rangle = (H_0 + \lambda H_\mathrm{p})\,|\psi(t)\rangle \tag{D.1}$$

in the limit $\lambda \ll 1$.[1] In our special case of interest, i.e., the decay of collective excitations in metallic nanoparticles, we identify $H_0 = H_\mathrm{cm} + H_\mathrm{rel}$, while $\lambda H_\mathrm{p} = H_\mathrm{c}$ is the coupling Hamiltonian between the center-of-mass system and the relative coordinates. Assuming that $H_0|n\rangle = \varepsilon_n|n\rangle$, the general solution of (D.1) is given by

$$|\psi(t)\rangle = \sum_n c_n(t)\mathrm{e}^{-\mathrm{i}\varepsilon_n t/\hbar}|n\rangle \tag{D.2}$$

where the time-dependent coefficients $c_n(t)$ remain to be determined. If the perturbation vanishes, i.e., $\lambda = 0$, we have $c_n(t) = c_n$ which is independent of time. For $\lambda \ll 1$, we thus assume $|\dot{c}_n(t)| \ll 1$.

Inserting the general solution (D.2) into the Schrödinger equation (D.1), and doing the scalar product with a state $|m\rangle$ ($\langle m|n\rangle = \delta_{mn}$), we obtain

$$\mathrm{i}\hbar\dot{c}_m(t) = \lambda\sum_n \langle m|H_\mathrm{p}|n\rangle \mathrm{e}^{\mathrm{i}\omega_{mn}t}c_n(t) \tag{D.3}$$

[1] The dot denotes the derivative with respect to the time t.

with $\omega_{mn} = (\varepsilon_m - \varepsilon_n)/\hbar$. Making the perturbative assumption

$$c_n(t) = c_n^{(0)} + \lambda c_n^{(1)}(t) + \lambda^2 c_n^{(2)}(t) + \mathcal{O}(\lambda^3), \tag{D.4}$$

and solving order-by-order, we get the evolution

$$\mathrm{i}\hbar \dot{c}_m^{(1)}(t) = \sum_n \langle m|H_\mathrm{p}|n\rangle \mathrm{e}^{\mathrm{i}\omega_{mn}t} c_n^{(0)}, \tag{D.5a}$$

$$\mathrm{i}\hbar \dot{c}_m^{(2)}(t) = \sum_n \langle m|H_\mathrm{p}|n\rangle \mathrm{e}^{\mathrm{i}\omega_{mn}t} c_n^{(1)}(t), \tag{D.5b}$$

for the first- and second-order coefficients, respectively.

Let us now assume that for $t < 0$, there is no perturbation, and the system described by H_0 is in its initial state $|i\rangle$. The perturbation is switched on at $t = 0$, until the time τ for which it is switched off. The question we address is then: What is the probability to find the system in the final state $|f\rangle$ after the application of the perturbation? If we work in a case where the first-order processes are suppressed, i.e., $c_f^{(1)} = 0$, and under the assumption that the final state is nondegenerate, the transition probability is simply $|c_f^{(2)}(\tau)|^2$.[2] Integrating the equations of motion (D.5) with the initial condition $c_n^{(0)} = \delta_{ni}$, we obtain

$$\left|c_f^{(2)}(\tau)\right|^2 = \frac{1}{\hbar^2} \frac{\sin^2(\omega_{fi}\tau/2)}{(\omega_{fi}/2)^2} \left| \sum_n \frac{\langle f|H_\mathrm{p}|n\rangle\langle n|H_\mathrm{p}|i\rangle}{\varepsilon_i - \varepsilon_n} \right|^2 . \tag{D.6}$$

In the above equation, we have neglected a highly oscillating term as a function of n, which is vanishing once the summation over n is performed.

We now assume that the time τ over which the perturbation acts is sufficiently large compared to the inverse difference in energy between the initial and final state ω_{fi} to guarantee Heisenberg's uncertainty principle. In practice, taking the limit $\tau \to \infty$ in (D.6), we obtain

$$\left|c_f^{(2)}(\tau)\right|^2 = \frac{2\pi}{\hbar^2} \tau \delta(\omega_{fi}) \left| \sum_n \frac{\langle f|H_\mathrm{p}|n\rangle\langle n|H_\mathrm{p}|i\rangle}{\varepsilon_i - \varepsilon_n} \right|^2 . \tag{D.7}$$

We have used the well-known identity [78]

$$\delta(x) = \lim_{\epsilon \to 0} \left[\frac{\epsilon}{\pi} \frac{\sin^2(x/\epsilon)}{x^2} \right] \tag{D.8}$$

to obtain this result.

The rate $\gamma_f^{(2)}$ of the second-order transition $|i\rangle \to |f\rangle$ is given by the derivative of (D.7) with respect to τ. If one has several possible final states, one has to sum over all those states to obtain the rate

$$\gamma^{(2)} = \frac{2\pi}{\hbar} \sum_f \left| \sum_n \frac{\langle f|H_\mathrm{p}|n\rangle\langle n|H_\mathrm{p}|i\rangle}{\varepsilon_i - \varepsilon_n} \right|^2 \delta(\varepsilon_f - \varepsilon_i), \tag{D.9}$$

[2] We have set $\lambda = 1$ for convenience.

given by Fermi's golden rule to the second order in the perturbation H_{p}. In the specific example of the Landau damping rate of the double plasmon state, we use $|i\rangle = |2, I_{\mathrm{rel}}\rangle$, $|n\rangle = |1, F'_{\mathrm{rel}}\rangle$ and $|f\rangle = |0, F_{\mathrm{rel}}\rangle$ to finally obtain the golden rule (7.1).

Bibliography

[1] Y. Imry, *Introduction to mesoscopic physics* (Oxford University Press, Oxford, 2002), 2nd ed.

[2] S. Datta, *Electronic transport in mesoscopic systems* (Cambridge University Press, Cambridge, 1997).

[3] E. Akkermans and G. Montambaux, *Physique mésoscopique des électrons et des photons* (EDP Sciences, CNRS Éditions, Paris, 2004).

[4] T. Dittrich, P. Hänggi, G.-L. Ingold, B. Kramer, G. Schön, and W. Zwerger, *Quantum transport and dissipation* (Wiley-VCH, Weinheim, 1998).

[5] W. D. Knight, K. Clemenger, W. A. de Heer, W. A. Saunders, M. Y. Chou, and M. L. Cohen, *Electronic shell structure and abundances of sodium clusters*, Phys. Rev. Lett. **52**, 2141 (1984).

[6] A. Bohr and B. R. Mottelson, *Nuclear structure* (Benjamin, Reading, 1975).

[7] P. Ring and P. Schuck, *The nuclear many-body problem* (Springer-Verlag, New York, 1980).

[8] R. D. Woods and D. Saxon, *Diffuse surface optical model for nucleon-nuclei scattering*, Phys. Rev. **95**, 577 (1954).

[9] N. W. Ashcroft and N. D. Mermin, *Solid state physics* (Harcourt, Orlando, 1976).

[10] W. A. de Heer, *The physics of simple metal clusters: Experimental aspects and simple models*, Rev. Mod. Phys. **65**, 611 (1993).

[11] M. Brack, *The physics of simple metal clusters: Self-consistent jellium model and semiclassical approaches*, Rev. Mod. Phys. **65**, 677 (1993).

[12] H. A. Jahn and E. Teller, *Stability of polyatomics molecules in degenerate electronic state. I. Orbital degeneracy*, Proc. R. Soc. London A **161**, 220 (1937).

[13] U. Kreibig and M. Vollmer, *Optical properties of metal clusters* (Springer-Verlag, Berlin, 1995).

[14] H. Haberland, ed., *Clusters of atoms and Molecules I*, vol. 52 of *Springer Series in Chemical Physics* (Springer-Verlag, Berlin, 1994).

[15] H. Haberland, ed., *Clusters of atoms and Molecules II*, vol. 56 of *Springer Series in Chemical Physics* (Springer-Verlag, Berlin, 1994).

[16] G. F. Bertsch and R. A. Broglia, *Oscillations in finite quantum systems* (Cambridge University Press, Cambridge, 1994).

[17] G. F. Bertsch, P. F. Bortignon, and R. A. Broglia, *Damping of nuclear excitations*, Rev. Mod. Phys. **55**, 287 (1983).

[18] C. Bréchignac, P. Cahuzac, J. Leygnier, and A. Sarfati, *Optical response of large lithium clusters: Evolution toward the bulk*, Phys. Rev. Lett. **70**, 2036 (1993).

[19] G. Mie, *Beiträge zur Optik trüber Medien, speziell kolloidaler Metallösungen*, Ann. Phys. (Leipzig) **25**, 377 (1908).

[20] M. Born and E. Wolf, *Principles of optics* (Pergamon, Oxford, 1964), 2^{nd} ed.

[21] W. A. de Heer, K. Selby, V. Kresin, J. Masui, M. Vollmer, A. Châtelain, and W. D. Knight, *Collective dipole oscillations in small sodium clusters*, Phys. Rev. Lett. **59**, 1805 (1987).

[22] C. Bréchignac, P. Cahuzac, N. Kebaïli, J. Leygnier, and A. Sarfati, *Collective resonance in large free potassium cluster ions*, Phys. Rev. Lett. **68**, 3916 (1992).

[23] H. Haberland, B. von Issendorff, J. Yufeng, and T. Kolar, *Transition to plasmonlike absorption in small Hg clusters*, Phys. Rev. Lett. **69**, 3212 (1992).

[24] T. Reiners, W. Orlik, C. Ellert, M. Schmidt, and H. Haberland, *Temperature dependence of the Na_n^+ optical response*, Chem. Phys. Lett. **215**, 357 (1993).

[25] T. Reiners, C. Ellert, M. Schmidt, and H. Haberland, *Size dependence of the optical response of spherical sodium clusters*, Phys. Rev. Lett. **74**, 1558 (1995).

[26] W. Ekardt, *Dynamical polarizability of small metal particles: self-consistent spherical jellium background model*, Phys. Rev. Lett. **52**, 1925 (1984).

[27] W. Ekardt, *Size-dependent photoabsorption and photoemission of small metal particles*, Phys. Rev. B **31**, 6360 (1985).

[28] W. Ekardt, *Collective multipole excitations in small metal particles: Critical angular momentum l^{cr} for the existence of collective surface modes*, Phys. Rev. B **32**, 1961 (1985).

[29] M. Barma and V. Subrahmanyam, *Optical absorption in small metal particles*, J. Phys.: Condens. Matter **1**, 7681 (1989).

[30] C. Yannouleas and R. A. Broglia, *Landau damping and wall dissipation in large metal clusters*, Ann. Phys. (N.Y.) **217**, 105 (1992).

[31] M. Madjet, C. Guet, and W. R. Johnson, *Comparative study of exchange-correlation effects on the electronic and optical properties of alkali-metal clusters*, Phys. Rev. A **51**, 1327 (1995).

[32] D. Boyer, P. Tamarat, A. Maali, B. Lounis, and M. Orrit, *Photothermal imaging of nanometer-sized metal particles among scatterers*, Science **297**, 1160 (2002).

[33] L. Cognet, C. Tardin, D. Boyer, D. Choquet, P. Tamarat, and B. Lounis, *Single metallic nanoparticle imaging for protein detection in cells*, PNAS **100**, 11350 (2003).

[34] M. Dahan, S. Lévi, C. Luccardini, P. Rostaing, B. Riveau, and A. Triller, *Diffusion dynamics of glycine receptors revealed by single-quantum dot tracking*, Science **302**, 442 (2003).

[35] B. Lamprecht, J. R. Krenn, A. Leitner, and F. R. Aussenegg, *Particle-plasmon decay-time determination by measuring the optical near-field's autocorrelation: Influence of inhomogeneous line broadening*, Appl. Phys. B **69**, 223 (1999).

[36] F. Stietz, J. Bosbach, T. Wenzel, T. Vartanyan, A. Goldmann, and F. Träger, *Decay times of surface plasmon excitation in metallic nanoparticles by persistent spectral hole burning*, Phys. Rev. Lett. **84**, 5644 (2000).

[37] J. Bosbach, C. Hendrich, F. Stietz, T. Vartanyan, and F. Träger, *Ultrafast dephasing of surface plasmon excitation in silver nanoparticles: Influence of particle size, shape, and chemical surrounding*, Phys. Rev. Lett. **89**, 257404 (2002).

[38] T. Klar, M. Perner, S. Grosse, G. von Plessen, W. Spirkl, and J. Feldmann, *Surface plasmon resonances in single metallic nanoparticles*, Phys. Rev. Lett. **80**, 4249 (1998).

[39] C. Sönnichsen, T. Franzl, T. Wilk, G. von Plessen, and J. Feldmann, *Plasmon resonances in large noble-metal clusters*, New J. Phys. **4**, 93.1 (2002).

[40] A. Arbouet, D. Christofilos, N. D. Fatti, F. Vallée, J. R. Huntzinger, L. Arnaud, P. Billaud, and M. Broyer, *Direct measurement of the single-metal-cluster optical absorption*, Phys. Rev. Lett. **93**, 127401 (2004).

[41] M. A. van Dijk, M. Lippitz, and M. Orrit, *Detection of acoustic oscillations of single gold nanospheres by time-resolved interferometry*, Phys. Rev. Lett. **95**, 267406 (2005).

[42] S. Berciaud, L. Cognet, G. A. Blab, and B. Lounis, *Photothermal heterodyne imaging of individual nonfluorescent nanoclusters and nanocrystals*, Phys. Rev. Lett. **93**, 257402 (2004).

[43] S. Berciaud, L. Cognet, P. Tamarat, and B. Lounis, *Observation of intrinsic size effects in the optical response of individual gold nanoparticles*, Nano Lett. **5**, 515 (2005).

[44] S. Berciaud, D. Lasne, G. A. Blab, L. Cognet, and B. Lounis, *Photothermal heterodyne imaging of individual nanoparticles: Theory versus experiment*, Phys. Rev. B **73**, 045424 (2006).

[45] U. Kreibig and L. Genzel, *Optical absorption of small metallic nanoparticles*, Surf. Sci. **156**, 678 (1985).

[46] R. H. Doremus, *Optical properties of small gold particles*, J. Chem. Phys. **40**, 2389 (1964).

[47] R. H. Doremus, *Optical properties of small silver particles*, J. Chem. Phys. **42**, 414 (1965).

[48] A. Kawabata and R. Kubo, *Electronic properties of fine metallic particles. III. Plasma resonance absorption*, J. Phys. Soc. Jpn. **21**, 1765 (1966).

[49] R. Kubo, *Statistical-mechanical theory of irreversible processes. I. General theory and simple applications to magnetic and conduction problems*, J. Phys. Soc. Japan **12**, 570 (1957).

[50] P. M. Chaikin and T. C. Lubensky, *Principles of condensed matter physics* (Cambridge University Press, Cambridge, 2000).

[51] D. Pines and P. Nozières, *The theory of quantum liquids. Vol. I: Normal Fermi liquids* (Benjamin, New York, 1966).

[52] R. Ruppin and H. Yatom, *Size and shape effects on the broadening of the plasmon resonance absorption in metals*, Phys. Status Solidi B **74**, 647 (1976).

[53] E. Merzbacher, *Quantum mechanics* (John Wiley & Sons, New York, 1970), 2nd ed.

[54] A. L. Fetter and J. D. Walecka, *Quantum theory of many-particle systems* (Dover, Mineola, 2003), corrected reprint ed.

[55] A. Zangwill and P. Soven, *Density-functional approach to local-field effects in finite systems: Photoabsorption in the rare gases*, Phys. Rev. A **21**, 1561 (1980).

[56] M. J. Stott and E. Zaremba, *Linear-response theory within the density-functional formalism: Application to atomic polarizabilities*, Phys. Rev. A **21**, 12 (1980).

[57] N. D. Lang and W. Kohn, *Theory of metal surfaces: Charge density and surface energy*, Phys. Rev. B **1**, 4555 (1970).

[58] E. K. U. Gross, J. F. Dobson, and M. Petersilka, *Density functional theory of time-dependent phenomena*, vol. 181 of *Topics in Current Chemistry* (Springer, Berlin, 1996), in *Density functional theory II*, ed. by R. F. Nalewajski.

[59] O. Gunnarsson and B. I. Lundqvist, *Exchange and correlation in atoms, molecules, and solids by the spin-density-functional formalism*, Phys. Rev. B **13**, 4274 (1976).

[60] L. G. Gerchikov, C. Guet, and A. N. Ipatov, *Multiple plasmons and anharmonic effects in small metallic clusters*, Phys. Rev. A **66**, 053202 (2002).

[61] J.-Y. Bigot, J.-C. Merle, O. Cregut, and A. Daunois, *Electron dynamics in copper metallic nanoparticles probed with femtosecond optical pulses*, Phys. Rev. Lett. **75**, 4702 (1995).

[62] V. Halté, J. Guille, J.-C. Merle, I. Perakis, and J.-Y. Bigot, *Electron dynamics in silver nanoparticles: Comparison between thin films and glass embedded nanoparticles*, Phys. Rev. B **60**, 11738 (1999).

[63] J.-Y. Bigot, V. Halté, J.-C. Merle, and A. Daunois, *Electron dynamics in metallic nanoparticles*, Chem. Phys. **251**, 181 (2000).

[64] N. D. Fatti, F. Vallée, C. Flytzanis, Y. Hamanaka, and A. Nakamura, *Electron dynamics and surface plasmon nonlinearities in metal nanoparticles*, Chem. Phys. **251**, 215 (2000).

[65] C. Voisin, N. D. Fatti, D. Christofilos, and F. Vallée, *Ultrafast electron dynamics and optical nonlinearities in metal nanoparticles*, J. Phys. Chem. B **105**, 2264 (2001).

[66] P.-A. Hervieux, A. Benabbas, V. Halté, and J.-Y. Bigot, *Electronic temperature effects on the optical response of silver nanoparticles*, Eur. Phys. J. D **24**, 185 (2003).

[67] P.-A. Hervieux and J.-Y. Bigot, *Surface plasmon dynamics of simple metal clusters excited with femtosecond optical pulses*, Phys. Rev. Lett. **92**, 197402 (2004).

[68] F. Calvayrac, P.-G. Reinhard, and E. Suraud, *Spectral signals from electronic dynamics in sodium clusters*, Ann. Phys. (N.Y.) **255**, 125 (1997).

[69] F. Calvayrac, P.-G. Reinhard, E. Suraud, and C. A. Ullrich, *Nonlinear electron dynamics in metal clusters*, Phys. Rep. **337**, 493 (2000).

[70] A. Domps, P.-G. Reinhard, and E. Suraud, *Semi-classical electron dynamics in metal clusters beyond mean-field*, Ann. Phys. (N.Y.) **280**, 211 (2000).

[71] G. F. Bertsch, N. V. Giai, and N. V. Mau, *Cluster ionization via two-plasmon excitation*, Phys. Rev. A **61**, 033202 (2000).

[72] R. Schlipper, R. Kusche, B. von Issendorff, and H. Haberland, *Multiple excitation and lifetime of the sodium cluster plasmon resonance*, Phys. Rev. Lett. **80**, 1194 (1998).

[73] R. Schlipper, R. Kusche, B. von Issendorff, and H. Haberland, *Thermal emission of electrons from highly excited sodium clusters*, Appl. Phys. A: Mater. Sci. Process. **72**, 255 (2001).

[74] U. Weiss, *Quantum dissipative systems* (World Scientific, Singapore, 1993).

[75] W. Kohn, *Cyclotron resonance and de Haas-van Alphen oscillations of an interacting electron gas*, Phys. Rev. **123**, 1242 (1961).

[76] J. D. Jackson, *Classical electrodynamics* (John Wiley & Sons, New York, 1975), 2^{nd} ed.

[77] L. Serra, F. Garcías, J. Navarro, N. Barberán, M. Barranco, and M. Pi, *Electronic surface excitations of cavities in metals*, Phys. Rev. B **46**, 9369 (1992).

[78] C. Cohen-Tannoudji, B. Diu, and F. Laloë, *Mécanique quantique* (Hermann, Paris, 1997).

[79] G. F. Bertsch, *An RPA program for jellium spheres*, Comput. Phys. Commun. **60**, 247 (1990).

[80] R. A. Molina, D. Weinmann, and R. A. Jalabert, *Oscillatory size dependence of the surface plasmon linewidth in metallic nanoparticles*, Phys. Rev. B **65**, 155427 (2002).

[81] R. A. Molina, D. Weinmann, and R. A. Jalabert, *Oscillatory behavior and enhancement of the surface plasmon linewidth in embedded noble metal nanoparticles*, Eur. Phys. J. D **24**, 127 (2003).

[82] C. Cohen-Tannoudji, J. Dupont-Roc, and G. Grynberg, *Atom-photon interactions: Basic processes and applications* (Wiley-VCH, New York, 1992).

[83] B. Diu, C. Guthmann, D. Lederer, and B. Roulet, *Physique statistique* (Hermann, Paris, 1989).

[84] C. W. Gardiner and P. Zoller, *Quantum Noise*, Springer Series in Synergetics (Springer-Verlag, Berlin, 2000), 2^{nd} enlarged ed.

[85] Y. Kurzweil and R. Baer, *Quantum memory effects in the dynamics of electrons in gold clusters*, Phys. Rev. B **73**, 075413 (2006).

[86] W. E. Lamb and R. C. Retherford, *Fine structure of the hydrogen atom by a microwave method*, Phys. Rev. **72**, 241 (1947).

[87] W. E. Lamb, *Anomalous fine structure of hydrogen and singly ionized helium*, Rep. Prog. Phys. **14**, 19 (1951).

[88] G. Lindblad, *On the generators of quantum dynamical semigroups*, Commun. Math. Phys. **48**, 119 (1976).

[89] V. Gorini, A. Kossakowski, and E. C. G. Sudarshan, *Completely positive dynamical semigroups of N-level systems*, J. Math. Phys. **17**, 821 (1976).

[90] D. F. Walls and G. J. Milburn, *Quantum Optics* (Springer-Verlag, Berlin, 1994).

[91] A. R. Edmonds, *Angular momentum in quantum mechanics* (Princeton University Press, Princeton, 1960), 2$^{\text{nd}}$ ed.

[92] C. Yannouleas, *The wall formula for nuclear dissipation as a special limit of RPA damping*, Nucl. Phys. A **439**, 336 (1985).

[93] M. Abramowitz and I. A. Stegun, eds., *Handbook of mathematical functions* (Dover, New York, 1970), 9$^{\text{th}}$ ed.

[94] M. C. Gutzwiller, *Chaos in classical and quantum mechanics* (Springer-Verlag, Berlin, 1990).

[95] S. Link and M. A. El-Sayed, *Size and temperature dependence of the plasmon absorption of colloidal gold nanoparticles*, J. Phys. Chem. B **103**, 4212 (1999).

[96] U. Kreibig, *Electronic properties of small silver nanoparticles: The optical constants and their temperature dependence*, J. Phys. F **4**, 999 (1974).

[97] J. M. Pacheco and R. A. Broglia, *Effect of surface fluctuations in the line shape of plasmon resonances in small metal clusters*, Phys. Rev. Lett. **62**, 1400 (1989).

[98] G. F. Bertsch and D. Tománek, *Thermal line broadening in small metal clusters*, Phys. Rev. B **40**, 2749 (1989).

[99] C. Yannouleas, E. Vigezzi, and R. A. Broglia, *Evolution of the optical properties of alkali-metal microclusters towards the bulk: The matrix random-phase approximation description*, Phys. Rev. B **47**, 9849 (1993).

[100] J. Babst and P.-G. Reinhard, *A separable approach to linear response in Na clusters*, Z. Phys. D **209**, 209 (1997).

[101] L. Rodríguez-Sánchez, J. Rodríguez, C. Blanco, J. Rivas, and A. López-Quintela, *Kinetics and mechanism of the formation of Ag nanoparticles by electromechanical techniques: A plasmon and cluster time-resolved spectroscopic study*, J. Phys. Chem. B **109**, 1183 (2005).

[102] K. Hagino, G. F. Bertsch, and C. Guet, *Variational RPA for the dipole surface plasmon in metal clusters*, Nucl. Phys. A **731**, 347 (2004), see also arXiv/cond-mat/0306058.

[103] M. Seidl and J. P. Perdew, *Size-dependent ionization energy of metallic cluster: Resolution of the classical image-potential paradox*, Phys. Rev. B **50**, 5744 (1994).

[104] O. Bohigas, A. M. Lane, and J. Mortell, *Sum rules for nuclear collective excitations*, Phys. Rep. **51**, 267 (1979).

[105] G. Bertsch and W. Ekardt, *Application of sum rules to the response of small metal particles*, Phys. Rev. B **32**, 7659 (1985).

[106] H. Haug and S. W. Koch, *Quantum theory of the optical and electronic properties of semiconductors* (World Scientific, Singapore, 1994).

[107] J. Z. Gu and H. A. Weidenmüller, *Coulomb excitation of double giant dipole resonances*, Nucl. Phys. A **690**, 382 (2001).

[108] G. F. Bertsch and H. Feldmeier, *Variationnal approach to anharmonic collective motion*, Phys. Rev. C **56**, 839 (1997).

[109] J. Ritman, F.-D. Berg, W. Kühn, V. Metag, R. Novotny, M. Notheisen, P. Paul, M. Pfeiffer, O. Schwalb, H. Löhner, et al., *First observation of the Coulomb-excited double giant dipole resonance in ^{208}Pb via double-γ decay*, Phys. Rev. Lett. **70**, 533 (1993).

[110] F. Catara, P. Chomaz, and N. V. Giai, *Two-plasmon excitation in metallic clusters*, Phys. Rev. B **48**, 18207 (1993).

[111] K. Hagino, *Anharmonicity of the dipole resonance of metal clusters*, Phys. Rev. B **60**, R2197 (1999).

[112] M. Koskinen and M. Manninen, *Photoionization of metal clusters*, Phys. Rev. B **54**, 14796 (1996).

[113] I. S. Gradshteyn and I. M. Ryzhik, *Table of integrals, series, and products* (Academic Press, San Diego, 2000), 6^{th} ed.

[114] F. Abelès, ed., *Optical properties of solids* (North-Holland, Amsterdam, 1972).

[115] K.-P. Charlé, W. Schulze, and B. Winter, *The size dependent shift of the surface plasmon absorption band of small spherical metal particles*, Z. Phys. D: At., Mol. Clusters **12**, 471 (1989).

[116] L. Landau and E. Lifchitz, *Quantum mechanics* (Pergamon, New York, 1959).

[117] G.-L. Ingold, R. A. Jalabert, and K. Richter, *Semiclassical analysis of level widths for one-dimensional potentials*, Am. J. Phys. **69**, 201 (2001).

[118] M. C. Desjonquères and D. Spanjaard, *Concepts in surface physics* (Springer-Verlag, Berlin, 1996), 2nd ed.

[119] M. Koskinen, P. O. Lipas, E. Hammerén, and M. Manninen, *Application of the nuclear shell model to atomic clusters*, Europhys. Lett. **19**, 165 (1992).

[120] M. Koskinen, P. O. Lipas, M. Manninen, J. Toivanen, and M. J. Puska, *Nuclear shell model applied to metallic clusters*, Z. Phys. D **26**, 261 (1993).

[121] M. Koskinen, M. Manninen, and P. O. Lipas, *Configuration-interaction calculations of jellium clusters by the nuclear shell model*, Phys. Rev. B **49**, 8418 (1994).

[122] M. Koskinen, M. Manninen, and P. O. Lipas, *Many-body origin of the plasmon resonance in small metal clusters*, Z. Phys. D **31**, 125 (1994).

[123] F. Catara, D. Gambacurta, M. Grasso, and M. Sambataro, *Configuration interaction study of single and double plasmon excitations in* Na_8, Phys. Lett. A **349**, 345 (2006).

[124] M. Brack and R. K. Bhaduri, *Semiclassical physics*, Frontiers in Physics (Addison-Wesley, Reading, 1997).

[125] M. C. Gutzwiller, *The semi-classical quantization of chaotic Hamiltonian systems*, Lecture Notes for the Summer School Les Houches (1989).

[126] K. Richter, *Semiclassical theory of mesoscopic quantum systems*, vol. 161 of *Springer tracts in modern physics* (Springer-Verlag, Berlin, 2000).

[127] R. A. Jalabert, *The semiclassical tool in mesoscopic physics* (Soc. Italiana di Fisica, Bologna, 2000), proceedings of the International School of Physics "Enrico Fermi", Course CXLIII, ed. by G. Casati, I. Guarneri, and U. Smilansky.

[128] J. H. van Vleck, *The correspondence principle in the statistical interpretation of quantum mechanics*, Proc. Natl. Acad. Sci. USA **14**, 178 (1928).

[129] R. P. Feynman, *Space-time approach to non-relativistic quantum mechanics*, Rev. Mod. Phys. **85**, 613 (1948).

[130] G.-L. Ingold, *Path integrals and their application to dissipative quantum systems*, vol. 611 of *Lecture Notes in Physics* (Springer-Verlag, Berlin, 2002).

[131] H. Goldstein, *Classical mechanics* (Addison-Wesley, Reading, 1981), 2nd ed.

[132] L. Landau and E. Lifchitz, *Mécanique* (Mir, Moscou, 1982).

[133] R. Balian and C. Bloch, *Distribution of eigenfrequencies for the wave equation in a finite domain: III. Eigenfrequency density oscillations*, Ann. Phys. (N.Y.) **69**, 76 (1972).

[134] M. V. Berry and M. Tabor, *Closed orbits and the regular bound spectrum*, Proc. R. Soc. Lond. A **349**, 101 (1976).

[135] M. V. Berry and M. Tabor, *Calculating the bound spectrum by path summation in action-angle variables*, J. Phys. A: Math. Gen. **10**, 371 (1977).

[136] R. E. Langer, *On the connection formulas and the solutions of the wave equation*, Phys. Rep. **51**, 669 (1937).

[137] J. Hainz and H. Grabert, *Centrifugal terms in the WKB approximation and semiclassical quantization of hydrogen*, Phys. Rev. A **60**, 1698 (1999).

[138] M. V. Berry and K. E. Mount, *Semiclassical approximations in wave mechanics*, Rep. Prog. Phys. **35**, 315 (1972).

[139] J. B. Keller and S. I. Rubinow, *Asymptotic solution of eigenvalue problems*, Ann. Phys. (N.Y.) **9**, 24 (1960).

[140] E. T. Whittaker and G. N. Watson, *A course of modern analysis* (Cambridge University Press, Cambridge, 1986), 4^{th} ed.

[141] M. Brack and S. R. Jain, *Analytical tests of Gutzwiller's trace formula for harmonic-oscillator potentials*, Phys. Rev. A **51**, 3462 (1995).